SEISMIC DESIGN AND EVALUATION OF MOMENT RESISTING FRAMES USING ELASTOMERIC DAMPERS

CHRISTOS A. BASAGIANNIS

A thesis submitted to the degree of

Doctor of Philosophy

University of Oxford

2018

Abstract

This study evaluates the characteristics of elastomeric dampers, and assesses their effectiveness in mitigating the effects of dynamic loading. As part of this evaluation a series of characterization tests were carried out in order to extract the main mechanical properties of the elastomer material in a range of strain amplitudes, loading frequencies, and ambient temperatures, since it has been proved that elastomeric materials depend on these parameters. It was found that strain amplitude was the most dominant factor not only regarding the values of their mechanical properties (shear storage modulus, and loss factor) but also with regard to the shape of the hysteresis loops. At the same time frequency was shown to have only a minor effect on their behaviour.

Based on the Generalised Maxwell Model, a new hysteretic model was developed and proposed in this thesis which is able to capture the behaviour of the material. As part of this model an equation was derived which describes the force-displacement relationship of the Generalised Maxwell Model for N Maxwell elements in time domain, and formed the basis for the proposed model.

The seismic performance of a 10 storey steel moment resisting frame was evaluated, and the effect of the dampers on the frame's performance was examined. The dampers were designed to provide an additional 10% damping to the Eurocode 8 compliant building. The structure was tested with and without dampers for two different levels of earthquake intensity. It was shown that the elastomeric dampers led to significant decrease of displacements, accelerations, base shear forces, and permanent damage of the structure, even after ground motions scaled to the Maximum Considered Earthquake level.

Lastly, Real Time Substructure tests were performed in order to further validate the proposed hysteretic model. Both SDOF and MDOF systems equipped with elastomeric dampers were tested under scaled version of the ElCentro ground motion and the corresponding force-displacement relationship of the dampers was compared with the analytical model. The results showed that the proposed model is able to capture the dynamic performance of the dampers under realistic earthquake conditions.

Acknowledgements

This study was conducted at the Engineering Department of Oxford University. I deeply appreciate the guidance and support of my supervisor Professor Martin Williams during all these years. I have to also thank Robin for his help regarding not only the actual implementation of the experiments but the background theory behind them, and Clive for his help at the laboratory. Special thanks to TARRC for providing us with the elastomeric specimens. Furthermore, I would like to deeply thank Mark for trusting me and believing in me, Antonis, Eleni, Maria, Marios, and especially Onelia for their support during all these years, and to everyone that helped me spend these years in Oxford as creative and happily as possible.

This dissertation is dedicated to the memory of my mother for her love, support, and patience during my first 23 years of my life. I would also like to thank my father for his innumerable patience and support, and for his guidance in a lot of aspects of my life. Lastly, this dissertation is also dedicated to my sister Katerina, and to the memory of my beloved uncle, Nasos.

Contents

List of Figures

Chapter 1

Introduction

The basic concept of conventional earthquake-resistant design aims to provide an acceptable structural performance level during the earthquakes. This level is usually dictated by the importance of the building and by the local authorities. The most common design philosophy is a non-collapse requirement under strong and rare earthquakes, while structures are also expected to experience no damage under more frequent and weaker earthquakes. However, the socio-economic reality, especially in developed countries, has pushed the barrier considerable higher [28], leading to design of damage-free or minimal-damage structures. Important structures such as hospitals, schools, and museums are therefore desired to exhibit a more advanced level of earthquake protection, in order to be functional even after a strong seismic event.

A variety of approaches of earthquake protection has been proposed, including base isolation, passive dissipative devices, and active or semi-active control devices. Dissipative devices aim to absorb a portion of the seismic energy input to a structure, which would otherwise be dissipated through mechanisms corresponding directly to structural damage. The most promising and feasible approach is the use of passive dissipative devices, which are likely to be most reliable in an extreme event, being activated by the movements of the main structural system without the need of any external power source.

The focus of this research is on passive dissipative devices, and more specifically on elastomeric dampers. Among the various forms of passive dissipative devices,

there has been much focus on fluid viscous, and metallic dampers, but elastomers offer a promising alternative and have been under-investigated. Their main advantages compared to other types of dissipative devices include their contribution of both stiffness and damping to the structure regardless the type of external loading, their low dependence on loading frequency compared to similar type of visco-elastic dampers, and their full recovery after the removal of the source which created the deformation.

The most common scenario is to apply the dampers between the connection of steel diagonal braces and the middle length of the upper floor beam. This method can be either designed in a new enhanced building, or as a retrofitting procedure of an existing one. Due to the elastomer's dependence on strain amplitude, loading frequency, and ambient temperature, it is very difficult to accurately model it and capture its dynamic characteristics during dynamic loading. Hence, the conventional way of modelling this type of damper is to assign an equivalent Kelvin-Voigt model with stiffness and damping values corresponding to the natural frequency of the structure and an accepted level of lateral drift. A new hysteretic model has been proposed as part of this research, based on sweep amplitude and frequency tests which has shown that it can accurately model the dampers behaviour for a specific range of strain amplitudes, loading frequencies, and ambient frequencies. It was found that the dominant factor which mainly controls not only their mechanical properties but also the shape of the hysteresis loop was the strain amplitude. However, both loading frequency and ambient temperature also affected the dampers' capacity to dissipate energy.

1.1 Research Objectives

Elastomeric dampers provide a promising means of earthquake protection. However, the application of this type of dampers as a mean of providing relatively uniform distribution of stiffness and damping throughout the height of buildings has not been widely used. In fact most of the elastomer applications in the earthquake community until now have been focused on dissipating energy through base isolation systems.

Moreover, a lot of models which target to capture the dynamic characteristics of the elastomeric dampers have been proposed and presented here 2.2.8. However, lack of clear understanding of elastomer properties, especially how they vary with frequency, amplitude, and time, and limited experimental validation of their performance still exists. Most of the proposed models are either based on linearised properties of the material or parameter optimization based on minimization of analytical formulas of shear storage modulus and the corresponding experimental values. Even though these models can effectively capture the elastomer's behaviour under specific conditions (specific values of temperature, frequency, and limited range of strain amplitudes), discrepancies may exist when the dampers function under a wider range of these parameters. Furthermore, even though parameters of the analytical models are optimised based on shear storage minimization techniques (analytical expressions of shear storage modulus are extracted in frequency domain for specific values of sinusoidal input loading and do not take into account any strain amplitude alterations), this does not necessarily mean that can capture the actual hysteresis behaviour of the dampers. The main innovative part of this research was to experimentally evaluate elastomer's characteristics, and define a new model which would be able to describe the behaviour of the dampers due to dynamic loading. Therefore, the main objectives of this research are:

- Evaluate the mechanical properties of the material
- Develop an analytical model for the dampers which would be adequate for non linear analyses of structures under earthquake loading
- Demonstrate through non-linear structural analysis the structural seismic performance enhancement that can be achieved through retrofitting with elastomeric dampers
- Validation of the proposed Adaptive Time Series method as a new time delay minimization technique applying it to elastomeric dampers
- Further validation of the proposed hysteretic model of the elastomeric dampers under realistic conditions using Real Time Substructure tests

1.2 Outline of Thesis

The remaining chapters of the thesis are organised as follows:

- *Chapter 2* introduces the reader to the main concept of passive energy dissipation and earthquake protection systems, the different types of dampers used in the past, while at the same time reviewing the previous work carried out by other researchers. At the end of this chapter the most widely used approaches of modelling elastomeric dampers are described.

- *Chapter 3* describes the experiments which were carried out in order to extract the main mechanical characteristics of the material. Since the dampers depend on strain amplitude, loading frequency, and ambient temperature, a series of cyclic tests was carried out in a range of values for the aforementioned parameters.

- *Chapter 4* presents the proposed hysteretic model which is based on sweep amplitude tests under different loading frequencies and ambient temperatures. The first part of this chapter focuses on developing a force-displacement model in time domain for the well known Generalised Maxwell Model, for N Maxwell elements. This constitutes the basis of the proposed model described later in the same chapter.

- *Chapter 5* describes a design process of a 10 storey steel moment resisting frame with elastomeric dampers, which targets an enhanced performance level. The seismic response of this building with and without the dampers is evaluated based on non linear time history analyses. The elastomeric dampers were analytically modelled based on the findings of Chapter 4.

- *Chapter 6* boosts our confidence with regard to the validation and the use of the hysteretic model of Chapter 4, by carrying out Real Time Substructure tests for both SDOF and MDOF simple steel frames equipped with elastomeric dampers. In order to minimise the time delay which has been proved to cause instability to the system, a new method proposed by Malloy and Blakeborough

(unpublished until now) was used.

- *Chapter 7* summarises the findings and conclusions of this research and suggests directions for future work.

Chapter 2

Literature Review

2.1 Introduction

Conventional seismic design is based on linear analysis and dictates that the performance of structures during earthquakes depends on the lateral force resisting system being able to absorb and dissipate energy for a number of cycles[31]. This design concept therefore requires a combination of strength and ductility in order to provide resistance to lateral loads [31, 114]. For major earthquakes, the structural design engineer relies upon the inherent ductility of conscientiously detailed buildings to prevent catastrophic results [114]. Energy dissipation is designed to occur in specially designed ductile plastic hinge regions of beams and columns bases. This design approach has been considered acceptable because of economic considerations provided, of course, that structural collapse is prevented and life safety is ensured [31]. However, under large earthquakes the damage may be irrepairable, with potential catastrophic and uneconomical results. Moreover, this conventional seismic philosophy cannot easily be applied to all types of structures. New structures are often designed to more demanding performance criteria, which may require the structure to remain linear or to have minimal damage. At the same time there are numerous existing structures with insufficient strength or ductility, which need strengthening in order to meet current seismic demands.

A lot of different approaches have been developed in order to improve the earthquake response performance and damage control of buildings, bridges, and other

structures, and can be divided into four groups: base isolation, a technique which is based on a separation of the main structure from its foundation incorporating flexible bearings or pads; passive systems, such as supplemental energy dissipation devices; active systems, which require the active participation of mechanical devices whose characteristics are made to change during the building response on the basis of current response measurements; and hybrid systems, which combine the passive and active systems in a manner so that safety of the building is not compromised even if the active system fails [48].

With regard to passive dissipative devices, much focus has been given to viscous and metallic dampers; however elastomeric dampers, which could form an alternative solution regarding the seismic protection of buildings, have received much less attention. Their characteristics alter in time when different strain amplitudes, loading frequencies, and ambient temperatures are applied, making the proposal of a hysteretic model a very difficult and challenging task. Furthermore, apart from lack of clear understanding on how elastomers' properties vary with time, limited experimental validation of their performance is another limiting factor. Finally, combining these limitations with the fact that the majority of elastomeric applications and proposed models has been focused on base isolation methods creates the need of further analytical evaluation and experimental validation of elastomeric dampers as passive dissipative devices being incorporated throughout the height of a building as uniformly as possible.

This section presents general background information and fundamental principles of the aforementioned earthquake protection systems. A more detailed insight into passive energy dissipation devices is given, and much more attention is paid to the behaviour of the viscoelastic and elastomeric materials which are used as dampers.

2.2 Passive Energy Dissipation Systems

The four groups mentioned earlier, are summarised in table 2.1. Each one of these approaches is different and may be applied based on the needs of the structure, either if the main target is to achieve enhanced seismic performance or to strengthen and

retrofit an already existing structure to cope under modern anti-seismic codes.

Base isolation involves placing isolation devices at the foundation of a structure, with the aim of protecting it from the damaging effects of earthquakes by uncoupling it from the ground [65]. The main philosophy is to provide a layer of low lateral stiffness between the foundation and the superstructure. This layer causes the natural period to highly increase, resulting in reduced input seismic loads, along with a large displacement. However, this displacement is concentrated at the base isolation system, while the structure's internal deformations remain relatively low. Furthermore, modern seismic isolation systems incorporate energy dissipation mechanisms. Examples are high damping elastomeric bearings, lead plugs in elastomeric bearings, mild steel dampers, fluid viscous dampers, and friction in sliding bearings[31]. Finally, it is worth mentioning that the inherent damping of the base isolation mechanism and the corresponding hysteretic energy are of minor importance regarding the reduced earthquake structural response. Base isolation is mainly so effective due to the lengthening of the natural period [27].

Table 2.1: Structural Protective Systems

Seismic Isolation	**Passive Energy Dissipation**	**Semi-Active and Active Control**
Elastomeric Bearings	Metallic Dampers	Active Bracing Systems
	Friction Dampers	Active Mass Dampers
	Viscoelastic Dampers	Variable Stiffness
Lead Rubber Bearings	Elastomeric Dampers	or Damping Systems
	Viscous Fluid Dampers	Smart Materials
	Tuned Mass Dampers	
Sliding Friction Pendulum	Tuned Liquid Dampers	

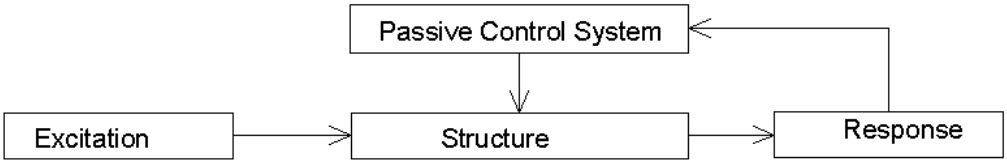

Figure 2.1: Passive Control Systems[31]

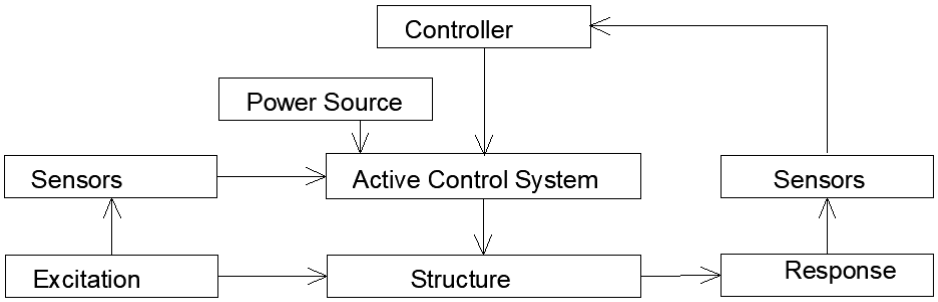

Figure 2.2: Active Control Systems[31]

The distinction between active and passive control systems is shown in figs. 2.1 and 2.2. Passive control systems (energy dissipation devices, dynamic vibration absorbers) and seismic isolation systems develop motion control forces at the points of attachment of the system. The power needed to generate these forces stems from the motion of the points of attachment during the loading history. Contrary to semi-active and active control systems, there is no need for external supply of power[114]. Moreover, an essential advantage over base isolation systems is their proven efficiency against both wind and earthquake forces[114]. In case of active control systems, the motion control forces are determined by a controller based on feedback information from the measured response, which is carried out by sensors, of the structure and/or feedforward information from the external excitation[115]. The recorded measurements from the response and/or excitation are monitored by a controller (a computer) which, based on a pre-determined control algorithm, determines the appropriate control signal for operation of the actuators [122]. Hybrid or semi-active control systems on the other hand, unlike fully active systems, cannot add energy to the system. They originate from passive control systems which have been subsequently modified to allow for the adjustment of mechanical properties[122], requiring only nominal amounts of external energy. For more information and actual implementation for base isolation systems see Kelly [65], and for semi-active and active control systems at Symans and Constantinou [122, 31], Soong[115].

The focus of this research is on passive energy dissipation devices, and more specifically on elastomeric dampers. Their relative simplicity with regard to incorporation into buildings and their modelling into Finite Element softwares, alongside

the fact that passive devices in contrast with active/semi active systems do not require any external power supply (which may become a critical factor during a strong earthquake), and their 40 years of history of research and structural applications make them more relatively reliable and preferable. Hence, a brief introduction about the main types of dampers, and a more comprehensive and detailed description of ViscoElastic and Elastomeric dampers will be presented in this section.

2.2.1 Dynamic Equations of Structures with Dampers

Consider the lateral motion of a Single Degree Of Freedom (SDOF) system, consisting of mass, m, stiffness, k, and linear damper with viscous damping coefficient, c (see Figure 2.3):

$$m\ddot{\mathbf{x}} + c\dot{\mathbf{x}} + k\mathbf{x} = -m\ddot{\mathbf{x}}_{\mathrm{g}} \tag{2.1}$$

where $\mathbf{x}$ and $\mathbf{x}_{\mathrm{g}}$ represent the time-dependent structure's displacement of the mass relative to the ground, and ground displacement respectively. It can also be written in the following form:

$$\ddot{\mathbf{x}} + 2\zeta\omega\dot{\mathbf{x}} + \omega^2\mathbf{x} = -\ddot{\mathbf{x}}_{\mathrm{g}} \tag{2.2}$$

Consider now the addition of a generic damper device (fig. 2.3), which may provide not only supplemental damping, but also stiffness, and perhaps mass. Hence, the symbol Γ corresponds for the whole contribution of the dampers to the SDOF system [114]:

$$m\ddot{\mathbf{x}} + c\dot{\mathbf{x}} + k\mathbf{x} + \Gamma = -(m + \bar{m})\ddot{\mathbf{x}}_{\mathrm{g}} \tag{2.3}$$

where $\overline{\mathrm{m}}$ represents the mass of the added element and $\Gamma = \bar{k}x + \bar{c}\dot{x} + \bar{m}\ddot{x}$. It can be seen that adding a damper to the original structure leads to a new more stiff, more damped, and heavier structure. This tends to reduce the seismic response of the structure, even though this is not always the case, since it should be treated like a new structure with different characteristics, instead of an improved version of the

prototype. However, if Γ has only damping contributions, then the SDOF response will be always reduced, since it will be equivalent to the initial system with increased damping. For all structures, careful analysis must be performed in order to ensure the beneficial effects of the added elements.

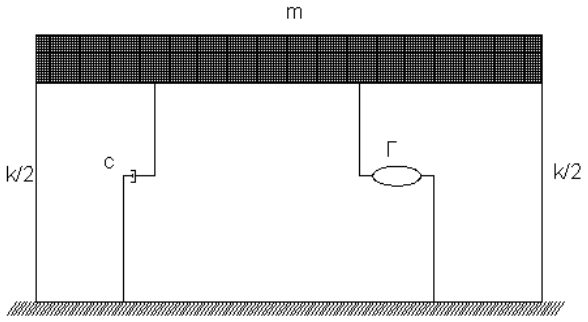

Figure 2.3: SDOF structure with added damper

In the case of Multi Degree of Freedom (MDOF) systems, Eq. 2.3 is adjusted to:

$$M\ddot{x} + C\dot{x} + Kx + \Gamma = -(M + \bar{M})\ddot{x}_{\mathrm{g}} \tag{2.4}$$

where M, C, and K are the mass, damping, and stiffness matrices of the MDOF structure, and Γ symbolizes a matrix of operators, which represent the added damper to the MDOF system. Since, this section covers only the basic principles, when added dampers are being used, the assumption that the damper's behaviour is a linear combination of mass, damping, and stiffness is made:

$$\Gamma = \bar{K}x + \bar{C}\dot{x} + \bar{M}\ddot{x} \tag{2.5}$$

Then, Eq. 2.4 is rewritten as:

$$\hat{M}\ddot{x} + \hat{C}\dot{x} + \hat{K}x = -\hat{M}\ddot{x}_{\mathrm{g}} \tag{2.6}$$

where:

$$\hat{M} = M + \bar{M} \tag{2.7a}$$

$$\hat{C} = C + \bar{C} \tag{2.7b}$$

$$\hat{K} = K + \bar{K} \tag{2.7c}$$

Now, Eq. 2.6 is in the form of classical matrix dynamic analysis problem. Assuming that all the matrix coefficients are constant, Eq. 2.6 represents a set of N linear second order ordinary differential equations with constant coefficients. Its solution can be computationally demanding, unless it can be uncoupled. This can be achieved, if $\hat{M}$, $\hat{C}$, and $\hat{K}$ are diagonalized. This can not be done for arbitrary matrices $\hat{M}$, $\hat{C}$, and $\hat{K}$. However, under certain restrictions on the damping matrix, $\hat{C}$, the transformation to modal coordinates can be achieved as shown below[114, 31]. Considering the generalized eigenvalue problem of the MDOF system:

$$(\hat{K} - \omega_0^2 \hat{M})\phi = 0 \tag{2.8}$$

where ω_0 represents the undamped natural frequency of the MDOF structure, including the added dampers, and ϕ is the associated mode shape vector. The MDOF system consists of N natural frequencies, and mode shapes, ω_{0i}, and ϕ_i respectively. Also, the mode shapes satisfy the following orthogonality conditions:

$$\phi_i^T \hat{M} \phi_j = \begin{cases} 1 & \text{for} \quad i = j \\ 0 & \text{for} \quad i \neq j \end{cases} \tag{2.9a}$$

$$\phi_i^T \hat{K} \phi_j = \begin{cases} \omega_{0i}^2 & \text{for} \quad i = j \\ 0 & \text{for} \quad i \neq j \end{cases} \tag{2.9b}$$

Eq. 2.9 provides the basis for transformation which can be applied to the whole MDOF system. The corresponding mode shape vectors are the columns of the NxN matrix, Φ. Hence, the relative displacements vector, x, can be rewritten:

$$x = \sum_{r=1}^{N} \phi_r q_r(t) = \Phi q(t) = \Phi q \tag{2.10}$$

where q is the vector of modal coordinates. Combining, Eqs. 2.6, 2.9, and 2.10 the equation of motion for the MDOF system can be written as:

$$\begin{aligned} \Phi^T \hat{M} \Phi \ddot{q} + \Phi^T \hat{C} \Phi \dot{q} + \Phi^T \hat{K} \Phi q = -\Phi^T \hat{M} e \ddot{x}_g \\ \hat{\mathbf{M}} \ddot{q} + \hat{\mathbf{C}} \dot{q} + \hat{\mathbf{K}} q = -\ddot{\mathbf{X}}_g \end{aligned} \tag{2.11}$$

where e is a column vector full of ones. Since, $\hat{\mathbf{M}}$, and $\hat{\mathbf{K}}$ are diagonal matrices of the generalized modal masses and stiffness respectively, Eq. 2.11 can be uncoupled only if $\Phi^T \hat{C} \Phi$ is also diagonal. Assuming proportional (Rayleigh) damping:

$$\hat{C} = \alpha_0 \hat{M} + \alpha_1 \hat{K} \tag{2.12}$$

The damping ratio for a system like this is[27]:

$$\zeta_i = \frac{\alpha_0}{2} \frac{1}{\omega_i} + \frac{\alpha_1}{2} \omega_i \tag{2.13}$$

Similar rules apply when Caughey series are used [27], instead of the Rayleigh damping. Now the equations are uncoupled, and can be written in the following form for each mode, i:

$$\ddot{q}_i + 2\zeta_i \omega_{0i} \dot{q} + \omega_{0i}^2 q_i = -\frac{\phi_i^T \hat{M} e}{\phi_i^T \hat{M} \phi_i} \ddot{x}_g \tag{2.14}$$

It can be seen that is similar equation to that of the SDOF system. The generalized displacement, and therefore the relative displacement, x, can be determined for each time step.

In reality, damping is not necessarily proportional; however for the low levels of damping encountered in most structures, the proportional damping approximation is accurate enough while considerably simplifying analysis. When damping is relatively high, especially if added dissipative devices are used, or for structures exhibiting non linearities, the errors incurred by this assumption become significant, and modal superposition analysis based on Eq. 2.14 is potentially unreliable. The direct time integration approach does not rely on any assumption about the form of the damping matrix, and therefore is a better way to go. Using the implicit Newmark algorithm

[13, 27] a brief presentation of the time domain analysis follows. According to this algorithm:

$$\dot{x}_{i+1} = \dot{x}_i + \frac{\Delta t}{2}(\ddot{x}_{i+1} + \ddot{x}_i) \tag{2.15a}$$

$$x_{i+1} = x_i + \dot{x}_i \Delta t + \frac{\Delta t^2}{4}(\ddot{x}_{i+1} + \ddot{x}_i) = x_i + \frac{\Delta t}{2}(\dot{x}_i + \dot{x}_{i+1}) \tag{2.15b}$$

For every time step, Eq. 2.6 takes the following form:

$$\hat{M}\ddot{x}_i + \hat{C}_i\dot{x}_i + \hat{K}_i x_i = -\hat{M}\ddot{x}_{g_i} \tag{2.16}$$

Assuming, that the response of the structure at time step, i, is already known, the aim is to obtain the MDOF system response for the $i+1$ time step:

$$\hat{M}\ddot{x}_{i+1} + \hat{C}_{i+1}\dot{x}_{i+1} + \hat{K}_{i+1}x_{i+1} = -\hat{M}\ddot{x}_{g_{i+1}} \tag{2.17}$$

Eq. 2.15 can be rewritten:

$$\ddot{x}_{i+1} = (\dot{x}_{i+1} - \dot{x}_i - \frac{\Delta t}{2}\ddot{x}_i)\frac{2}{\Delta t} \tag{2.18a}$$

$$\dot{x}_{i+1} = (x_{i+1} - x_i - \frac{\Delta t}{2}\dot{x}_i)\frac{2}{\Delta t} \tag{2.18b}$$

Substituting Eq. 2.18 into 2.17:

$$K_{i+1}^{tot} x_{i+1} = F_{i+1}^{tot} \tag{2.19}$$

where

$$K_{i+1}^{tot} = \hat{K}_{i+1} + \tfrac{2}{\Delta t}\hat{C}_{i+1} + \tfrac{4}{\Delta t^2}\hat{M} \tag{2.20}$$

and

$$F_{i+1}^{tot} = -\hat{M}\ddot{x}_{g,i+1} + [\tfrac{4\hat{M}}{\Delta t^2} + \tfrac{2\hat{C}_{i+1}}{\Delta t}]x_i + [\tfrac{4\hat{M}}{\Delta t} + \hat{C}_{i+1}]\dot{x}_i + \hat{M}\ddot{x}_i \tag{2.21}$$

Finally, using iteration algorithms such as the modified Newton-Raphson method [27] the displacement at time step $i+1$ can be determined, provided that the criteria defined by the algorithm are satisfied. Usually , these criteria are based on the convergence between x_n^{i+1} and x_{n+1}^{i+1}, where n represents the number of iteration. We can see that Eq. 2.21 can be simplified a lot, if the matrices K, and C are constant during the whole time history analysis, as in the case of linear systems with Rayleigh damping. In this case, K^{tot} from Eq. 2.20 can be calculated only once, at the beginning of the analysis.

2.2.2 Metallic Dampers

The concept of using metallic yielding dampers within a structure to absorb seismic energy was first proposed by Kelly [66], and Skinner [113], considering torsional beams, flexural beams, and other devices. Later research included the effect of more efficient devices, such as the X-shaped and triangular-plate energy dissipators [130], as shown in Figure 2.4. Other devices have the ability to dissipate energy either using different materials such as lead and shape memory alloys [10], or even a complete different configuration [131, 130, 139]. A different approach to the above type of dampers is followed in case of the Buckling Restrained Braces (BRBs)[14], where a yielding steel core is encased in a concrete-filled steel tube, avoiding buckling phenomena, and targeting to a tension/compression steel brace (Figure 2.5). An additional coating is provided at the steel core in order to minimize the friction with the concrete.

Due to the detailed past and ongoing research a number of existing structures in New Zealand, Mexico, Japan, Italy, and United States now include metallic dampers [114]. They are usually added within a bay between chevron braces and the overlying beam. The main concept behind metallic dampers is that they resist horizontal forces via flexural deformation of all the steel plates combined. After a certain level of force, the plates start to yield resulting in hysteretic behaviour. Even though most metallic dampers are modelled as elastic perfectly-plastic materials or Ramsberg-Osgood [104] idealizations, more rigorous models have been suggested, such as that suggested by Ozdemir [46]. It is worth mentioning that even though that addition

of metallic dampers may be effective regarding the reduction of inter-storey drifts, they are less effective at reducing accelerations and base shear forces [86].

Since the primary contribution of metallic dampers is additional stiffness to the main structure, this may lead to large dynamic characteristics' alterations of the building (change of natural frequencies, mode shapes, and mass). Thus, this does not guarantee an enhanced performance due to seismic loading. In some instances, the structure may experience larger deformations, accelerations, and shear forces, based on the frequency content of the imposed earthquake, compared to the original unretrofitted building.

Whittaker et al. [14] carried out experimental evaluation of X-shaped steel dampers (ADAS) under both cyclic and time history displacements, which were determined from a scaled version of the ElCentro ground motion. The experimental rig consisted of a 3-storey, 1-bay moment resisting frame and the corresponding results regarding the cyclic and the hysteretic response of the dampers are shown at Figure 2.6. This Figure represents a typical hysteretic behaviour of metallic dampers.

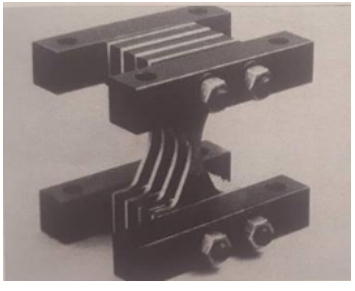

(a) X-shaped plate damper[48]

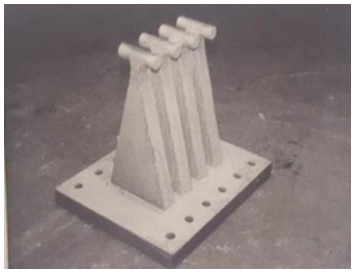

(b) Triangular plate damper[48]

Figure 2.4: a: X-shaped plate damper, b: Triangular plate damper

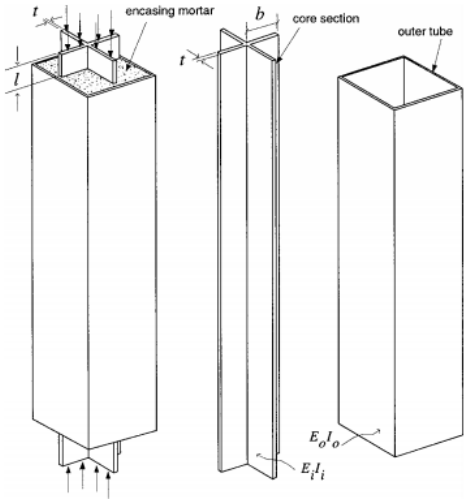

Figure 2.5: Main components of BRB[14]

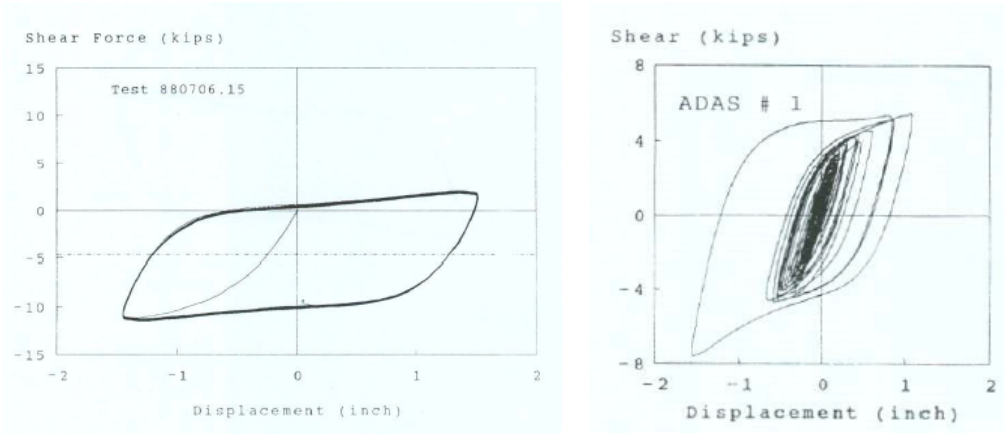

(a) Cyclic response

(b) Hysteretic response

Figure 2.6: a: X-shaped ADAS damper - cyclic response, b: X-shaped ADAS damper - hysteretic response [14]

2.2.3 Friction Dampers

Friction dampers have the ability to dissipate energy through friction developed between two solid bodies sliding relative to each other. Several different types of friction dampers have been developed [101, 102, 10, 98, 44]through the years.

Generally, friction dampers generate rectangular hysteretic loops, similar to the characteristics of Coulomb friction, based on the following assumptions:

- The total frictional force that can be developed is independent of the apparent surface area of contact

- The total frictional force that can be developed is proportional to the normal force acting across the interface
- For the case of sliding with low relative velocities, the total frictional force is independent of that velocity

The relationship between the frictional and the normal force is given as:

$$F_t = \mu F_n \tag{2.22}$$

where F_{t}, and F_{n} represent the friction and the normal force, respectively, and μ the friction coefficient. Even though frictional forces are simple to measure or calculate based on Eq. 2.22, the actual phenomena that friction action is based on are much more complex. These main phenomena are discussed by Christopoulos and Filiatrault [28], concluding that the main factors which affect the frictional forces are the shape and contour of surfaces, the way asperities on the surfaces deform when normal pressure is applied, how they adhere, the role of surface films, and how energy is lost when the surfaces are deformed during sliding.

One of the earliest experimental efforts was carried out by A.S. Pall [102], who conducted both static and dynamic testing on sliding elements, with different configurations, incorporated in the form of braced frames (Figure 2.7). The tests were based on the normal force applied by pre-tensioning 12.7 mm diameter high strength bolts. Best results were determined when brake lining pads were used, in order to limit the available slip deformation. A nearly elasto-plastic behaviour with negligible degradation was observed for any sliding surface used (Figure 2.8), which is a common friction damper behaviour. The friction dampers are designed not to slip under normal service loads and moderate earthquakes. During strong ground motions, however, the device slips at a predetermined load. It should be noted that visco-plastic models have been proposed to model friction phenomena as well, similarly to modelling of metallic dampers.

However, even though friction dampers can effectively dissipate hysteretic energy, they are not very widely used. It has been shown [98] that addition of friction dampers does not reduce structural response in the low frequency range. Moreover,

the very sharp non-linearities which friction dampers exhibit, the need for regular maintenance, and the need for a high clamping force across the device are prohibiting factors of friction dampers use.

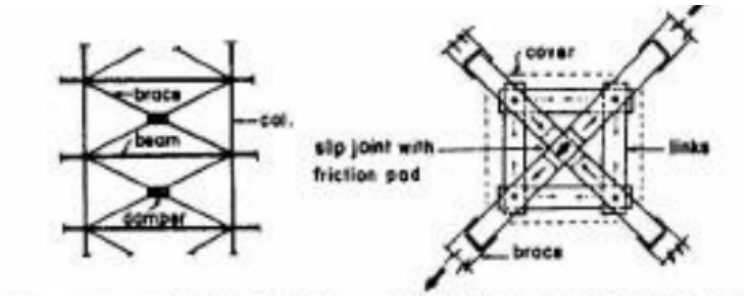

Figure 2.7: Friction Dampers incorporated in the form of braced frames[101]

s

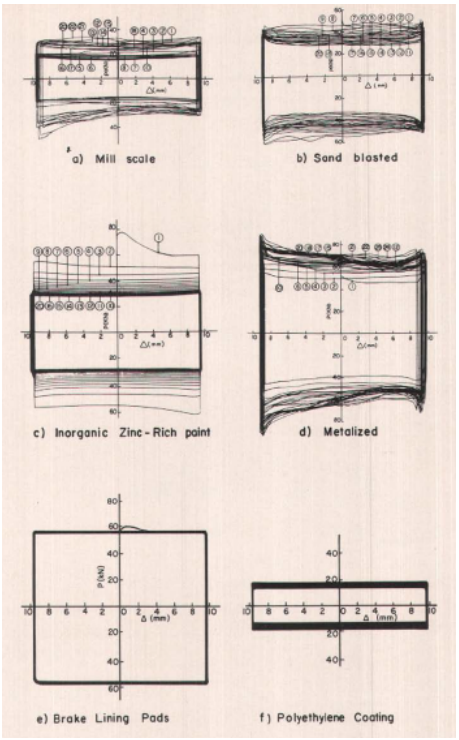

Figure 2.8: Hysteretic behaviour of limited bolted joints using different surface treatments [102]

2.2.4 Viscous Fluid Dampers

Fluid dampers can also be very effective under seismic loads [54, 87, 12, 28]. An effective concept, which was one of the first applications designed for seismic protec-

tion by Sumitomo Construction Company [11], consists of a viscous damping wall (Figure 2.9), where a piston (steel plate) is constrained to move within a rectangular steel container filled with viscous fluid. In order for this concept to be applied to a real structure, the piston is attached at the overlying floor, while the container is at the floor below. The energy dissipation is accomplished through relative inter storey drifts. Adding a sufficient number of viscous damping walls within the structure, will lead to a significant increase in damping.

In order to increase the energy dissipation capacity of the viscous fluid dampers, another more efficient approach can be followed, using orificed fluid dampers incorporated within the bracing system of the structure(Figure 2.10) [32]. However, in this case a high level of sophisticated analytical and detailed experimental work has to be carried out before implementation to real structures. Makris and Constantinou et al. [83, 82] carried out experimental tests on viscous walls, and found that the following fractional derivative Maxwell force-displacement model was in a very good agreement with the data they obtained:

$$P(t) + \lambda \frac{d^v P(t)}{dt^v} = C_0 \frac{dx(t)}{dt} \tag{2.23}$$

where P is the applied force to the piston, x is the corresponding displacement. C_0, λ, and v are parameters that are either determined based on the experimental data. Typical hysteretic loops of viscous dampers are presented at Figure 2.11. Another modelling approach taking into account any non linearities is based on the following equation:

$$P(t) = Cx(t)^{\alpha} \tag{2.24}$$

Even though in reality viscous dampers exhibit non-linearities, they are frequently treated as linear. For example Chang et. al. [26] carried out experimental tests on viscous dampers. Modelling them using Eq. 2.24, he determined that a nonlinear coefficient in the range of 0.48-0.55 was more suitable to capture the behaviour of the viscous dampers. Furthermore, orificed viscous dampers tested by Constantinou and Symans[32] were found to be less dependent on loading history and the proposed

linear analytical model was simplified to:

$$P(t) + \lambda \frac{dP(t)}{dt} = C_0 \frac{dx(t)}{dt} \tag{2.25}$$

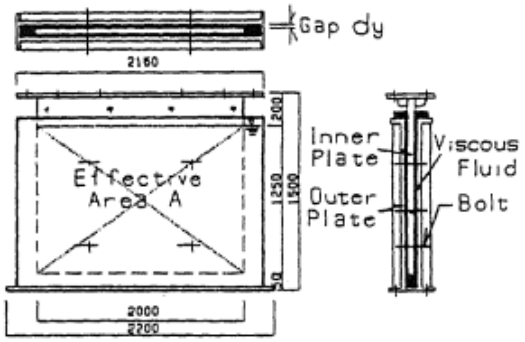

Figure 2.9: Viscous Fluid Damper [11]

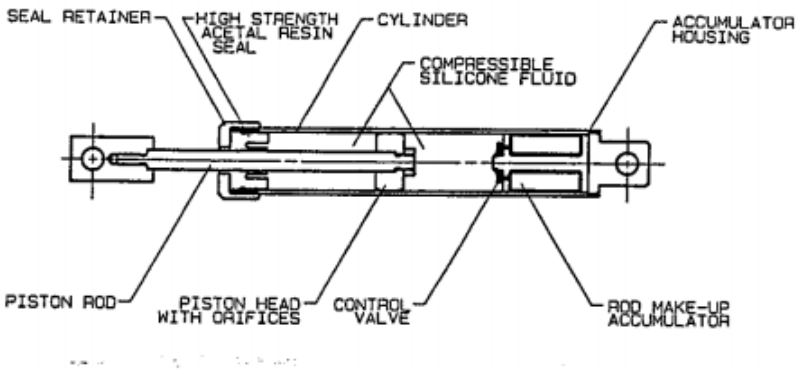

Figure 2.10: Orificed Viscous Fluid Damper [32]

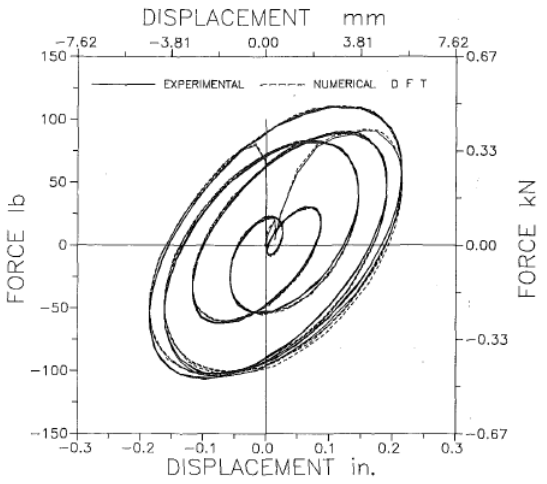

Figure 2.11: Force Displacement results for cyclic loading [82]

2.2.5 Tuned Mass Dampers

The concept of the implementation of Tuned Mass Dampers (TMDs) is based on the early studies carried out by Fram [45], and Den Hartog [34]. Figure 2.12 shows Frahm's absorber, which consists of the main mass connected with an additional smaller mass through a spring with stiffness k. The main target was to select appropriate values of k, and m, in order for the natural frequency of the added absorber to be close to the excitation frequency. The result was that the main mass, M, can stay completely stationary under a harmonic load. Despite its effectiveness, this method was mostly developed for mechanical engineering systems. In the case of buildings, where loads consist of many components of frequency, Figure 2.13 shows the main concepts in simple form. The equations of motion describing the behaviour of the SDOF structure along with the added TMD are:

$$m\ddot{z}(t) + c\dot{z}(t) + kz(t) = -m\ddot{y}_1(t) + g(t) \tag{2.26}$$

$$M\ddot{y}_1(t) + C\dot{y}_1(t) + Ky_1(t) = c\dot{z}(t) + kz(t) + f(t) \tag{2.27}$$

where $y_1(t)$ is the displacement of the SDOF system relative to its base, $z(t)$ is the relative displacement of the TMD with respect to the SDOF system, $f(t)$ is

the external force of the main system, and $g(t)$ the associated force applied on TMD, which is zero in case of wind load, and $\frac{m}{M}f(t)$ in case of earthquake loading. Summation of Eqs. 2.26, and 2.27 leads to the final equation of motion for the total system:

$$(M+m)\ddot{y}_1(t) + C\dot{y}_1(t) + Ky_1(t) = -m\ddot{z}(t) + f(t) + g(t) \tag{2.28}$$

Apart from the obvious decrease in natural frequency, and a slight increase in the force in case of earthquake loading, the added inertia force of the TMD, $-m\ddot{z}(t)$, is the reason behind the TMD's effectiveness. Maximum effectiveness of the added TMD comes when the secondary mass lags the main SDOF mass by a phase angle of 90^0. This is as if every time the main mass trying to move towards one direction another force pushes it back to its initial position. Optimizing techniques for both the secondary mass and damping ratio have been developed by many researchers [34, 105, 135, 71], which lead to the final design of the TMD. Recent versions of TMDs are rested on top of elastomeric rubber bearings, which function as shear springs, and rubber compound elements, which provide viscoelastic damping capability. The effectiveness of the TMDs is optimised based on the natural frequency of the building. Hence, it is worth mentioning that inelastic deformations of the structure may lead to a decrease of this effectiveness, since the TMD loses its tuning effect. This fact makes TMDs use inefficient for seismic applications.

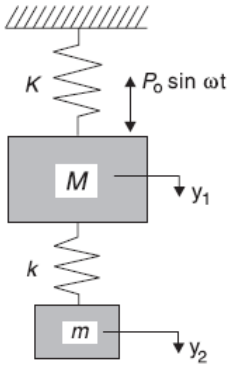

Figure 2.12: Undamped Absorber and main mass subject to harmonic excitation [45]

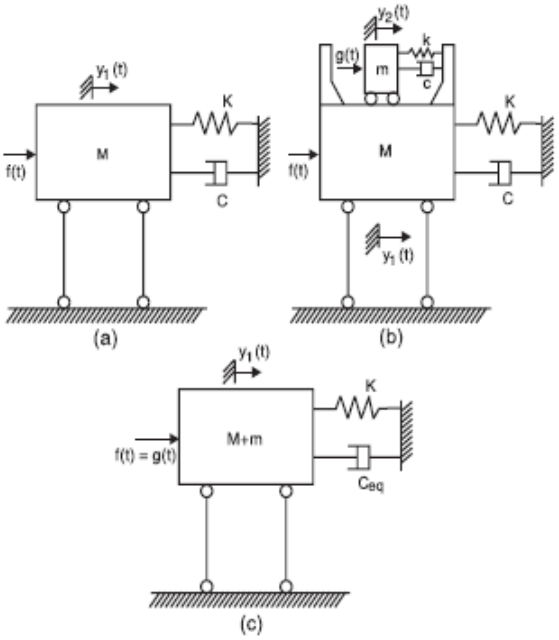

Figure 2.13: Application of TMD to SDOF structure [31]

2.2.6 Tuned Liquid Dampers

The concept of adding Tuned Liquid Dampers (TLDs) in order to increase the dynamic performance of a structure is similar to the TMD case, discussed earlier. In the case of the TLD, a mass of water replaces the solid mass (Figure 2.14). However, unlike TMDs, which often behave linearly, the behaviour of the TLDs is governed by non linearities, either liquid sloshing or the presence of orifices[114]. Hence, most of the work, which is based on characterizing the dynamic response of the TLDs, is based on experiments[31]. Assuming moderate amplitude sloshing, no wave breaking shallow water gravity waves theory can be applied [90]. Lepelletier and Raichlen [74] studied the response of a fluid layer within a rectangular tank, due to horizontal excitation(Figure 2.15).

The motion of the fluid is governed by the wave elevation, $n(x,t)$, and the depth-averaged horizontal velocity, $u(x,t)$:

$$\dot{n} + [(h+n)u]_{,x} = 0 \tag{2.29}$$

$$u,t + u_{,x} + gn_{,x} - \frac{h^2}{3}\dot{u}_{,x}\, x + \frac{1}{h}\frac{v\omega}{2}^{\frac{1}{2}}(1 + \frac{2h}{b} + C)u + \ddot{x}_b = 0 \tag{2.30}$$

where the subscripts following commas denote differentiation.

Parameters $v, \omega, g, \ddot{x}_b$ represent the kinematic viscosity of the fluid, the characteristic frequency of the fluid motion, the gravitational acceleration, and the horizontal acceleration of the tank respectively. Parameter, C governs the additional dissipation due to free surface contamination. Assuming linearised response without dissipation, the resulting natural frequency of the $k_t h$ mode of the associated waves created by the fluid motion, can be written as:

$$\omega_k = (2k-1)\pi\frac{(gh)^{\frac{1}{2}}}{L}[1 - \frac{1}{6}(2k-1)^2\pi^2(\frac{h}{L})^2] \tag{2.31}$$

All the above parameters show the complexity of the TLDs, especially when application in earthquake protection is involved, where time history analysis is often necessary. Hence, another more recent approach, is modelling the TLD with a TMD analogy [120, 143, 99]. Equivalent values for mass and damping coefficient were extracted[120]:

$$m_v = m_\alpha \frac{(1-\Omega^2)+(2\zeta_\alpha\Omega)^2}{(1-\Omega^2)^2+(2\zeta_\alpha\Omega)^2} \tag{2.32}$$

$$c_v = c_\alpha \frac{\Omega^4}{(1-\Omega^2)^2+(2\zeta_\alpha\Omega)^2} \tag{2.33}$$

where m_α, c_α, and $\Omega = \frac{\omega}{\omega_\alpha}$ can be calibrated based on experimental data

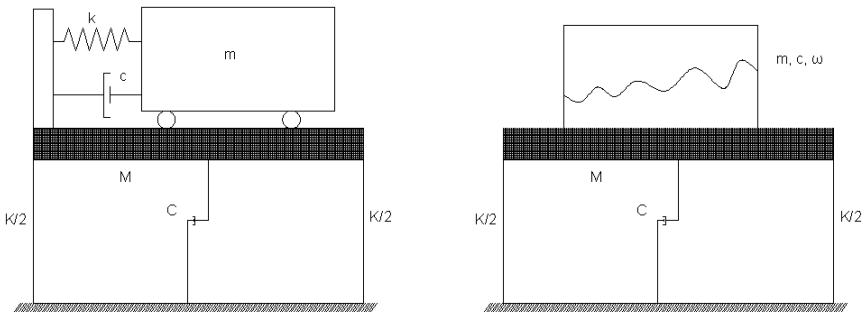

Figure 2.14: Configuration for: a) General TMD, b) TLD

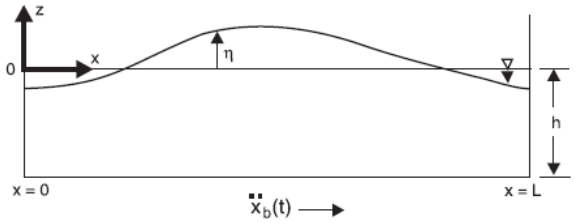

Figure 2.15: TLD Geometric definition[74]

Even though the mathematical theory behind TLDs is complicated, their application to real structures has become quite popular due to their easy implementation, and maintenance, along with the fact that they are not very sensitive to the actual frequency ratio between the structure and the damper, in contrast with the TMDs.

2.2.7 ViscoElastic Dampers

Since ViscoElastic (VE) dampers show similar characteristics with the elastomeric ones, they will be given much more attention and detailed description compared to the types of damper presented earlier. In contrast with the viscous dampers, VE dampers have the ability to provide both velocity-dependent force, which provides supplemental viscous damping to the system (similar with viscous dampers), and displacement-dependent elastic restoring force [28], adding stiffness to the system (similar to metallic dampers). They typically consist of layers of polymers bonded between steel plates (Figure 2.16). Visco-elasticity is a property which defines the ability of a material to exhibit both elastic and viscous characteristics; typical examples are polymers which exhibit viscoelastic behaviour at all temperatures - they are never simple elastic solids [89]. A more detail description of viscoelastic dampers and their comparison to elastomeric ones is given in 2.2.8.

VE dampers are incorporated in the structure between concentrical braces and the overlying beam. Hence, their ability to dissipate energy is based on their shear deformation due to the drift between two adjacent floors. It appears that their application began to gain attention after their first implementation at the World Trade Center in New York (Figure 2.30), in order to improve the structural behaviour due to wind loads. However, seismic applications usually require higher damping

contributions compared to wind.

In the case of low rise buildings, where moment resisting frames are mainly used (as in the current research project), a rational assumption is that the supplemental damping devices aim to minimize the horizontal deformations, and therefore the above implementation method with the concentric diagonal braces seems rational. However, tall buildings usually consist of the combination of moment resisting frames along with shear walls. The deflected shape of the shear walls is similar to a cantilever, which actually highly affects the global deflected shape of the structure. High axial deformations are created, and in order to take this into consideration, the damping philosophy should be adapted as well, and designed in such a way so they will resist these axial deformations through shear. Based on current research, and on actual implementations of supplemental damping devices on skyscrapers, VE dampers can actually replace the reinforced concrete coupling beams, resulting in reducing the vertical deformations created at the ends of the beams due to high shear forces. This solution has been already suggested and implemented into real projects in order to mitigate both seismic and wind actions [91, 29]. It has been also suggested to add both VE dampers along with diagonal braces for optimal results [88].

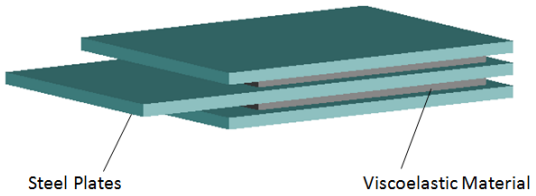

Figure 2.16: Typical VE damper configuration

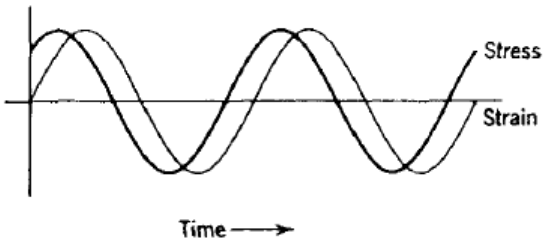

Figure 2.17: VE stress-strain behaviour under sinusoidal loading [145]

Even though the basic characteristics of VE materials are creep, stress relaxation, and dynamic behaviour, the last one is the main focus here, due to the interest in the dynamic loads applied at the structure. Considering the case of applying a sinusoidal shear strain, γ, with frequency, ω, the corresponding viscoelastic stress will oscillate at the same frequency but out of phase (Figure 2.17):

$$\gamma(t) = \gamma_0 sin\omega t \tag{2.34}$$

$$\tau(t) = \tau_0 sin(\omega t + \delta) \tag{2.35}$$

where γ_0, and τ_0 represent the maximum strain and stress respectively, and δ is the phase lag. Rewriting Eq. 2.35 in a different form:

$$\tau(t) = \gamma_0[G'(\omega)sin\omega t + G''(\omega)cos\omega t] \tag{2.36}$$

where

$$G'(\omega) = \tfrac{\tau_0}{\gamma_0}cos\delta, G''(\omega) = \tfrac{\tau_0}{\gamma_0}sin\delta \tag{2.37}$$

Replacing $\gamma_0 sin\omega t$ with $\gamma(t)$, and using the identity $cos\omega t = \sqrt{1 - sin^2\omega t}$, Eq.2.36 can be rewritten as:

$$\tau(t) = G'(\omega)\gamma(t) \pm G''(\omega)\sqrt{\gamma_0^2 - \gamma^2(t)} \tag{2.38}$$

Eq. 2.38 defines the characteristic VE relationship of the material in the form of the ellipse shown at Figure 2.18. The area of this ellipse defines the energy dissipated in each cycle of oscillation:

$$\begin{gathered} E_H = \int_0^{2\pi/\omega} \tau(t)\dot{\gamma}(t)dt \\ = \int_0^{2\pi/\omega} \gamma_0^2\omega cos\omega t[G'(\omega)sin\omega t + G''(\omega)cos\omega t]dt \\ = \pi\gamma_0^2 G''(\omega) \end{gathered} \tag{2.39}$$

Using Eq. 2.34, and its derivative with respect to time, then Eq. 2.35 can take the following form:

$$\tau(t) = G'(\omega)\gamma(t) + \frac{G''(\omega)}{\omega}\dot{\gamma}(t) \tag{2.40}$$

where it can be noticed that the term $G'(\omega)$ represents the elastic modulus, called the shear storage modulus, and the term $G''(\omega)$ represents the energy dissipation component, and is called the shear loss modulus. Both $G'(\omega)$, and $G''(\omega)$ are functions of frequency, and are considered as basic characteristics of every VE material giving a measure of the energy stored and recovered, and energy dissipated per cycle, respectively.

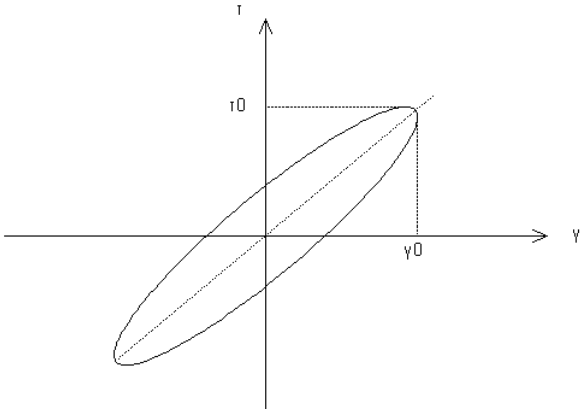

Figure 2.18: VE stress-strain behaviour under sinusoidal loading

Since, the quantity $G''(\omega)/\omega$ is the damping coefficient, the corresponding damping ratio is determined as:

$$\zeta = \frac{G''(\omega)}{\omega}\left(\frac{\omega}{2G'(\omega)}\right) = \frac{G''(\omega}{2G'(\omega)} \tag{2.41}$$

And the loss factor, n as:

$$n = \frac{G''(\omega)}{G'(\omega)} = tan\delta \tag{2.42}$$

Comparing, Eqs, 2.41, and 2.42:

$$\zeta = \frac{n}{2} \tag{2.43}$$

In order to determine the shear complex modulus of the material (which forms one of the basic parameters used to characterise a VE/elastomeric material) another way of determining the stress-strain relationship is followed, using complex notation and adjusting Eqs. 2.34, 2.35:

$$\gamma(t) = \gamma_0 e^{i\omega t} \tag{2.44}$$

$$\tau(t) = \tau_0 e^{i(\omega t+\delta)} \tag{2.45}$$

Eqs. 2.44, and 2.45 lead to:

$$\tau(t) = G^*(\omega)\gamma(t) \tag{2.46}$$

where $G^*(\omega)$ is the complex modulus of the VE material:

$$G^*(\omega) = \frac{\tau(t)}{\gamma(t)} = \frac{\tau_0}{\gamma_0} e^{i\delta} = G'(\omega) + iG''(\omega) = G'(\omega)(1 + in) \tag{2.47}$$

and

$$|G^*(\omega)| = G_{eq} = \frac{\tau_0}{\gamma_0} = \sqrt{(G'(\omega))^2 + (G''(\omega))^2} \tag{2.48}$$

Therefore, it is observed that the parameters, G' and G'', or G' and n define the dynamic behaviour of a VE material when it is subjected to sinusoidal loading. As will be seen later, these parameters do not only depend on the frequency, but on temperature and shear strain as well. Hence, a proper constitutive equation describing the stress-strain or the force-displacement relationship should take these into account. VE mechanical response is usually simulated by different spring-viscous damper combinations [141].

All the above equations are based on the stress-strain relationship of a VE material. When this relationship has to be applied in terms of the force-displacement relationship for a damper with shear area, A, and total thickness, h, then Eq. 2.38 is adjusted to:

$$F(t) = \bar{k}(\omega)u(t) + \bar{c}(\omega)\dot{u}(t) \tag{2.49}$$

where

$$\bar{k}(\omega) = \frac{AG'(\omega)}{h}, \bar{c}(\omega) = \frac{AG''(\omega)}{\omega h} \tag{2.50}$$

Eq. 2.49 represents pure VE behaviour captured by a Kelvin-Voigt model (spring and dashpot connected in parallel). Following a slightly different approach, the equivalent stiffness can be also determined in this case, and its connection with the equivalent shear modulus can be shown, assuming a sinusoidal imposed displacement:

$$u(t) = u_0 sin\omega t \tag{2.51}$$

which gives the corresponding derivatives with respect to time:

$$\dot{u}(t) = \omega u_0 cos\omega t \tag{2.52}$$

$$\ddot{u}(t) = -\omega^2 u_0 sin\omega t \tag{2.53}$$

Replacing $u(t)$, and $\dot{u}(t)$ in Eq. 2.49:

$$F(t) = \bar{k}(\omega)u(t) + \bar{c}(\omega)\omega\sqrt{u_0^2 - u^2} \tag{2.54}$$

which is the same as Eq. 2.38, but in force-displacement terms, and is representative of pure VE behaviour. Since, the equivalent stiffness is defined as F_0/u_0, the maximum force has to be determined. Hence, assuming that the maximum force occurs

when its derivative with respect to time is zero, the displacement corresponding to the maximum force (in elastic systems the maximum displacement corresponds to the maximum force) can be calculated as:

$$\frac{dF(t)}{dt} = \bar{k}(\omega)\dot{u}(t) + \bar{c}(\omega)\ddot{u}(t) = 0 \tag{2.55}$$

Replacing Eqs. 2.52, and 2.53 to Eq. 2.55 the displacement corresponding to the maximum force is extracted:

$$u_{F_0} = \frac{\bar{k}(\omega)}{\sqrt{\bar{k}(\omega)^2 + \bar{c}(\omega)^2\omega^2}} u_0 \tag{2.56}$$

Replacing Eq. 2.56 in Eq. 2.54, the maximum force is determined:

$$F_0 = u_0\sqrt{\bar{k}(\omega)^2 + \bar{c}(\omega)^2\omega^2} \tag{2.57}$$

Hence, the equivalent stiffness is:

$$k_{eq} = \sqrt{\bar{k}(\omega)^2 + \bar{c}(\omega)^2\omega^2} \tag{2.58}$$

which is the force-displacement version of Eq. 2.48. Moreover, the force will correspond with a time delay, δ, comparing with the imposed displacement, similarly with Eq. 2.35:

$$\bar{k}(\omega) = \frac{F_0}{u_0} cos\delta => F_0 = \frac{\bar{k}(\omega)}{cos\delta} u_0 \tag{2.59}$$

Combining Eqs. 2.57, and 2.59:

$$tan\delta = \frac{\bar{c}(\omega)\omega}{k} \tag{2.60}$$

where again the association with the stress-strain terms is obvious. If $\bar{k}(\omega)$, and $\bar{c}(\omega)$ are replaced using Eq. 2.50 then the loss factor obtained from Eq. 2.60 equals the one from Eq. 2.42).

A full description of the VE behaviour was presented here. These parameters, even

though are very simple, form the basic formulas in order to capture the main characteristics of VE/elastomeric material and will be used in the folllowing chapter. However, more sophisticated models have been proposed as well. Apart from the Kelvin-Voigt (spring and dashpot connected in parallel) and Zener model (spring connected in parallel with a spring-dashpot series connection), the Generalized Maxwell Model (GMM) was found to be more adequate to capture the mechanical VE characteristics [89, 141, 42, 75]. The GMM (Figure 2.19) consists of a linear spring, with stiffness, k_0, connected in parallel with Maxwell elements (linear springs with stiffness, k_i, connected in series with dashpots, c_i).

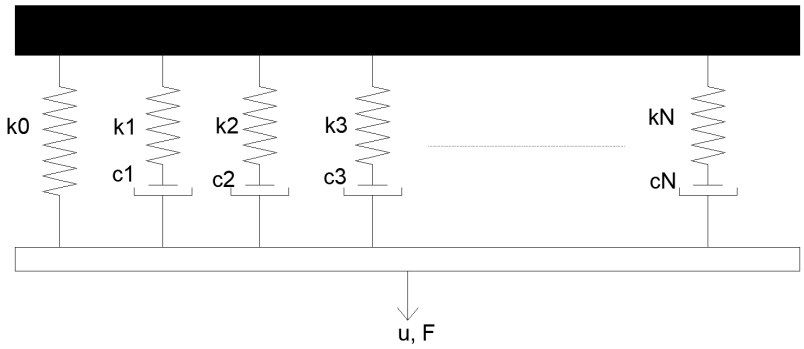

Figure 2.19: Generalized Maxwell Model (GMM) presentation

It can be expressed either in stress-strain or force-displacement form. When dynamic displacement, in the form of Eq. 2.34 is applied, then the corresponding shear storage modulus, and the shear loss modulus are determined as[89]:

$$G' = G_0 + \sum_{i=1}^{N} \frac{G_i \omega^2 {\tau_i}^2}{1 + \omega^2 {\tau_i}^2} \tag{2.61}$$

$$G'' = \sum_{i=1}^{N} \frac{G_i \omega {\tau_i}^2}{1 + \omega^2 {\tau_i}^2} \tag{2.62}$$

The above equations are valid only under sinusoidal loading with a specific frequency ω. Minimizing the error between the experimental and analytical values of the shear storage modulus and the shear loss modulus. Fan [42] carried out a comparative analysis between Kelvin-Voigt, GMM, and two different Fractional–Derivatives

models (one proposed by Kasai [64] and one from Fan). The Fractional-Derivative models are explained in the next subsection. A relatively good agreement was achieved for the shear storage modulus, especially for the GMM (Figure 2.20). However, the only available hysteretic loops which were found were comparing the aforementioned models between them (Figure 2.21), and no comparison with experimental values was possible. The only figure which was found to be comparing any of these models with experimental data in time domain was the roof displacement time history (Figure 2.22) of a 2/5-scale five-story 1-bay steel frame test structure with diagonal-braced VE dampers [108]. However, careful comparison of these results show the actual deviation of the GMM model.

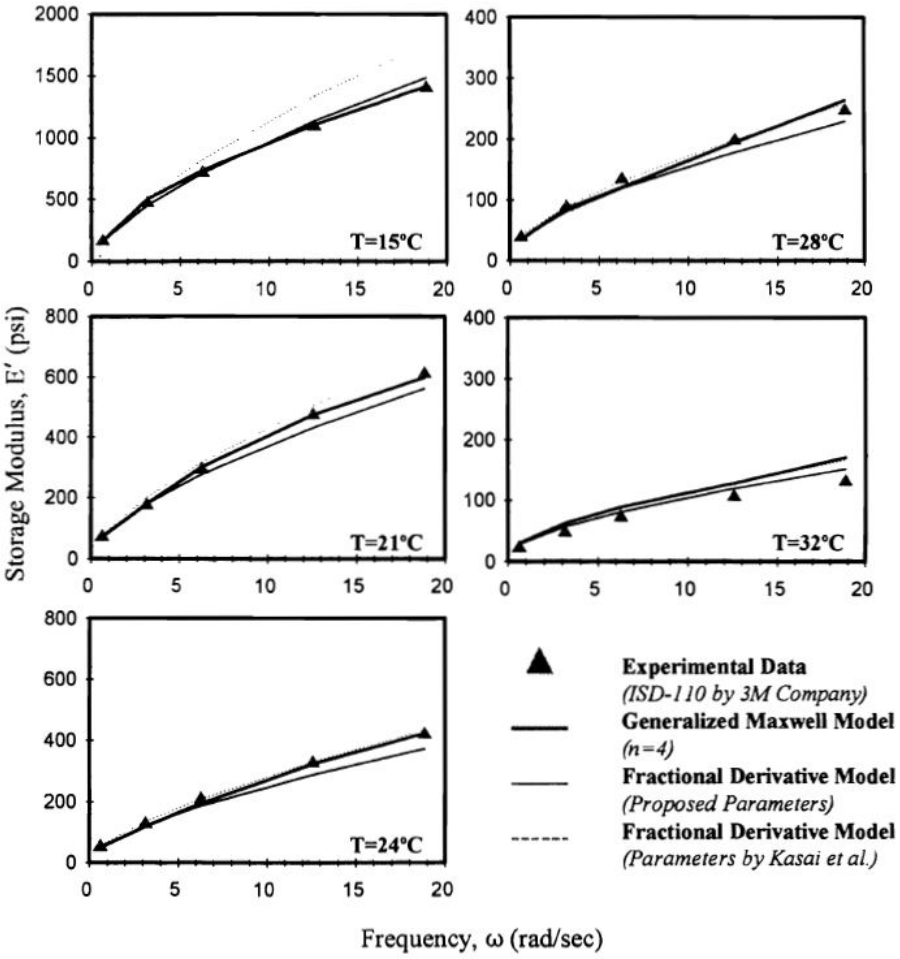

Figure 2.20: Comparison of analytical and experimental values of shear storage modulus for GMM, Fractional-Derivative models [42]

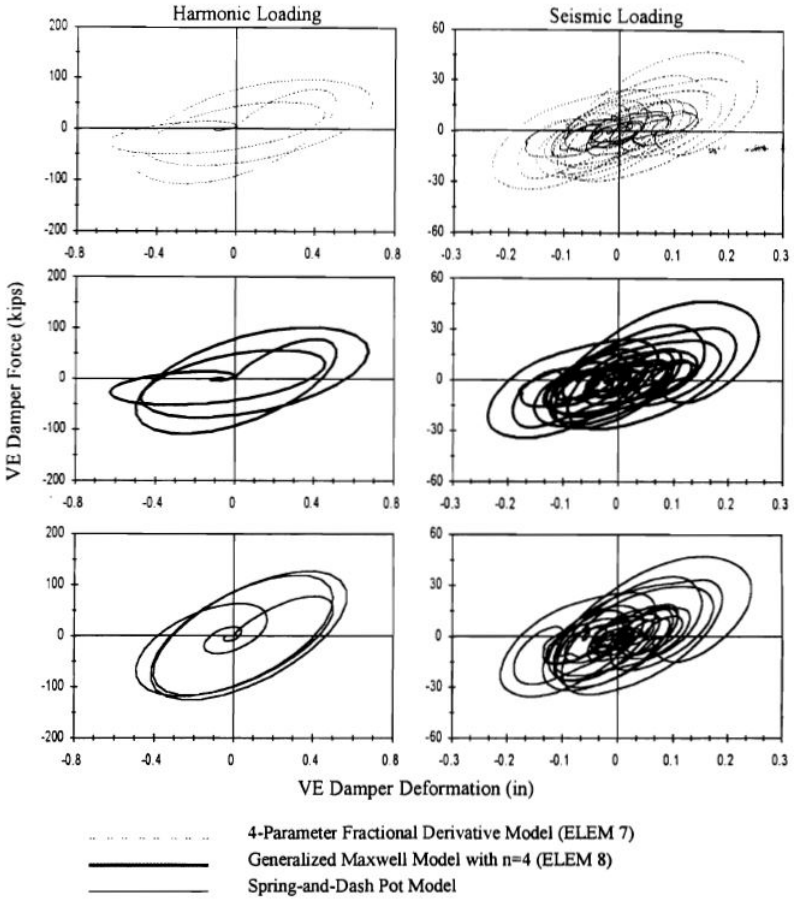

Figure 2.21: Comparison of hysteretic behaviour of the 3 models(GMM, and Fractional-Derivative models) [42]

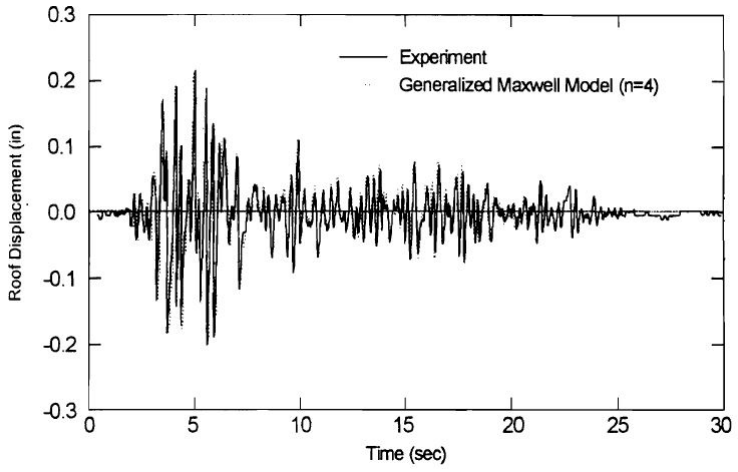

Figure 2.22: Comparison of analytical and experimental values of roof displacement' time history of a test structure with diagonal-braced VE dampers [42]

2.2.8 Elastomeric Dampers

Elastomer Material Background

The ASTM standard D 1566 (ASTM: American Society for Testing and Materials) defines elastomers as high-polymeric, organic networks that are capable of absorbing large deformations in a reversible manner. Elastomers are rubber-like materials, they are made up of long chains of atoms, mainly carbon, and hydrogen, which have a degree of cross-linking with their neighbouring chains. It is these cross-linking bonds that pull the elastomer back into shape when the deforming force is removed. Polymers are characterized by their glass transition temperature, T_g. Below the glass transition temperature, the proper motion of the molecules, which is also known as Brownian motion – freezes. The material is in a rigid, glassy state [6]. When the glass transition is exceeded, the molecules start becoming mobile once again and the polymer undergoes a "transition" phase. When the temperature increases to levels more than the "transition" phase, the polymer exhibits a more rubbery behaviour, where stiffness and damping are generally lower but vary much less with the temperature [77]. It is in this region where the elastomers are usually used. If the temperature continues to rise, first rubbery and then viscous flow occurs followed by decomposition of the polymer. During the rubbery flow phase and the glass transition phase the polymer behaves as a visco-elastic material [111]. The above description of how polymers are behaving with different temperatures can be seen in Figure 2.23, where a typical specimen is subjected to a stress which is held for a time, t, at a temperature T, measuring the modulus: $E(T,t) = \frac{\sigma}{\epsilon(T,t)}$, where σ is the applied stress, and ϵ the corresponding displacement. It should be mentioned that even though not all polymers are purely viscoelastic, and even fewer are linearly viscoelastic [106], a variety of dampers has been modelled as pure linear viscoelastic materials which is actually a very good approximation, especially for low strain amplitudes or for polymers used with relatively high glass T_g.

Another interesting characteristic of the elastomeric materials, known as the Mullin's effect, is the softening of the material under the first few cycles of deformation, after which the stress-strain behaviour approaches a steady state [50]. The

main properties of elastomers (at least in a macro-scale which is the main interest here) can be summarised as:

- exhibit linear VE behaviour, especially under relatively small strains
- extremely high extensibility
- complete recovery after removal of the imposed stress
- strain hardening at relative large strains

Some of these define their main advantages comparing with other types of materials used in passive dissipation devices, since even after strong earthquakes, the elastomeric dampers will not exhibit any damage or permanent deformation, resulting in more economical solutions as well.

Since elastomers, like many other polymers, show VE properties, they highly depend on the strain amplitude, frequency, and ambient temperature. Moreover, a distinct feature of the hysteresis loops of elastomers is that softening at a small strain amplitude and hardening at a relatively large strain amplitude may occur in the amplitude range of practical interest [107]. Similar softening-hardening hysteretic behavior was observed for elastomeric dampers [107], and for high damping rubber base isolators [127, 9]. Typical elastomeric hysteretic behaviour can be seen at Figure 2.24.

It should be noted that most of the elastomer applications, with regard to seismic protection of structures have been implemented for seismic isolated structures [68, 65, 144, 103] in the form of elastomeric bearings.

To capture the dynamic behaviour of elastomeric-rubber dampers several models have been proposed. Five different models are presented here, which have been used by either researchers or by design codes to model elastomeric and rubber dissipative devices:

- Linearised model [5]
- Rate dependent model [107]
- Fractional derivatives [72, 68, 55]

- Bouc-Wen model [84]
- Modified Bouc-Wen model [62]

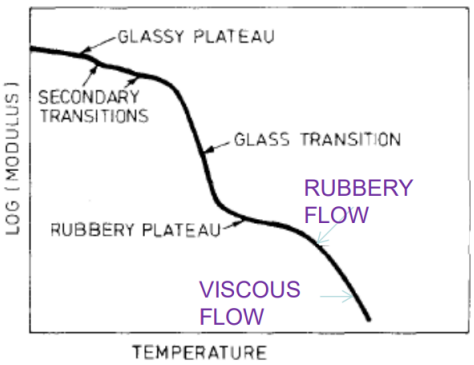

Figure 2.23: Different regimes of polymers behaviour when temperature increases [111]

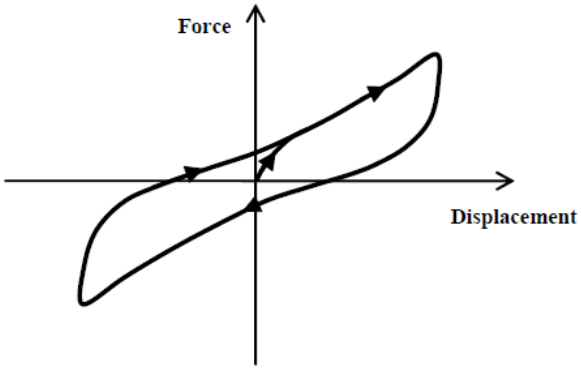

Figure 2.24: Typical hysteretic behaviour of elastomer [69]

Linearised Model

The most simplified, but at the same time practical way of presenting the basic characteristic of either an elastomeric or VE damper/bearing, at least for design purposes, is a linearised model with an equivalent stiffness, k_{eff}, and equivalent damping ratio, ζ_{eff}, proposed by FEMA [5]. These parameters are determined as:

$$K_{eff} = \frac{|F^+|+|F^-|}{|u^+|+|u^-|} \tag{2.63}$$

$$\zeta_{eff} = \zeta + \frac{\sum W_i}{4\pi W_k} \tag{2.64}$$

where:

- K' is the storage stiffness
- u^+, u^- are the maximum, and minimum displacements
- F^+, F^- are the forces corresponding to u^+, u^-
- ζ is the inherent damping ratio of the structure
- W_i is the work dissipated by the device i per cycle of oscillation
- W_k is the maximum strain energy

Rate Dependent Model

Sause [107] on the other hand proposed a rate-dependent hysteretic model, which is far more sophisticated than the linearised model proposed by FEMA, based on asymptote functions. Simulating softening and hardening behaviour, which the elastomer experiences, with second and third order polynomials the final model is:

$$\tau(\gamma) = \bar{\tau}(\gamma) - e_0[1 + \frac{k[n-1][\bar{\tau}(\gamma)-\bar{\tau}(\gamma_0)]}{e_0}]^{(-1)/(n-1)} \tag{2.65}$$

when $n > 1$

$$\tau(\gamma) = \bar{\tau}(\gamma) - e_0 exp[-\frac{k[\bar{\tau}(\gamma)-\bar{\tau}(\gamma_0)]}{e_0}] \tag{2.66}$$

when $n = 1$ where:

- γ is the applied shear strain
- $\tau(\gamma)$ is the shear stress
- $\bar{\tau}(\gamma)$ is the asymptote function for loading and unloading direction
- $e_0 = \bar{\tau}(\gamma_0) - \bar{\tau}_0$ is the stress deviation at the most recent strain reversal, γ_0, and corresponding stress τ_0

- k, and n are parameters which control the shape of the hysteretic loop

A linear dashpot was also added to the proposed model in order to take into account rate dependent effects. According to Sause[107], the slope of the stress-strain path, $\tau(\gamma)$ asymptotically approaches the function $\bar{\tau}(\gamma)$. The parameters of this model were determined using data from cyclic tests in a frequency range 0.5-3.0Hz. Good correlation was achieved comparing the analytical model and experimental results (see Figure 2.25). However, this model is based on a very similar hysteretic model to previous studies [72], where even though a very good agreement between analytical and experimental results had been achieved for selected strains, and frequencies2, large discrepancies were observed for high frequencies, and strains below 100% (see Figure 2.26). The dynamic analysis results presented are limited, and more validation methods and experimental data need to demonstrate the computational stability and general applicability of the current proposed model[107].

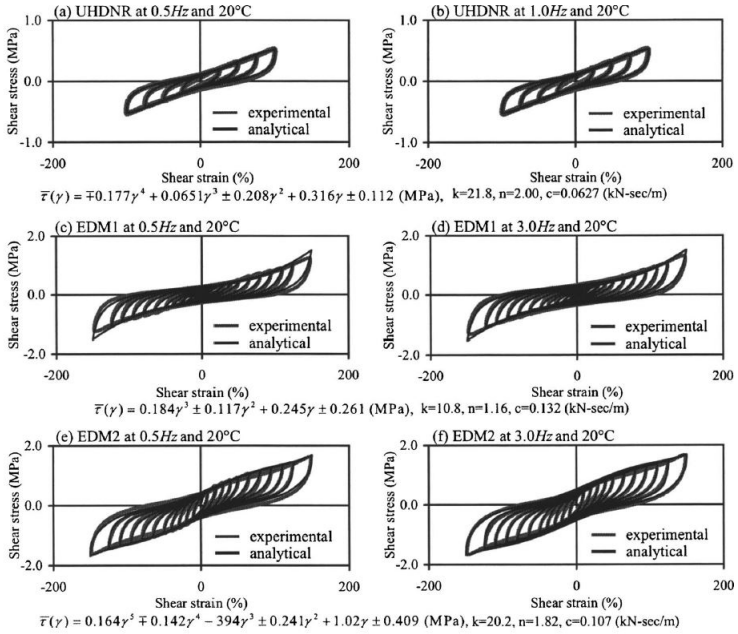

Figure 2.25: Comparison between analytical model proposed by Sause and experimental data [107]

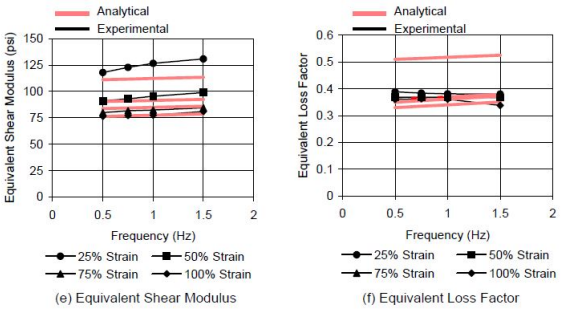

Figure 2.26: Comparison between analytical model proposed by Lee and experimental data [72]

Bouc-Wen Model

The Bouc-Wen model,which was originally proposed by Bouc [19] and later generalized by Wen [137], has been widely used to model the hysteretic behaviour of structures experiencing non linearities, or dynamic behaviour of individual devices, such as dampers, and base isolation systems [33, 144, 92, 118] . Based on the model proposed by Bouc-Wen:

$$F(x, \dot{x}) = \alpha \frac{F_y}{Y} x + (1 - \alpha) F_y z \tag{2.67}$$

in which Z is a dimensionless hysteretic component satisfying the following nonlinear differential equation:

$$Y\dot{z} = -\gamma|\dot{x}|z|z|^{n-1} - \beta\dot{x}|z|^n + A\dot{x} \tag{2.68}$$

Y, and F_y represent the the yield displacement and force of the hysteretic damper respectively; x, and $\dot{x}$ the displacement and velocity, respectively; and β, γ, A dimensionless parameters. The parameter n is an integer which controls the smoothness of the transition from elastic to plastic response, and α is the post to pre-yielding stiffness ratio. The Bouc-Wen model is very efficient, however force and deformation errors have been observed [128, 142] under certain conditions. Moreover, Ni et al [97] concluded that the Bouc-Wen model can not capture the characteristics of rubbery materials.

However, Constaninou [33] carried out a comparison between different dampers and the Bouc-Wen model. One of the dampers was a lead-rubber damper, used for base isolation. Figure 2.27 shows the comparison between the hysteretic loops of the analytical model and experimental hysteresis. The parameters were optimised based on minimizing the error between between the corresponding forces under 60 mm amplitude, 0.9 loading frequency, and a vertical load of 450 kN. Even though the results are found to be in a very good agreement it should be noted that this model was valid under this specific test under the aforementioned conditions. The data were obtained from Skinner [112].

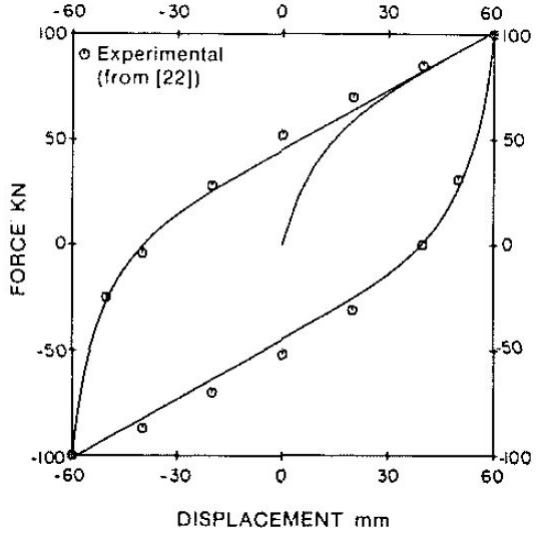

Figure 2.27: Comparison between experimental data and Bouc-Wen model [33]

Modified Bouc-Wen Model

Karavasilis et al [62] proposed a hysteretic model for a compressed elastomeric damper. This model was based on a modified Bouc-Wen model [138], connected in parallel with a non linear dashpot. The dampers' behaviour consists of two different phases: before and after slip of the elastomer, which is allowed due to the unbonding interface between the elastomer and the steel material. The force of the dashpot is:

$$F_d = C|v|^{\alpha} sgn(v) \tag{2.69}$$

where C is the damping coefficient, v is the deformation rate, andα is the velocity exponent. The force of the dashpot was combined with the force from a modified Bouc-Wen model, where the stiffness term F_Y/Y of Eq. 2.67 was modified to:

$$k = k_1 e^{-\frac{u_{max}}{uref}} + k_2 \tag{2.70}$$

where k_1, k_2,u_{ref} are constants, and u_{max} is the average of the maximum absolute deformation amplitudes in both positive ($u_{max,p}$), and negative ($u_{max,n}$) direction:

$$u_{max} = \frac{|u_{max,n}|+u_{max,p}}{2} \tag{2.71}$$

The aforementioned values were determined from characterization tests. The proposed model was found to capture satisfactorily the dampers' behaviour for both pre-slip and post-slip displacements (Figure 2.28), and was used for non linear analyses to evaluate the seismic performance of steel moment resisting frames equipped with elastomeric dampers.

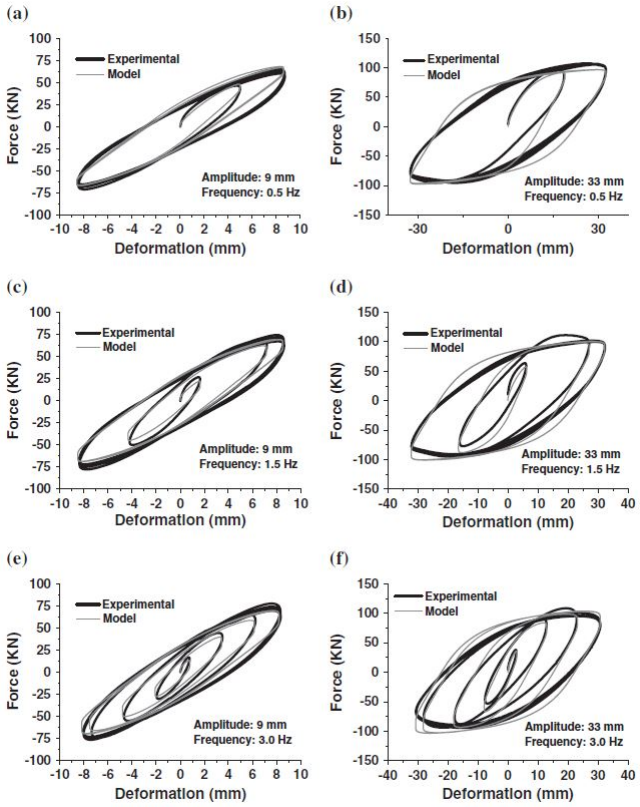

Figure 2.28: Comparison between experimental data and analytical model proposed by Karavasilis [62]

Fractional Derivatives Model

Finally, Fractional Derivatives is also an approach of modelling the hysteretic behaviour of both viscous[82], viscoelastic[42, 70], and elastomeric or rubber materials[55, 68, 129] as passive dissipation devices. This model is based on the standard linear model [95]:

$$\sigma + \alpha \frac{d\sigma}{dt} = E\epsilon + \beta E \frac{d\epsilon}{dt} \tag{2.72}$$

This model is a more complex stress-strain relationship between the simple Hooke's law ($\sigma = E\epsilon$) or the dashpot-spring combination ($\sigma = E\epsilon + \beta E d\epsilon/dt$). Adding more derivatives of σ, and ϵ in Eq. 2.72:

$$\sigma + \sum_{n=1}^{\infty} \alpha_n \frac{d^n\sigma}{dt^n} = E\epsilon + E\sum_{n=1}^{\infty} \beta_n \frac{d^n\epsilon}{dt^n} \tag{2.73}$$

Proper choices of β_n, and α_n lead to fit the experimental data with the proposed model. Replacing the integral derivatives with fractional derivatives leads to:

$$\sigma + \sum_{n=1}^{\infty} \alpha_n D^{\alpha_n} \sigma(t) = E\epsilon(t) + E \sum_{n=1}^{\infty} \beta_n D^{\beta_n} \epsilon(t) \tag{2.74}$$

where the generalized derivatives D^{α_n}, and D^{β_n} are defined as:

$$D^{\alpha_n}[x(t)] = \frac{1}{\Gamma(1-\alpha_n)} \frac{d}{dt} \int_0^t \frac{x(\tau)}{(t-\tau)^{\alpha_n}} dt \tag{2.75}$$

with $0 < \alpha_n < 1$, and Γ is the gamma function. Hysteretic plots of derivative models used for modelling VE materials can be seen at Figure 2.21. Moreover, Kasai et al [64] used the fractional derivative model to model VE damper's behaviour under cyclic and ramp tests. Even though relatively good correlation was achieved for both the shear storage modulus and the loss factor for 24, and 32 °C, results were disappointing for the 15 °C case (see Figure 2.29).

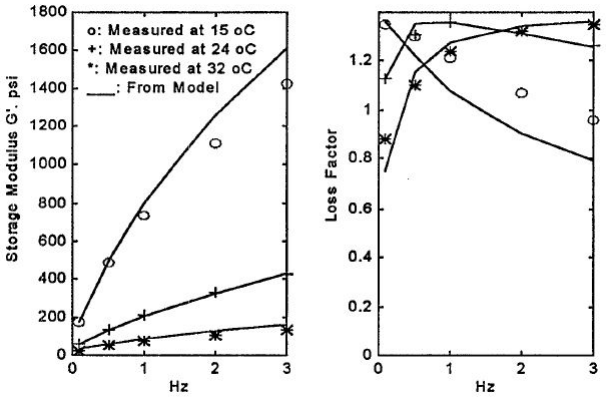

Figure 2.29: Comparison between experimental data and analytical model proposed by Kasai [64]

Another scenario is that a different form of Eq. 2.74 is used, called the $'$fractional Kelvin Model$'$, omitting any additional derivatives of the stress:

$$\sigma = E_0(1 + cD^{\beta})\epsilon(t) \tag{2.76}$$

The most common approach of determining the parameters of the aforementioned models is to obtain analytical expressions of the shear storage modulus, G',

and shear loss modulus, G'' under cyclic tests of specific strain amplitudes and frequencies, and then optimising the models' parameters fit the experimental data to these expressions. However, as was shown, matching the experimental values of G', G'' does not necessarily mean that the proposed model can capture the dynamic characteristics of the damper. The same approach is followed when minimizing the experimental and analytical force is preferred.

2.2.9 Past applications of VE/Elastomeric Dampers

It should be mentioned that most of the elastomeric materials' applications were used in base isolation techniques, where they were usually incorporated between steel plates, rather than actual implementation on frames along with diagonal braces. On the other hand, the majority of the VE dampers were used in retrofitting structures connecting the damper with the braces. The main target of the first implementations of the VE dampers was to reduce wind induced vibrations. Therefore, one of the first applications of VE dampers was in the World Trade Center (1969) in order to reduce the acceleration levels due to wind [81]. About 10000 VE dampers were installed in each tower from the 10th to the 110th floor. Their design was carried out in such a way to assist the steel frame mitigating the wind induced movement (Figure 2.30). The were located between the lower chords of the horizontal trusses and the the outer columns of the structure. The total achieved damping was calculated and found to be in the range of 2.5%-3% of critical. Seismic applications started a lot later, and more specifically in 1993, when the 13 story Santa County building in San Jose, CA, was retrofitted, since it was found that the viscous damping in the fundamental mode was less than 1% of critical. VE dampers were chosen as the final solution, since they could provide increased damping for both frequent low-level ground shaking and strong ground motions. Two VE dampers were added to each building face per floor (Figure 2.31), increasing the fundamental damping to 17% of the critical. More recent applications of VE dampers connected with steel diagonal braces include the Beijing 7 Star Morgan Plaza Hotel C (China, Beijing) in 2007 where 108 viscous and viscoelastic dampers were added for both wind and earthquake protection, and the Hotel Stockton (USA, Stockton, CA), where a combination of both viscous and

viscoelastic dampers were added to reduce the structure's responce due to seismic loads [4].

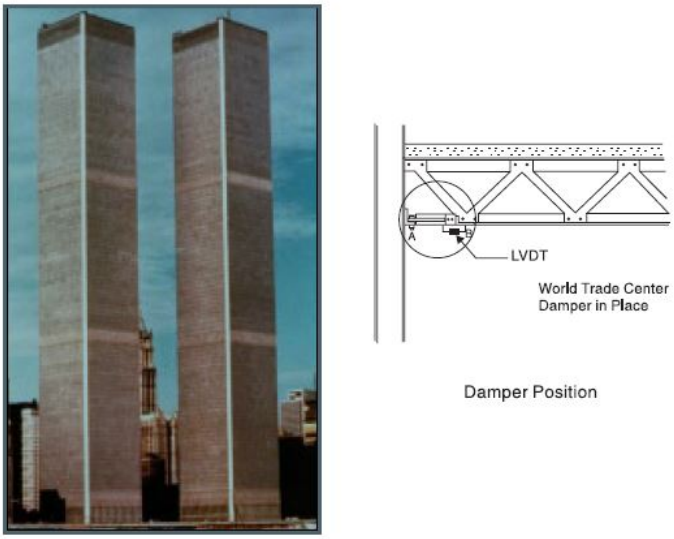

Figure 2.30: Damper Installation at the World Trade Center [31]

Figure 2.31: Santa Clara County building San Jose - Seismic application [31]

Another different approach was followed by Rant [38], where a 110-story, 630 m mega-tall building was retrofitted with VE dampers, which replaced the coupling beams connecting the shear walls. The main concept behind this decision is that since the deflected shape of very tall buildings due to horizontal loads is similar to a cantilever, rather than the shear deflection of moment resisting frames which

consists the main resisting system of low-rise buildings. Hence, the whole dampers philosophy was adjusted as well (Figure 2.32). The dampers replaced about 60% of the diagonally reinforced concrete coupling beams of the original structure. The results showed that the peak inter-story drift ratios were reduced by up to 15% under the Maximum Considered Earthquake, and the peak floor accelerations by approximately 24%.

One of the rare applications of rubber-like dampers connected with the surrounding structure with diagonal braces that could be found in the literature, was carried out by Teramoto [125] on an 11 storey, 44 m tall building which was under construction when the research paper was published. The main target of the added dampers was to reduce the vibrations due to both seismic loads and traffic motion since the building was close to subway lines. The results improved the building's performance by reducing both the maximum accelerations and storey drifts by approximately 20%. Another seismic retrofit was carried out in the Gentile-Fermi School in Fabriano, after the building suffered sufficient damage during an earthquake in the Umbria-Marche region (September 1997). A total of 33 elastomeric dampers were added at the second and the third floor of the building, absorbing 50% of the input energy. However, as already mentioned, the vast majority of the applications of elastomeric dampers to structures were carried out as part of base isolation methods.

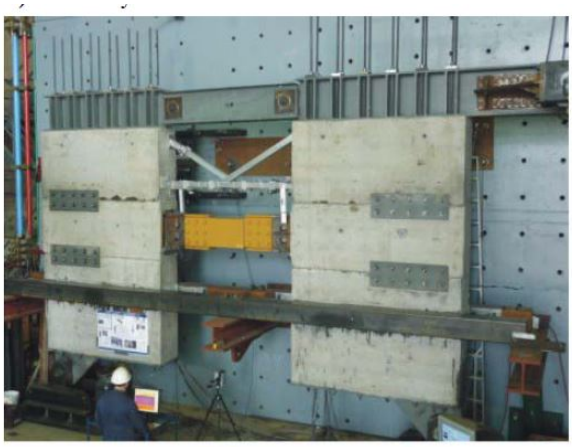

Figure 2.32: Experimental rig for VE dampers replacing coupling beams [38]

Figure 2.33: Elastomeric dampers used for seismic retrofit in the Gentile-Fermi School in Fabriano [8]

2.3 Conclusions

This section has presented the main principles of structures with supplemental dissipation devices, and their main characteristics, along with alterations in the equation of motion during earthquakes, for the case of both SDOF and MDOF structures. Furthermore, a brief introduction into each of the passive energy devices was presented. Passive energy devices are generally preferred for their simplicity, and reliability even during strong earthquakes. A more detailed insight was given in case of viscoelastic and elastomeric dampers, with the latter case to be the research focus of this study. Their main advantage is their ability to provide both stiffness and damping in contrast with other types of dampers, while they can be also effective under low amplitude forces not needing a specific value of either force or deformation to trigger their mechanism. Finally, material models which have been used by previous researches to capture the dynamic characteristics of elastomeric materials were briefly described, and actual applications of VE/elastomeric dampers to buildings were presented.

Elastomers have been mainly used in base isolation methods when they have been actually applied in the form of dampers distributed in buildings they were usually modelled assuming visco-elastic behaviour, which has been proved to be valid under only low strain amplitudes. Hence, a need for a more general hysteretic model which

would be able to capture the elastomers' characteristics beyond the deformation for which visco-elasticity can be accurate is covered by this research.

The fact that not only elastomers behaviour changes with frequency, strain amplitude, and temperature, but also elastomers hysteresis shape makes extremely difficult the modelling process with regard to seismic interest, because the main earthquake scope is to effectively capture the dynamic characteristics of the dampers under random loading for a few seconds. Even though a lot of models have been proposed, most of them are based on linearised properties of the elastomers or on models parameters optimisation based on minimization of the error of analytical expressions of shear storage modulus and corresponding experimental values under imposed sinusoidal loading with specific values of frequencies. These analytical formulas do not usually take into account any temperature and strain amplitude alterations, and depend only on the imposed loading frequency. However, these modelling techniques do not guarantee the actual representation of the elastomers hysteresis loops. Furthermore, a lack of models predicting the dynamic behaviour of the elastomeric materials under different temperatures was observed. Moreover, the majority of research of elastomeric dampers is based on base isolation techniques and not when the dampers are incorporated throughout the height of the structure with additional steel diagonals braces. These techniques are highly different and target in different expected structural performances. The uniform distribution of the dampers throughout the height of buildings offers more damping and stiffness to each floor level, as opposed to base isolation techniques where most of the seismic energy is dissipated at the structure's base. A new model is presented in this thesis, which is based on a new time domain Generalised Maxwell Model equation, and is able to predict the dynamic behaviour of elastomeric dampers for a range of strain amplitudes, loading frequencies, and ambient temperatures. Non linearities and strain-stress time history are taken into account, while the model was further validated under earthquake loading using real time substructure tests (see Chapter 6).

Chapter 3

Characterization Tests

3.1 Introduction

This chapter presents the experimental procedure which was followed in order to determine the main characteristics of two elastomeric dampers, provided by the Tun Abdul Razak Research Centre (TARRC). It is well known that elastomeric materials depend on strain amplitude, loading frequency, and ambient temperature. Therefore, sinusoidal displacements under a specific range of strain, frequency, and temperature were applied to the assemblage of the two dampers, and the corresponding force was measured. Based on the force-displacement hysteretic loops the main characteristics of the elastomer were determined.

3.2 Experimental rig

Figure 3.1 shows one of the two individual elastomeric dampers, which were provided by TARRC. It consists of an elastomeric material bonded between two steel plates. Each of these dampers has overall dimensions of 260x260 mm^2, of which only 180x230 mm^2 corresponds to the elastomer's dimensions(fig. 3.2). The 230 mm dimension coincides with the loading direction. The four A-holes, and the two B-holes allowed each of the dampers to be connected with adjacent steel plates (fig. 3.3): an additional steel plate, A, was connected with both the outer plate of the damper and with a fixed and stable reacting wall, which in turn was considered fixed at its

base; the interior plate of the damper was connected to a plate (B), which in turn enables connection to the actuator via a central plate , C. The final configuration of the rig can be seen in Figures 3.3 and 3.4.

It should be noted that the focus of this research is on the effect of the elastomeric dampers on structures due to earthquake loads. Therefore, the elastomeric dampers were tested for the earthquake scenario only.

In order to investigate the strain amplitude, frequency, and temperature dependence, a series of tests was carried out based on sinusoidal displacement histories at the Elastomeric Dampers (EDs). In order to avoid large initial displacement and velocity, ramping cycles were implemented, along with 18 full sinusoidal cycles (see Figure 3.5). This process, which is similar with the one proposed by FEMA356 [5], was repeated for frequencies of 0.25, 0.5, 1.0, 2.0, 3.0, and 4.0 Hz, for strain amplitudes of 10, 20, 30, 40, and 50%, and for ambient temperatures of 20, 25, 30, and 35°C. The maximum shear strain amplitude was limited to 50%, to avoid any potential permanent damage, severe cracking, or debonding of the elastomer. The first series of tests was conducted at room temperature (20°C), while the same process was repeated for 25, 30, and 35°C, with the use of a heater, and a temperature control chamber (fig. 3.6), so that the target temperature was kept stable during the test. Two thermocouples were attached at the elastomer, one at the top and one at the bottom surface of the elastomer, for measuring the ambient temperature along with any increase in temperature during the loading history. For every test which was carried out at higher than room temperature, the elastomer was heated until convergence was achieved between the temperature shown at the two thermocouples, typically between 8-12 hours.

A 100 kN Instron servo-hydraulic actuator was used to carry out the experimental procedure. The actuator has a stroke of ±125 mm, receiving its power via pressurised oil through Moog servo valves, which control the piston movements by directing the oil to one side of it and connecting the other side to the return line [18]. The pressurised oil is delivered through the laboratory's substations, which are installed directly on the main hydraulic high pressure line, driven by three 60 l/min oil pumps, resulting in a peak flow of 180 l/min. Hydraulic accumulators which

are capable of storing highly pressurised oil, provide enhanced flow rates at times of peak consumption when the instantaneous supply from the pumps is not enough [18]. The substations are also connected to the return line to the oil reservoir. During low consumption, individual pumps can be switched off. In order to mitigate any floor vibration effects all the hydraulic equipment is installed on a large concrete block of 9.1x4.2 m in surface area, 1.6m deep and weighing 166 tonnes. The testing area of the floor is 7.5x3.5m. The communication between the actuators and the substation (closed loop control) is controlled by an Instron Labtronic 8800 controller, which provides four channels of position or force control, and is based on a proportional-integral-derivative-lag (PIDL) controller, with its parameters set either by an auto-tuning process or by hand. The controller parameters are accessible to the user through the Instron program RS+. More information regarding the laboratory equipment is given in Chapter 6, where real time substructure tests are conducted.

A linear encoder is also attached to the damper in order to capture the actual deformation, and not the one achieved by the actuator, since some flexibility of the connecting elements is anticipated. It was connected at the mid-height of the central plate of the rig assemblage. A thermocouple was attached to the top and bottom surface of the elastomer in order to measure the ambient temperature, but also to capture any increase in temperature during the tests. Hence, the experimental tests were focused on verifying non linear dependence on strain amplitude, frequency, and ambient temperature. Among these parameters, it is has been shown that strain dependence is the dominant factor [72, 103].

Figure 3.1: Elastomeric Damper provided by TARRC

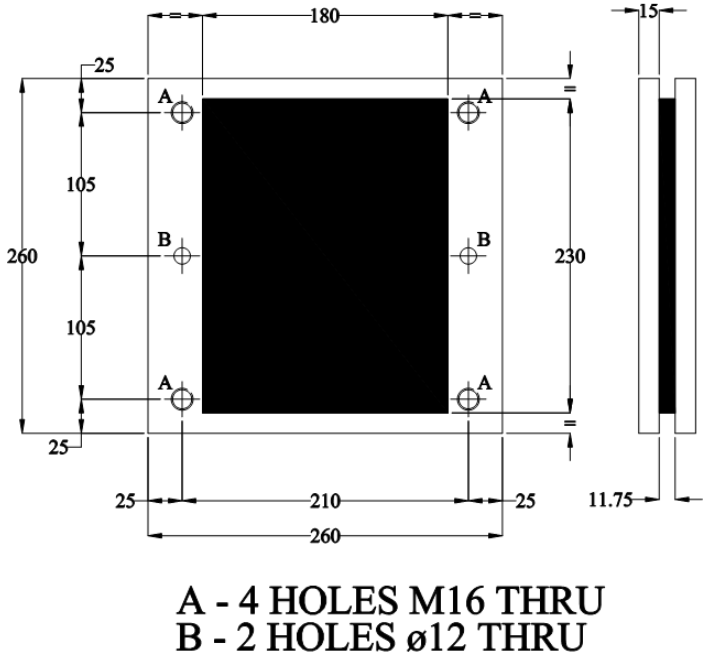

Figure 3.2: Elastomeric Damper Dimensions

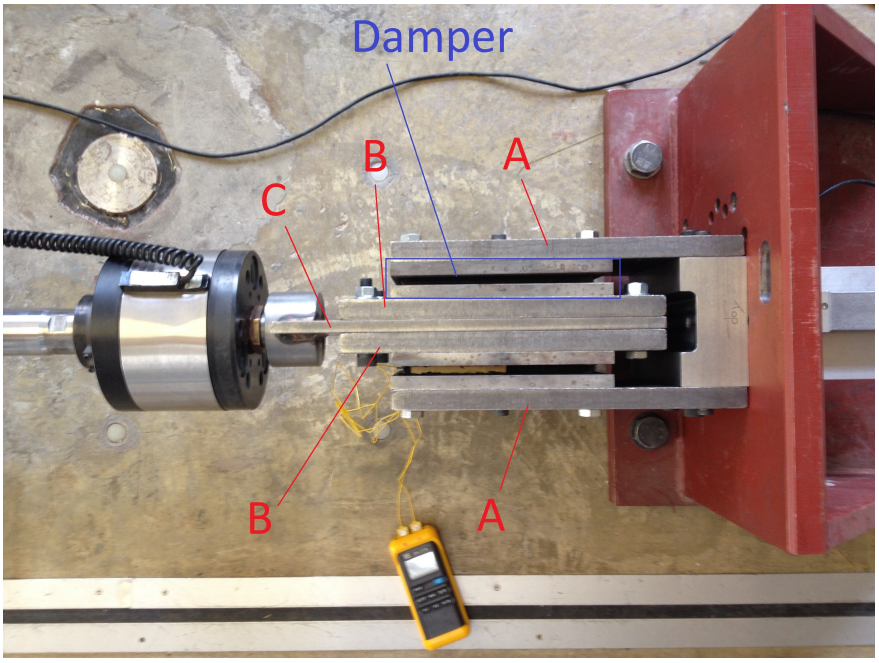

Figure 3.3: Plan of the final rig: elastomeric damper connected with actuator

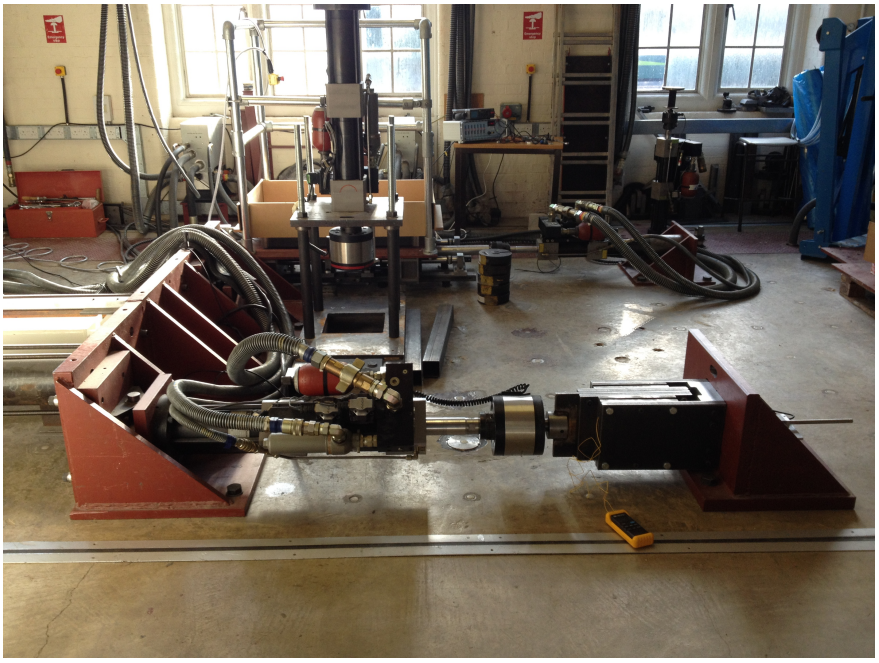

Figure 3.4: Final Rig: elastomeric damper connected with actuator

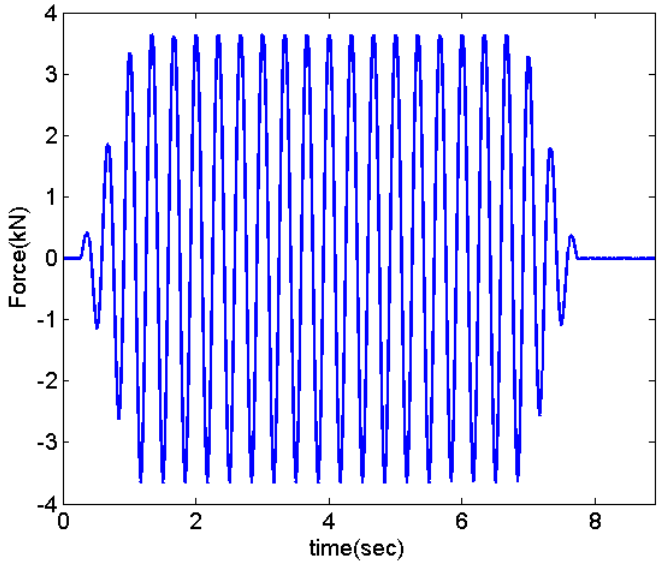

Figure 3.5: Typical Displacements' command - (30% shear strain, 2 Hz)

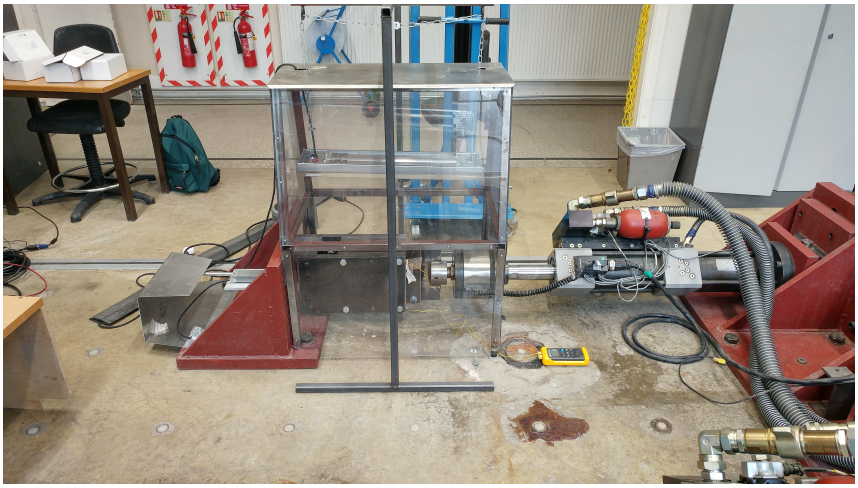

Figure 3.6: Temperature chamber

3.3 Mechanical Properties

Figure 3.7 shows a typical hysteretic loop of the elastomeric dampers corresponding to 40% maximum shear strain amplitude, 3 Hz frequency, and 20°C temperature. It can be seen that after the first cycles, the hysteretic loops become more and more steady and approximately repeatable, corresponding to smaller and smaller stiffness degradation. Hence, in order to determine the mechanical properties of the dampers the average value of the hysteretic loops of cycles 5-15 was taken. As already mentioned in Chapter 2, the shear storage modulus, G', and either the shear loss modus, G'', or the loss factor, n, govern the main characteristics of the dynamic behaviour of viscoelastic and elastomeric materials. Instead of G', the equivalent shear modulus, G_{eq} can be determined in a similar way that equivalent stiffness was defined in Chapter 2 (see section 2.2.7). All the above parameters can be extracted from each of the hysteretic loops as:

$$G' = \frac{\tau(\gamma=\gamma_{max}) - \tau(\gamma=\gamma_{min})}{\gamma_{max} - \gamma_{min}} \tag{3.1}$$

$$G_{eq} = \frac{\tau_{max} - \tau_{min}}{\gamma_{max} - \gamma_{min}} \tag{3.2}$$

$$n = \frac{1}{2\pi}\frac{ED}{ES} \tag{3.3}$$

where $\tau(\gamma = \gamma_{max})$ is the shear stress corresponding to the maximum strain γ_{max}, $\tau(\gamma = \gamma_{min})$ is the shear stress corresponding to the minimum strain γ_{min}, τ_{max} is the maximum shear stress, τ_{min} is the minimum shear stress, ED and ES are the dissipated energy per cycle of oscillation, and the maximum energy stored respectively. ED can be calculated based on the area of the hysteretic loop. ES can be calculated as:

$$ES = \frac{1}{2}G'\gamma_{max}^2 \tag{3.4}$$

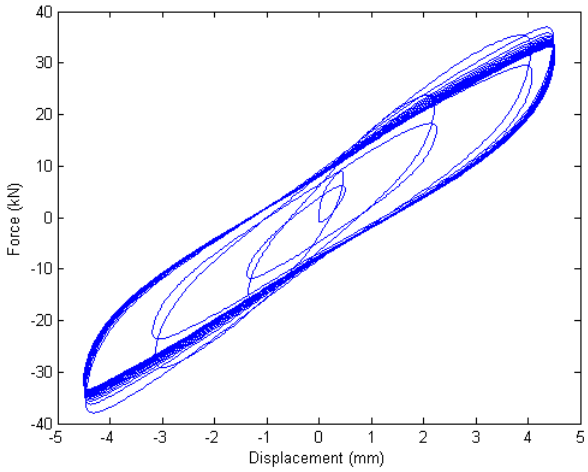

Figure 3.7: Typical force-displacement relationship for ED under frequency of 3Hz, strain amplitude of 40%, 20°C temperature

3.4 Results

All the aforementioned parameters are summarised in Appendix 1 (tables A.1 to A.4) for all the strain amplitudes, frequencies, and temperatures. Comparing the range of the values of both the loss factor and the shear storage modulus shows that they are close to the rubbery materials used by Lee[72], and other researchers [125, 114]. It should be also mentioned that any temperature variations during testing were found to be almost negligible.

The results showed that strain amplitude had a larger impact on the EDs' behaviour, in contrast with frequency, and temperature. This can be seen by two different approaches. The first one is to compare the amplitude dependence at a range of frequencies at fixed temperature, in the form of Figures 3.17 and 3.18. These figures prove the above statement that the dominant factor which affects the elastomers' dynamic behaviour is the amplitude and not the frequency, especially in the case of the loss factor, which practically remains the same regardless of any change in frequency. It is also noticeable that when the strain amplitude increases above 30% (which is the key point, as be seen in the second approach, for the transition between the viscoelastic phase to elastomeric phase) the rates of change of both the shear storage modulus and the loss factor reduce significantly. Below 30%, a large decrease, especially in the loss factor, can be observed. Furthermore, it seems that amplitude and frequency have exactly opposite effects, since increasing strain amplitude leads to decreasing the mechanical properties of the elastomer, while increasing the loading frequency leads to increasing them.

The second approach of demonstrating that the strain amplitude has the largest effect on the elastomer's behaviour is by plotting the hysteretic loops of the dampers keeping the other two parameters (frequency, and temperature) constant. Hence, observing Figures 3.8 to 3.13, it can be seen that the elastomer exhibits approximately viscoelastic behaviour for strain amplitudes of 10%-30%, proving that elastomers exhibit viscoelastic behaviour under relatively low amplitudes, which is one of the main material characteristics addressed in Chapter 2. The more the strain amplitude increases, the more the hysteretic behaviour tends to form a more typical elastomeric shape (compare for example Figures 3.9a and 3.9e), which as explained in Chapter 2 has slightly different characteristics from the conventional viscoelastic shape. On the other hand, this is not the case when the frequency is altered (compare for example Figures 3.8a and 3.13a or Figures 3.8e and 3.13e). In that case, even though the mechanical properties change, the overall shape of the hysteresis loops remain the same (Figures 3.8 to 3.13) . In case of elastomer dependence on strain amplitude, not only the mechanical characteristics change, but also the whole behaviour of the material changes as well. This fact makes extremely difficult the

modelling procedure of the material. But, at the same time it shows that when the material has larger strain amplitudes, and hence behaves more like a typical elastomer, it tends to be more and more independent of the frequency, in contrast with its viscoelastic phase when the strain amplitudes are relatively low.

With regard to the effect of ambient temperature, both the shear storage modulus, and the loss factor decrease with the increase of temperature. This can be observed by plotting the hysteretic curves of the dampers for different temperatures, while keeping the frequency, and the strain amplitude constant. Figure 3.14 shows how the ability of the dampers to dissipate energy becomes smaller as the ambient temperature increases. However, it can also be seen that the shape of the hysteresis remains unchanged, leading to the conclusion that only strain amplitude leads to different hysteresis shapes, in contrast with frequency and temperature, which affect, more or less, the dampers' characteristics but not their hysteresis shape.

The effect of the temperature on the elastomers' properties can be more clearly seen in Figures 3.15 and 3.16, where the values of loss factor and shear storage modulus are plotted against frequency for different temperatures, while keeping the strain amplitude constant at 40%. Two different conclusions can be made through these figures: a) increase of temperature leads to decrease of dampers' efficiency. However, the rate of this decrease slows as the temperature gets higher, b) the dampers' mechanical properties remain almost constant, especially in the case of the loss factor, with any frequency alteration. Moreover, similar observations with the 20°C case, can be determined from Figures 3.19 to 3.24. These figures validate the observations determined from ambient temperature, and lead to the estimation that the elastomer behaves similarly at different temperatures. Its mechanical characteristics are reduced. However, at the same time it seems that any alteration in strain amplitude and frequency results in a quite similar change in the loss factor, and the shear storage modulus. Finally, it should be noted that the tests at the ambient temperature of 20°C were repeated after approximately two years and no noticeable ageing effects were observed. Figure 3.25 shows this resemblance comparing the hysteretic response of the EDs for a strain amplitude of 40%, frequency 2Hz and ambient temperature of 20°C. The figures are almost identical.

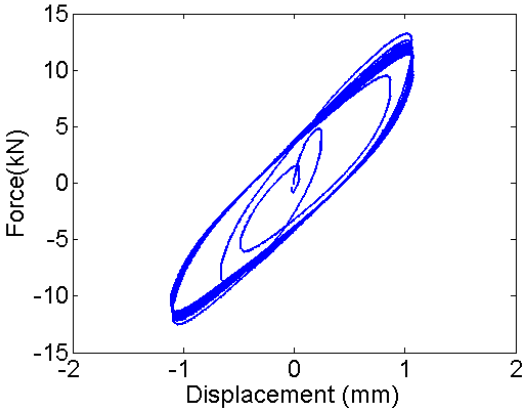

(a) 10% maximum strain

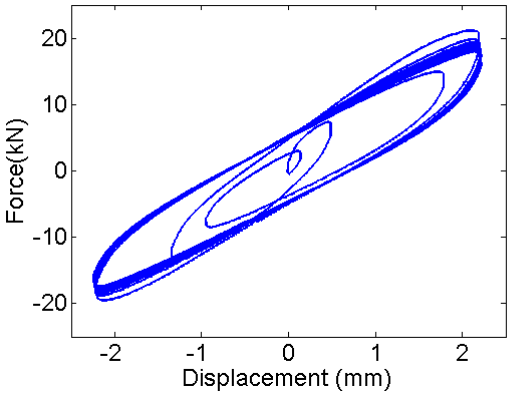

(b) 20% maximum strain

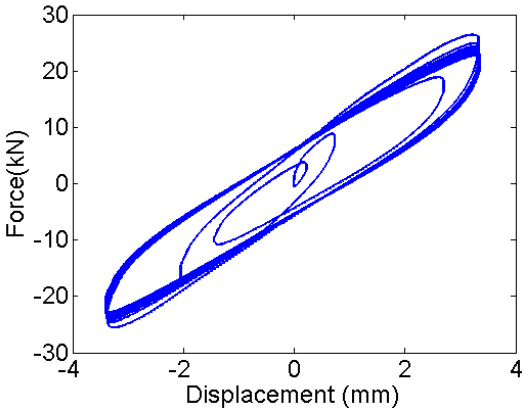

(c) 30% maximum strain

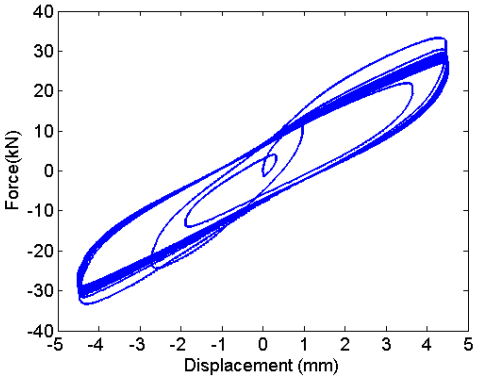

(d) 40% maximum strain

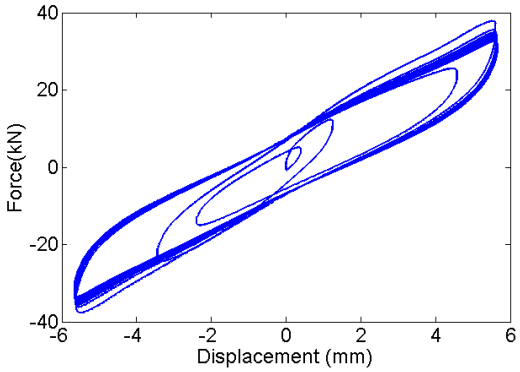

(e) 50% maximum strain

Figure 3.8: ED's hysteretic loops for 0.25 Hz and 20°C

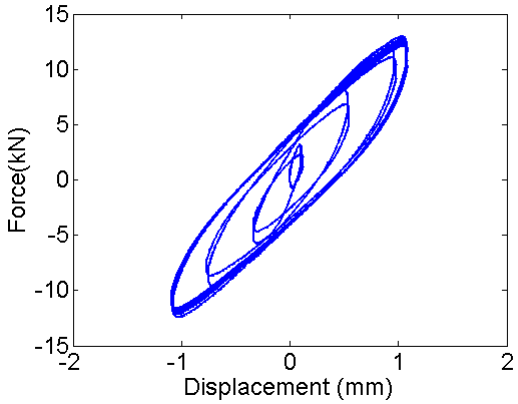

(a) 10% strain

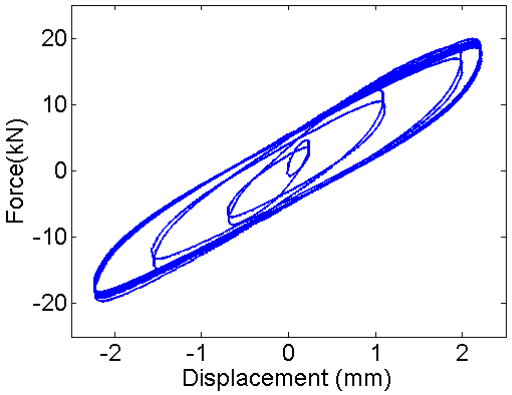

(b) 20% strain

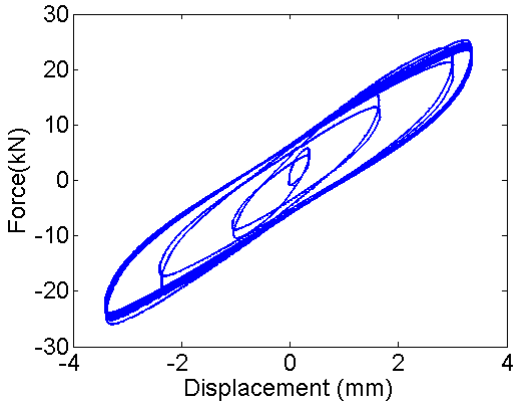

(c) 30% strain

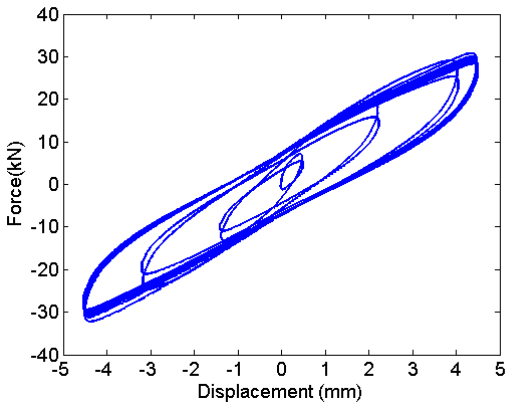

(d) 40% strain

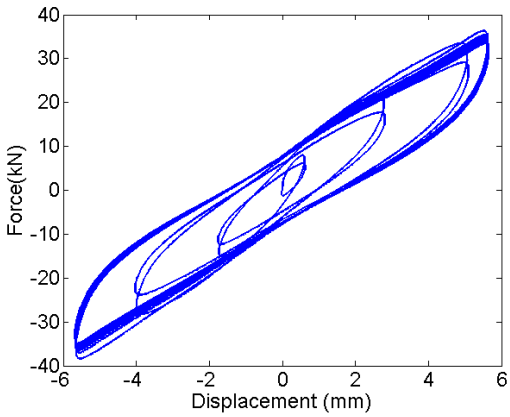

(e) 50% strain

Figure 3.9: ED's hysteretic loops for 0.5 Hz and 20°C

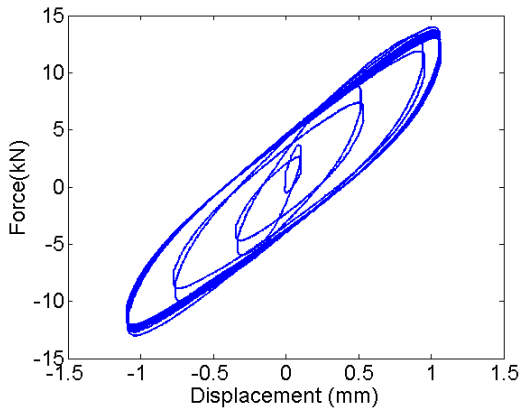

(a) 10% strain

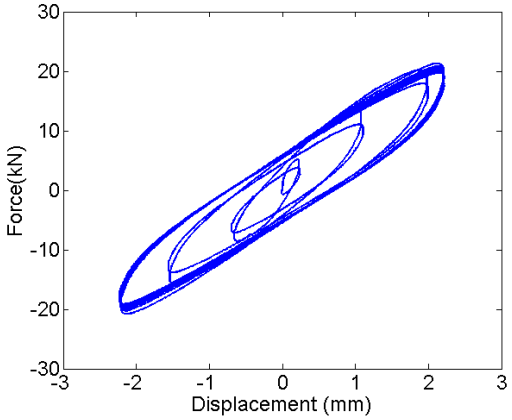

(b) 20% strain

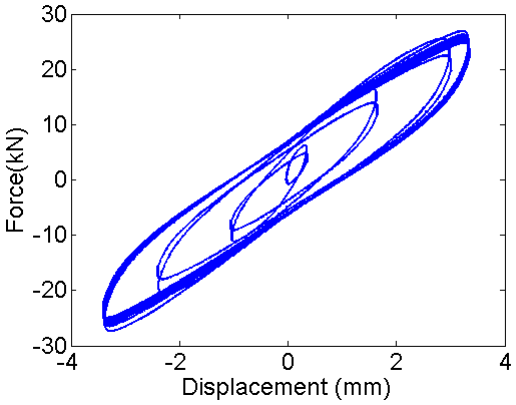

(c) 30% strain

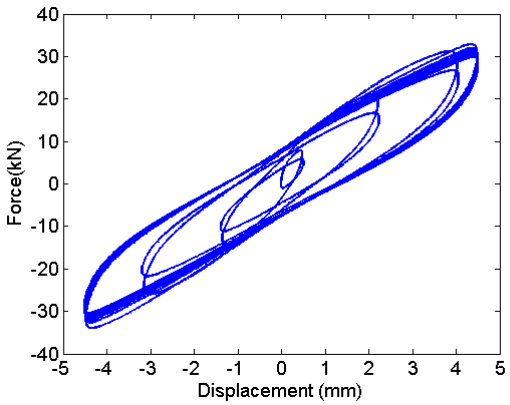

(d) 40% strain

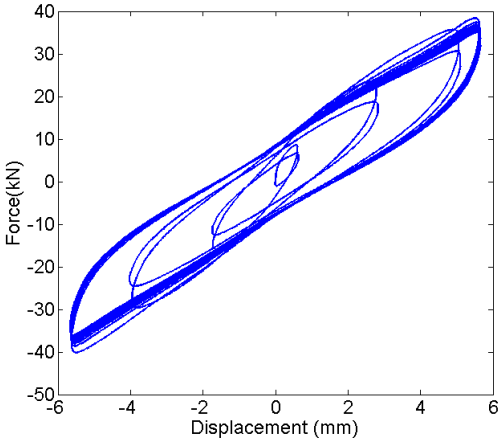

(e) 50% strain

Figure 3.10: ED's hysteretic loops for 1.0 Hz and 20°C

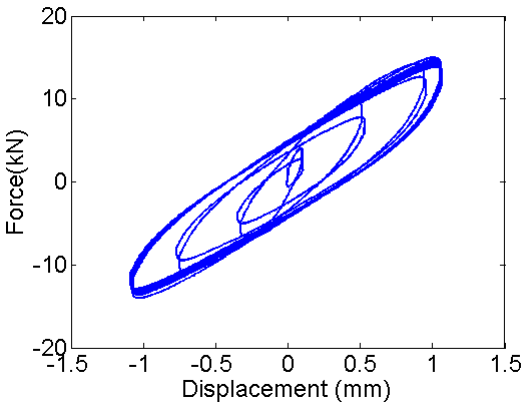

(a) 10% strain

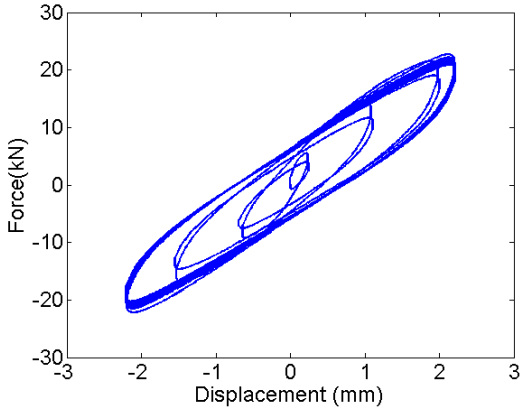

(b) 20% strain

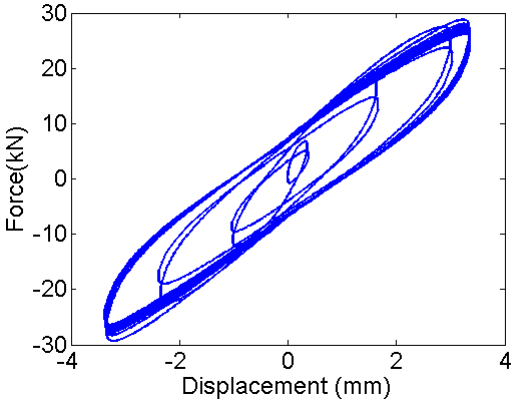

(c) 30% strain

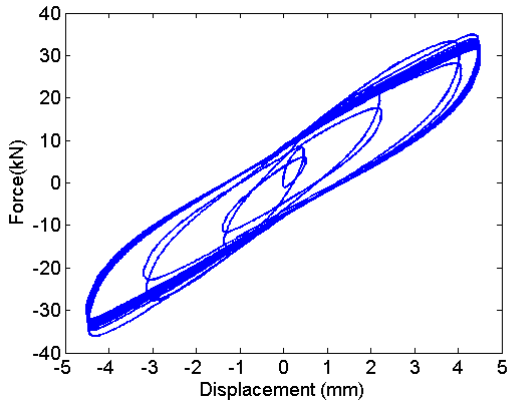

(d) 40% strain

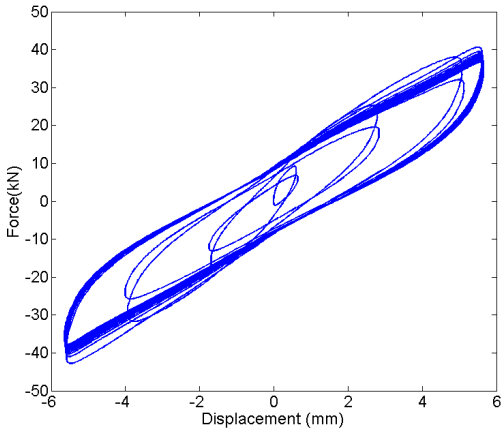

(e) 50% strain

Figure 3.11: ED's hysteretic loops for 2.0 Hz and 20°C

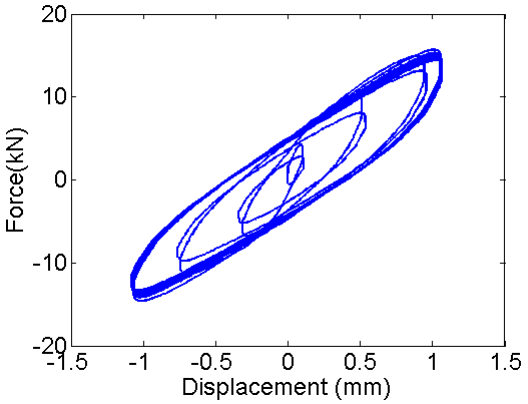

(a) 10% strain

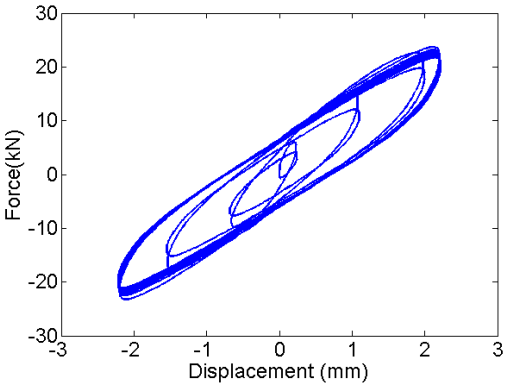

(b) 20% strain

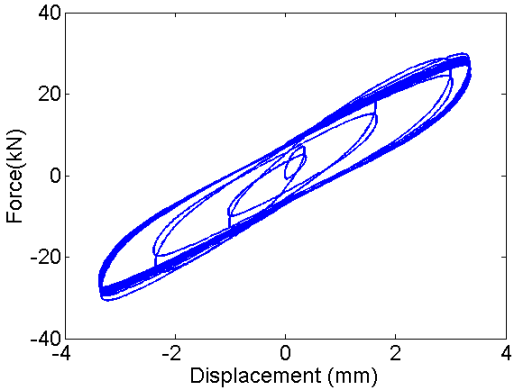

(c) 30% strain

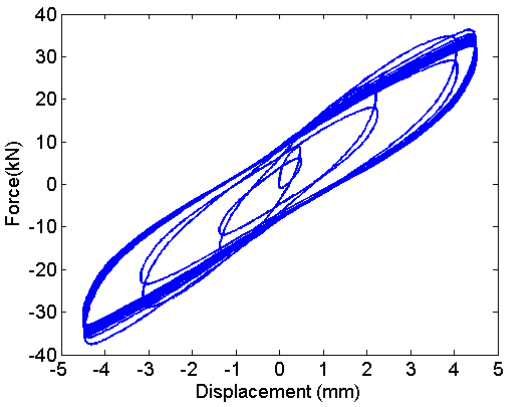

(d) 40% strain

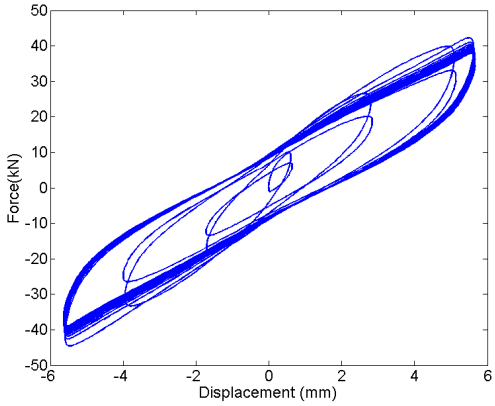

(e) 50% strain

Figure 3.12: ED's hysteretic loops for 3.0 Hz and 20°C

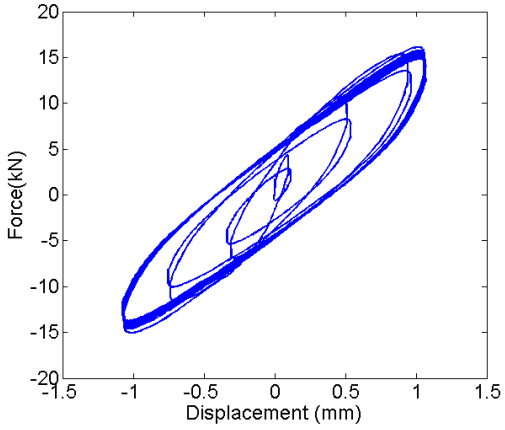

(a) 10% strain

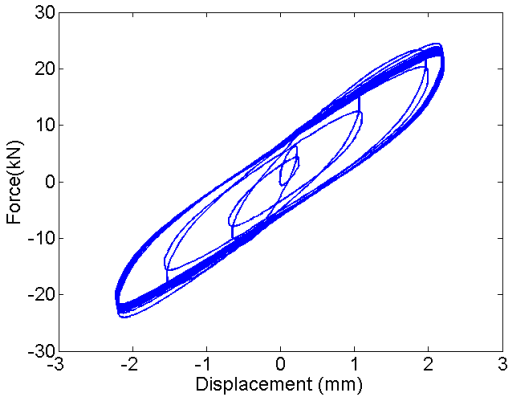

(b) 20% strain

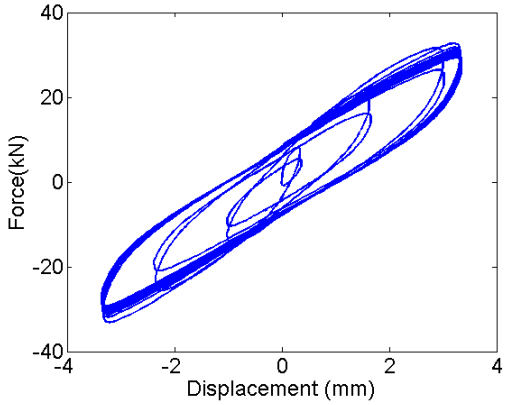

(c) 30% strain

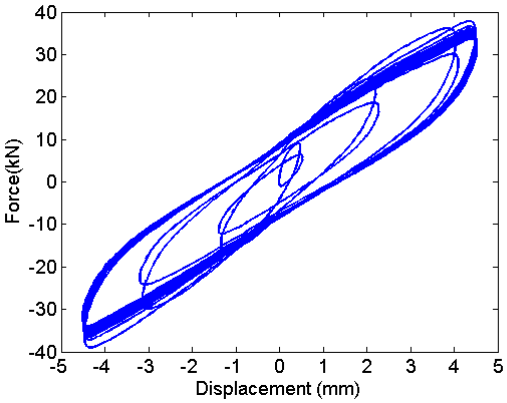

(d) 40% strain

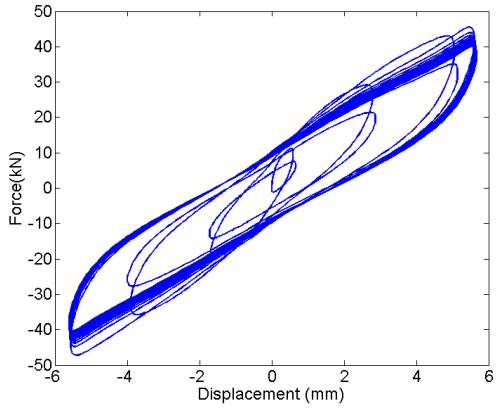

(e) 50% strain

Figure 3.13: ED's hysteretic loops for 4.0 Hz and 20°C

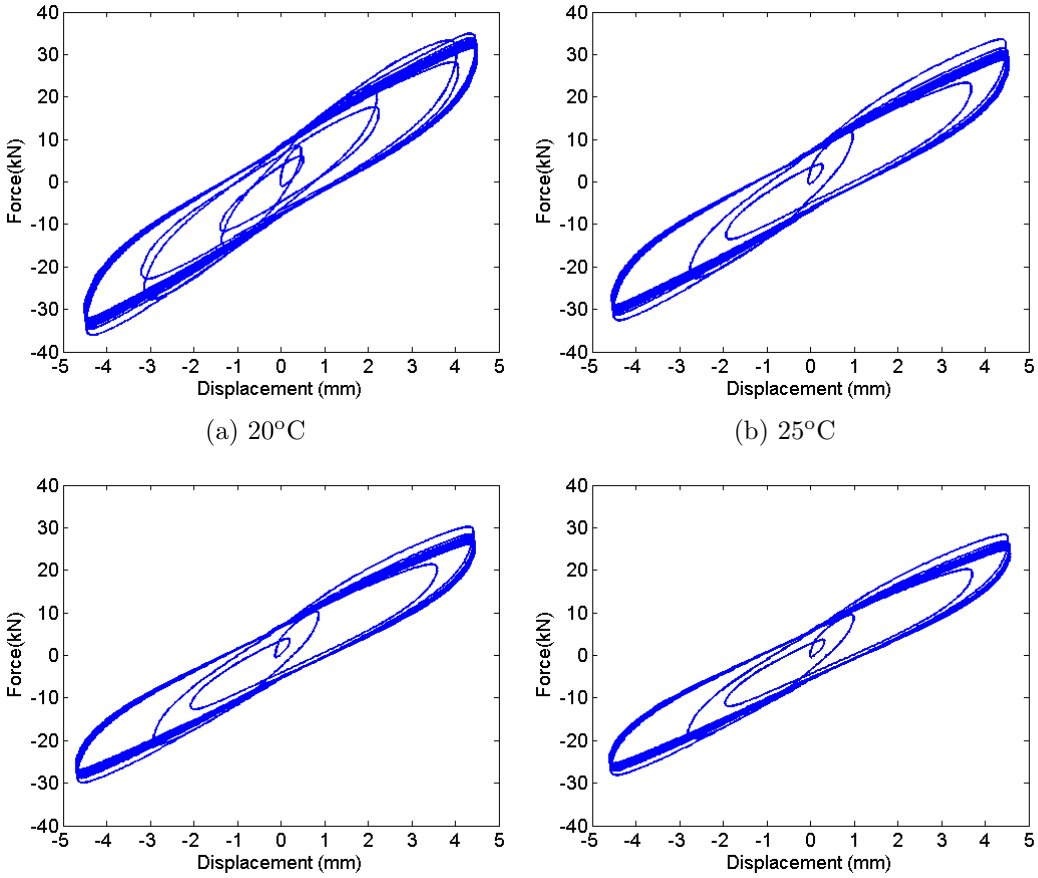

(a) 20°C (b) 25°C

(c) 30°C (d) 35°C

Figure 3.14: ED's hysteretic loops for 2.0 Hz, 40% shear strain, under 20-35°C

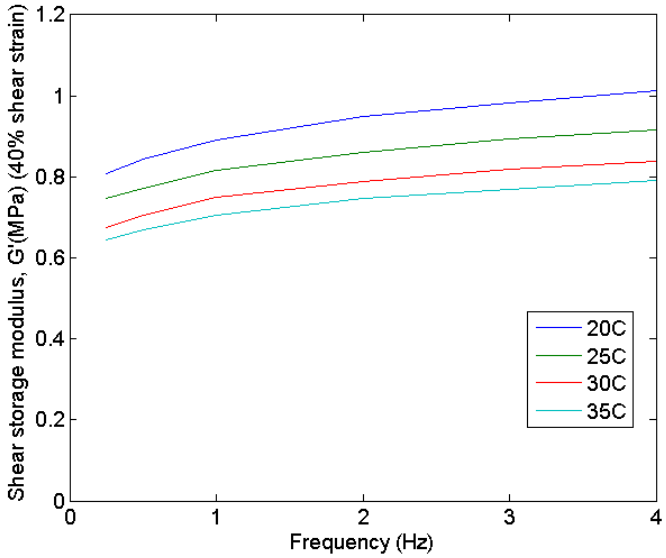

Figure 3.15: Shear storage modulus, G', under various temperatures, and frequencies for constant 40% shear strain

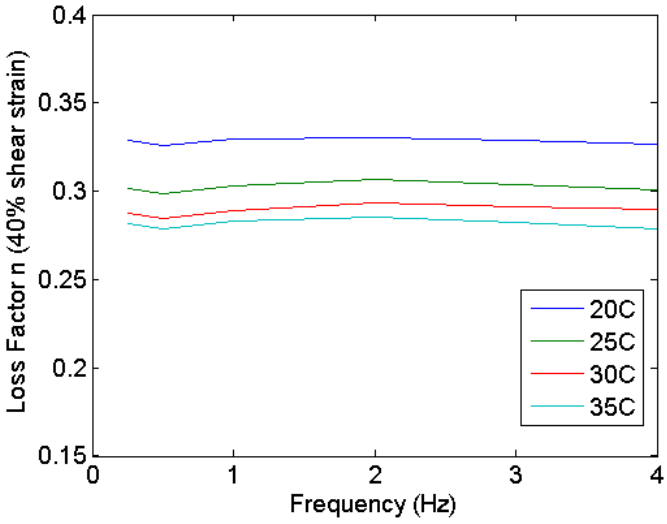

Figure 3.16: Loss factor, n, under various temperatures, and frequencies for constant 40% shear strain

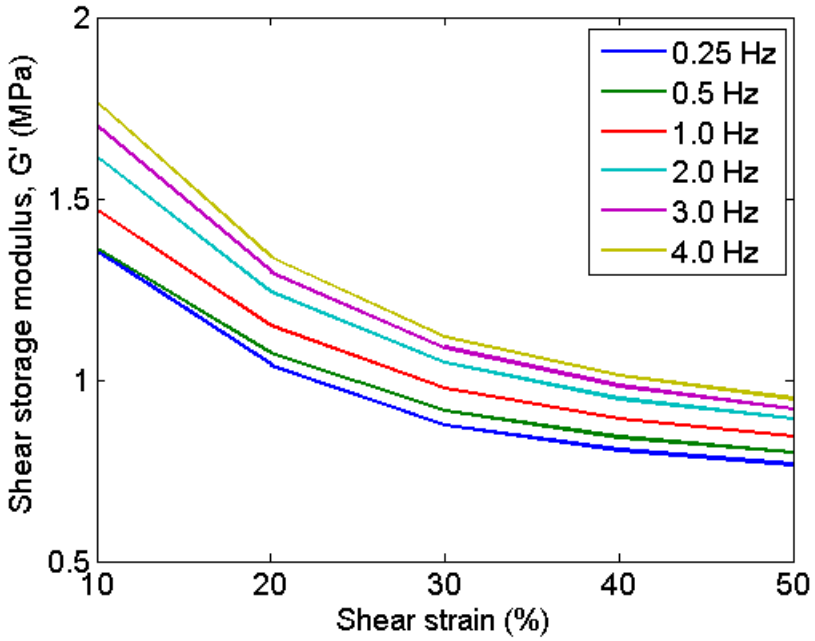

Figure 3.17: Shear storage modulus, G', at 20°C

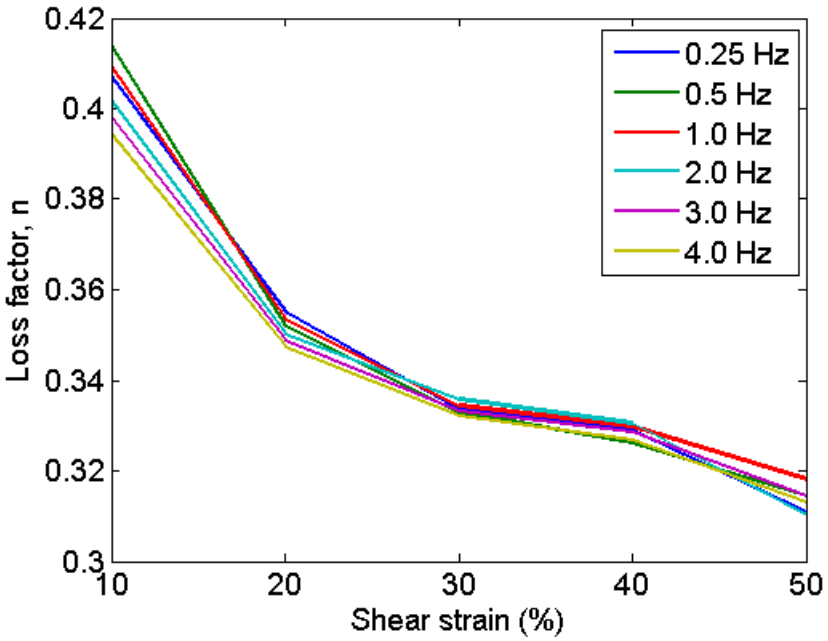

Figure 3.18: Loss factor, n, at 20°C

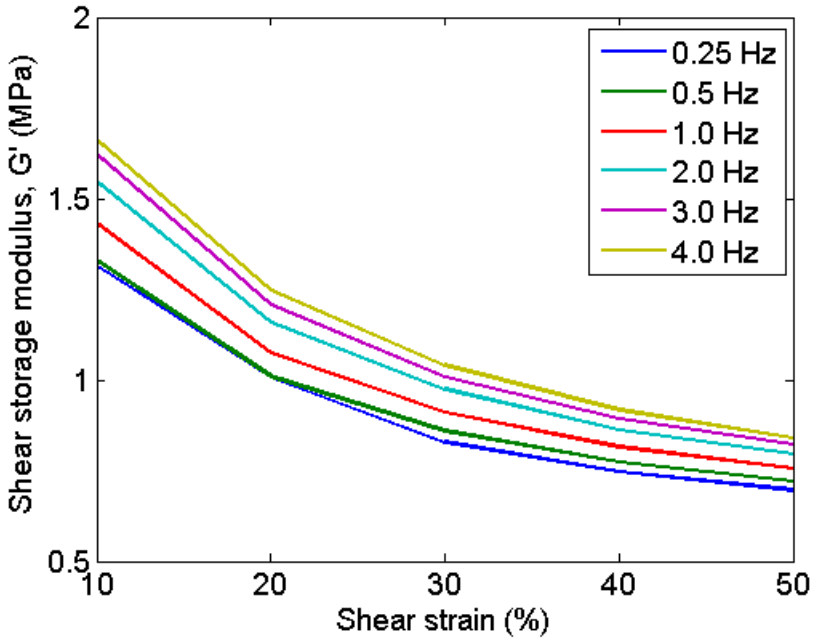

Figure 3.19: Shear storage modulus, G', under 25°C

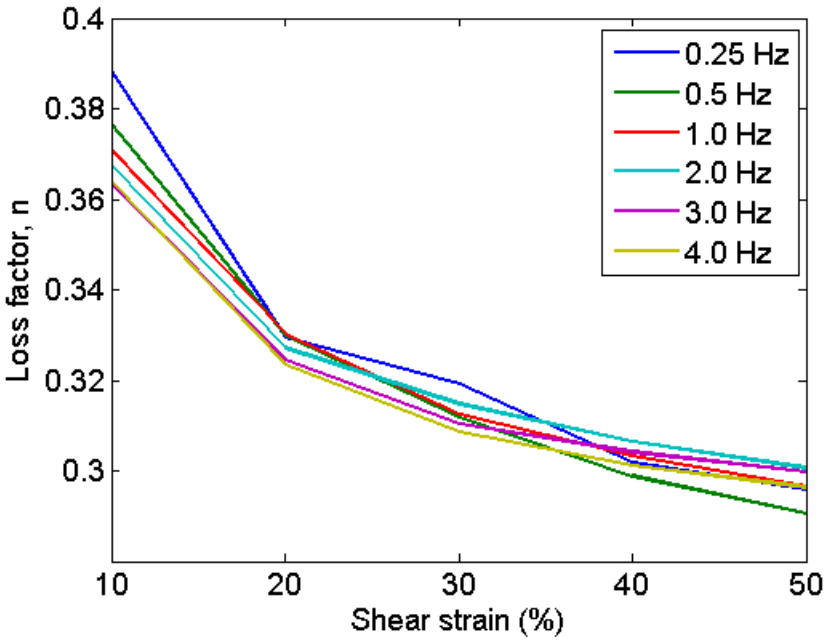

Figure 3.20: Loss factor, n, under 25°C

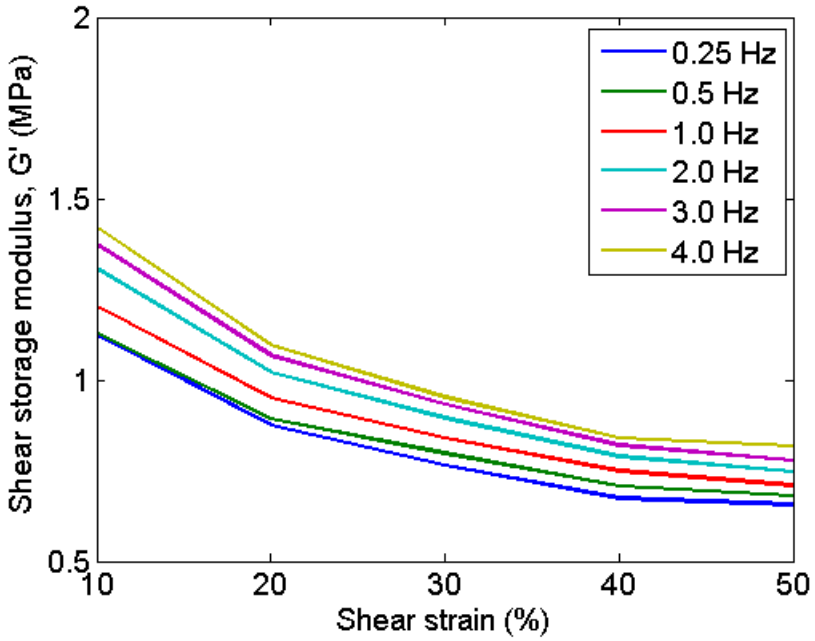

Figure 3.21: Shear storage modulus, G', under 30°C

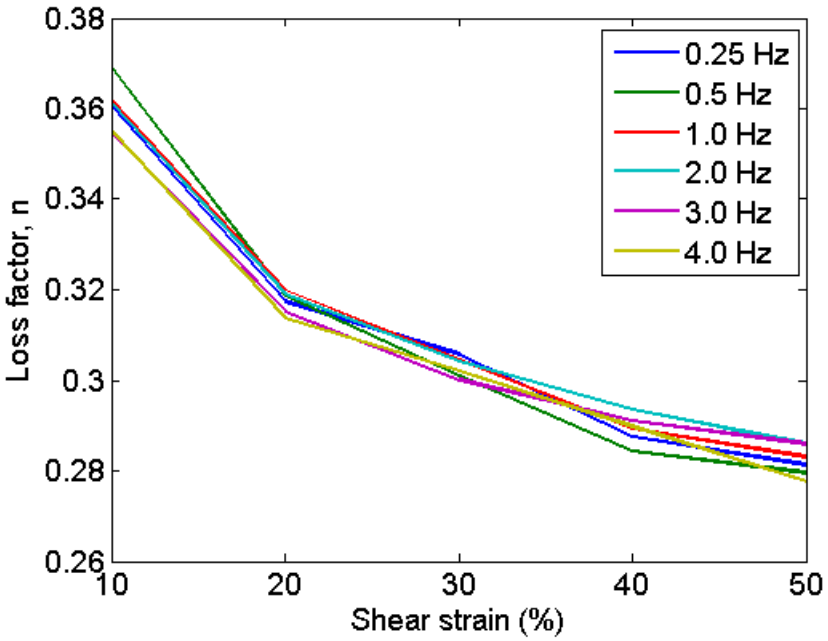

Figure 3.22: Loss factor, n, under 30°C

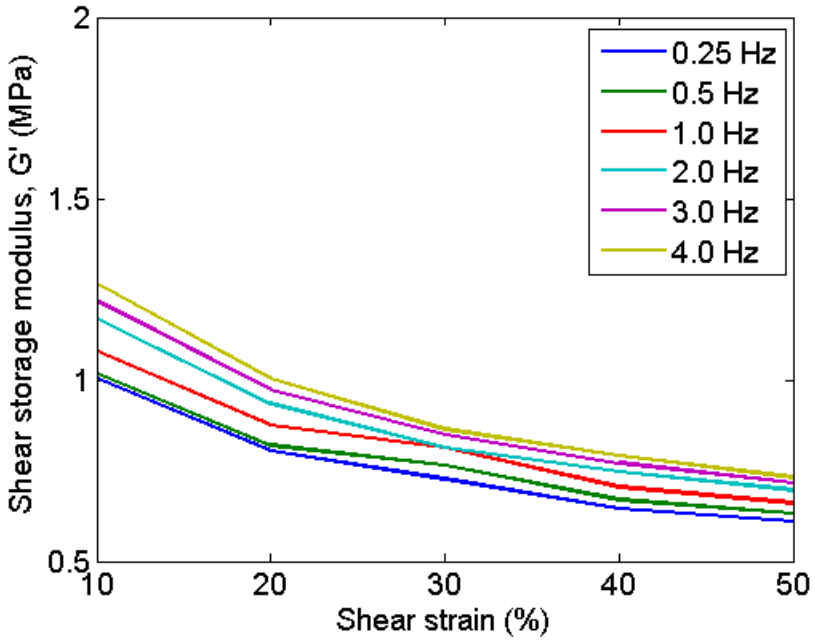

Figure 3.23: Shear storage modulus, G', under 35°C

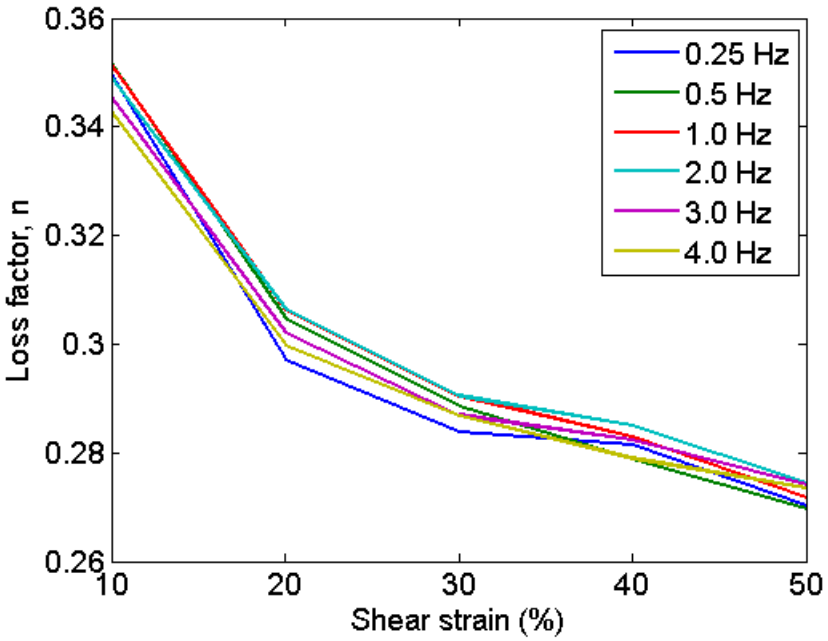

Figure 3.24: Loss factor, n, under 35°C

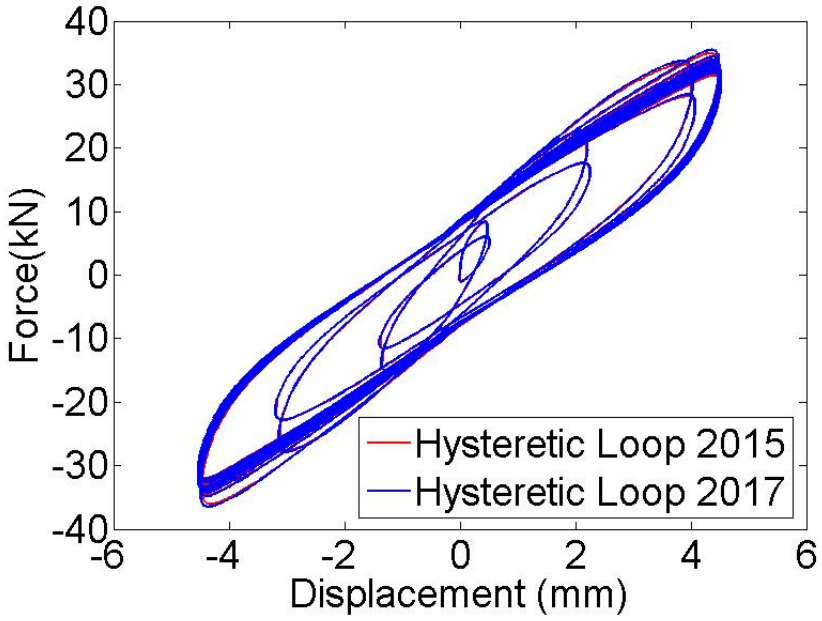

Figure 3.25: Comparison of EDs hysteretic Loops for degradation effects due to time

3.5 Conclusions

This chapter describes the experimental procedure which was followed in order to obtain the main mechanical characteristics of the elastomeric dampers, which were provided by TARRC. Similar to viscoelastic materials, elastomers' behaviour depends on strain amplitude, frequency, and ambient temperature. Hence, the tests were based on sinusoidal strain time histories in a range of different maximum strain amplitudes, loading frequencies, and temperatures. The results showed that the dominant factor which highly affected elastomers' performance was the strain amplitude, since it not only affected the values of loss factor, and shear storage modulus, but also was responsible for alteration of the hysteresis shape from viscoelastic to pure elastomeric. On the other hand, the elastomers' parameters, especially the loss factor, were found to be insensitive to any frequency alteration. This was observed under every different ambient temperature that the dampers were tested. With regard to temperature effect, it seems that any increase in ambient temperature resulted in decreasing the dissipative capacity of the dampers. However, the deterioration becomes smaller and smaller as the temperatures gets higher. One other

important observation is that elastomer's mechanical properties tended to have only a low variability when the strain amplitude was more than 30%, which, as explained earlier, was the transition point from the viscoelastic to the elastomeric phase. This leads to the conclusion that, comparing with conventional viscoelastic materials, elastomers can be much less dependent not only on frequency but on strain amplitude as well, providing that the strain amplitude has relatively large values.

Chapter 4

Hysteretic Constitutive Model Elastomeric Dampers

4.1 Introduction

The description of the characterization tests was presented in Chapter 3, in order to evaluate the elastomer's dependence on strain amplitude, loading frequency, and ambient temperature. It was observed that the elastomer exhibited highly non linear behaviour, which was dependent on these factors, especially strain amplitude. In order to represent the damper's dynamic behaviour a modified version of the Generalised Maxwell Model (GMM) is proposed in this chapter, with an effort to take into account any non linearities. Moreover, the GMM force-displacement relationship for N Maxwell elements, in the time domain, is also proposed. This equation was then modified, assuming $N = 1$ Maxwell elements, and to form the final proposed hysteretic constitutive model.

4.2 Generalised Maxwell Model

4.2.1 General Background

The proposed model for the hysteretic behaviour of the EDs is based on the well known Generalized Maxwell Model (GMM). The GMM has been proposed as a numerical representation of VE materials [60, 89] and can be graphically represented

as shown in Figure 4.1. It was briefly presented in Chapter 2, as a modelling option of VE materials, and will be presented in more detail here, since it forms the basis of the proposed hysteretic model. As already mentioned, it consists of a linear spring, with stiffness k_0 (or shear modulus G_0 in case of a stress-strain relationship), connected in parallel with N Maxwell elements. Each Maxwell element is a linear spring, with stiffness k_i (N/m), connected in series with a linear dashpot, with damping parameter c_i $(Nsec/m)$ (or shear modulus G_i (N/m^2) and shear damping coefficient n_i $(Nsec/m^2)$ in case of a stress-strain relationship).

The most common procedure of determining the parameters of a VE or elastomeric material, when the GMM is used, is to minimize the error between the analytical values of the shear storage and the shear loss modulus, and the corresponding values which are based on characterization experiments. With regard to how these values are extracted based on the experimental data, Chapters 2 and 3 provide relevant information. With regard to analytical expressions which predict the shear storage modulus, and the shear loss modulus, or loss factor, these can be determined from Eqs 4.1, and 4.2. These equations are based on the assumption that the applied strain has sinusoidal form, with a frequency ω. Therefore, the corresponding shear storage modulus, G' and the shear loss modulus, G'' are determined as[89]:

$$G' = G_0 + \sum_{i=1}^{N} \frac{G_i \omega^2 {\tau_i}^2}{1 + \omega^2 {\tau_i}^2} \tag{4.1}$$

$$G'' = \sum_{i=1}^{N} \frac{G_i \omega {\tau_i}^2}{1 + \omega^2 {\tau_i}^2} \tag{4.2}$$

where

$$\tau_i = \frac{c_i}{k_i} \tag{4.3}$$

is known as the relaxation time.

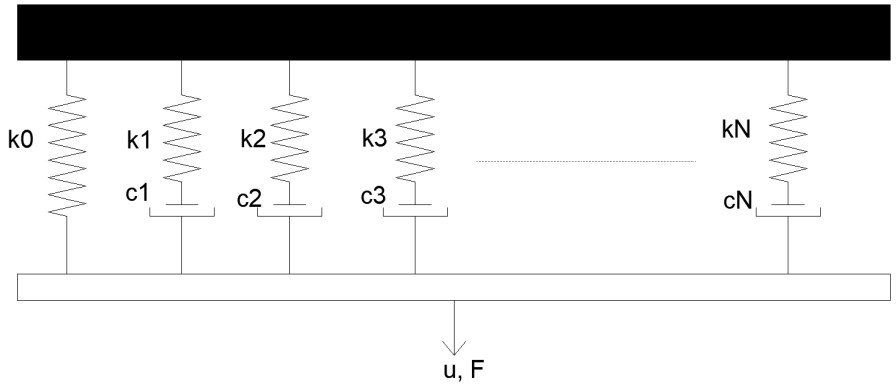

Figure 4.1: GMM representation in terms of Force-displacement

As already mentioned, the above procedure is based on matching the results of shear storage modulus and shear loss factor for discrete values of the loading frequencies, and is valid only for sinusoidal loading. However, in order to be generalised and validated under random loading, as in the case of seismic loading, these values are normally determined based on a frequency range close to the frequency content of earthquakes (usually 0.25-4 Hz), which is also similar with the content of the natural frequencies of many structures.

A different approach was used here, where the main focus of the GMM is on extracting the force-displacement relationship in the time domain for any N number of Maxwell elements, and therefore the model can be validated under any random loading. Although, it is very easy to extract this relationship when only one Maxwell element is used, this becomes much more complicated when more elements are being used. Therefore, a force-displacement relation for N Maxwell elements has been also developed here based on Laplace transformation, and presented in the following section.

4.2.2 GMM force-time relationship for N elements - Derivation

For every Maxwell element of the GMM the force displacement relationship in time domain is given as:

$$k_i F_i + c_i \frac{dF_i}{dt} = k_i c_i \frac{du_i}{dt} \tag{4.4}$$

where k_{i} and c_{i} are the stiffness and the dashpot coefficients of the *ith* Maxwell element, u_{i} is the imposed displacement and F_{i} the corresponding force for every i Maxwell element. In the case of parallel connection of Maxwell elements $u_i = u$ for every Maxwell element. Assuming zero initial conditions for both the displacement and the force, and applying Laplace Transformation to Eq.4.4:

$$(k_i + c_i s)F_{i,L} = k_i c_i s u_L \tag{4.5}$$

where $F_{\mathrm{i,L}}$ is the Laplace transform of the force corresponding to the *ith* Maxwell element, and u_{L} is the Laplace transform of the displacement. Equation 4.5 can be rewritten in the following form:

$$F_{i,L} = \frac{k_i c_i s}{k_i + c_i s} u_L \tag{4.6}$$

And for N Maxwell elements the Laplace transform of the total force can be determined as:

$$F_L = \sum_{i=1}^{N} F_{i,L} + F_{0,L} = \sum_{i=1}^{N} \frac{k_i c_i s}{k_i + c_i s} u_L + F_{0,L} \tag{4.7}$$

where $F_{0,L}$ represents the Laplace transform of the additional force corresponding to the linear spring (in this case), which is connected in parallel with the N Maxwell elements. Multiplying throughout by the minimum common multiple of the denominators of the operators of the right side of Equation 4.7 and rearranging:

$$\Big[\prod_{h=1}^{N}(k_h + c_h s)\Big]F_L = \Big[\sum_{i=1}^{N}(k_i c_i s)\prod_{j=1}^{N}(k_j + c_j s)\Big]u_L + \Big[\prod_{g=1}^{N}(k_g + c_g s)\Big]F_{0,L} \tag{4.8}$$

where Σ represents summation, Π represents a series multiplication, and $j \neq i$.

Focusing only on the left hand side of Equation 4.8:

$$
\begin{gathered}
\Big[\prod_{h=1}^{N}(k_h + c_h s)\Big] F_L = \\
\Big[(k_1 + c_1 s)(k_2 + c_2 s)(k_3 + c_3 s)...(k_{N-1} + c_{N-1} s)(k_N + c_N s)\Big] F_L = \\
\Big[(k_1 k_2 k_3 ... k_{N-2} k_{N-1} k_N) + \\
(k_1 k_2 k_3 ... k_{N-2} k_{N-1} c_N + k_1 k_2 k_3 ... k_{N-2} k_N c_{N-1} + ... + \\
k_1 k_3 ... k_{N-2} k_{N-1} k_N c_2 + k_2 k_3 ... k_{N-2} k_{N-1} k_N c_1) s + \\
(k_1 k_2 k_3 ... k_{N-2} c_{N-1} c_N + k_1 k_2 k_3 ... k_{N-4} k_{N-3} k_{N-1} c_{N-2} c_N + ... + \\
k_1 k_4 k_5 ... k_{N-2} k_{N-1} k_N c_2 c_3 + k_3 k_4 k_5 ... k_{N-2} k_{N-1} k_N c_1 c_2) s^2 + \\
(k_1 k_2 k_3 ... k_{N-4} k_{N-3} c_{N-2} c_{N-1} c_N + k_1 k_2 k_3 ... k_{N-4} k_{N-2} c_{N-3} c_{N-1} c_N + ... + \\
k_1 k_5 k_6 ... k_{N-1} k_N c_2 c_3 c_4 + k_4 k_5 k_6 ... k_{N-1} k_N c_1 c_2 c_3) s^3 \\
+ ... + \\
(k_1 c_2 c_3 ... c_{N-2} c_{N-1} c_N + k_2 c_1 c_3 ... c_{N-2} c_{N-1} c_N + ... + \\
k_{N-1} c_1 c_2 ... c_{N-3} c_{N-2} c_N + k_N c_1 c_2 ... c_{N-2} c_{N-1}) s^{N-1} + \\
(c_1 c_2 c_3 ... c_{N-2} c_{N-1} c_N) s^N \Big] F_L
\end{gathered}
\tag{4.9}
$$

Dividing 4.9 by $\prod_{d=1}^{N}(k_d)$:

$$
\begin{gathered}
\Big[1 + (\tfrac{c_N}{k_N} + \tfrac{c_{N-1}}{k_{N-1}} + ... + \tfrac{c_2}{k_2} + \tfrac{c_1}{k_1}) s + \\
(\tfrac{c_N}{k_N}\tfrac{c_{N-1}}{k_{N-1}} + \tfrac{c_N}{k_N}\tfrac{c_{N-2}}{k_{N-2}} + \tfrac{c_N}{k_N}\tfrac{c_{N-3}}{k_{N-3}} + ... + \tfrac{c_2}{k_2}\tfrac{c_3}{k_3} + \tfrac{c_1}{k_1}\tfrac{c_2}{k_2}) s^2 + \\
(\tfrac{c_N}{k_N}\tfrac{c_{N-1}}{k_{N-1}}\tfrac{c_{N-2}}{k_{N-2}} + \tfrac{c_N}{k_N}\tfrac{c_{N-1}}{k_{N-1}}\tfrac{c_{N-3}}{k_{N-3}} + ... + \tfrac{c_2}{k_2}\tfrac{c_3}{k_3}\tfrac{c_4}{k_4} + \tfrac{c_1}{k_1}\tfrac{c_2}{k_2}\tfrac{c_3}{k_3}) s^3 \\
+ ... + \\
(\tfrac{c_2}{k_2}\tfrac{c_3}{k_3}...\tfrac{c_{N-1}}{k_{N-1}}\tfrac{c_N}{k_N} + \tfrac{c_1}{k_1}\tfrac{c_3}{k_3}...\tfrac{c_{N-1}}{k_{N-1}}\tfrac{c_N}{k_N} + ... + \tfrac{c_1}{k_1}\tfrac{c_2}{k_2}...\tfrac{c_{N-3}}{k_{N-3}}\tfrac{c_{N-2}}{k_{N-2}}\tfrac{c_N}{k_N} + \tfrac{c_1}{k_1}\tfrac{c_2}{k_2}...\tfrac{c_{N-2}}{k_{N-2}}\tfrac{c_{N-1}}{k_{N-1}}) s^{N-1} + \\
(\tfrac{c_1}{k_1}\tfrac{c_2}{k_2}...\tfrac{c_{N-1}}{k_{N-1}}\tfrac{c_N}{k_N}) s^N \Big] F_L
\end{gathered}
\tag{4.10}
$$

Equation 4.10 can be rewritten in the following format:

$$
F_L + \sum_{a=1}^{N} \Big[s^a F_L \{ \sum_{m_i \in A_i} \{ \prod_{r \in B} (\frac{c_r}{k_r}) \} \} \Big] \tag{4.11}
$$

where:

- $i \in \{1,2,...,\alpha\}$
- $A_i \in \{i, i+1, i+2, ..., N-\alpha+i\}$
- $m_i > m_{i-1}$, for $i>1$
- $B \in \{m_1, m_2, ..., m_{\alpha-1}, m_\alpha\}$

. Focusing now on the first part of the right hand side of Equation 4.8:

$$\begin{gathered}\Big[\sum_{i=1}^{N}(k_i c_i s)\prod_{j=1}^{N}(k_j + c_j s)\Big]u_L = \\ \Big[k_1 c_1 s(k_2 + c_2 s)(k_3 + c_3 s)...(k_{N-1} + c_{N-1} s)(k_N + c_N s) + \\ k_2 c_2 s(k_1 + c_1 s)(k_3 + c_3 s)...(k_{N-1} + c_{N-1} s)(k_N + c_N s) + \\ +...+ \\ k_{N-1} c_{N-1} s(k_1 + c_1 s)(k_2 + c_2 s)...(k_{N-2} + c_{N-2} s)(k_N + c_N s) + \\ k_N c_N s(k_1 + c_1 s)(k_2 + c_2 s)...(k_{N-2} + c_{N-2} s)(k_{N-1} + c_{N-1} s)\Big]u_L\end{gathered} \tag{4.12}$$

Rearranging Equation 4.12:

$$
\begin{aligned}
&\Big[(c_1k_1k_2...k_{N-1}k_N + c_2k_1k_2...k_{N-1}k_N + ...+ \\
&c_{N-1}k_1k_2...k_{N-1}k_N + c_Nk_1k_2...k_{N-1}k_N)s+ \\
&\big[c_1(c_2k_1k_3k_4...k_{N-1}k_N + c_3k_1k_2k_4...k_{N-1}k_N + ...+ \\
&c_{N-1}k_1k_2...k_{N-2}k_N + c_Nk_1k_2...k_{N-2}k_{N-1})+ \\
&c_2(c_1k_2k_3...k_{N-1}k_N + c_3k_2k_1k_4...k_{N-1}k_N + ...+ \\
&c_{N-1}k_2k_1k_3...k_{N-2}k_N + c_Nk_2k_1k_3...k_{N-2}k_{N-1})+ \\
&c_3(c_1k_3k_2k_4...k_{N-1}k_N + c_2k_3k_1k_4...k_{N-1}k_N + ...+ \\
&c_{N-1}k_3k_1k_2...k_{N-2}k_N + c_Nk_3k_1k_2...k_{N-2}k_{N-1}) + ...+ \\
&c_{N-1}(c_1k_{N-1}k_2k_3...k_{N-2}k_N + c_2k_{N-1}k_1k_3...k_{N-2}k_N + ...+ \\
&c_{N-2}k_{N-1}k_1k_2...k_{N-3}k_N + c_Nk_{N-1}k_1k_2...k_{N-3}k_{N-2})+ \\
&c_N(c_1k_Nk_2k_3...k_{N-2}k_{N-1} + c_2k_Nk_1k_3...k_{N-2}k_{N-1} + ...+ \\
&c_{N-2}k_Nk_1k_2...k_{N-3}k_{N-1} + c_{N-1}k_Nk_1k_2...k_{N-3}k_{N-2})\big]s^2+ \\
&\big[c_1(c_2c_3k_1k_4...k_N + c_2c_4k_1k_3k_5...k_N + ... + c_{N-1}c_Nk_1k_2...k_{N-2})+ \\
&c_2(c_1c_3k_2k_4...k_N + c_1c_4k_2k_3k_5k_6...k_N + ... + c_{N-1}c_Nk_2k_1k_3...k_{N-2})+ \\
&c_3(c_1c_2k_3k_4...k_N + c_1c_4k_3k_2k_5...k_N + ... + c_{N-1}c_Nk_3k_1k_2k_4...k_{N-2}) + ...+ \\
&c_{N-1}(c_1c_2k_{N-1}k_3...k_{N-2}k_N + c_1c_3k_{N-1}k_2k_4...k_{N-2}k_N + ... + c_{N-2}c_Nk_{N-1}k_1...k_{N-3})+ \\
&c_N(c_1c_2k_Nk_3...k_{N-1} + c_1c_3k_Nk_2k_4...k_{N-1} + ... + c_{N-2}c_{N-1}k_Nk_1...k_{N-3})\big]s^3 \\
&+...+ \\
&\big[c_1(c_2...c_{N-1}k_1k_N + c_2...c_{N-2}c_Nk_1k_{N-1} + ... + c_3...c_Nk_1k_2)+ \\
&c_2(c_1c_3...c_{N-1}k_2k_N + c_1c_4...c_Nk_2k_3 + ... + c_3...c_Nk_2k_1) + ...+ \\
&c_{N-1}(c_1....c_{N-2}k_{N-1}k_N + ... + c_2...c_{N-2}c_Nk_{N-1}k_1)+ \\
&c_N(c_1...c_{N-2}k_Nk_{N-1} + ... + c_2...c_{N-1}k_Nk_1)\big]s^{N-1}+ \\
&\big[k_1c_1...c_N + k_2c_2c_1c_3...c_N + ... + k_Nc_Nc_1...c_{N-1}\big]s^N\Big]u_L
\end{aligned}
\tag{4.13}
$$

Equation 4.13 can be rewritten as:

$$\begin{gathered}\Bigg[\big[(c_1+c_2+...+c_{N-1}+c_N)k_1k_2...k_{N-1}k_N\big]s+\\ \big[c_1c_2(k_1+k_2)k_3...k_N+c_1c_3(k_1+k_3)k_2k_4...k_N+...+\\ c_{N-1}c_N(k_{N-1}+k_N)k_1k_2...k_{N-2}\big]s^2+\\ \big[c_1c_2c_3(k_1+k_2+k_3)k_4...k_N+c_1c_2c_4(k_1+k_2+k_4)k_3k_5...k_N+...+\\ c_{N-2}c_{N-1}c_N(k_{N-2}+k_{N-1}+k_N)k_1...k_{N-3}\big]s^3\\ +...+\\ \big[c_1c_2...c_{N-2}c_{N-1}(k_1+k_2+...+k_{N-2}+k_{N-1})k_N+...+\\ c_2c_3...c_{N-1}c_N(k_2+k_3...+k_{N-1}+k_N)k_1\big]s^{N-1}+\\ \big[c_1c_2...c_{N-1}c_N(k_1+k_2+...+k_{N-1}+k_N)\big]s^N\Bigg]u_L\end{gathered} \tag{4.14}$$

And now dividing Equation 4.14 by $\prod_{d=1}^{N}(k_d)$, as was done with Equation 4.9:

$$\begin{gathered}\Bigg[\big[c_1+c_2+...+c_{N-1}+c_N\big]s+\\ \big[\tfrac{c_1}{k_1}\tfrac{c_2}{k_2}(k_1+k_2)+\tfrac{c_1}{k_1}\tfrac{c_3}{k_3}(k_1+k_3)+...+\\ \tfrac{c_{N-2}}{k_{N-2}}\tfrac{c_{N-1}}{k_{N-1}}(k_{N-2}+k_{N-1})+\tfrac{c_{N-1}}{k_{N-1}}\tfrac{c_N}{k_N}(k_{N-1}+k_N)\big]s^2+\\ \big[\tfrac{c_1}{k_1}\tfrac{c_2}{k_2}\tfrac{c_3}{k_3}(k_1+k_2+k_3)+\tfrac{c_1}{k_1}\tfrac{c_2}{k_2}\tfrac{c_4}{k_4}(k_1+k_2+k_4)+...+\\ \tfrac{c_{N-2}}{k_{N-2}}\tfrac{c_{N-1}}{k_{N-1}}\tfrac{c_N}{k_N}(k_{N-2}+k_{N-1}+k_N)\big]s^3\\ +...+\\ \big[\tfrac{c_1}{k_1}\tfrac{c_2}{k_2}...\tfrac{c_{N-2}}{k_{N-2}}\tfrac{c_{N-1}}{k_{N-1}}(k_1+k_2+...+k_{N-2}+k_{N-1})+\\ \tfrac{c_1}{k_1}\tfrac{c_3}{k_3}...\tfrac{c_{N-1}}{k_{N-1}}\tfrac{c_N}{k_N}(k_1+k_3+...+k_{N-1}+k_N)+...+\\ \tfrac{c_2}{k_2}\tfrac{c_3}{k_3}...\tfrac{c_{N-1}}{k_{N-1}}\tfrac{c_N}{k_N}(k_2+k_3+...+k_{N-1}+k_N)\big]s^{N-1}+\\ \big[\tfrac{c_1}{k_1}\tfrac{c_2}{k_2}...\tfrac{c_{N-1}}{k_{N-1}}\tfrac{c_N}{k_N}(k_1+k_2+...+k_{N-1}+k_N)\big]s^N\Bigg]u_L\end{gathered} \tag{4.15}$$

Which leads to:

$$\sum_{\beta=1}^{N}\Big[s^\beta u_L\{\sum_{x_c\in Q_c}\{\prod_{z\in W}(\frac{c_z}{k_z})\sum_{z\in W}k_z\}\}\Big] \tag{4.16}$$

where:

- c∈{1,2,...,β}
- Q_c∈{c,c+1,c+2,...,N-β+c}
- x_c>$x_{c\text{-}1}$ for c>1
- W∈{x_1,x_2,...,$x_{\beta\text{-}1}$,x_β}

The last part of the right hand side of the Equation 4.8 can be rearranged similarly to its left part and can be presented in its final format:

$$F_{0,L} + \sum_{d=1}^{N} \left[s^d F_{0,L} \{ \sum_{p_v \in H_v} \{ \prod_{f \in L} (\frac{c_f}{k_f}) \} \} \right] \tag{4.17}$$

where:

- v∈{1,2,...,d}
- H_v∈{v,v+1,v+2,...,N-d+v}
- p_v>$p_{v\text{-}1}$ for v>1
- L∈{p_1,p_2,...,$p_{d\text{-}1}$,p_d}

Combining Equations 4.11,4.16, and 4.17, then 4.8 can be rewritten as:

$$F_L + \sum_{a=1}^{N} \left[s^a F_L \{ \sum_{m_i \in A_i} \{ \prod_{r \in B} (\frac{c_r}{k_r}) \} \} \right] =$$
$$\sum_{\beta=1}^{N} \left[s^\beta u_L \{ \sum_{x_c \in Q_c} \{ \prod_{z \in W} (\frac{c_z}{k_z}) \sum_{z \in W} k_z \} \} \right] + \left[F_{0,L} + \sum_{d=1}^{N} \left[s^d F_{0,L} \{ \sum_{p_v \in H_v} \{ \prod_{f \in L} (\frac{c_f}{k_f}) \} \} \right] \right] \tag{4.18}$$

Applying inverse Laplace transformation to 4.18:

$$F + \sum_{a=1}^{N} \left[\frac{\partial^a F}{\partial t^a} \{ \sum_{m_i \in A_i} \{ \prod_{r \in B} (\frac{c_r}{k_r}) \} \} \right] =$$
$$\sum_{\beta=1}^{N} \left[\frac{\partial^\beta u}{\partial t^\beta} \{ \sum_{x_c \in Q_c} \{ \prod_{z \in W} (\frac{c_z}{k_z}) \sum_{z \in W} k_z \} \} \right] + \left[F_0 + \sum_{d=1}^{N} \left[\frac{\partial^d F_0}{\partial t^d} \{ \sum_{p_v \in H_v} \{ \prod_{f \in L} (\frac{c_f}{k_f}) \} \} \right] \right] \tag{4.19}$$

where:

- $i \in \{1,2,...,\alpha\}$, c$\in\{1,2,...,\beta\}$, $v \in \{1,2,...,$d$\}$
- $A_i \in \{i, i+1, i+2, ..., N-\alpha+i\}$, $Q_c \in \{c, c+1, c+2, ..., N-\beta+c\}$, $H_v \in \{v, v+1, v+2, ..., N-d+v\}$
- B$\in\{m_1, m_2, ..., m_{\alpha-1}, m_\alpha\}$, W$\in\{x_1, x_2, ..., x_{\beta-1}, x_\beta\}$, and L$\in\{p_1, p_2, ..., p_{d-1}, p_d\}$
- $m_i > m_{i-1}$, $x_c > x_{c-1}$, $p_v > p_{v-1}$ for i, c, $v > 1$

For illustrative purposes, the cases of N=1, N=2, and N=3 will be presented. If N=1 Eq. 4.19 becomes:

$$F + \frac{dF}{dt}\left[\frac{c_1}{k_1}\right] = F_0 + \frac{dF_0}{dt}\frac{c_1}{k_1} + \frac{du}{dt}c_1 \tag{4.20}$$

In the case of N=2 Eq. 4.19 is determined as:

$$\begin{gathered} F + \frac{dF}{dt}\left[\frac{c_1}{k_1} + \frac{c_2}{k_2}\right] + \frac{d^2F}{dt^2}\left[\frac{c_1}{k_1}\frac{c_2}{k_2}\right] = F_0 + \frac{dF_0}{dt}\left[\frac{c_1}{k_1} + \frac{c_2}{k_2}\right] + \frac{d^2F_0}{dt^2}\left[\frac{c_1}{k_1}\frac{c_2}{k_2}\right] + \\ \frac{du}{dt}[c_1 + c_2] + \frac{d^2u}{dt^2}\left[\frac{c_1}{k_1}\frac{c_2}{k_2}(k_1 + k_2)\right] \end{gathered} \tag{4.21}$$

In the case of N=3 Eq. 4.19 is determined as:

$$\begin{gathered} F + \frac{dF}{dt}\left[\frac{c_1}{k_1} + \frac{c_2}{k_2} + \frac{c_3}{k_3}\right] + \frac{d^2F}{dt^2}\left[\frac{c_1}{k_1}\frac{c_2}{k_2} + \frac{c_1}{k_1}\frac{c_3}{k_3} + \frac{c_2}{k_2}\frac{c_3}{k_3}\right] + \frac{d^3F}{dt^3}\left[\frac{c_1}{k_1}\frac{c_2}{k_2}\frac{c_3}{k_3}\right] = \\ F_0 + \frac{dF_0}{dt}\left[\frac{c_1}{k_1} + \frac{c_2}{k_2} + \frac{c_3}{k_3}\right] + \frac{d^2F_0}{dt^2}\left[\frac{c_1}{k_1}\frac{c_2}{k_2} + \frac{c_1}{k_1}\frac{c_3}{k_3} + \frac{c_2}{k_2}\frac{c_3}{k_3}\right] + \frac{d^3F_0}{dt^3}\left[\frac{c_1}{k_1}\frac{c_2}{k_2}\frac{c_3}{k_3}\right] + \\ \frac{du}{dt}[c_1 + c_2 + c_3] + \frac{d^2u}{dt^2}\left[\frac{c_1}{k_1}\frac{c_2}{k_2}(k_1 + k_2) + \frac{c_1}{k_1}\frac{c_3}{k_3}(k_1 + k_3) + \frac{c_2}{k_2}\frac{c_3}{k_3}(k_2 + k_3)\right] + \\ \frac{d^3u}{dt^3}\left[\frac{c_1}{k_1}\frac{c_2}{k_2}\frac{c_3}{k_3}(k_1 + k_2 + k_3)\right] \end{gathered} \tag{4.22}$$

It is obvious, from the above equations that the number of derivatives of both the force and the displacement is the same as the number N of Maxwell elements. The advantage of Eq. 4.19, apart from the fact that it may be useful in the mathematical and physical fields, is that it can be used for random loading and not only sinusoidal loading, and the force-displacement relationship can now be extracted in the time domain for any number N of Maxwell elements. Furthermore, comparing Eq. 4.19 with Eq.2.73, which is based on generalised derivatives (see Chapter 2), it can be concluded that they are very similar. However, the parameters α_n, β_n of Eq.2.73 are

now determined, and are functions of the stiffness k_i, and the damping coefficients c_i of the GMM. Even though fractional derivative models are usually based on fewer parameters, it was found that additional parameters were necessary to capture the dynamic characteristics of the EDs tested. However, for preliminary analysis of structures, a simplified Kelvin-Voigt model (spring and dashpot connected in parallel) can be used, the parameters of which can be determined based on the natural frequency of the structure and a design dampers' displacement.

4.3 Hysteretic Model

In trying to fit the GMM to the experimental data, it was found that the GMM was only adequate to describe VE behaviour, regardless of the number of Maxwell elements used, and could not adequately represent the frequency or amplitude dependence. Hence, a Modified Generalised Maxwell Model (MGMM) is proposed here. In order to take into account the non linear part of the elastomer's behaviour, a non linear damper was added to the main GMM equation:

$$F_{NL} = c_{NL}|\dot{u}|^{\alpha} sgn(\dot{u}) \tag{4.23}$$

It was also found that the ED's behaviour depended on both the maximum displacement and the maximum velocity obtained during the loading history. Karavasilis et al [62] proposed a modified stiffness based on the maximum displacement to take into account the softening of the elastomer:

$$k_{mod} = k_a e^{-\frac{u_{max}}{u_{ref}}} + k_b \tag{4.24}$$

where k_{a}, k_{b} and u_{ref} are constants, and u_{max} is the average of the maximum absolute deformation amplitudes in the negative ($u_{\mathrm{max,n}}$) and positive ($u_{\mathrm{max,p}}$) directions, and can be determined as follows:

$$u_{max} = \frac{u_{max,p} + |u_{max,n}|}{2} \tag{4.25}$$

The values of $u_{\mathrm{max,p}}$ and $u_{\mathrm{max,n}}$ are updated for every time step and are fed into the constitutive equation to calculate the overall response. Similar modelling approach was followed by Summers [119]. Following the same philosophy in terms of velocity instead of displacement, a modified damping coefficient is introduced here, which was found to significantly contribute to the elastomer's dynamic behaviour:

$$c_{mod} = c_a e^{-\frac{v_{max}}{v_{ref}}} + c_b \tag{4.26}$$

The parameters c_{a}, c_{b}, v_{ref}, and $v_{\max}$ are defined in a similar way to the terms in k_{mod}, of Eq. 4.24.

Hence, the final form of the Modified Generalized Maxwell Model (MGMM) consists of the following parts:

- The linear GMM obtained from Equation 4.19
- The final version of F_0, which consists of a linear spring:

$$F_0 = k_0 u \tag{4.27}$$

- The non linear damper (see Eq. 4.23)
- The modified stiffness from Equation 4.24
- The modified damping coefficient from Equation 4.26

Since a generalised equation for N Maxwell elements is now available, efforts were made in order to use more than one element. More specifically, analytical models were determined with $N = 2, 3$ and 4 Maxwell elements respectively. The Normalised Root Mean Square (NRMS) error, defined by Eq. 4.28, was determined for every combination (Table 4.1) and it was found that using only one Maxwell element was adequate for the specific material without any significant compromise in the accuracy.

$$NRMS = \frac{\sum_{i=1}^{N}(F_A - F_E)^2}{\sum_{i=1}^{N}(F_A)^2} \tag{4.28}$$

where F_A, and F_E represent the force extracted from the analytical model and the experiments respectively.

Hence, the final equation describing the MGMM is:

$$F + \frac{c_1}{k_1}\dot{F} = (k_0 + k_{mod})u + (\frac{c_1}{k_1}k_0 + c_1 + c_{mod})\dot{u} + c_{NL}|\dot{u}|^{\alpha} sgn(\dot{u}) \tag{4.29}$$

Table 4.1: NRMS error based on different values of Maxwell Elements

Frequency (Hz)	1 Maxwell Element	2 Maxwell Elements	3 Maxwell Elements	4 Maxwell Elements
0.25	1.60	1.59	1.59	1.59
0.5	1.45	1.44	1.44	1.44
1	1.72	1.70	1.70	1.70
2	1.73	1.73	1.73	1.73
3	1.41	1.43	1.42	1.42
4	1.57	1.60	1.60	1.60
Average NRMS Error	**1.580**	**1.582**	**1.580**	**1.580**

It should be noted that this forms an equation which can mechanically capture the dynamic behaviour of the elastomeric dampers under specific conditions on a macroscopic level. Unlike the model proposed by Lee [107], the MGMM takes into account the loading history. In order for Lee to take loading history into consideration and avoid potential overshooting under variable cyclic loading, additional modifications were made in order to adjust the stress-strain path, which were not taken into account on the proposed MGMM, which may cause discrepancies if sudden strain reversals occur. Examples of more realistic loading histories are presented in Chapter 6 along with the Real-Time Substructure tests. For comparison reason both the GMM (using one Maxwell element), and the model proposed by Lee [107] were compared with experimental data. More specifically, these models were compared with the 2 Hz sweep amplitude test (which is analytically described later) and presented at Figures 4.9 and 4.10. It can be concluded that both of these models in a good overall agreement with corresponding NRMS error of 2.1 %, and 2.5 % for Lee's model and GMM respectively. However, when frequency was altered the results were far from satisfying. Specifically, GMM model could only capture linear VE behaviour under a target frequency, while Lee's model presented some discrepancies when different frequencies and strain amplitudes compared with the ones which were used to calibrate the model were used.

4.4 Parameter Estimation

Least squares minimization is one of the most widely used methods [42, 72, 60] of fitting the numerical parameters of a proposed model into the experimental data. However, as mentioned earlier, in case of GMM this minimization technique has been based on the frequency domain, trying to minimize the shear storage modulus

(from Eq. 4.1), and the loss factor, $n = \frac{G''}{G'}$ (combining Eq. 4.1, and Eq. 4.2) for every frequency and temperature that the damper was experimentally tested, as:

$$min\Big\{ \sum_{j=1}^{N} \Big[G'_{anal} - G'_{exp} \Big]^2 \Big\} \tag{4.30}$$

$$min\Big\{ \sum_{j=1}^{N} \Big[n_{anal} - n_{exp} \Big]^2 \Big\} \tag{4.31}$$

where N denotes the number of experimental data available. With regard to fitting the numerical model to the experimental data, researchers have used various techniques. The most common one is to assume constant one of the three main parameters [42] that the material is dependent upon (strain amplitude, loading frequency, ambient temperature). On the other hand, minimization of the corresponding error for every cyclic experiment that was carried out [62] has been used as well, taking the average value of these parameters in order to generate the model through the whole range of shear strain amplitudes, frequencies, and temperatures. Finally, another widely used method is to include all the available data into one least squares equation [72, 42].

Furthermore, in the case of the models which were minimised based on their shear storage modulus, and loss factor for specific frequencies, even though the numerical values of G', and n seem to fit well with the experimental data, the corresponding model will not necessarily be valid in the time domain for random loading (and more specifically for random displacements), since these parameters will only be adequate to predict the shear storage modulus, and the loss factor of the damper under cyclic testing with constant frequency, and constant maximum displacement, and not the actual elastomer's dynamic behaviour.

Another approach was therefore used here, which takes into account the alteration of displacements (since it was found to be the most dominant factor in the elastomer's dependence). Sweep amplitude sinusoidal tests (the shear strain amplitude was ranging from 10%-50%), which were carried out for the same frequency range used in the characterization tests of Chapter 3, formed the basis for the afore-

mentioned minimization. The sweep amplitude tests were based on proposals from Dorka and Garcia[39]. Keeping the frequency and the temperature constant within each test, and setting the maximum strain amplitude to be 50%, the sweep amplitude tests consisted of the following steps: 1.5 cycles of $u_{max}/2$, 1.5 cycles of u_{max}, 1.5 cycles of $u_{max}/3$, 1.5 cycles of $u_{max}/6$, 1.5 cycles of $u_{max}/2$, 1.5 cycles of $2u_{max}/3$, 1.5 cycles of $5u_{max}/6$, 3 cycles of u_{max}, 1.5 cycles of $5u_{max}/6$, 1.5 cycles of $2u_{max}/3$, 1.5 cycles of $u_{max}/2$, 1.5 cycles of $u_{max}/3$, 1.5 cycles of $u_{max}/6$. Figure 4.2 shows a typical example of both the sweep sinusoidal command displacement and the ED's response for a test at a frequency of 3.0 Hz.

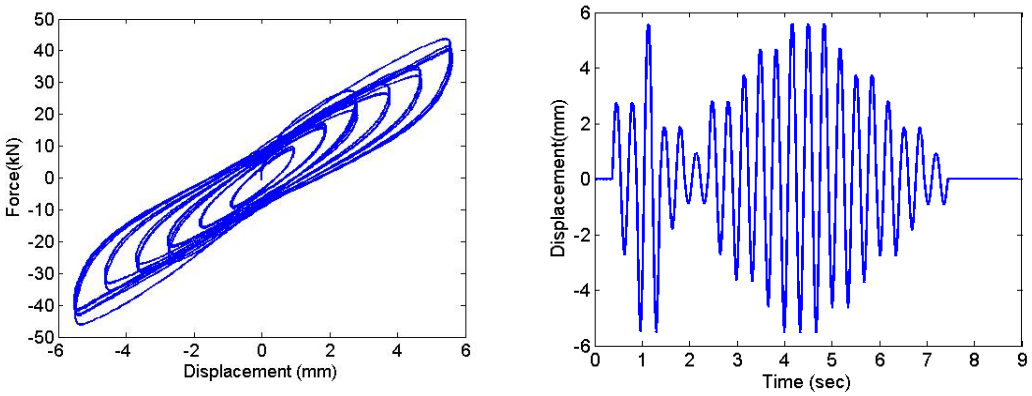

Figure 4.2: Sweep amplitude test for frequency of 3 Hz

The sweep amplitude test is believed to be a more representative test, at least for fitting the parameters because of the strong amplitude dependence of the elastomer. In contrast, previous characterization tests were based on a fixed strain amplitude and frequency. The MGMM (Eq. 4.29) contains 11 parameters which need to be determined: k_1, c_1, k_0, k_a, k_b, u_{ref}, c_a, c_b, v_{ref}, c_{NL}, α. In order to optimize these parameters a least squares method was used:

$$min\Big\{\sum_i \sum_k \Big[F_{anal(i,k)} - F_{exp(i,k)}\Big]^2\Big\} \tag{4.32}$$

where i is the index for frequency content (e.g., $i = 2$ is equivalent with frequency of 0.5 Hz), and k stands for the force-displacement data set at a specific frequency and displacement. Stress relaxation and very low frequency tests were used as starting

points of determining initial assumptions of the aforementioned parameters.

Table 4.2 provides the parameters of the hysteretic model, while Figures 4.3 to 4.8 show the hysteretic response of the damper for both the analytical and experimental case. It can be seen that the results are in a very good agreement. It is also worth mentioning that the proposed model is valid under any random earthquake loading, and its parameters do not depend on the imposed displacement or frequency. Chapter 6 provides further validation of the proposed model, where real time hybrid tests with alterations of both displacement and frequency are carried out. Furthermore, Table 4.3 shows the NRMS error calculated based on comparison of the proposed model and the fixed amplitude characterization tests described in Chapter 3. The error determined for these tests was slightly larger compared to the sweep amplitude tests; however the agreement observed was very good as well.

Table 4.2: Material Parameters

k1 (kN/mm)	**c1 (kNsec/mm)**	**k0 (N/mm)**	**c_NL(kN(sec/mm)$^{0.374}$)**	**α**	
0.515	0.0151	0.107	1.585	0.374	
k_a (kN/mm)	**k_b (kN/mm)**	**u_ref (mm)**	**c_a (kNsec/mm)**	**c_b (kNsec/mm)**	**v_ref (mm/sec)**
3.741	3.613	7.966	0.902	0.190	13.468

Table 4.3: NRMS error based on comparison of the proposed model and the characterization tests described in Chapter 3

Shear Strain %	**Frequency**					
	0.25Hz	**0.5Hz**	**1Hz**	**2Hz**	**3Hz**	**4Hz**
10	1.65	1.48	1.78	1.75	1.46	1.65
20	1.61	1.49	1.81	1.79	1.5	1.64
30	1.6	1.49	1.76	1.81	1.49	1.64
40	1.59	1.52	1.79	1.8	1.51	1.71
50	1.63	1.53	1.84	1.81	1.55	1.68

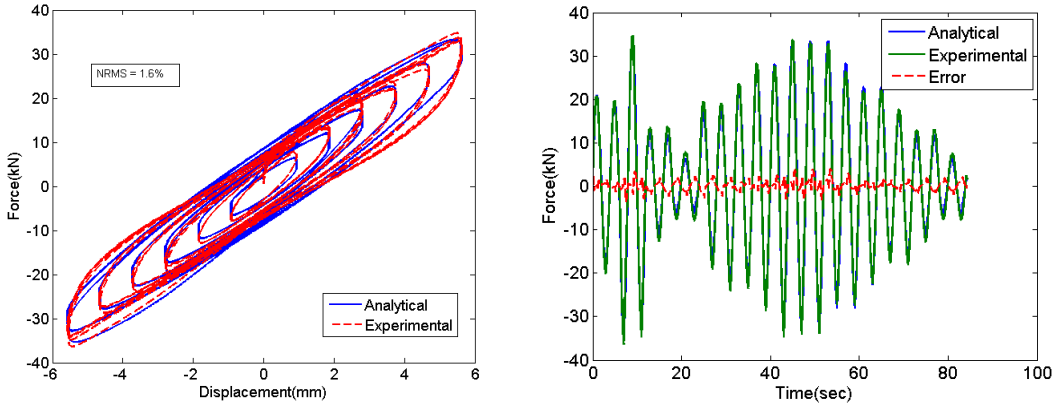

Figure 4.3: Comparison of force between experiment and MGMM model for sweep amplitude test - 0.25 Hz, 20°C

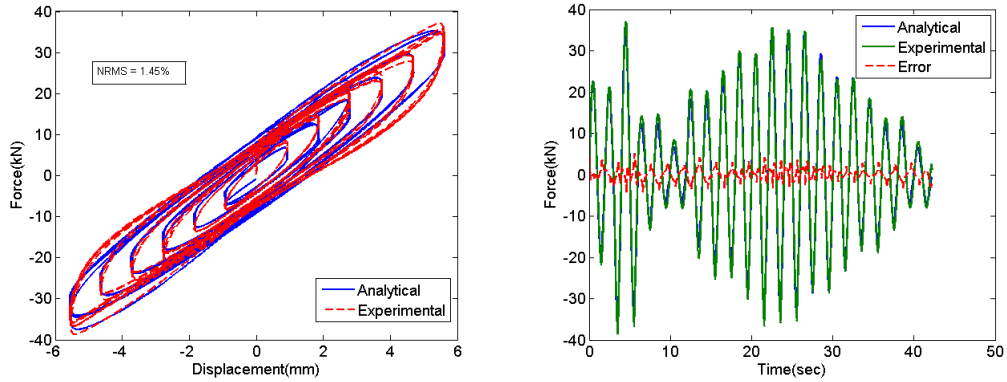

Figure 4.4: Comparison of force between experiment and MGMM model for sweep amplitude test - 0.5 Hz, 20°C

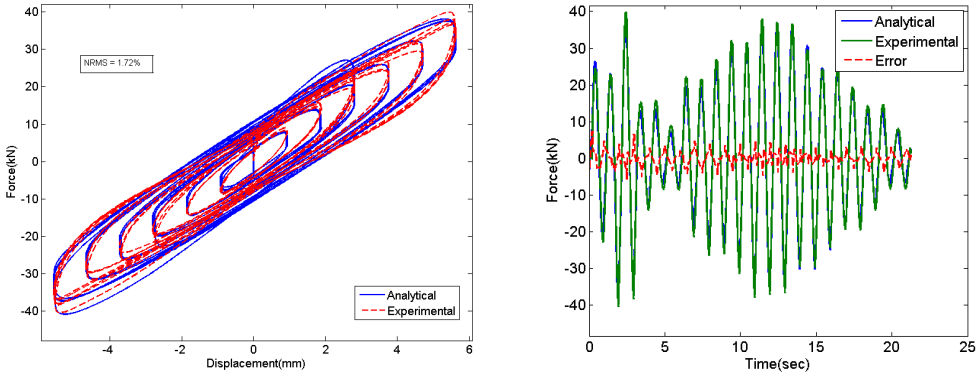

Figure 4.5: Comparison of force between experiment and MGMM model for sweep amplitude test - 1 Hz, 20°C

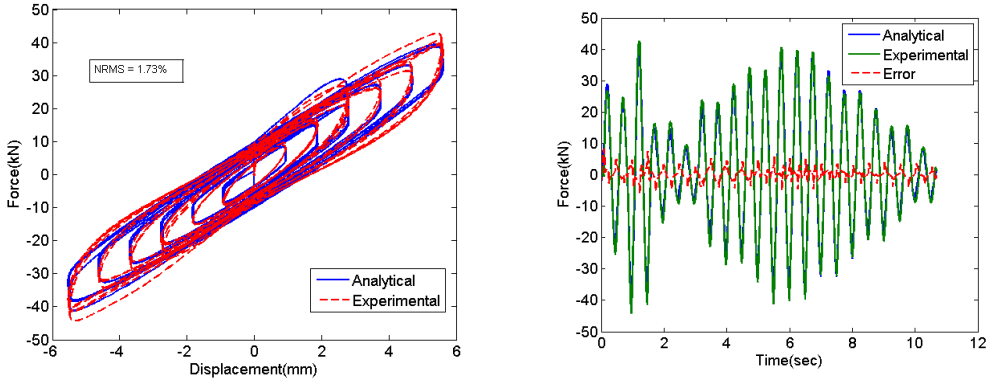

Figure 4.6: Comparison of force between experiment and MGMM model for sweep amplitude test - 2 Hz, 20°C

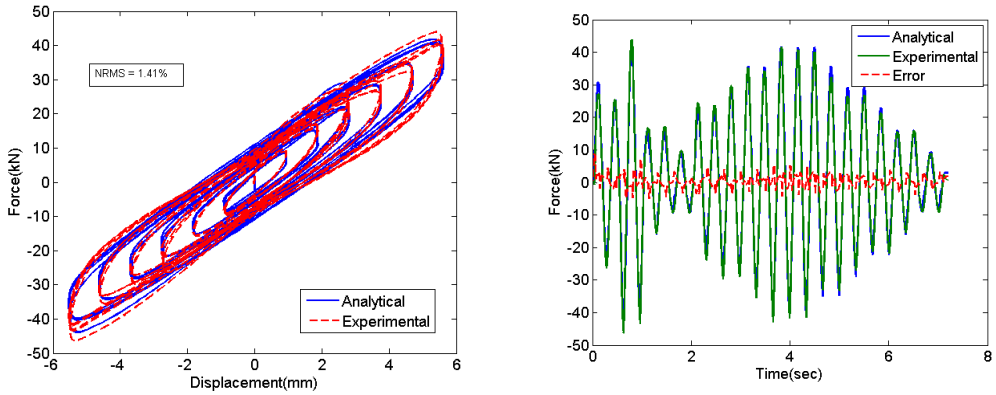

Figure 4.7: Comparison of force between experiment and MGMM model for sweep amplitude test - 3 Hz, 20°C

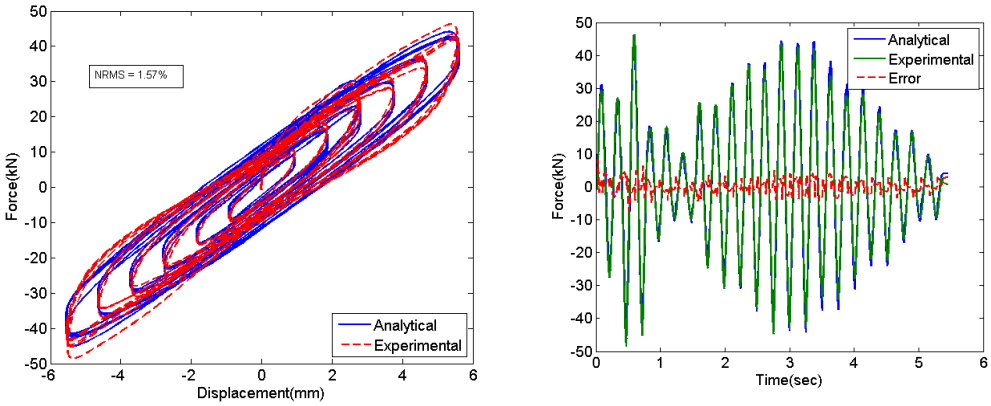

Figure 4.8: Comparison of force between experiment and MGMM model for sweep amplitude test - 4 Hz, 20°C

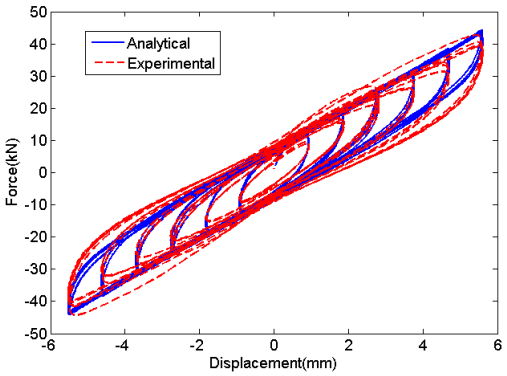

Figure 4.9: Model proposed by Lee [107] compared with 2 Hz sweep amplitude test

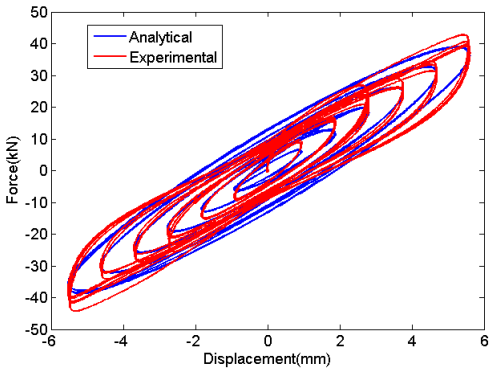

Figure 4.10: GMM compared with 2 Hz sweep amplitude test

4.5 Effect of Temperature

One of the most widely used procedure in order to take into account temperature effects of polymeric materials tested under loading is the one proposed by Ferry [43]. According to this method a shifting function, α_T with two parameters p_1, p_2 was proposed:

$$\alpha_T(T, T_{ref}) = e^{\frac{-p_1(T-T_{ref})}{p_2+(T-T_{ref})}} \tag{4.33}$$

G' increases as the temperature decreases from a reference temperature T_{ref} to a temperature T at a reference frequency ω_{ref}. This increase of G' is equivalent to the increase of G' as the frequency changes from ω_{ref} to $\alpha_T(T, T_{ref}\omega_{ref})$ at T_{ref}. Incorporating the shifting function α_T into the analytical values of G', and G'' cap-

tures any alterations of the material's characteristics due to change of temperature. A much simpler method was followed in this research. In order to capture the behaviour of the EDs under different ambient temperatures, both the characterization tests and the sweep amplitude tests were repeated at different temperatures: 25, 30, and 35°C. The same model (MGMM), which was developed and validated for the experiments which were carried out at room temperature (20°C), will be used here as well, by introducing a new parameter, γ_T. However, a simplifying assumption that all parameters change at the same rate with temperature was made. This led to very good agreement between experimental and numerical results. The original proposed hysteretic model in this case has been adjusted:

$$\begin{gathered} F_T + \tfrac{c_1}{k_1}\dot{F}_T = \\ \gamma_T(k_0 + k_{mod,T})u + (\tfrac{c_1}{k_1}k_0\gamma_T + \gamma_T c_1 + c_{mod_T})\dot{u} + \gamma_T k_{NL}(\dot{u})^{\alpha\gamma_T} \end{gathered} \tag{4.34}$$

where:

$$c_{mod,T} = \gamma_T c_a e^{-\frac{v_{max}}{\gamma_T v_{ref}}} + \gamma_T c_b \tag{4.35}$$

and

$$k_{mod,T} = \gamma_T k_a e^{-\frac{u_{max}}{\gamma_T u_{ref}}} + \gamma_T k_b \tag{4.36}$$

where T denotes the ambient temperature, and γ_T the coefficient which controls the parameters of the model in different temperatures. Again, the same minimization techniques introduced earlier were used to determine the γ_T parameter for different temperatures. These values are summarised in Table 4.4.

Table 4.4: Values of γ_T for different ambient temperatures

γ_{20}	γ_{25}	γ_{30}	γ_{35}
1	0.935	0.875	0.820

As expected from the results of the characterization tests carried out at different temperatures (Chapter 3), the values of γ_T reduce with the increase of temperature. This reduction can be schematically seen at Figure 4.11 and can be approximately

determined as 0.116/°C. Figures 4.12 to 4.14 show the comparison between the experimental data and the proposed model for the 4Hz sweep amplitude tests. It can be seen that the MGMM can capture adequately the dynamic behaviour of the EDs under every temperature. More figures regarding the full comparison of the proposed model against the dynamic behaviour of the EDs in different temperatures are available in Appendix 2.

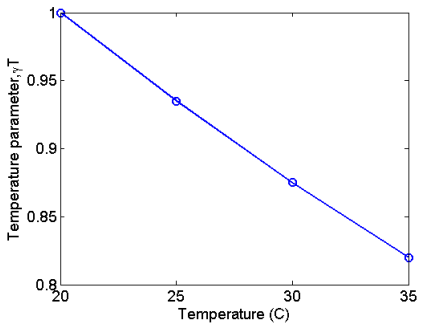

Figure 4.11: Alteration of temperature parameter γ_T with different temperatures

4.6 Conclusions

A new model has been developed in this chapter, the Modified Generalised Maxwell Model (MGMM), based on the well known Generalised Model (GMM), in order to capture the dynamic behaviour of elastomeric dampers. In order to extract this model, the force-displacement relationship of the GMM for N Maxwell elements in the time domain was determined (Eq. 4.19). However, it was observed that the GMM was able to capture only visco-elastic behaviour, and not follow the elastomer's performance, regardless the number N used. Hence, the MGMM, based on N=1 Maxwell element, was proposed which was found to be able to predict the dynamic performance of the elastomeric dampers under a range of strain amplitudes and frequencies. In order to take into consideration the effect of the ambient temperature, a new parameter was introduced into the proposed model, and the analytical results were found to be in very good agreement with the experimental data for every strain amplitude, frequency, and temperature, with the maximum NRMS error observed during these tests to reach 1.8%.

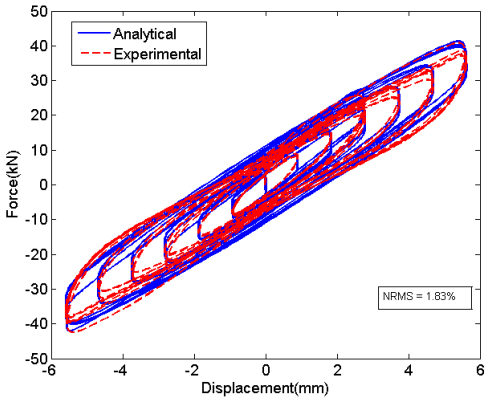

Figure 4.12: Comparison of force between experiment and MGMM model for sweep amplitude test - 4.0 Hz, 25°C

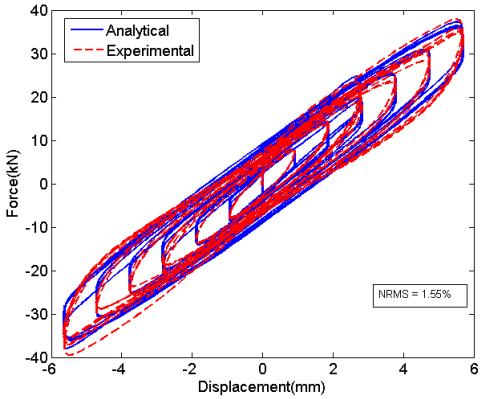

Figure 4.13: Comparison of force between experiment and MGMM model for sweep amplitude test - 4.0 Hz, 30°C

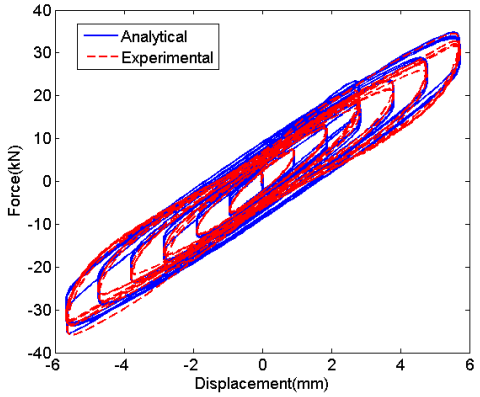

Figure 4.14: Comparison of force between experiment and MGMM model for sweep amplitude test - 4.0 Hz, 35°C

The proposed model was also evaluated under the characterization tests carried out in Chapter 3; a very good agreement was achieved as well even though the NRMS error was slightly larger, reaching 1.84%. The proposed hysteretic model was later implemented in an incremental way as a new material into OpenSees, so that an in depth analysis of the effect of the EDs could be carried out in Chapter 5.

Chapter 5

Seismic Response of Steel Moment Resisting Frames using Elastomeric Dampers

5.1 Introduction

In Chapter 3, the characterization tests carried out at the Dynamics Laboratory of the Oxford University Engineering Department were analytically described. Based on these tests, a hysteretic model was proposed at Chapter 4, and incorporated into the Finite Element software OpenSees[3]. The current chapter describes the analysis of a 10-storey steel moment-resisting frame, designed according to Eurocode 3 and Eurocode 8, and its dynamic response under non-linear time histories. In order to improve the building's performance, elastomeric dampers were added at a second stage. A uniform damper distribution throughout the height of the structure was used, and elastomers' deformation limit was constrained to be in the shear strain target range. With regard to the dampers' selection, a design process [114] was followed, so the target performance level was achieved. Both the initial and the retrofitted steel frame seismic performance were evaluated under seismic actions with 2% and 10% probability of exceedance in 50 years.

5.2 Prototype Building

Figures 5.2 and 5.3 show the 10-storey, 3-bay by 4-bay prototype building, which was used for this study. The length of the beams was assumed 7.2m, making the plan of the building 21.6m x 28.8m, while the height of each storey was assumed 3.5m, leading to a total height of 35m. The building, which was assumed to be located on a dense sand (type C ground), was designed according to Eurocode 3 [1], and Eurocode 8 [2]. The structure was designed based only on q factor and not on interstorey drift ratio (IDR) in order to obtain more flexible structure. Concentric braces provide the main resistance to horizontal forces in the global Y direction, and Moment Resisting Frames (MRFs) in the global X direction. The strong axis of the columns was aligned with the global X axis [56].

The design dead load used at each floor was assumed 4.5 kN/m^2, and the live load 2 kN/m^2, made up as shown in table 5.1. An additional dead load of 1.2 kN/m was assigned to perimeter beams, due to glazing.

The structure was designed for Ductility Class High (DCH), and behaviour factor of 4 along the global Y axis, where the diagonal braces are mainly responsible for resisting the seismic forces, and 6.5 in the global X direction in which moment resisting frames is the main mechanism for the horizontal actions. DCH was implemented in this research in order to obtain larger q factor, and therefore more flexible structure. This will potentially result in larger lateral displacements, and will even further highlight the efficiency of the dampers.

The following assumptions were made in structural modelling of the building:

- Beam column connections were assumed as fully rigid for the moment resisting frames, and simple connections for the direction where diagonal braces were used
- The yield stress of the steel members is assumed to be 275 MPa
- The columns were assumed fixed at their bases
- Rigid Diaphragms were assigned to each floor

The FE model was first validated under simple static and cyclic loading before proceeding to more complex seismic loading. The first 3 natural modes of the building are shown in Figure 5.1.

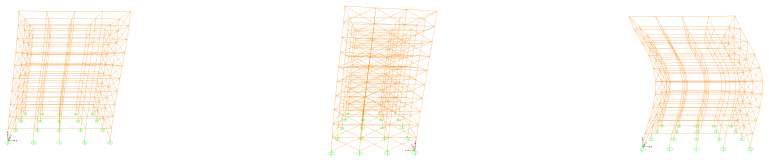

(a) Mode 1 (b) Mode 2 (c) Mode 3

Figure 5.1: First 3 modes of the prototype structure

With regard to the representation of seismic action, the EC8 elastic response spectrum type 1 was used, and the design of the structure was based on modal response spectrum analysis according to Eurocode 8 [2]. The design seismic action is expressed in terms of two parameters: 1) the probability of exceedance in a time period of 50 years, and 2) the importance factor, γ_1. Both of these factors are explained later in detail (see 5.3.3). In case of Eurocode 8, structures shall be designed for a seismic action having 10% probability of exceedance in 50 years. The two orthogonal components of the horizontal seismic action are assumed independent and represented by the same response spectrum. The ability of the structure to exhibit non linearities during seismic actions permits to design for smaller seismic forces than those corresponding to a linear elastic response. Hence, to avoid complicated and explicit inelastic analyses, the capacity of the structure to dissipate energy in a ductile way, can be taken into consideration by performing elastic analysis based on the elastic response spectrum reduced by the behaviour factor, q. Briefly, the horizontal components of the seismic action of the design spectrum are:

$$0 \leq T \leq T_{\mathrm{B}}\text{: } S_{\mathrm{d}}(T) = a_{\mathrm{g}} S[\tfrac{2}{3} + \tfrac{T}{T_{\mathrm{B}}}(\tfrac{2.5}{q} - \tfrac{2}{3})] \tag{5.1}$$

$$T_{\mathrm{B}} \leq T \leq T_{\mathrm{C}}\text{: } S_{\mathrm{d}}(T) = a_{\mathrm{g}} S \tfrac{2.5}{q} \tag{5.2}$$

$$T_{\mathrm{C}} \leq T \leq T_{\mathrm{D}} : S_{\mathrm{d}}(T) = \begin{cases} a_{\mathrm{g}} S \frac{2.5}{q} [\frac{T_{\mathrm{c}}}{T}] \\ \geq \beta a_{\mathrm{g}} \end{cases} \tag{5.3}$$

$$T_{\mathrm{D}} \leq T : S_{\mathrm{d}}(T) = \begin{cases} a_{\mathrm{g}} S \frac{2.5}{q} [\frac{T_{\mathrm{C}} T_{\mathrm{D}}}{T^2}] \\ \geq \beta a_{\mathrm{g}} \end{cases} \tag{5.4}$$

where:

$S_{\mathrm{D}}(T)$ is the design spectrum

T is the vibration period of a linear single-degree-of-freedom system

$a_{\mathrm{g}} = \gamma_1 a_{\mathrm{gR}}$ is the design ground acceleration

a_{gR} is the reference peak ground acceleration on type A ground (=0.36g based on the National Annex of Greece for zone 3 areas)

γ_1 is the importance factor

$T_{\mathrm{B}}, T_{\mathrm{C}}$, and T_{D} are given values by Eurocode 8, depending on the corresponding elastic response spectrum

q is the behaviour factor

β is the lower bound factor for the horizontal design spectrum

Figures 5.4, and 5.5 show the corresponding design spectrum according to EC8.

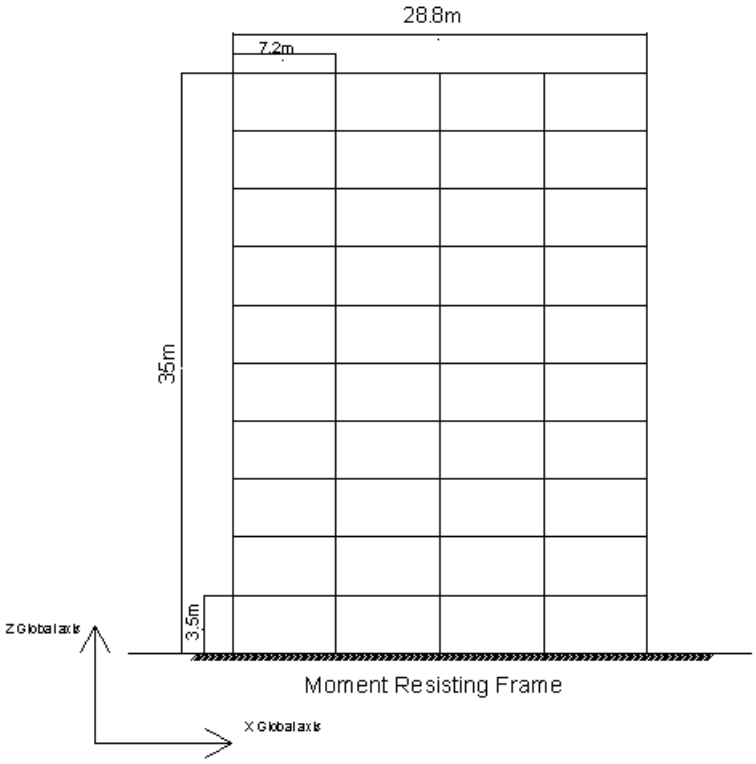

Figure 5.2: Elevation of the Prototype Building

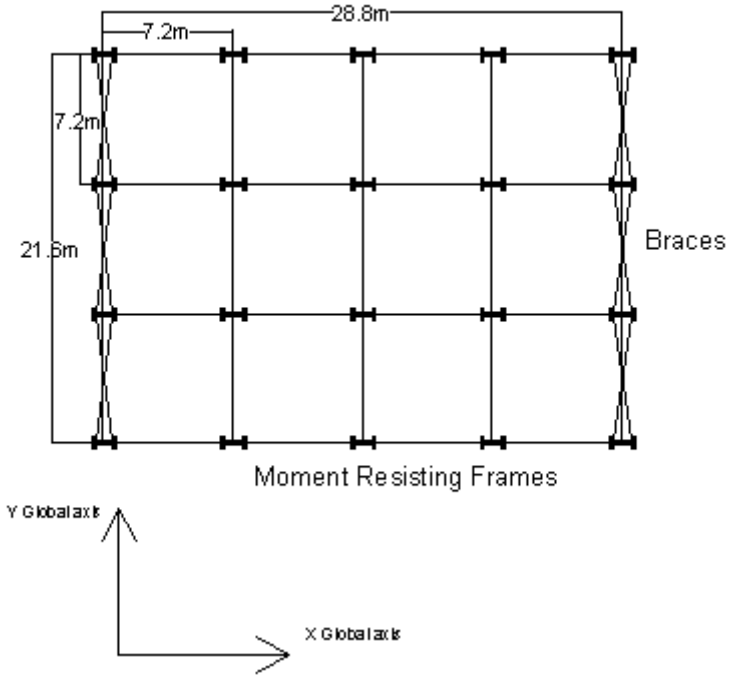

Figure 5.3: Plan of the Prototype Building

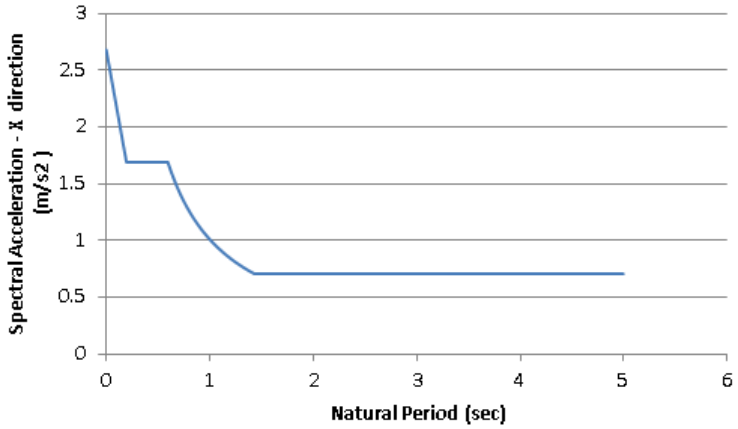

Figure 5.4: Design Spectrum for X axis according to Eurocode 8

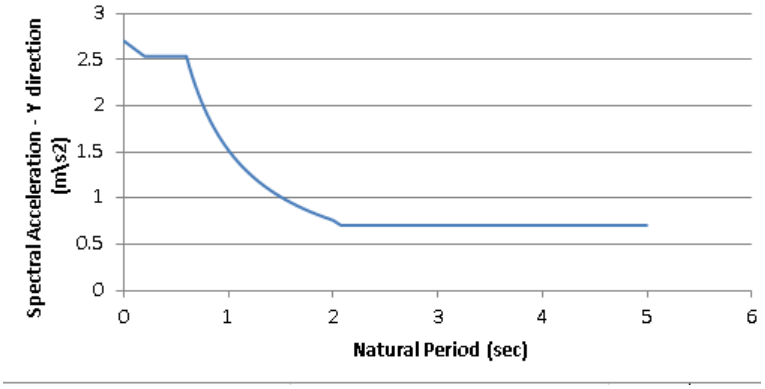

Figure 5.5: Design Spectrum for Y axis according to Eurocode 8

The masses were determined from the load combination of dead + 0.3 live load, the design of the structure was based on the following load combinations:

$1.35G + 1.5Q$

$G + Q$

$G + 0.3Q + E_{\mathrm{X}} + 0.3E_{\mathrm{Y}}$

$G + 0.3Q + E_{\mathrm{X}} - 0.3E_{\mathrm{Y}}$

$G + 0.3Q - E_{\mathrm{X}} + 0.3E_{\mathrm{Y}}$

$G + 0.3Q - E_{\mathrm{X}} - 0.3E_{\mathrm{Y}}$

$G + 0.3Q + E_{\mathrm{Y}} + 0.3E_{\mathrm{X}}$

$G + 0.3Q + E_{\mathrm{Y}} - 0.3E_{\mathrm{X}}$

$G + 0.3Q - E_{\mathrm{Y}} + 0.3E_{\mathrm{X}}$

$G + 0.3Q - E_{\mathrm{Y}} - 0.3E_{\mathrm{X}}$

where

G is the dead load

Q is the live load

E is the seismic action The final sections of the structural members are summarized in table Table 5.2, while the dynamic characteristics of the structure are given in table Table 5.3. It can be noticed that the difference between the periods corresponding to the first 2 modes is slightly large. This is due to the design philosophy followed for this structure: design as flexible as possible the direction where the dampers are going to be added, whereas provide stiff diagonal braces at the other direction.

Table 5.1: Permanent and Live loads of the Prototype Building

Item	**Equivalent Uniform Load**
Slab with Metal Deck	3.2 kN/m^2
Ceiling and Services	0.5 kN/m^2
Partitions	0.8 kN/m^2
Glazing	1.2 kN/m
Live Load	2 kN/m^2

Table 5.2: Sections of Steel Structure

Floors	**Columns**	**Beams (X axis)**	**Beams (Y axis)**	**Braces (Y axis)**
1	HEB450	IPE450	IPE360	SHS200x200x10
2	HEB450	IPE450	IPE360	SHS200x200x10
3	HEB450	IPE450	IPE360	SHS200x200x10
4	HEB450	IPE450	IPE360	SHS200x200x10
5	HEB360	IPE400	IPE360	SHS180x180x10
6	HEB360	IPE400	IPE360	SHS180x180x10
7	HEB360	IPE400	IPE360	SHS180x180x10
8	HEB320	IPE360	IPE360	SHS160x160x10
9	HEB320	IPE360	IPE360	SHS160x160x10
10	HEB320	IPE360	IPE360	SHS160x160x10

Table 5.3: Dynamic Characteristics of the Prototype Building

Number of	Natural	Natural	Mass Participation Ratios		
Mode Shape	Period (sec)	Frequency (Hz)	UX	UY	RZ
1	2.651286	0.37718	0.74817	6.617E-11	0.19531
2	0.973412	1.0273	5.796E-09	0.79867	0.36919
3	0.923146	1.0833	0.12323	3.262E-08	0.02966
4	0.747592	1.3376	0.000005825	0.000001858	0.22303
5	0.51529	1.9407	0.04826	3.038E-12	0.01216
6	0.32702	3.0579	0.02625	1.52E-10	0.00682
7	0.320467	3.1204	7.637E-12	0.13171	0.06094
8	0.248166	4.0296	0.000004159	0.000005787	0.03576
9	0.232642	4.2985	0.01844	1.355E-09	0.00518
Sum			0.96435999	0.930387679	0.93805

5.3 Non Linear Analysis

5.3.1 Performance Criteria

FEMA356[5] defines three discrete levels of structural damage, referred to as Performance Levels (PLs):

- Immediate Occupancy (IO): Post-earthquake damage state that remains safe to occupy, essentially retains the pre-earthquake design strength and stiffness of the structure
- Life Safety (LS): Post-earthquake damage state that includes damage to structural components but retains a margin against onset of partial or total collapse
- Collapse Prevention (CP): Post-earthquake damage state that includes damage to structural components such that the structure continues to support gravity loads but retains no margin against collapse

Every structure can be designed according to a target performance level under a specific earthquake hazard level. According to Table 5.4[5], rehabilitation objectives h in combination with l (blue color) are the basic objectives under which the structures are usually designed. Hence, the main target of conventional structures is the design of a structure for a seismic action of 10% probability of exceedance in 50 years for Life Safety performance level (Design Basis Earthquake: DBE) or 2% probability of exceedance in 50 years (Maximum Considered Earthquake: MCE)

for Collapse Prevention performance level. However, as already mentioned earlier, under different circumstances the design of the structure may be determined based on different combinations of earthquake hazard levels and target performance levels. The rehabilitation objectives coloured with yellow are considered as enhanced design objectives (a,d,g,j,k), while those without colour (objectives: b,c,e,f,i) are considered as reduced rehabilitation objectives. Table 5.5 summarizes the expected behaviour of the primary elements of steel frames, and the expected drift for every performance level. These drifts have been used as the main evaluation tool for seismic response of structures in previous studies[72, 62].

The steel frame in this study was analysed under both DBE, and MCE hazard levels. In order to prevent or to minimize damage, and potential economic loss which is associated with the repair and limited occupancy after a strong earthquake [72], elastomeric dampers were later added and the Damped Moment Resisting Frame (DMRF) was evaluated under the same hazard levels of the seismic action. The target performance levels used in this study, in case of the retrofitted frame, are different for the hazard level of 10% probability of exceedance in 50 years and the hazard level of 2% probability of exceedance in 50 years compared to the ones described in Table 5.4, 5.5, and are summarised as follows:

- All columns remain elastic under the DBE
- All columns remain either elastic or are allowed to exhibit minor plastic deformations under the MCE
- All beams remain either elastic or exhibit minor plastic deformations under DBE
- Plastic hinges are allowed to be created at beams under the MCE, if plastic deformations are minor in most of the columns
- 0.7%-1.3% interstorey drift under the DBE
- 0.2%-0.5% residual interstorey drift under the DBE
- 2.3%-2.7% drift under the MCE

- 0.5%-1.0% residual interstorey drift under the MCE

It should be mentioned, that the main target the retrofit design which will be described in detail in Section 5.3.4 is based on the DBE, and not the MCE. Hence, the main focus should be on fulfilling the acceptance criteria set for DBE. However, improved behaviour is anticipated for the MCE as well, and therefore some additional criteria have been set.

Table 5.4: Rehabilitation Objectives (blue colour: main rehabilitation objectives, yellow colour: enhanced rehabilitation objectives)

Earthquake Hazard Levels	**Target Building Performance**		
	Immediate Occupancy	Life Safety	Collapse Prevention
50% in 50 years	a	b	c
20% in 50 years	d	e	f
10% in 50 years	g	h	i
2% in 50 years	j	k	l

Table 5.5: Expected drifts

Type	**Immediate Occupancy**	**Life Safety**	**Collapse Prevention**
Transient Drift	0.70%	2.50%	5%
Permanent Drift	0%	1%	5%

5.3.2 Conventional Moment Resisting Frame Model

All the non linear analyses and the evaluation of the retrofit of the steel frame, are carried out using the finite element software OpenSees, focusing on an interior steel frame, in the global X direction of the prototype building (see fig Figure 5.3). The main target of this chapter is to demonstrate the enhancement of the structural performance level of the prototype Conventional Moment Resisting Frame (MRF), adding Elastomeric Dampers (EDs), and evaluate their effectiveness under strong ground motions. In order to achieve this, the 10-storey MRF was modelled in OpenSees and tested under ground motions, which were scaled in order to be compatible with the design hazard level, according to EC8. Elastomeric dampers were later added to the MRF, following a design method proposed by Lee [114]. The hysteretic model described in chapter 4 formed the basis of modelling the EDs used

in this analysis. These frames were compared with regard to displacements, drift ratios, moments, and shear forces in order to fully evaluate the EDs' efficiency.

The MRF is illustrated in Figure 5.2, and is modelled based on the principles of the prototype building. Steel01 was selected from the OpenSees[3] Material class, with 275MPa yield strength, and zero strain hardening ratio, corresponding to an elastic-perfectly plastic material representing the non linear behaviour of the building, following the principles of Eurocode 3 [1]. P-Delta effects are taken into account through the P-Delta geometric transformation command in OpenSees. Distributed plasticity force-based beam column elements [96, 126] were used to capture the non linear behaviour of the beams and columns elements, based on fiber sections. More specifically, after a preliminary sensitivity analysis in a 1-storey, 1-bay steel frame subjected to ground motions, 16 fibers were assigned along the width of the flange and the height of the web, while 4, and 2 fibers were assigned along the thickness of the flange and the thickness of the web respectively. The beams were loaded with a dead load of 23 kN/m and live load of 9.6 kN/m and the corresponding masses were assigned at the nodes of the columns as: 29.5 tons at the interior columns and 19.35 tons at the corner columns. A Rayleigh damping matrix was assigned to the model, representing the 2% inherent critical damping of the structure at the first two modes of vibration. In order to take into account any changes on the Rayleigh damping due to yielding, the stiffness matrix was updated at each time step, instead of using the initial matrix.

5.3.3 Ground Motions

A total of 20 ground motions were used to evaluate the seismic performance of both the SMRF and DMRF. In EC8[2], it is clearly stated that in order to use ground motions for nonlinear analysis the following criteria should be met:

- A minimum of 3 accelerograms should be used
- The mean of the zero period spectrum response acceleration values (calculated from the individual time histories) should not be smaller than the value of $a_{\mathrm{g}}S$ for the site in question, where a_{g} is the design ground acceleration, and S is

the soil factor.

- In the range of periods between $0.2T_1$ and $2T_1$, where T_1 is the fundamental period of the structure in the direction where the accelerogram will be applied; no value of the mean 5% damping elastic spectrum, calculated from all time histories, should be less than 90% of the corresponding value of the 5% damping elastic response spectrum.

In order for the above conditions to be satisfied, the spectrum matching method [41, 133] was selected. The basis of this method is for the time history response spectrum to gradually match the response spectrum of EC8, by increasing some components of the frequency spectrum, and reducing some others. In essence, this method does not create new ground motions, but it modifies selected records in order to satisfy the above criteria. The whole procedure is shown in Fig. 5.6 and can be summarized as follows: After calculating the EC8 target spectrum, the response spectrum of the ground motion is calculated [27], and is compared with the target spectrum from EC8, by dividing the values of the two spectra for each time increment. Then, the outcome ratio is transmitted from the time domain to the frequency domain (Figures 5.6d and 5.6e). The Fourier transform [100] of the accelerogram is then being determined (Figure 5.6f). Then the components of the Fourier transform from Figure 5.6f are multiplied by the ratio components of Figure 5.6e, (only for the frequency range of interest), giving a new Fourier transform (Figure 5.6g). The inverse Fourier transform is now used in order to obtain new ground motion, which is shown at Figure 5.6h. If the response spectrum of the scaled record is in good agreement with the one proposed from EC8, and the above criteria are satisfied, then the whole procedure stops. Otherwise, it has to be repeated until a satisfactory convergence has been achieved. This method could be very useful in regions that strong ground motions recordings are unavailable[49].

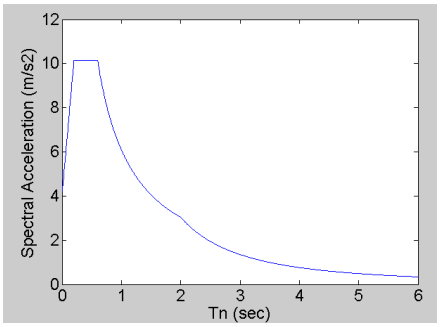

(a) Target Spectrum

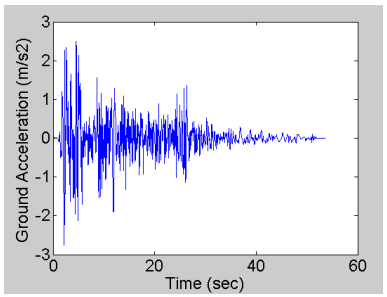

(b) Ground motion

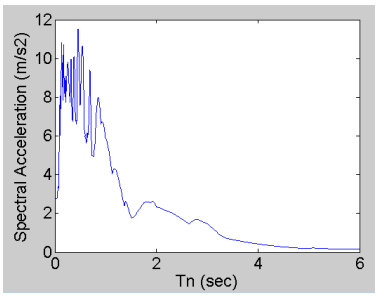

(c) Response Spectrum of ground motion

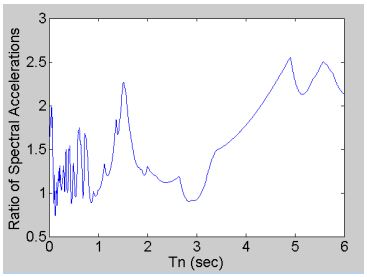

(d) Ratio of Target Spectrum to Response Spectrum (Time domain)

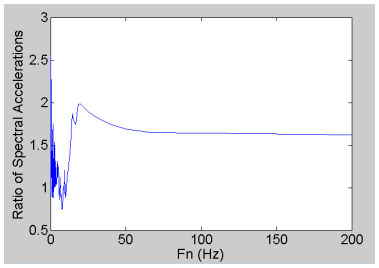

(e) Ratio of Target Spectrum to Response Spectrum (Frequency domain)

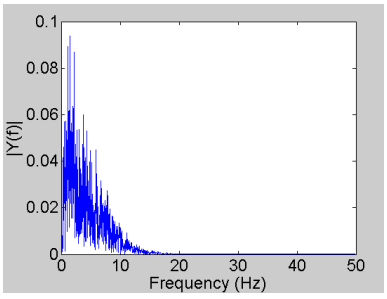

(f) Fourier Transform of original ground motion

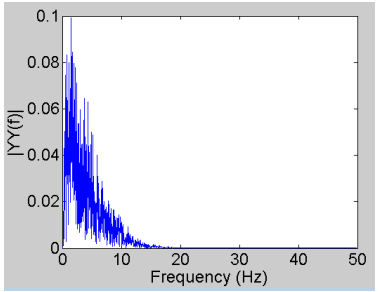

(g) Fourier Transform of scaled ground motion

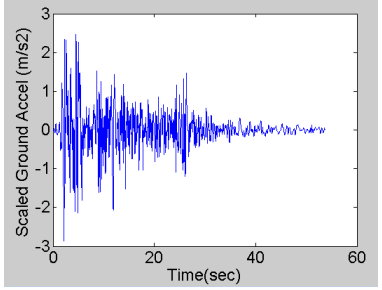

(h) Scaled ground motion

Figure 5.6: Scaling Procedure of ground motions

Response-history analysis was performed using both near-field and far-field ground motions. The magnitude of the ground motions ranges between 6.5 and 7.36 and the site to source distance ranges between 0.07 and 222.42 km. These records have been selected from PEER Ground Motion Database[67]. The original ground motions used in this study are summarized in table 5.6. However, from this point on the scaled versions of these ground motions are going to be used, and therefore, any reference to any of the names of these ground motions will be referred to their scaled version, unless specified otherwise. The response spectra of each original unscaled ground motion, and the resulting spectra from the scaled earthquake histories are compared with the EC8 spectrum in Figure 5.7, and 5.8. It can be clearly seen that there is a very good agreement between the response spectrums of the scaled ground motions with the EC8 spectrum. Figure 5.9 shows the mean value of the response spectra of both the scaled and the unscaled time histories in comparison with the EC8 spectrum. All these ground motions were scaled in order to comply under EC8 principles. Figure 5.10 presents a typical ground motion (Imperial Vallley-02) compared with its scaled to DBE version, with the latter being the one which was used for the non-linear analyses of the steel frame.

In order to evaluate the steel frames under stronger ground motions, representing a seismic action of 2% probability of exceedance in 50 years, EC8 adopts the following philosophy: The main goal is the alteration of the design seismic action, which is represented by a hazard level of 10% probability of exceedance in 50 years. According to EC8, this can be achieved not by upgrading the performance level for a given earthquake level, but by modifying the reference seismic action[76]. This can be done, by altering the importance factor, γ_1 depending on the target performance level[20].

Table 5.6: Ground Motions used for non linear analyses

Earthquake Name	**Year**	**Station Name**	**Magnitude**	**Distance (km)**	**Component**
Imperial Valley-02	1940	El Centro Array #9	6.95	6.09	I-ELC180
Northwest Calif-02	1941	Ferndale City Hall	6.6	91.15	C-FRN045
Borrego	1942	El Centro Array #9	6.5	56.88	B-ELC000
Kern County	1952	LA - Hollywood Stor FF	7.36	114.62	PEL090
Northern Calif-03	1954	Ferndale City Hall	6.5	26.72	H-FRN044
Imperial Valley-06	1979	El Centro - Meloland Geot. Array	6.53	0.07	H-EMO000
Imperial Valley-06	1979	El Centro Array #7	6.53	0.56	H-E07140
Superstition Hills-02	1987	Parachute Test Site	6.54	0.95	B-PTS225
Imperial Valley-06	1979	El Centro Array #8	6.53	3.86	H-E08140
Imperial Valley-06	1979	Chihuahua	6.53	7.29	H-CHI012
Imperial Valley-06	1979	EC County Center FF	6.53	7.31	H-ECC002
Imperial Valley-06	1979	Brawley Airport	6.53	8.54	H-BRA225
El Alamo	1956	El Centro Array #9	6.8	121	ELC180
Borrego Mtn	1968	El Centro Array #9	6.63	45.12	A-ELC180
Borrego Mtn	1968	LA - Hollywood Stor FF	6.63	222.42	A-PEL090
Borrego Mtn	1968	LB - Terminal Island	6.63	199.84	A-TLI249
San Fernando	1971	2516 Via Tejon PV	6.61	55.2	PVE065
Tabas_ Iran	1978	Ferdows	7.35	89.76	FER-L1
Tabas_ Iran	1978	Kashmar	7.35	193.91	KSH-L1
Tabas_ Iran	1978	Sedeh	7.35	150.33	SED-L1

EC8 associates the importance factor with the target performance level by:

$$\gamma_1 = (\frac{P_{\mathrm{L}}}{P_{\mathrm{LR}}})^{-1/k} \tag{5.5}$$

where: P_{LR} is the reference probability of exceedance in 50 years
P_{L} is the probability of exceedance in 50 years, of the target performance level
k is recommended to be 3

Figure 5.11 graphically shows how importance factor and different probabilities of exceedance in 50 years are related. Hence, in the case of the the hazard level of 2% probability of exceedance in 50 years: P_{LR}=0.1, P_{L}=0.02, and therefore the reference seismic action has to be multiplied by γ_1=1.7. This will be particularly important in the following sections, since the frames were tested for both the hazard levels (2% and 10% probability of exceedance). What is worth mentioning is that the same spectral shape is meant to be used for the seismic action for both of the aforementioned performance levels, with a universal multiplicative factor reflecting the difference in hazard level. The corresponding response spectrum, given by EC8, under which the original ground motions have to be scaled for a seismic action of

2% probability of exceedance in 50 years, can be seen at Figure 5.12.

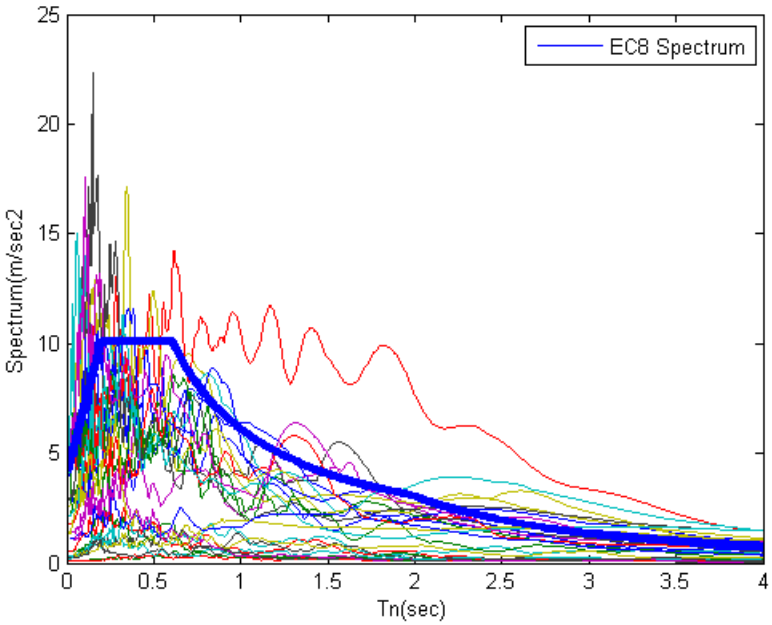

Figure 5.7: Comparison of EC8 Spectrum with each of the 20 original ground motions response spectrum

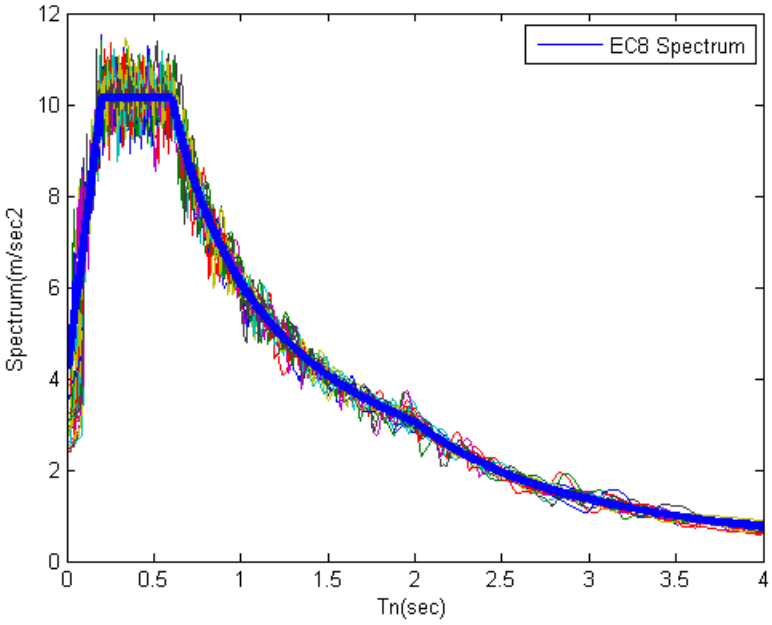

Figure 5.8: Comparison of EC8 Spectrum with each of the 20 ground motions scaled to DBE

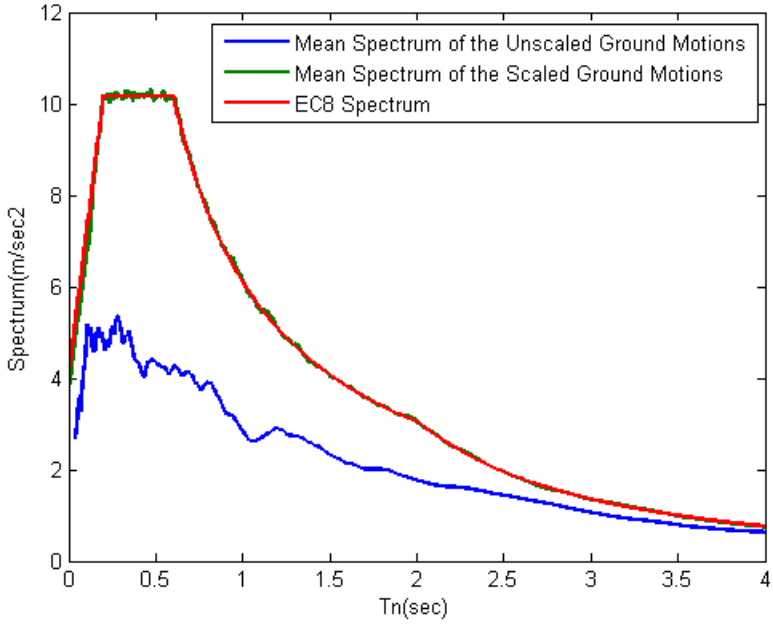

Figure 5.9: Comparison of EC8 Spectrum with the mean Spectrum of 20 ground motions for DBE

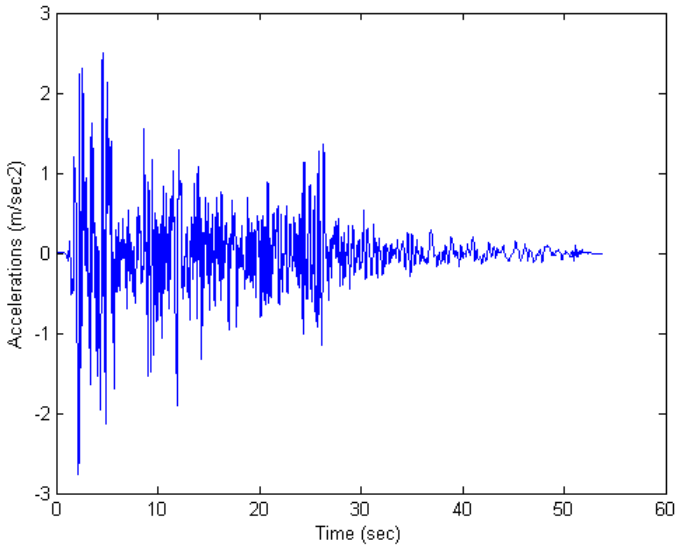

(a) Original

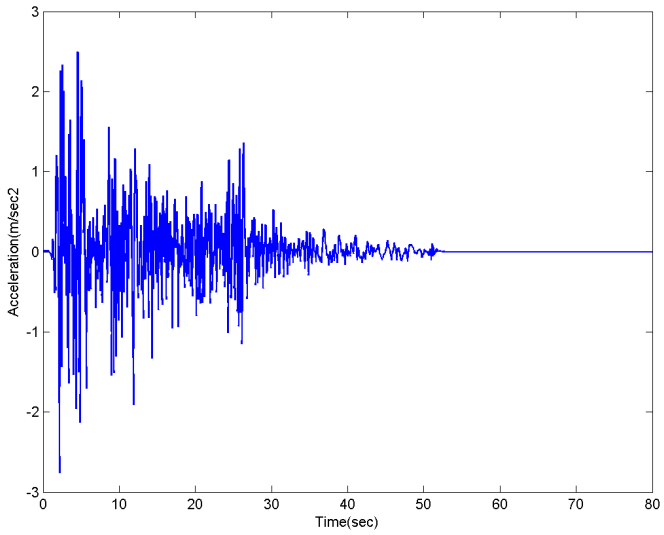

(b) Scaled to DBE

Figure 5.10: Ground motionL: IMPVALLI-I-ELC180

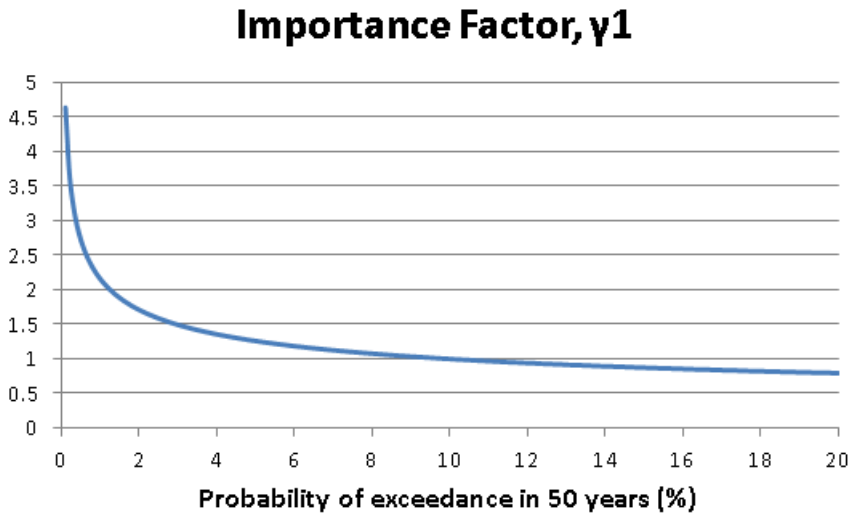

Figure 5.11: Importance factor in terms of probability of exceedance in 50 years

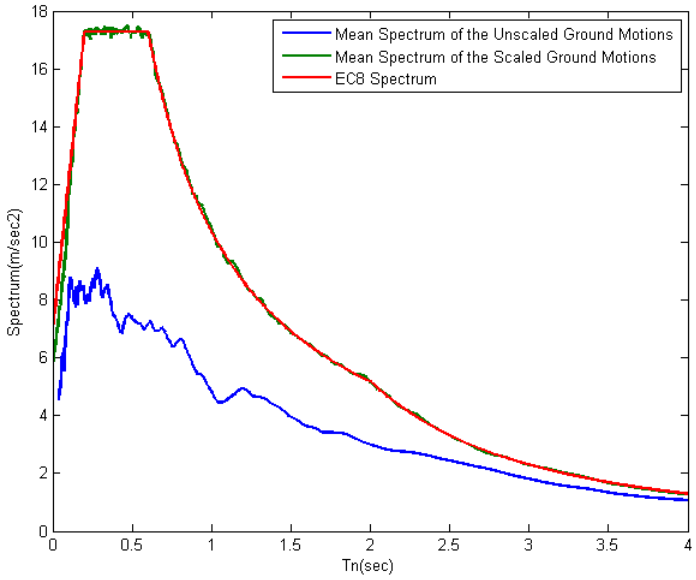

Figure 5.12: Comparison of EC8 Spectrum with the mean Spectrum of 20 ground motions for MCE

5.3.4 Retrofitting Procedure

Dampers Design Recommendations

Although several few retrofitting procedures have been proposed in the same academic literature [23, 31, 25, 24, 48, 73, 85, 110], while others have been applied to real structures [59, 136, 40, 47], only the most widely used will be presented here.

The first method was initially proposed by Fan [42] for implementation of ViscoElastic dampers, and later extended to elastomeric dampers by Lee [73]. It is a Simplified Design Procedure (SDP), which is used for performance based design of MRFs, and uses an elastic-static analysis to determine the frame's response and compare it with the initially assumed earthquake performance criteria, assuming the dampers' behaviour is purely viscoelastic. More specifically it consists of the following steps:

1. Establish seismic performance criteria:

   A target performance level, as explained in 5.3.1, is selected

2. Idealize the non-linear damping material as a linear VE material:

   Since elastomeric materials exhibit non linear behaviour which is dependant on strain amplitude, frequency, and temperature, an equivalent linear VE model has to be assumed for the static analysis. This model would have an equivalent shear stiffness, and loss factor, in the same way as they were determined and presented in Chapter 3, based on the natural frequency of the building.

3. Choose the design temperature:

   Since, the characteristics of elastomers depend on temperature, a design temperature must be selected.

4. Select an appropriate value for α and β:

   α is the ratio of the brace stiffness per storey in the global direction to the storey stiffness without dampers and braces, and β is the ratio of the damper stiffness per storey in the global direction to the storey stiffness without dampers and braces. Moreover, the locations where the dampers are going

to be applied must be determined as well. Kasai [63], Chang [22], Hanson and Soong [48], Karavasilis [62], and Constantinou [31] have used these ratios for preliminary design analyses. A value between 10 and 30 is recommended for α, in order for the braces to be sufficiently stiff, and between 0.5 and 5.0 for β.

5. Perform elastic-static analysis based on equivalent lateral forces
6. Compare the response from the static analysis with the target earthquake performance level
7. Select minimum β that satisfies design criteria and provides target seismic performance
8. Determine the structural response at the low-end of the design temperature range and compare structural response with design criteria. Since a temperature decrease leads to an increase of stiffness, the structural response under the minimum allowed temperature is investigated, under which the structure will not be so flexible.
9. Determine damper area and thickness
10. Verify the procedure through non linear time history analysis (optional step)

The second method [114, 48, 24] is an iterative procedure, based on the principle that the stiffness added due to the dampers should be proportional to the storey stiffness of the structure. The design process consists of the following steps:

1. Determine structural properties of the building and perform structural analysis. An analysis of the structure without dampers is a necessary step in order to capture the dynamic behaviour of the building, and how this can be further improved.
2. Select target performance criteria. Either define new performance criteria (as was done in this study), or adapt already defined criteria from design codes (see section 5.3.1). This will be the target structural behaviour under the design loads when dampers are added

3. Determine target desired damping ratio. Either through time history analyses or through modal response analysis, the approximate required damping ratio can be extracted.

4. Select desirable and available damper locations. Even though in this study, this does not seem to create any important issues, in the case of irregular 3D buildings, the location in which the dampers will be allocated could highly contribute to the seismic response of the structure.

5. Select damper stiffness and loss factor. In order to achieve the target damping ratio, the required dampers' characteristics have to be determined (see 5.3.4). These characteristics have to be extracted based on dampers' characterization tests which have to be carried out at frequencies and amplitudes, which the structure, and therefore also the dampers, are expected to experience during a seismic event

6. Estimate the equivalent damping ratio using the modal strain energy method, at section 5.3.4 [132, 116, 57, 108]

7. Perform structural analysis using the desired damping ratio. Time history analyses can now be carried out, in order to evaluate the performance of the structure with added dampers

When steps 6 and 7 satisfy the desired damping ratio and the target performance criteria then the analysis is complete. Otherwise, a new analysis has to be carried out with either new structural properties or damper locations, dimensions or properties (see Fig. 5.13). Based on Lee's [73] principle to assume that the elastomer behaves in a pure viscoelastic way, the second design process will be performed here.

Modal Strain Energy Method

Before proceeding to the damper design for the MRF, a brief presentation of the modal strain energy method, mentioned earlier in the second dampers design proposal, will be given. The $\imath_{\text{th}}$ modal damping ratio can be determined as [57]:

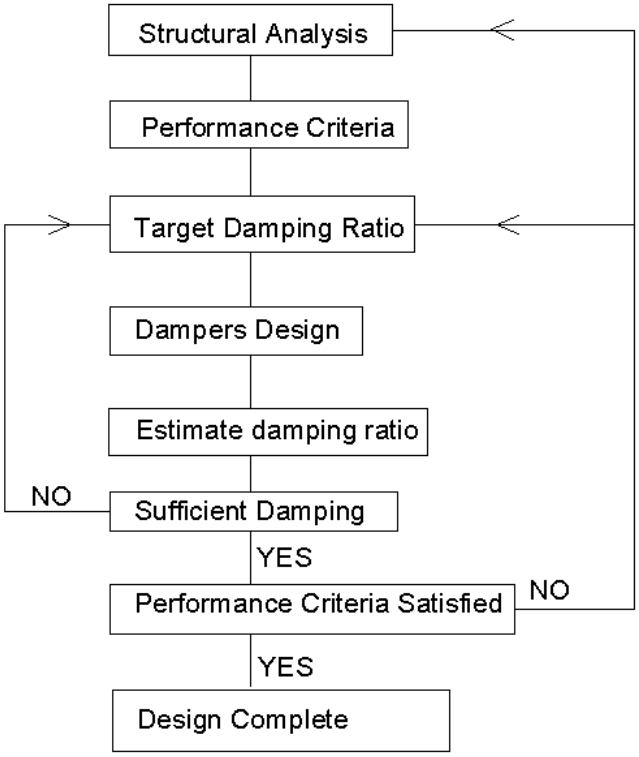

Figure 5.13: Dampers Design Procedure

$$\zeta_{\mathrm{D,i}} = \frac{n(\omega_{\mathrm{i}})}{2} \frac{\phi_i^T (K_{\mathrm{D}}) \phi_{\mathrm{i}}}{\phi_i^T (K_{\mathrm{S}} + K_{\mathrm{D}}) \phi_{\mathrm{i}}} \tag{5.6}$$

where $n(\omega_{\mathrm{i}})$ is the loss factor of the material, extracted from characterization tests (see Chapter 3) at the frequency ω_{i} of the original structure, ϕ_{i} is the $\imath_{\mathrm{th}}$ mode shape vector corresponding to the frequency ω_{i}, K_{S} is the stiffness matrix of the original structure, and K_{D} is the stiffness matrix corresponding only to the dampers. The frequency ω_i can be written as:

$$\omega_{\mathrm{i}} = [\frac{\phi_i^T (K_{\mathrm{S}} + K_{\mathrm{D}}) \phi_{\mathrm{i}}}{\phi_i^T (M) \phi_{\mathrm{i}}}]^{1/2} \tag{5.7}$$

where M is the mass matrix of the structure. Assuming that the addition of the dampers will not affect the mode shapes, and combining Eqs. 5.6, 5.7, the i_{th} modal

damping ratio can be rewritten as:

$$\zeta_{\mathrm{D,i}} = \frac{n(\omega_{\mathrm{i}})}{2}[1 - \frac{\phi_i^T K_{\mathrm{S}} \phi_{\mathrm{i}}}{\phi_i^T (K_{\mathrm{S}} + K_{\mathrm{D}}) \phi_{\mathrm{i}}}] = \frac{n(\omega_{\mathrm{i}})}{2}(1 - \frac{\omega_i^2}{\omega_{D,i}^2}) \tag{5.8}$$

Elastomeric Dampers Design

One of the first steps of the retrofitting procedure described earlier, is the determination of the target performance criteria, which are going to be repeated here for convenience:

- All columns remain elastic, while specifically the base columns can exhibit minor plastic deformations under the DBE
- All columns remain either elastic or are allowed to exhibit minor plastic deformations under the MCE
- All beams remain either elastic or exhibit minor plastic deformations under DBE
- Plastic hinges are allowed to be created at beams under the MCE, if plastic deformations are minor in most of the columns
- 0.7%-1.3% drift under the DBE
- 2.3%-2.7% drift under the MCE

The design process is based on fulfilling the target criteria set for the DBE, and not the MCE. Nevertheless, additional criteria have been set in case the structure experiences a seismic action equivalent to the MCE. Now that the performance criteria have been set, a target damping ratio of 12% will be assumed, corresponding to an additional 10% of critical damping. This number was chosen based on a trial and error procedure, carrying out time history analyses. Based on theses analyses, it was found that an additional 10% damping should be adequate in order for the structure to comply with the performance criteria. Regarding the location of the dampers,

bays 1 and 4 have been selected (Fig. 5.14 shows the locations of the dampers). The selection of the loss factor and the dampers stiffness can be determined based on a modified version of Eq. 5.8[114]:

$$k_{\mathrm{D,j}} = \frac{2\zeta}{n-2\zeta} k_{\mathrm{S,j}} \tag{5.9}$$

where ζ is the target damping ratio, $k_{\mathrm{S,j}}$ is $k_{\mathrm{D,j}}$ is the story stiffness and the damper stiffness at the $\mathrm{J_{th}}$ story. It should be noted here, that $k_{\mathrm{D,j}}$ is the total contribution of the dampers along with the diagonal braces, and not only the dampers. This ensemble can be modelled assuming that the brace stiffness is connected in series with the damper, and then both the damper and the brace connected in parallel with the structure (Figure 5.15) [48].

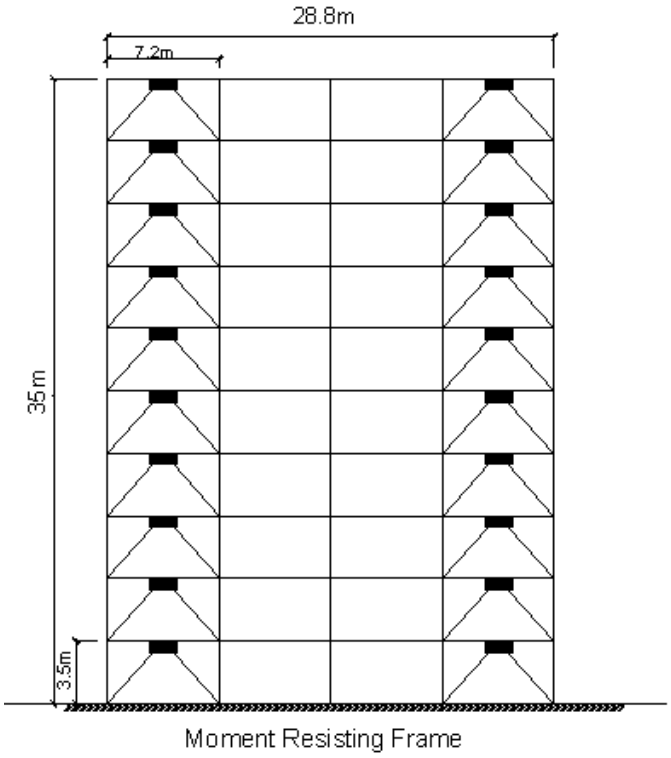

Figure 5.14: Location of Dampers

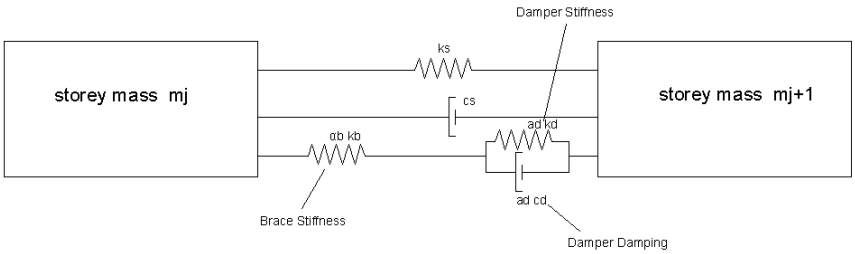

Figure 5.15: Simplified Frame-Braces-Damper representation

In this figure, k_{S}, and c_{S} are the story stiffness of the structure, and the damping coefficient between the story j and $j+1$. k_{b} is the braces stiffness, while k_{d}, and c_{d} are the damper stiffness and damping respectively. With regard to α_{b}, and α_{d}, these values correspond to attachment coefficients, and depend on the dampers-braces geometric configuration (see Figure 5.16). In this specific case, where chevron diagonal braces are used, and the damper main direction is horizontal and coincides with the loading direction of the frames, $\alpha_{\mathrm{b}} = 2cos^2\theta$ (taking into account the stiffness of both braces), and $\alpha_{\mathrm{D}} = 1$ [48].

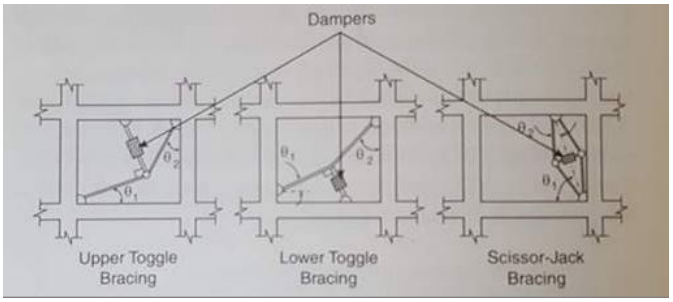

(a)

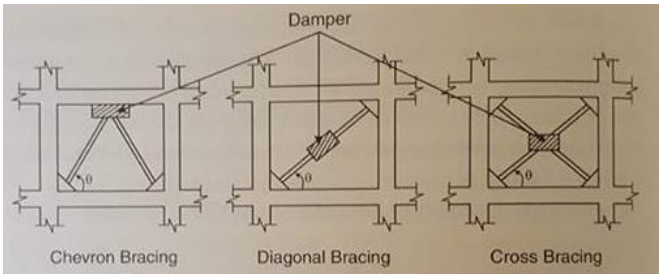

(b)

Figure 5.16: Dampers-Bracing geometric configuration [48]

The equivalent storey stiffness and damping are derived as:

$$k = k_{\mathrm{S}} + \frac{\alpha_{\mathrm{d}}\alpha_{\mathrm{b}}k_{\mathrm{d}}k_{\mathrm{b}}(\alpha_{\mathrm{d}}k_{\mathrm{d}}+\alpha_{\mathrm{b}}k_{\mathrm{b}})+\omega^2\alpha_{\mathrm{b}}\alpha_d^2k_{\mathrm{b}}c_d^2}{(\alpha_{\mathrm{d}}k_{\mathrm{d}}+\alpha_{\mathrm{b}}k_{\mathrm{b}})^2+\omega^2\alpha_d^2c_d^2} \tag{5.10}$$

$$c = c_{\mathrm{S}} + \frac{\alpha_b^2\alpha_{\mathrm{d}}k_b^2c_{\mathrm{d}}}{(\alpha_{\mathrm{d}}k_{\mathrm{d}}+\alpha_{\mathrm{b}}k_{\mathrm{b}})^2+\omega^2\alpha_d^2c_d^2} \tag{5.11}$$

In the case where the braces are assumed rigid, which is approximately the case here since they were modelled to be 7 times stiffer than the storey stiffness, the above equations can be simplified to:

$$k = k_{\mathrm{S}} + \alpha_{\mathrm{d}}k_{\mathrm{d}} \tag{5.12}$$

$$c = c_{\mathrm{S}} + \alpha_{\mathrm{d}}k_{\mathrm{d}} \tag{5.13}$$

Taking into consideration the above parameters, it can be concluded that $k_{\mathrm{D,j}}$ in Eq. 5.9 equals with the dampers stiffness. Now, the design of the EDs can be determined. One of the first assumptions will be that the maximum allowed elastomer strain would be 50%, which coincides with the maximum strain amplitude under which the EDs were tested (see Chapter 3 for more information). For design purposes, the characteristics of the dampers which are going to be used are based on the characterization tests under 40% of the maximum allowed strain (corresponds to 20% strain amplitude), and under frequency range 0.25-0.5 Hz (the natural frequency of the building lies between these values). The shear storage modulus, and the loss factor of the elastomer can now be determined as 1.06 MPa, and 0.3535 respectively. Therefore, Eq. 5.9 can now be used. For example, for the first storey the stiffness is 51,776 kN/m, and based on Eq. 5.9, the total stiffness that needs to be provided by the dampers is 67,309 kN/m.

It is recalled here that the target performance criterion is the achievement of 1% lateral drift. Furthermore, as already mentioned, all the characterization tests

have been carried out with a 50% maximum shear strain, which results in a damper thickness of $h = 35/0.5 = 70$ mm. Assuming that each damper consists of two layers, and a total of two dampers are added per story, the area of each elastomeric layer is 1.11 m^2 and is determined from Eq 5.14.

$$AD = \frac{1}{4} k_{\mathrm{D}} \frac{h}{G_{\mathrm{S}}} \tag{5.14}$$

A similar process is repeated for each floor, and the final stiffnesses of the dampers along with the storey stiffnesses of the structure are summarized in Table 5.7. Now using the modal strain energy and Eq. 5.8 the estimated damping is 9.86%, which validates our initial assumption of a 10% damping ratio.

Table 5.7: Story and Damper Stiffness

Story	**Story Stiffness (kN/m)**	**Total Damper Stiffness (kN/m)**	**Damper Area/layer (m2)**	**AD/AP**
1	51776	67309	1.11	26.84
2	26820	34867	0.58	13.90
3	22744	29567	0.49	11.79
4	20863	27121	0.45	10.82
5	16934	22014	0.36	8.78
6	15144	19687	0.33	7.85
7	14515	18870	0.31	7.52
8	12776	16608	0.27	6.62
9	11591	15069	0.25	6.01
10	9592	12469	0.21	4.97

However, all of these properties are based on the designed dampers which are different from the prototype dampers which were tested in the Laboratory, and formed the basis for the hysteretic model proposed in Chapter 4. In order to adjust this model for the designed dampers, some modifications needed to be made. Assuming that the shear storage modulus, the loss factor, and the shear strain of the design and the prototype damper are the same:

$$G_{\mathrm{S,D}} = G_{\mathrm{S,P}} \tag{5.15}$$

$$n_{\mathrm{D}} = n_{\mathrm{P}} = n \tag{5.16}$$

$$\gamma_{\mathrm{D}} = \gamma_{\mathrm{P}} \tag{5.17}$$

where P and D denote for Prototype and Design dampers. Equations 5.15, and 5.17 can be rewritten as:

$$k_{\mathrm{S,D}} = \frac{A_{\mathrm{D}}}{A_{\mathrm{P}}} \frac{h_{\mathrm{P}}}{h_{\mathrm{D}}} k_{\mathrm{S,P}} \tag{5.18}$$

$$u_{\mathrm{D}} = \frac{h_{\mathrm{D}}}{h_{\mathrm{P}}} u_{\mathrm{P}} \tag{5.19}$$

where k_{S} denotes for the storage stiffness, associated with the shear storage modulus. Taking into account Eq. 5.18, the equivalent stiffness of the design damper can be determined as:

$$\begin{gathered} k_{\mathrm{eq,D}} = \sqrt{{k_{\mathrm{S,D}}}^2 + {k_{\mathrm{D,D}}}^2} = \\ \sqrt{{k_{\mathrm{S,D}}}^2 + (n k_{\mathrm{S,D}})^2} = \\ k_{\mathrm{S,D}} \sqrt{n^2 + 1} = \\ \frac{A_{\mathrm{D}}}{A_{\mathrm{P}}} \frac{h_{\mathrm{P}}}{h_{\mathrm{D}}} \sqrt{n^2 + 1} k_{\mathrm{P}} = \\ \frac{A_{\mathrm{D}}}{A_{\mathrm{P}}} \frac{h_{\mathrm{P}}}{h_{\mathrm{D}}} k_{\mathrm{eq,P}} \end{gathered} \tag{5.20}$$

where $k_{\mathrm{D,D}}$ is the stiffness loss modulus, corresponding to the shear loss modulus. Combining Eq. 5.19, and 5.20 the force of the design damper in terms of the prototype damper force is given:

$$F_{\mathrm{D}} = \frac{A_{\mathrm{D}}}{A_{\mathrm{P}}} F_{\mathrm{P}} \tag{5.21}$$

The above procedure was based on transforming the force displacement relationship for the tested dampers to the equivalent shear strain relationship, and then back to the force displacement relationship for the design dampers, based on the design dimensions. All of these parameters are summarized in Table 5.7. Non linear analyses with added dampers can now be performed. Regarding the braces stiffness, it was assumed that were 7 times stiffer than the stiffness of the corresponding storey. The aim was to add braces which were adequate to produce elastomer rather than brace deformation, and at the same time capable of resisting horizontal loads without buckling.

5.3.5 Earthquake Response of steel Conventional Moment Resisting Frame

This section describes the earthquake behaviour of the undamped SMRF under the ground motions scaled to DBE and MCE (see section 5.3.3). Special attention should be given to the columns' behaviour, since they might experience larger axial forces than those for which they were initially designed. An ambient temperature of 20^{o}C was assumed. Results include the seismic response of the MRF with respect to shear forces, interstorey drifts, residual displacements, roof displacements and accelerations. Since 20 different ground motions were used, the response of the structure is presented in terms of mean and maximum values.

With regard to the performance of the MRF under the DBE, the maximum roof displacement, according to Figure 5.17, is 78cm, which results in 2.2% drift ratio, while the mean value is approximately 42cm and 1.2% lateral drift. The DBE level also led to permanent deformations (Figure 5.19) of 38 cm and 12 cm being the maximum and the mean value. Figure 5.18, shows the inter storey drift ratios determined for each ground motion, and their corresponding mean value which is shown with a clear bold blue line. A maximum drift ratio of 3.75% was observed under the $BorregoMtn - A - ELC180$ ground motion, while the maximum drift ratio of the mean values was found to be 2.1%. This is very close to the Life Safety performance level (see 5.3.1). The associated mean and maximum residual drifts reached 0.6% and 1.8% respectively (Figure 5.20).

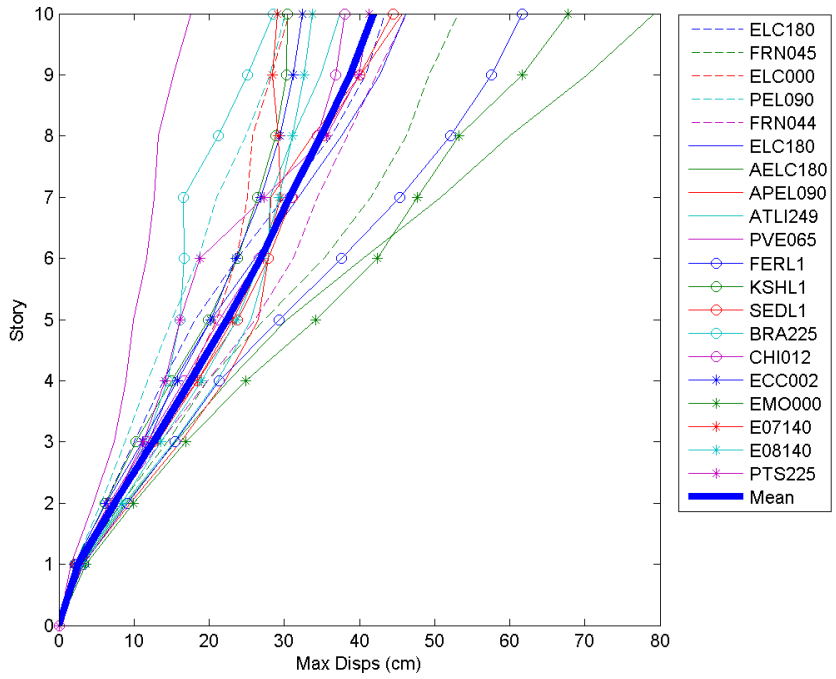

Figure 5.17: Storey maximum Displacements for SMRF under the DBE

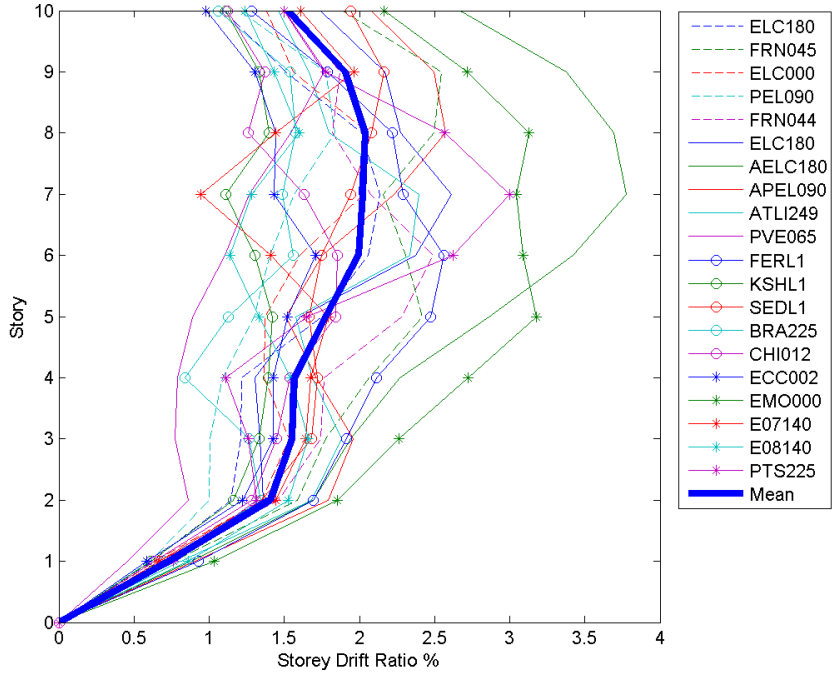

Figure 5.18: Storey Drift Ratios for SMRF under DBE

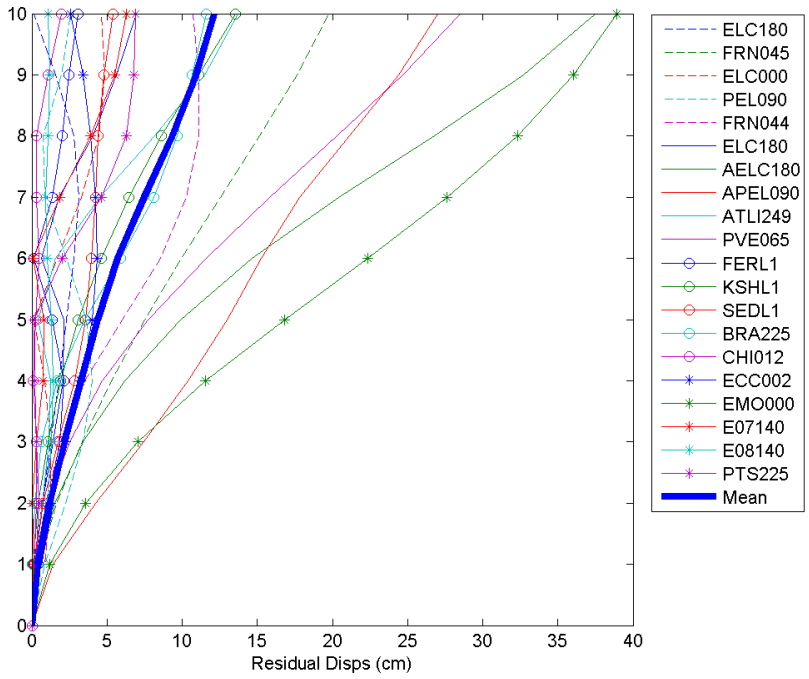

Figure 5.19: Storey residual displacements for SMRF under the DBE

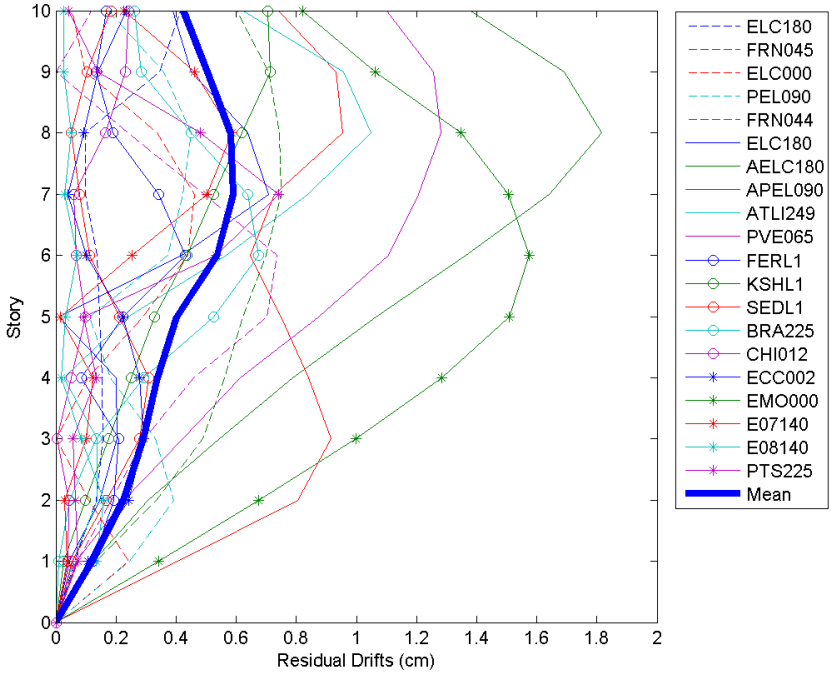

Figure 5.20: Storey residual drifts for SMRF under the DBE

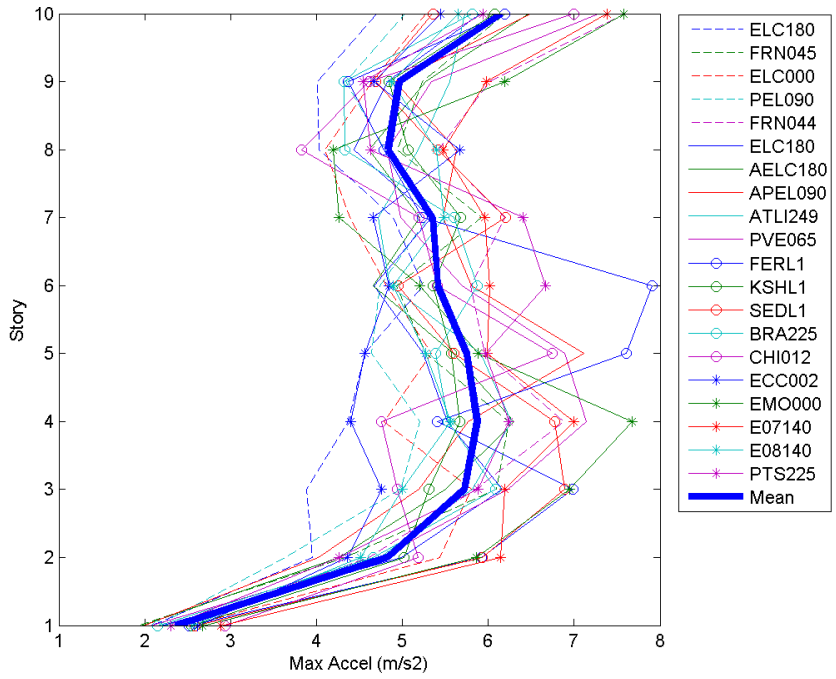

Figure 5.21: Storey maximum accelerations for SMRF under the DBE

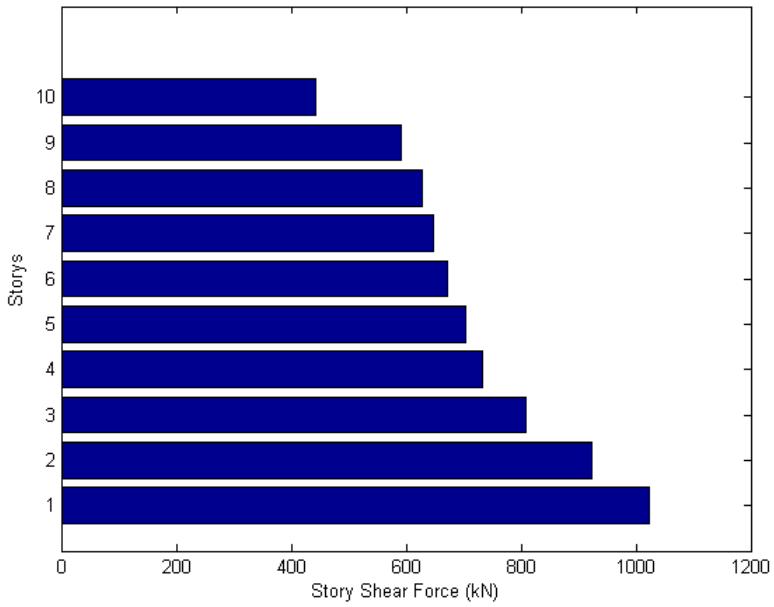

Figure 5.22: Mean Shear forces for SMRF under the DBE

Regarding the roof accelerations in Figure 5.21, 6.8 m/sec^2 and 5.5 m/sec^2 were

observed during the non linear time history analyses, as the maximum and mean values. The mean storey shear forces are also presented in Figure 5.22. The detailed time history response of the SMRF under the $Tabas - Iran - FER - L1$ ground motion scaled to DBE (Figure 5.23), with regard to roof displacement, and acceleration are shown in Figures 5.24 and 5.25. The beam and the left corner column of the 2nd bay of the 1st floor were found to be the most critical. Hence, the moment-rotations relationships are determined and shown at Figures 5.26 and 5.27, where plastic hinges have been created in both of these elements. Running all these 20 ground motions, it was generally observed that plastic hinges were created at almost all the beams, and at the base joints of the 1st floor columns, which is practically the wanted and anticipated form of behaviour, since the steel frame was designed according to EC8 philosophy which has adopted the design capacity rule.

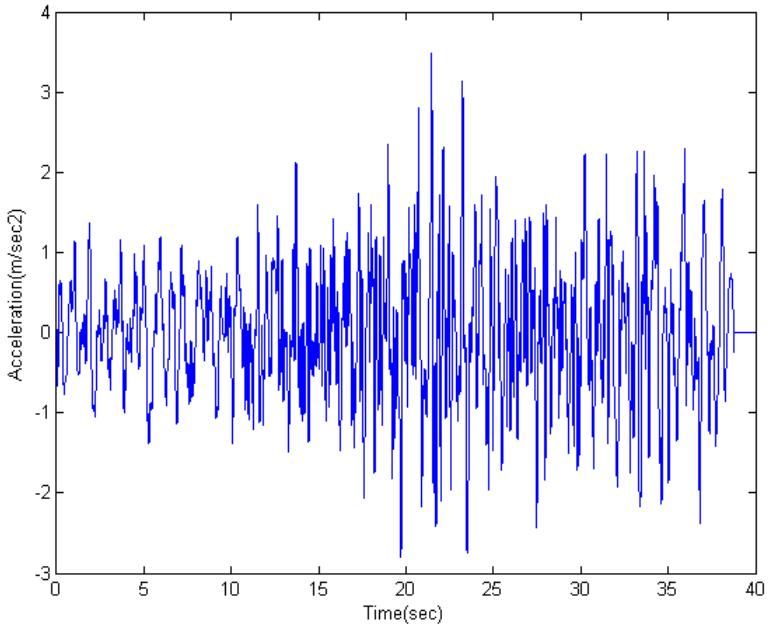

Figure 5.23: Ground Motion: $Tabas - Iran - FER - L1$ scaled to DBE

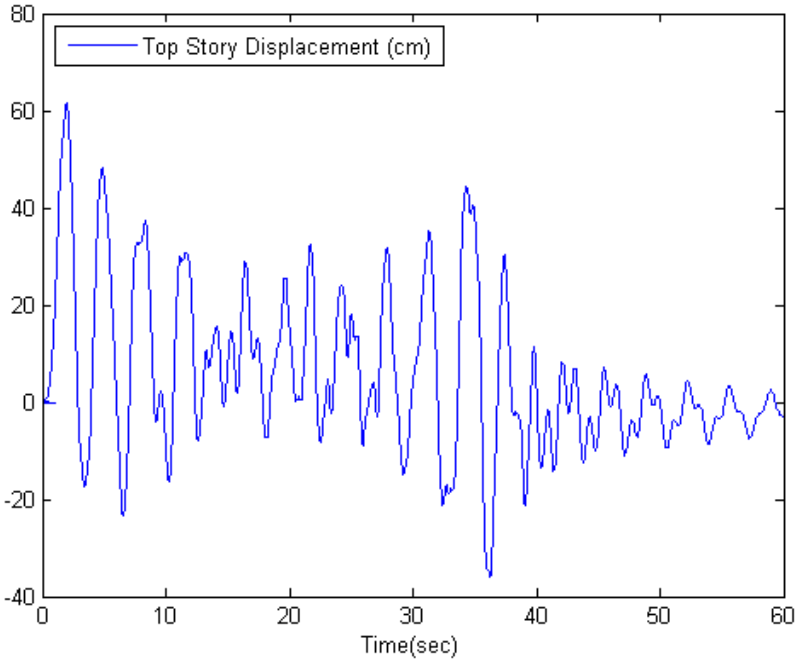

Figure 5.24: Roof displacement time history under the $Tabas - Iran - FER - L1$ grounnd motion scaled to DBE

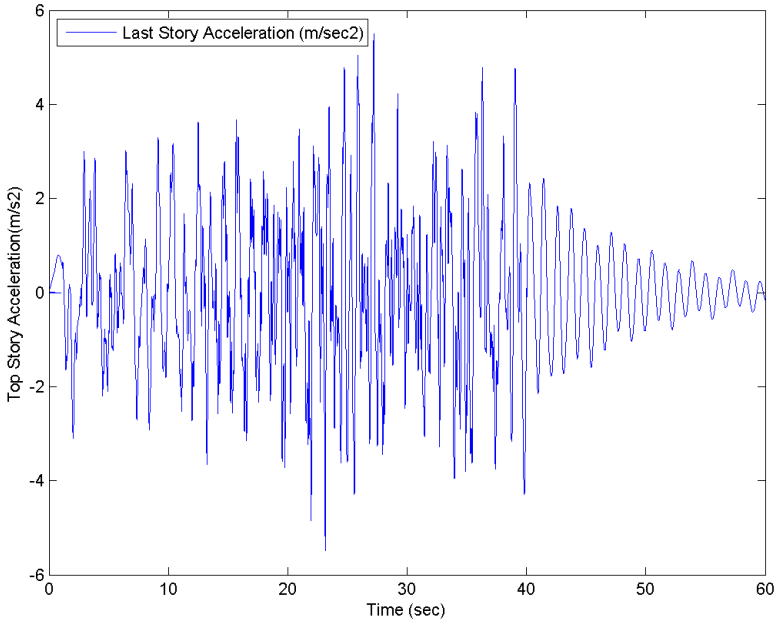

Figure 5.25: Roof acceleration time history under the $Tabas - Iran - FER - L1$ ground motion scaled to DBE

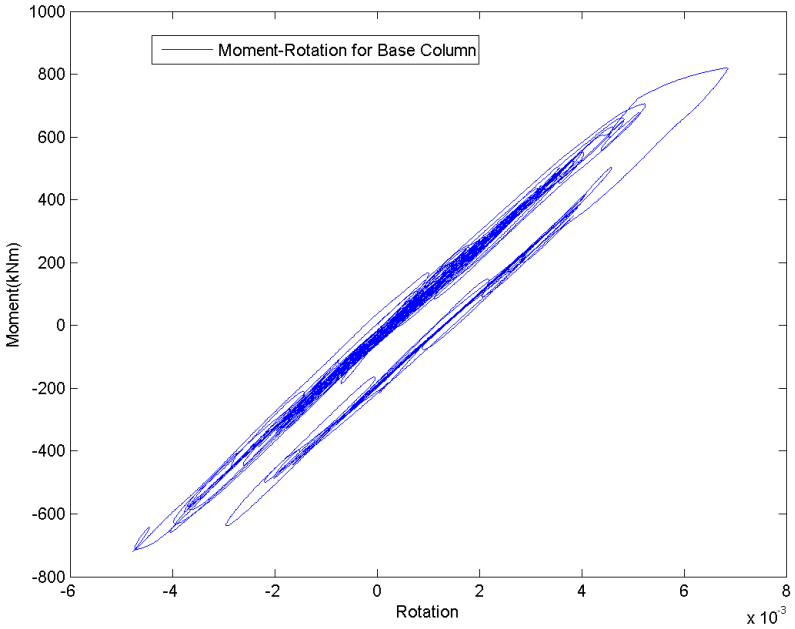

Figure 5.26: Moment-Rotation relationship for 1st story column of SMRF under the $Tabas - Iran - FER - L1$ ground motion scaled to DBE

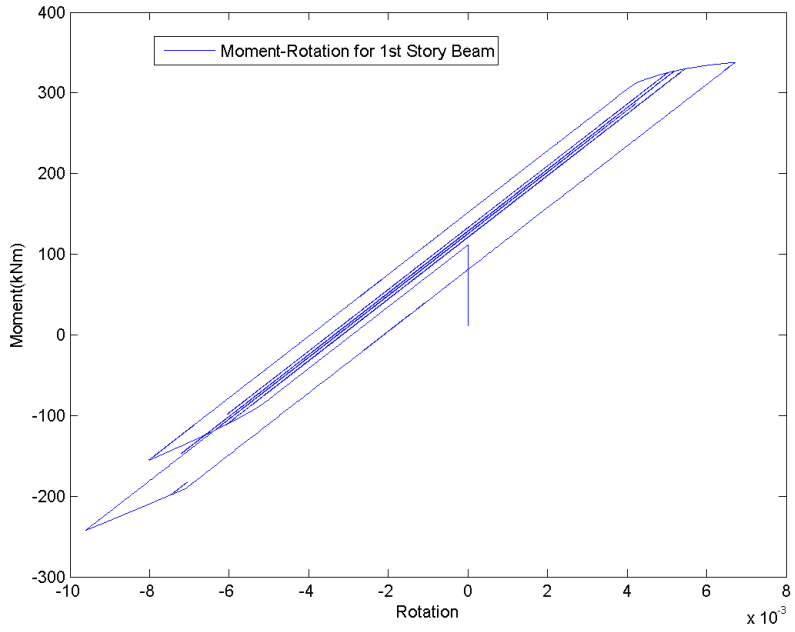

Figure 5.27: Moment-Rotation relationship for 1st story beam of SMRF under the $Tabas - Iran - FER - L1$ ground motion scaled to DBE

Regarding the response of the SMRF under MCE, the concept of section 5.3.3

was applied. For comparison, the same parameters used to evaluate the response of the MRF under DBE will be used here as well. Hence, Figure 5.28 shows the maximum and mean storey displacements, corresponding to 127 cm and 62 cm respectively. Figure 5.29 shows that the MCE led to severe damage, resulting in a 77 cm and 35 cm maximum and mean values of residual displacements. The corresponding storey drifts can be seen at Figure 5.30, where a value of 5.1% has been observed during $Tabas - Iran - FERl1$ ground motion, while the mean value increased from 2.1% under DBE to 3.1% when the frame was subjected to the MCE. The corresponding residual drifts are presented at Figure 5.31, where a maximum drift of 2.8%, and a mean drift of 1.3% was observed. With respect to the floors' accelerations, Figure 5.32 shows that they have also been increased, compared to the DBE level, reaching a maximum and mean value of 13.8 m/sec^2 and 9.1 m/sec^2 respectively. The shear forces (Figure 5.33) were also increased to 1449kN (maximum). And finally, the time history response under the $Tabas - Iran - FERl1$ ground motion scaled to MCE level is presented at (Figures 5.34 and 5.35). The corresponding moment-rotation relationship of the same beam and column used for the DBE is shown at Figures 5.36 and 5.37. It can be clearly seen that these elements have experienced much larger plastic rotations, in comparison with DBE. The MRF being tested under the MCE hazard level has exhibited large permanent displacements, while plastic hinges were created at all the beams and most of the columns. The behaviour of the frame is far from achieving a Life Safety performance level, even if we take into account only the mean values, and not the maximum values of the frame's response.

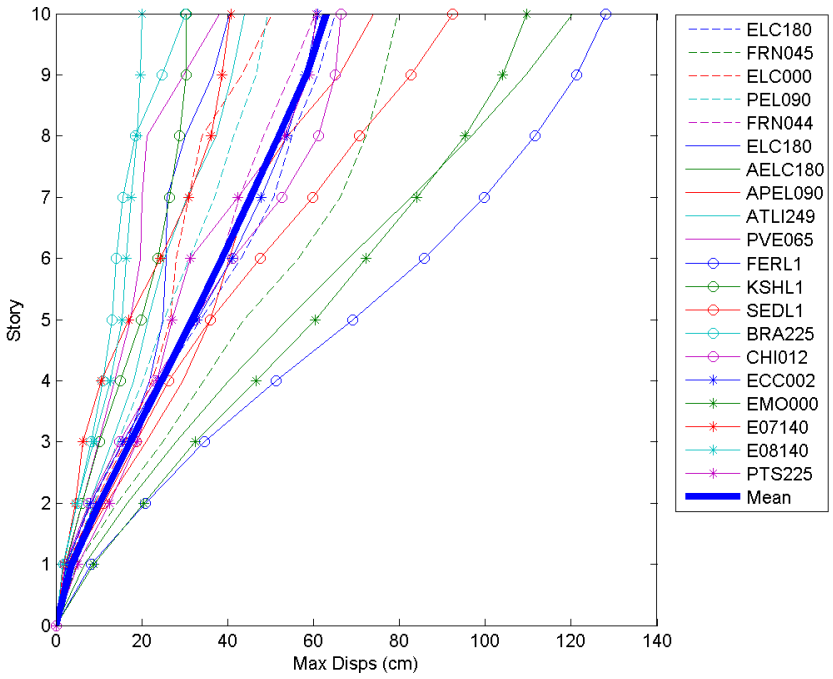

Figure 5.28: Storey maximum Displacements for SMRF under the MCE

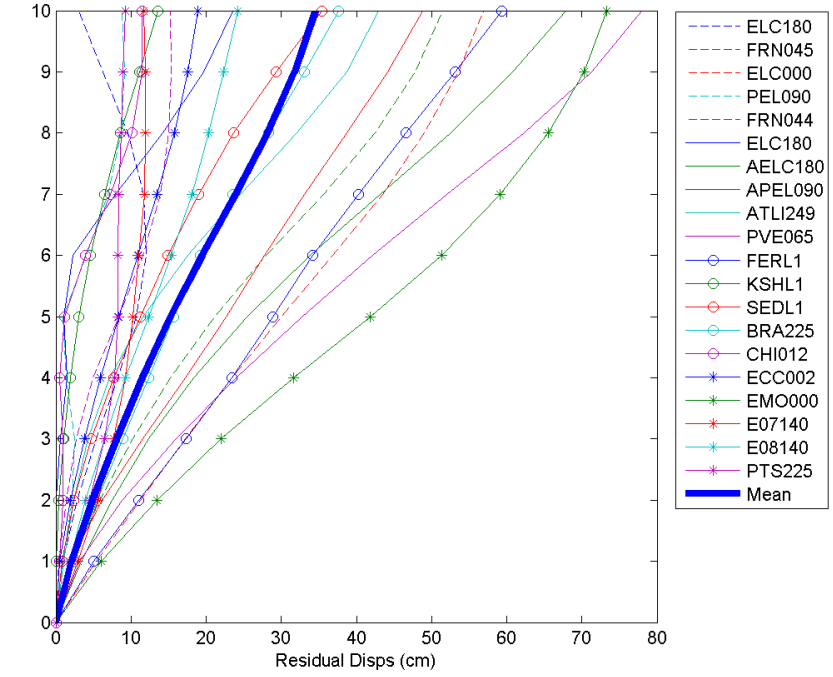

Figure 5.29: Storey residual displacements for SMRF under the MCE

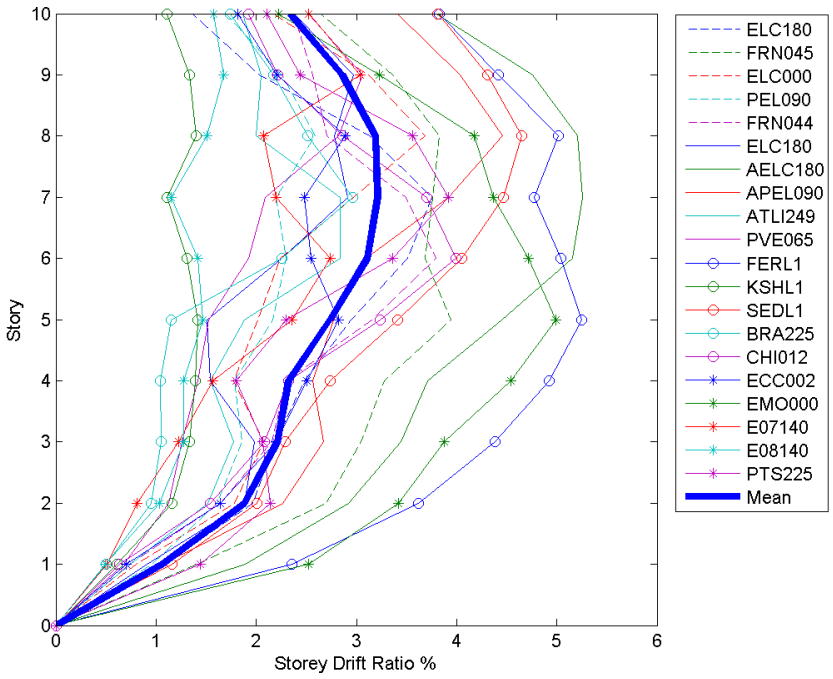

Figure 5.30: Storey Drift Ratios for SMRF under MCE

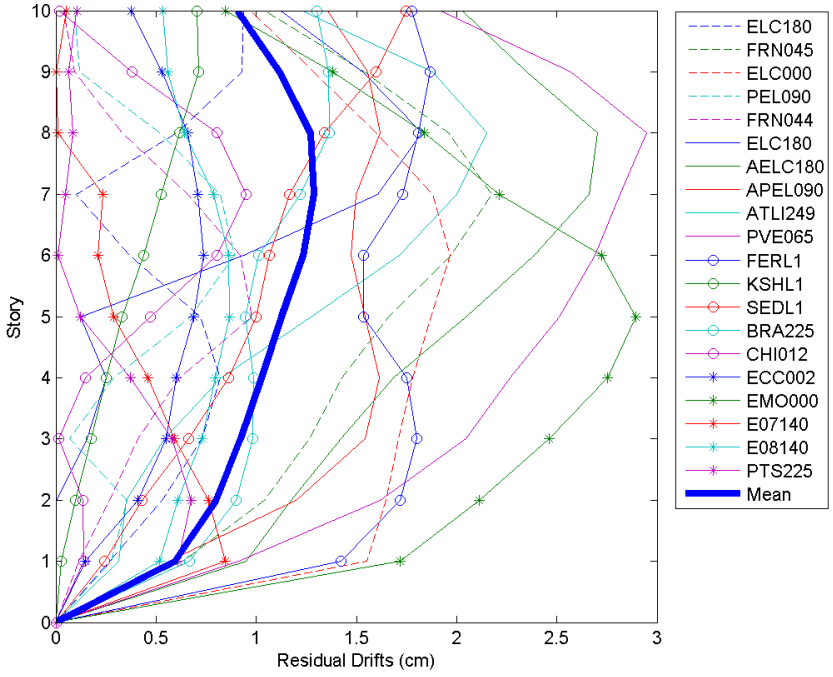

Figure 5.31: Storey residual drifts for SMRF under the MCE

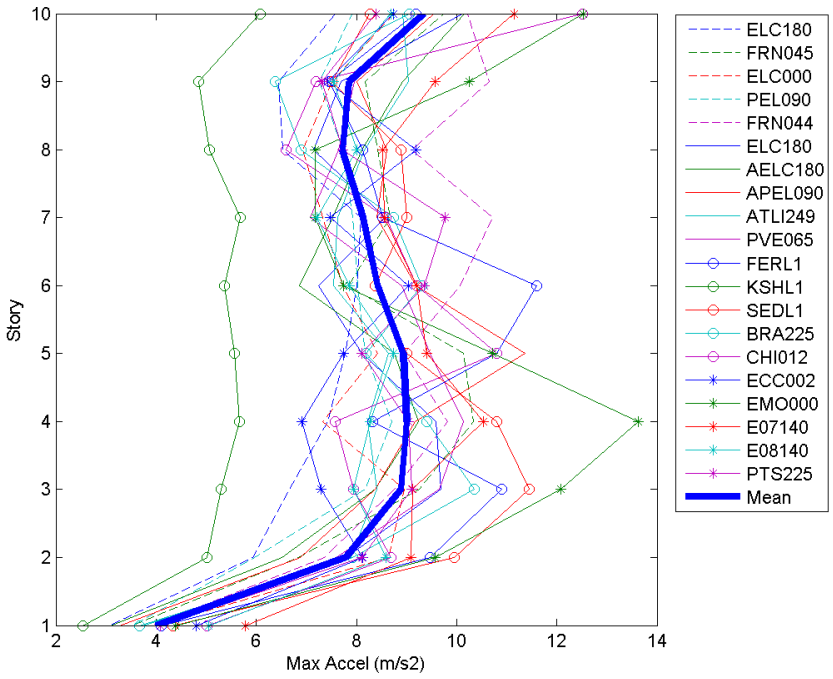

Figure 5.32: Storey maximum accelerations for SMRF under the MCE

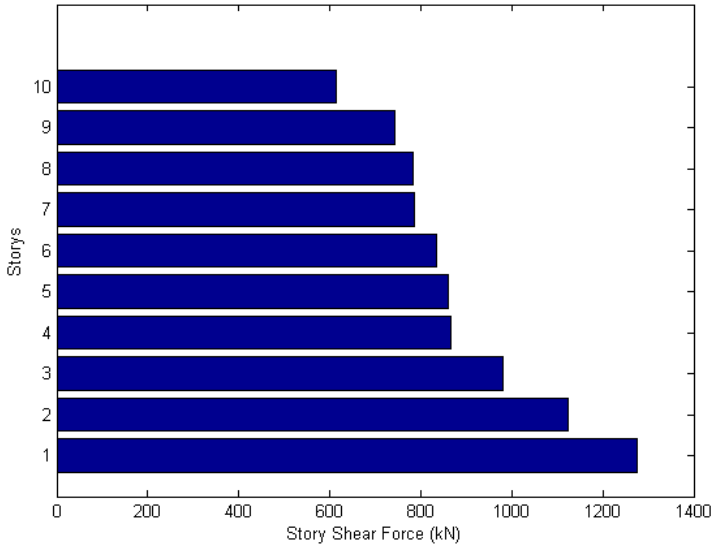

Figure 5.33: Mean Storey shear forces for SMRF under the MCE

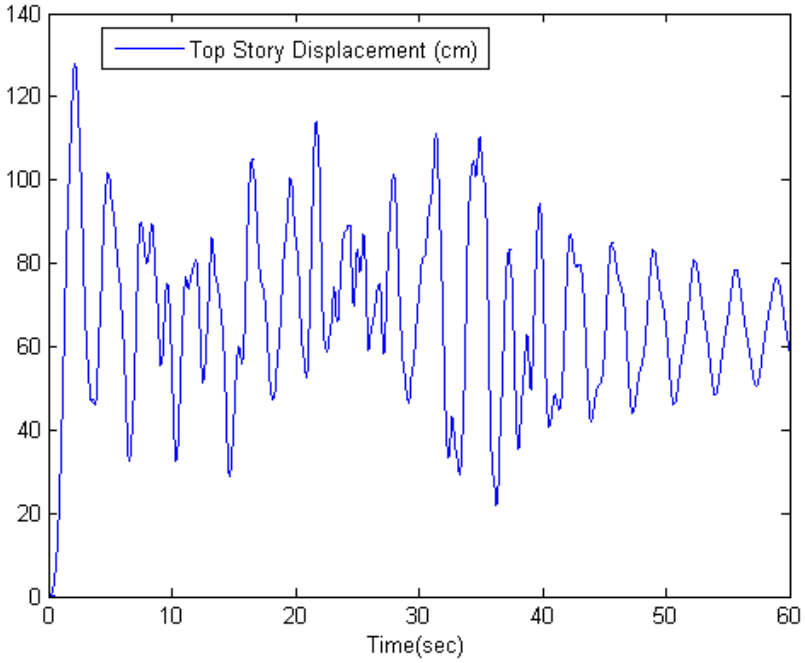

Figure 5.34: Roof displacement time history under the $Tabas - Iran - FER - L1$ grounnd motion scaled to MCE

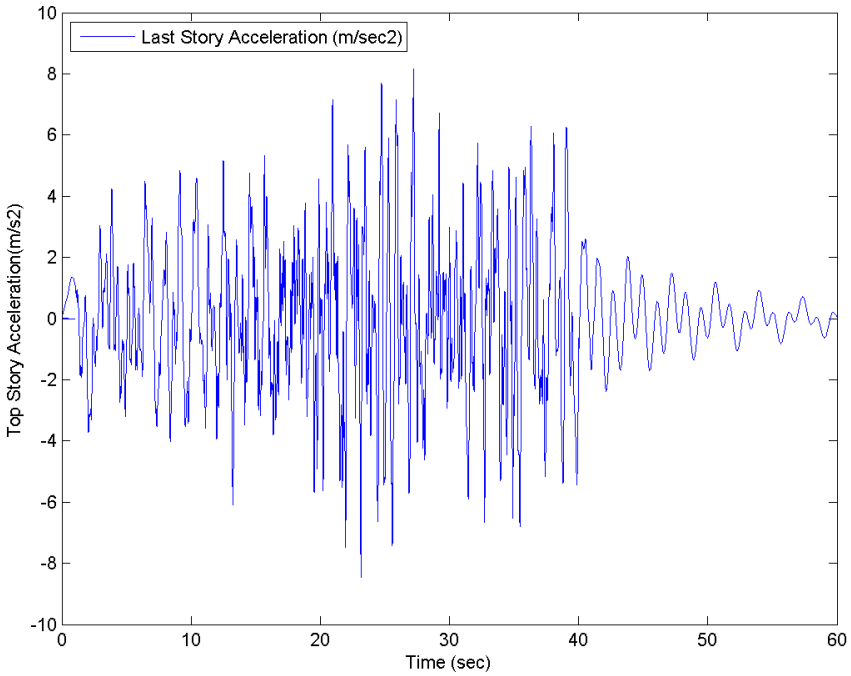

Figure 5.35: Roof acceleration time history under the $Tabas - Iran - FER - L1$ ground motion scaled to MCE

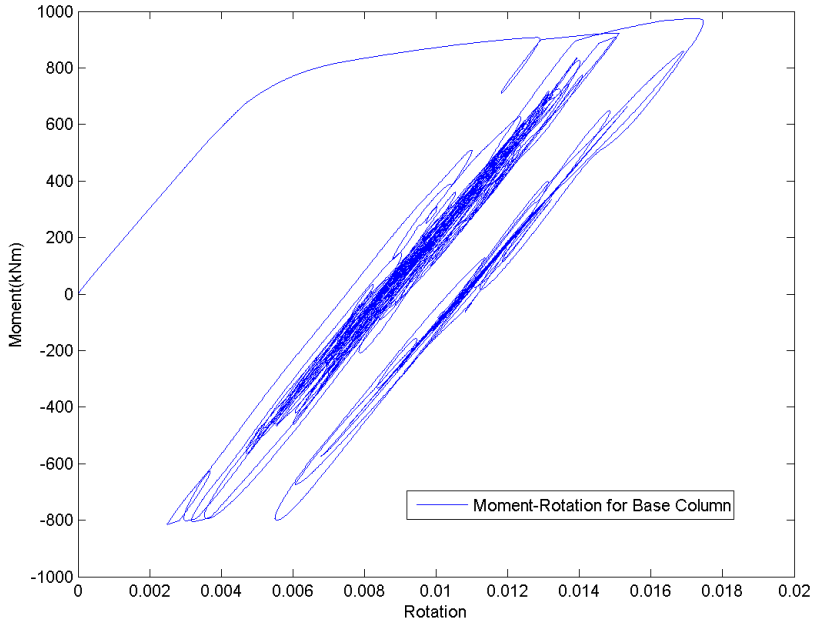

Figure 5.36: Moment-Rotation relationship for 1st story column of SMRF under the $Tabas - Iran - FER - L1$ ground motion scaled to MCE

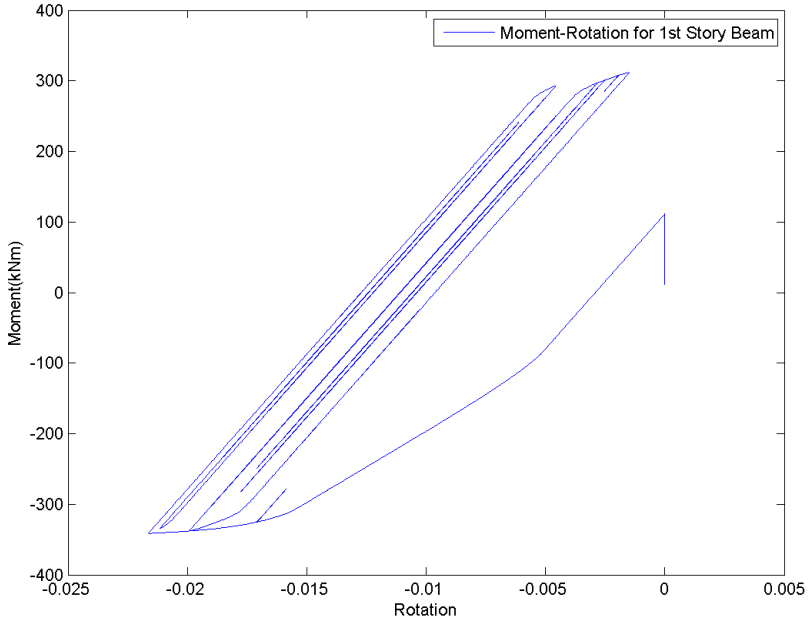

Figure 5.37: Moment-Rotation relationship for 1st story beam of SMRF under the $Tabas - Iran - FER - L1$ ground motion scaled to MCE

5.3.6 Earthquake Response of steel Moment Resisting Frame with Elastomeric Dampers

While energy dissipation systems have the ability to lead to lateral drift reduction, this is not always the case for the columns axial forces [10] and the base shear of the structure. If the dissipation devices are attached to moment frames in chevron brace form, then this changes the building's configuration from moment resisting frame to braced frame configuration, resulting in changes at the load paths as well. Therefore, even though the retrofitted structure aims not to highly alter the dynamic characteristics of the prototype building, it should be evaluated not as an enhanced and better version of the prototype structure but as a new and different structure. Of course, if this "new" structure fails to achieve the target performance level, then a different type of retrofitting procedure is required. Applying the retrofitting procedure of section 5.3.4, and testing the DMRF under the same ground motions under which the MRF was tested, evaluation of the effectiveness of the EDs can be determined.

Figures 5.38 and 5.40 show the effect of the EDs on the maximum displacements and on the corresponding residual displacements. It can be observed that the maximum displacements were decreased dramatically with a maximum and a mean value of 35 and 29 cm respectively. EDs were able to minimize residual displacements, resulting in a mean value of 2.5 cm, and a maximum value of 13.5 cm. Furthermore, Figure 5.39 shows the large storey drift reduction from 3.7% to 1.48% for the maximum values, and from 2% to 1.1% for the mean values. Therefore, the DMRF complies with the target performance criteria, with respect to the lateral drift for the majority of the ground motions (the target performance criteria was to achieve interstorey drifts from 0.7-1.3%). EDs had also huge effect on the reduction of the residual displacements (Figure 5.41).

Accelerations (Figure 5.42) did not follow the same rate of decrease, as storey displacements did, but a noticeable mitigation was observed. A comparison of the maximum storey shear forces between the MRF and DMRF under the DBE is also presented in Figure 5.43, where a slight reduction is observed in every floor. In

order for evaluation of the influence of the EDs on the time history response of the DMRF to become more clear, Figures 5.44 and 5.45 show both the time history response of the MRF and DMRF under the $Tabas - Iran - FER - L1$ ground motion scaled to DBE level, where it can be clearly seen that the addition of the EDs led to large deformation reductions and more moderate accelerations reductions at the top storey of the building. Regarding the moment rotation relationship for the same beam and column evaluated in MRF case, Figures 5.46 and 5.47 show the EDs effect on both of them. A plastic hinge was not created in the column, which remained completely linear in the DMRF, in contrast with the MRF case. In the case of the beam, a plastic hinge was not avoided, but the the plastic rotations, along with the total energy absorbed by the element were greatly reduced. Regarding the dampers hysteretic response, Figure 5.48 shows that the initial design assumption of a maximum elastomer deformation of 35 mm has been satisfied as well.

It can be concluded that EDs enhanced the seismic behaviour of the prototype frame, decreasing both the displacements, accelerations, shear forces, and structural elements seismic demands leading the structure to comply with all the target performance criteria which had been set at the beginning of the analysis, and perform very close to the Immediate Occupancy performance level. Plastic hinges were not created to any of the columns, including those of the 1st floor, while only a few beams, especially on the first 2-3 floors exhibited non linearities.

However, the shear forces exhibited the smallest reductions comparing with the all the other aforementioned parameters. Similar problems or even worse have been noted in case of metallic and friction dampers as well [114]. This is mainly due to two reasons: a) the nature of the dissipation mechanism of elastomeric dampers is based on the forces being extracted from the dampers and transferred to the rest of the structure through the diagonal braces and eventually creating additional shear forces to each storey, and b) the non-linear nature of the materials used in the analyses sometimes leads to large decreases of displacements, which can be reduced to a level close to the yield point of the structural elements; however the forces are still going to be near the yield level.

It can be also noted that some ground motions which caused high responses in the

DMRF, caused only moderate structural response in the SMRF. Even though the initial target was to alter the dynamic properties of the original frame as less as possible, the addition of the EDs led to a slight reduction of the natural period. This caused some ground motions which have very high frequency peaks on these specific periods to amplify the response of the DMRF.

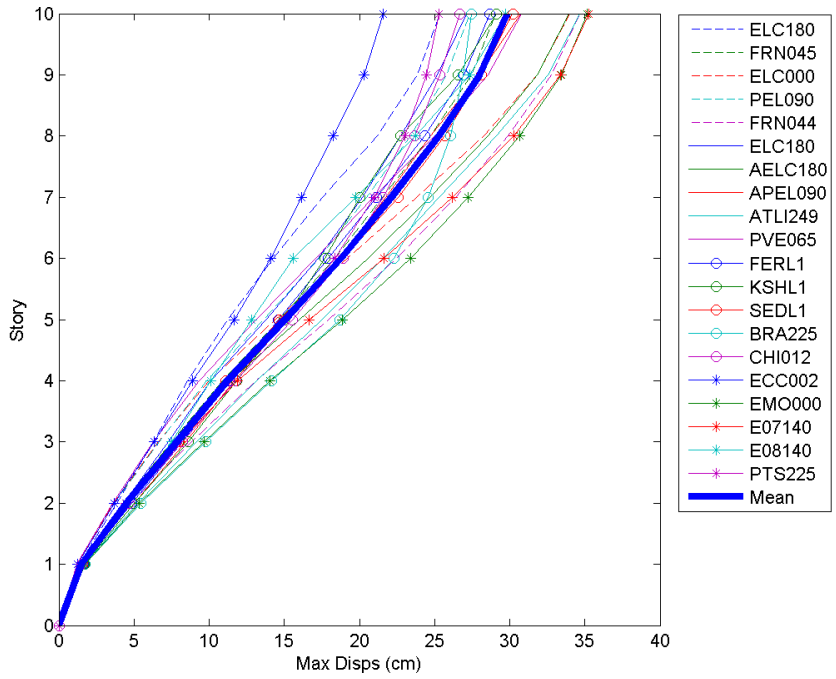

Figure 5.38: Storey maximum Displacements for DMRF under the DBE

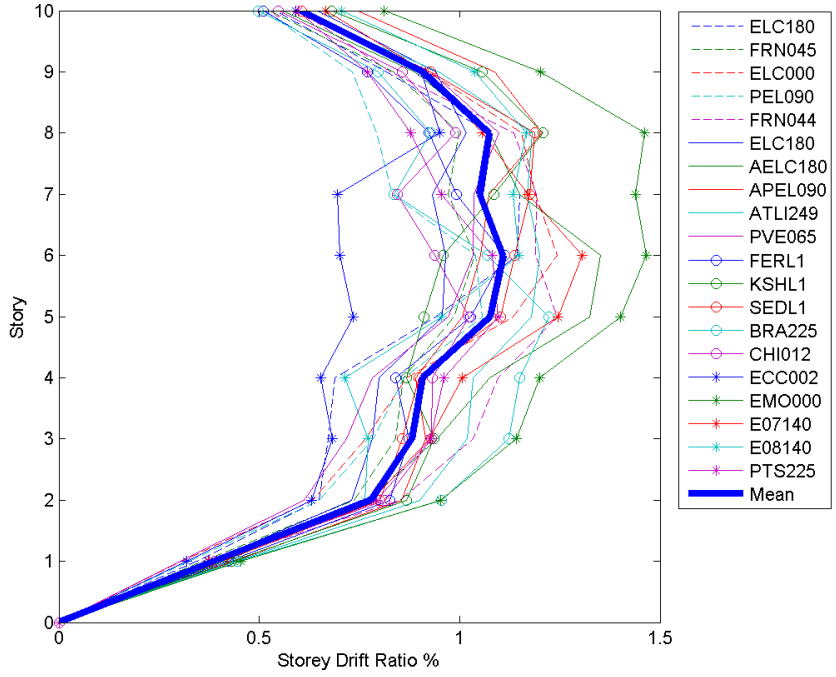

Figure 5.39: Storey Drift Ratios for DMRF under DBE

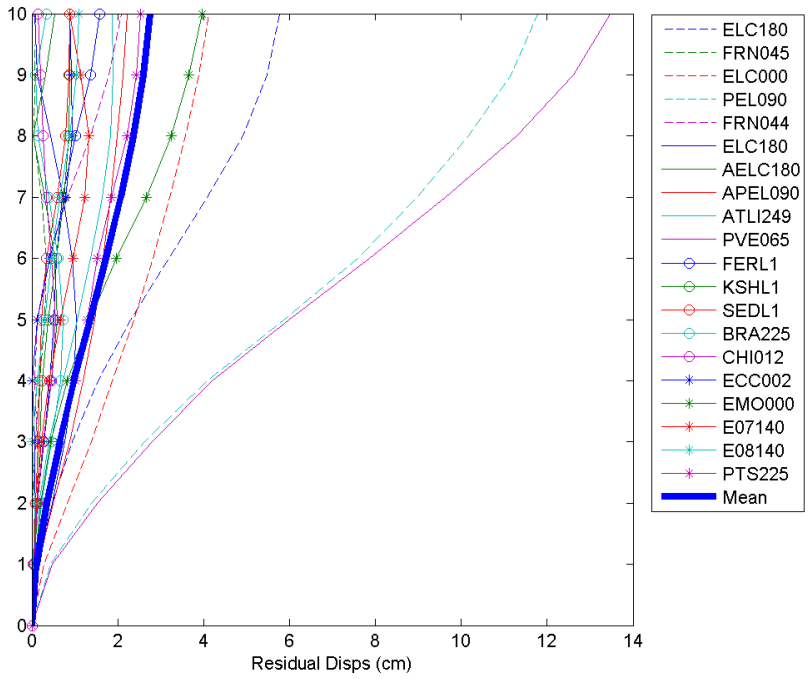

Figure 5.40: Storey residual displacements for DMRF under the DBE

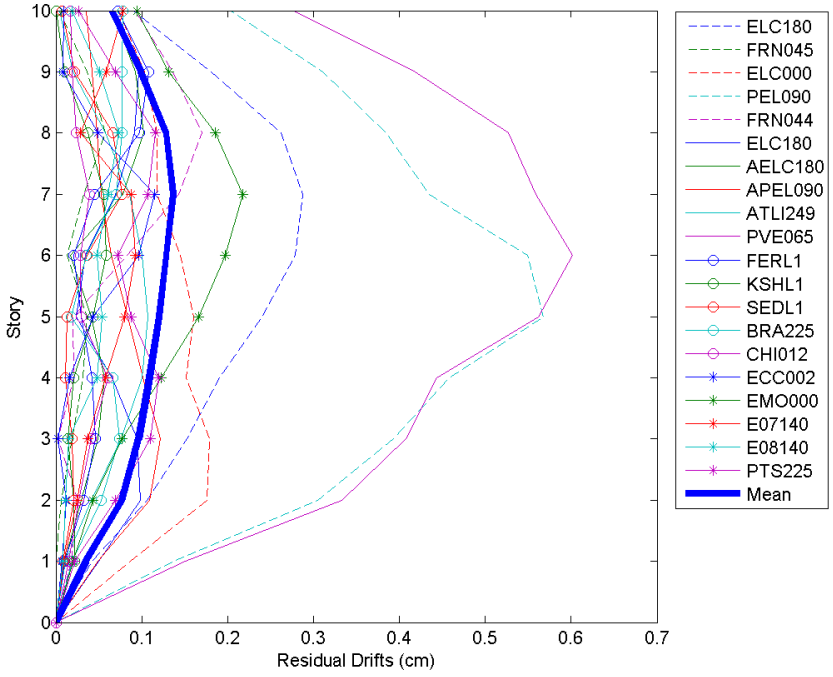

Figure 5.41: Storey residual drifts for DMRF under the DBE

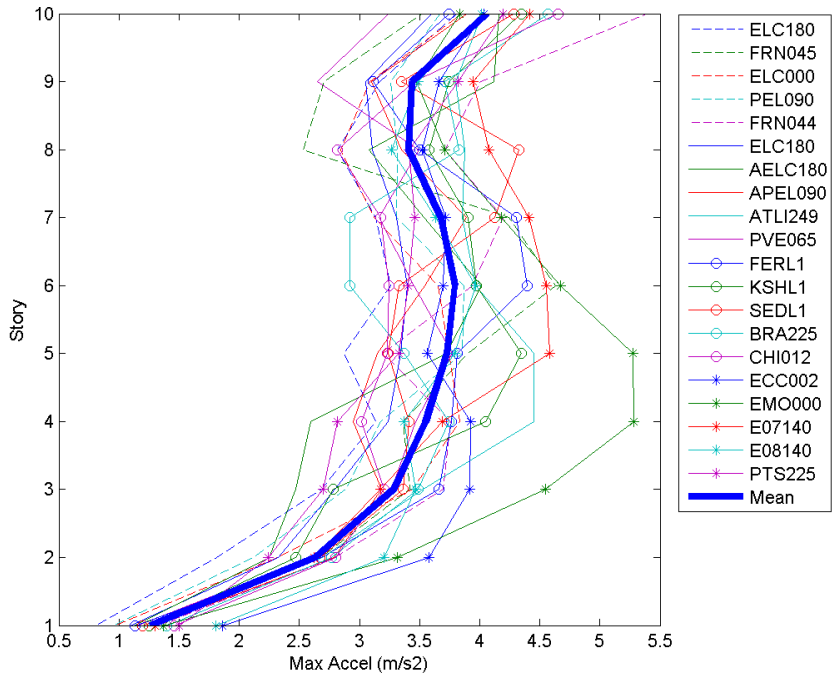

Figure 5.42: Storey maximum accelerations for DMRF under the DBE

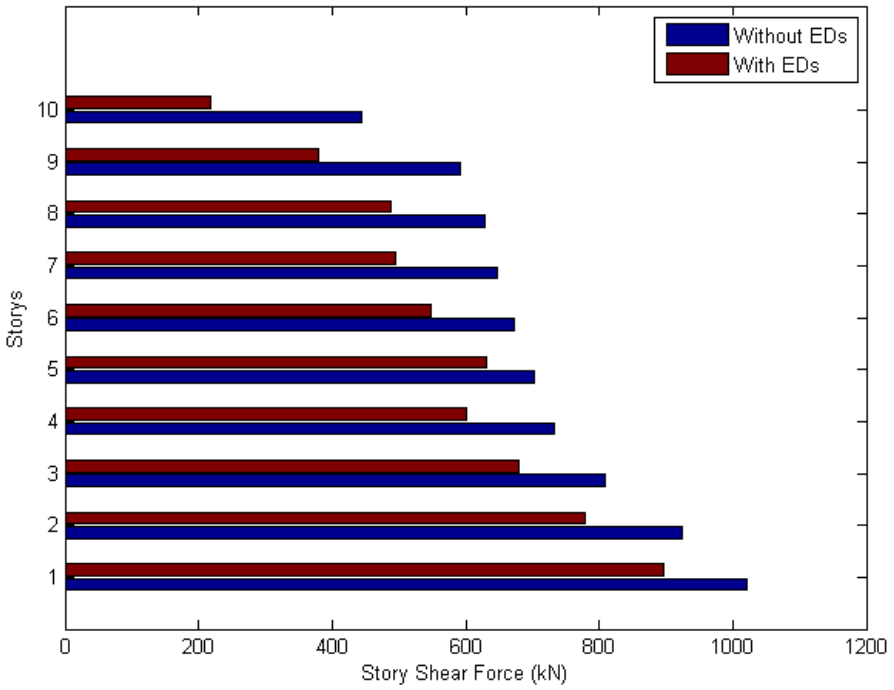

Figure 5.43: Mean Storey Shear Forces for DMRF and SMRF under the DBE

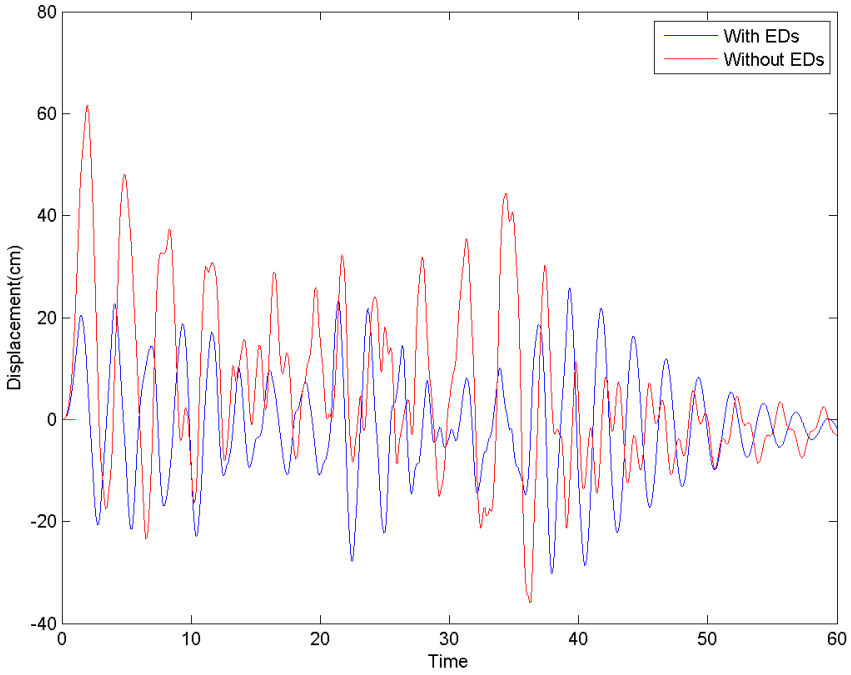

Figure 5.44: Top Storey Displacement comparison for the SMRF and DMRF under DBE

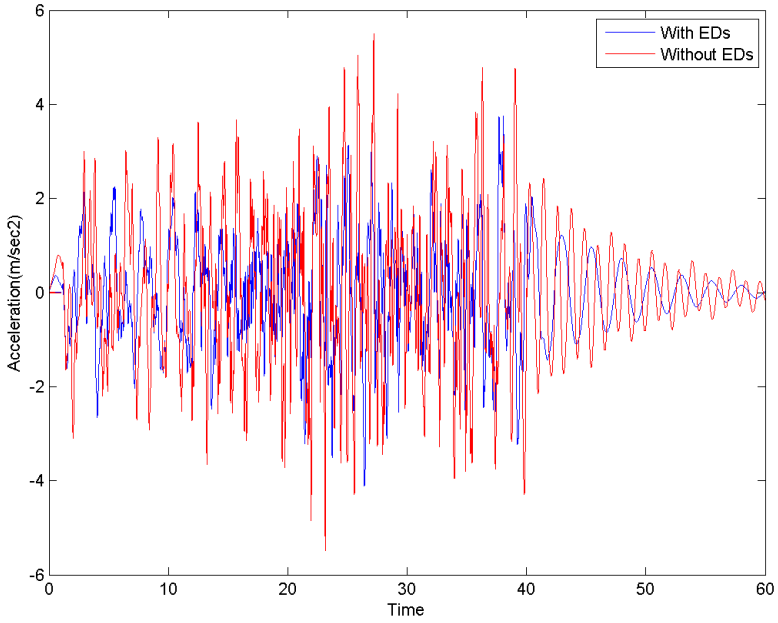

Figure 5.45: Top Storey Acceleration comparison for the SMRF and DMRF under DBE

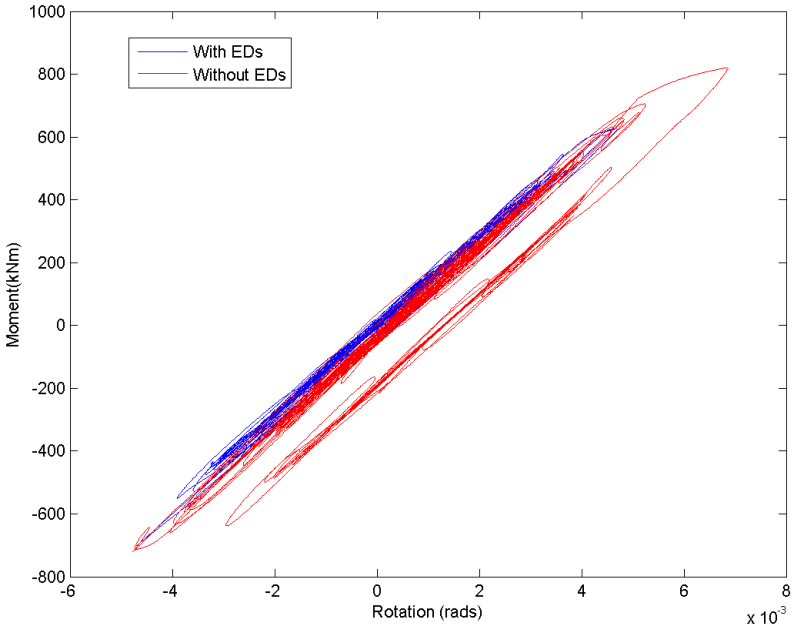

Figure 5.46: Moment Rotation relationship for base column under the$Tabas_Iran - FER - L1$ ground motion scaled to DBE

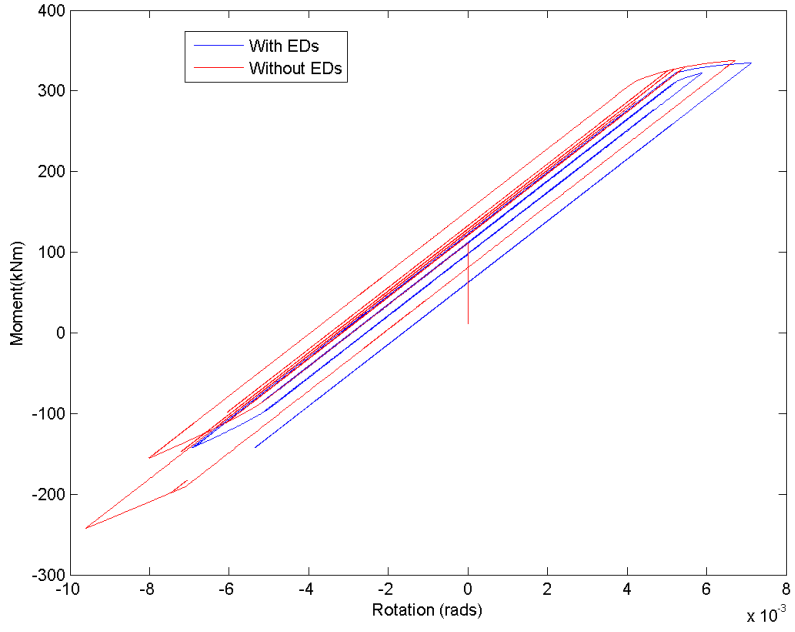

Figure 5.47: Moment Rotation relationship for base beam under the$Tabas_Iran - FER - L1$ ground motion scaled to DBE

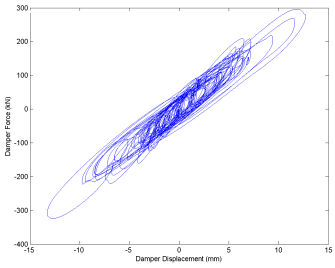

(a) 1st floor-DBE

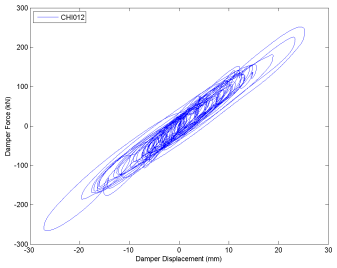

(b) 2nd-DBE

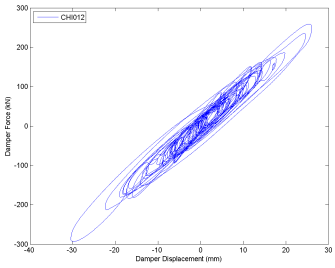

(c) 3rd floor-DBE

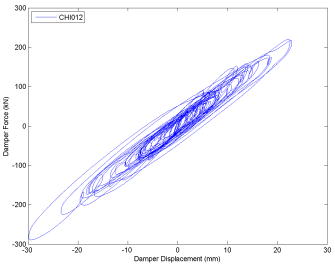

(d) 4th floor-DBE

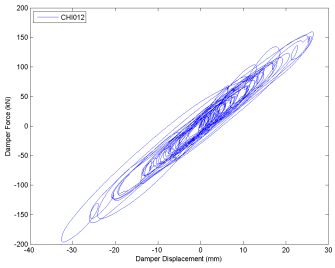

(e) 5th floor-DBE

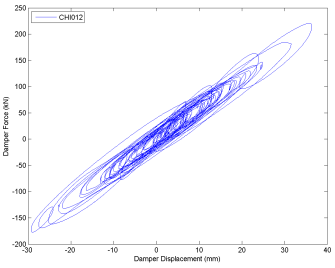

(f) 6th floor-DBE

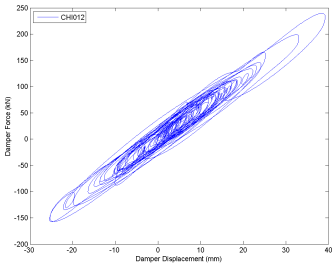

(g) 7th floor-DBE

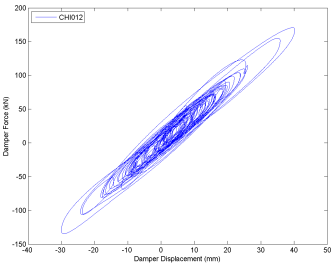

(h) 8th floor-DBE

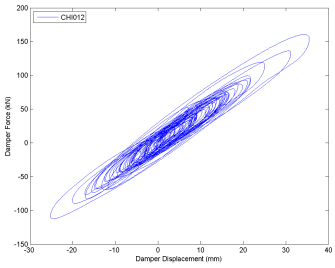

(i) 9th floor-DBE

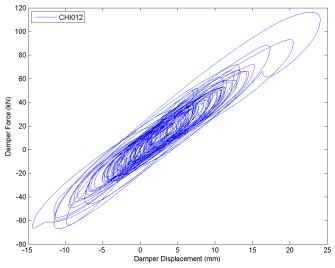

(j) 10th floor-DBE

Figure 5.48: ED hysteretic response for each floor under DBE

Regarding, the effect of the EDs under the MCE, Figure 5.49 presents the corresponding displacements, which were highly decreased, dropping from 127 cm to 56 cm and from 62 cm to 41 cm for the maximum and mean values respectively. The residual displacements (Figure 5.50) were highly reduced as well; a fact which validates the EDs effectiveness, since a total reduction of 60.7% and 83.1% for the maximum and mean value was achieved, leading the structure to behave slightly above its linear limit. Figures 5.51 and 5.52 shows the effect of the EDs on the inter storey drift ratios, where a maximum value of 2.4% and a mean value of 1.6% was achieved, leading the frame to achieve lateral drifts much smaller than the ones proposed for the Life Safety performance level. Similar reductions were observed in terms of residual displacements, where exceptional structural behaviour was observed.

Regarding the accelerations (Figure 5.53), EDs seem to be more efficient, when the frame is tested under MCE rather than DBE, since a reduction of 36.2% and 30.8% for maximum and mean values was achieved. The maximum shear forces obtained from the analyses were again compared here, under the MCE, (Figure 5.54). However, they were found to be approximately the same (1% decrease at the 1st floor). In addition, time histories of roof displacements and accelerations under the $Tabas - Iran - FER - L1$ ground motion scaled to the MCE are presented in Figures 5.55 and 5.56, according to which EDs led the total displacements not only to highly decrease but also the residual displacements to be almost eliminated. Regarding the accelerations, again they did not follow the same reduction rate as the displacements. The comparison of the relationship of the same beam and column with the corresponding rotation for the MRF and DMRF under the MCE is shown at Figures 5.57 and 5.58. It can be seen that even though plastic hinges were not avoided for either of these two elements, plastic rotations were greatly reduced. Finally, the dampers' hysteretic response under MCE is shown at Figure 5.59.

The DMRF behaved satisfactorily under the MCE hazard level. Actually, it behaved better even comparing with the MRF seismic performance under the DBE.

Another important parameter, as already mentioned, is the evaluation of the axial forces acting at the columns, which were anticipated to be increased. Indeed,

table 5.9 shows that the axial forces of the left corner base column of the second bay (which was found to be the most critical) increased by 28% and 40% under DBE and MCE respectively. However, as Figures 5.46 and 5.57 show, even though the axial forces were increased, at the same time the total behaviour of the element was highly improved, due to decreased rotations and displacements. Hence, it can be concluded that all the target performance criteria can be achieved under the DBE hazard level even by using lighter and weaker column sections.

The main target in the case of frame tested under MCE, as in the conventional design of buildings, is the creation of plastic hinges at the bottom joints of the base columns, and at the ends of the beams, leading to a ductile seismic performance, and not a brittle collapse. This target has been achieved for this frame, and therefore all the target performance criteria have been achieved. It can also be observed that EDs' effectiveness increases when the intensity of the ground motion increases. Finally, the total response of MRF and DMRF under both DBE and MCE can be summarized at Tables 5.8 and 5.9 with respect to maximum and mean values of the parameters examined earlier.

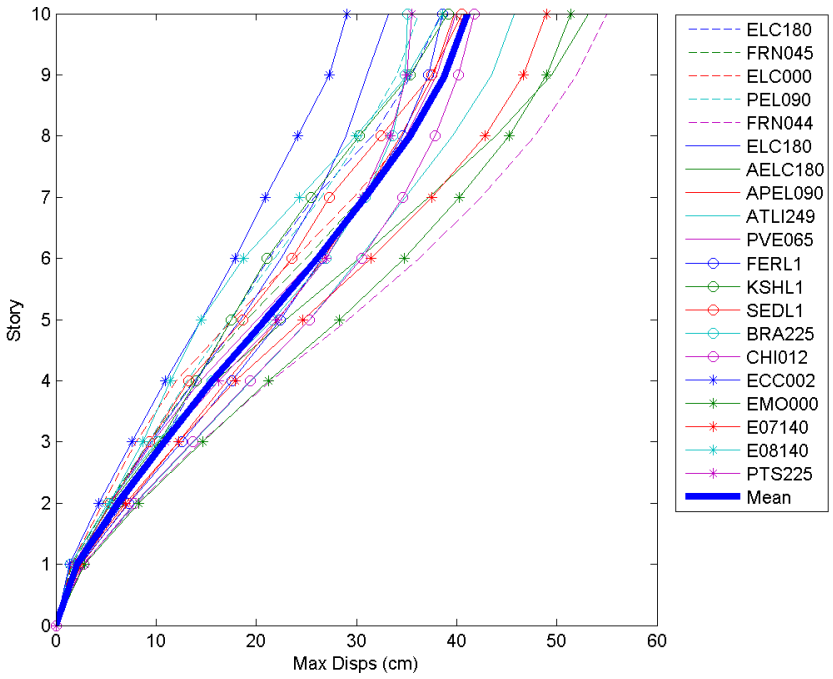

Figure 5.49: Storey maximum Displacements for DMRF under the MCE

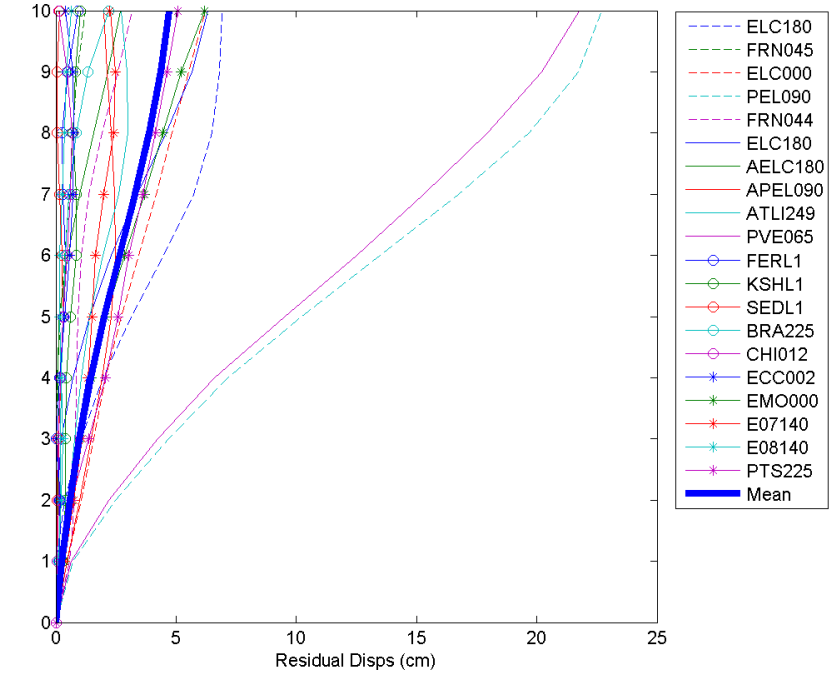

Figure 5.50: Storey residual displacements for DMRF under the MCE

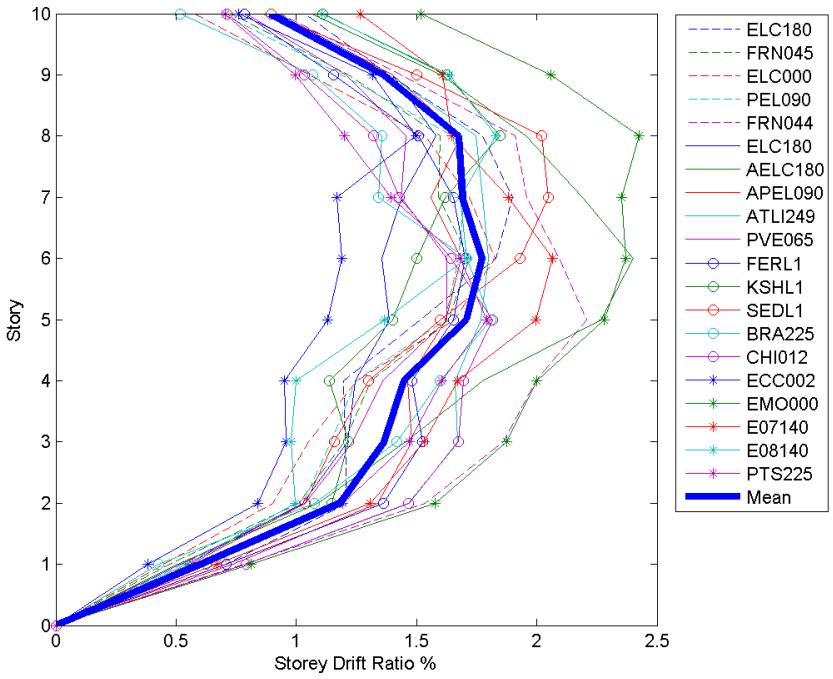

Figure 5.51: Storey Drift Ratios for DMRF under MCE

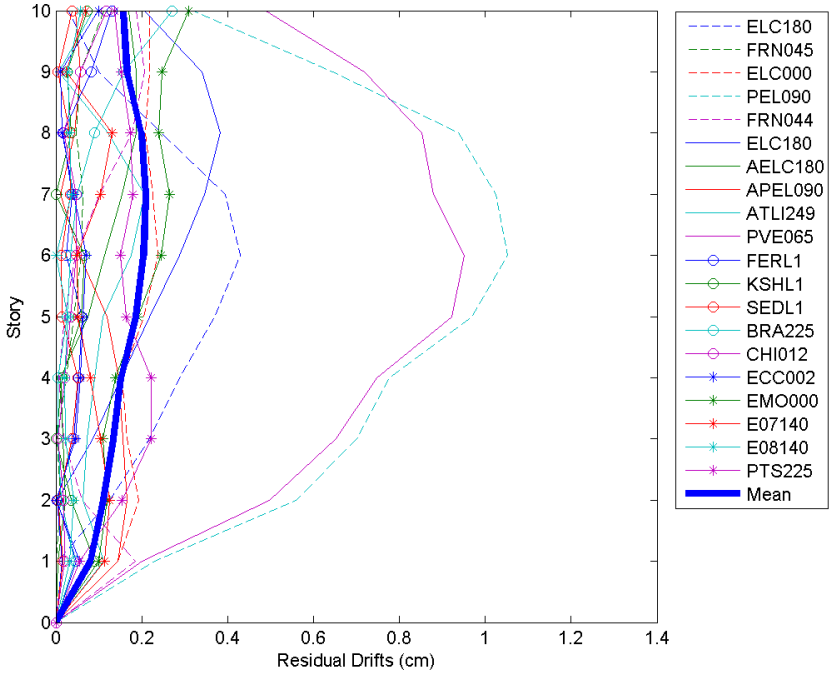

Figure 5.52: Storey residual drifts for DMRF under the MCE

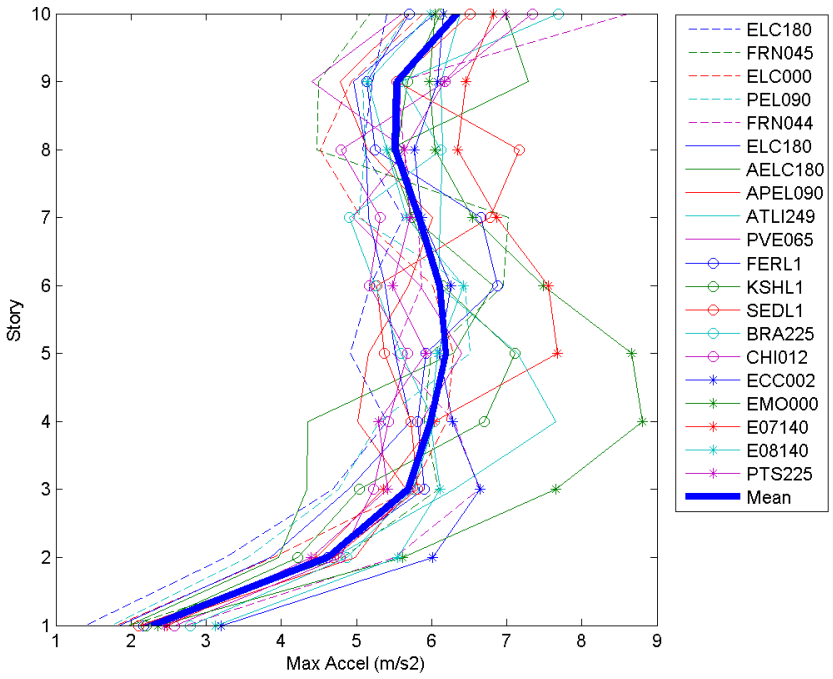

Figure 5.53: Storey maximum accelerations for DMRF under the MCE

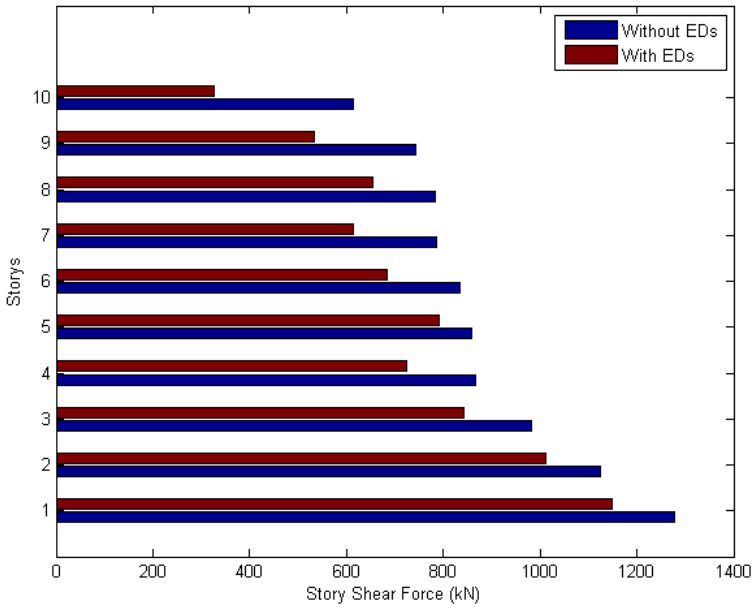

Figure 5.54: Mean Storey Shear Forces for DMRF and SMRF under the MCE

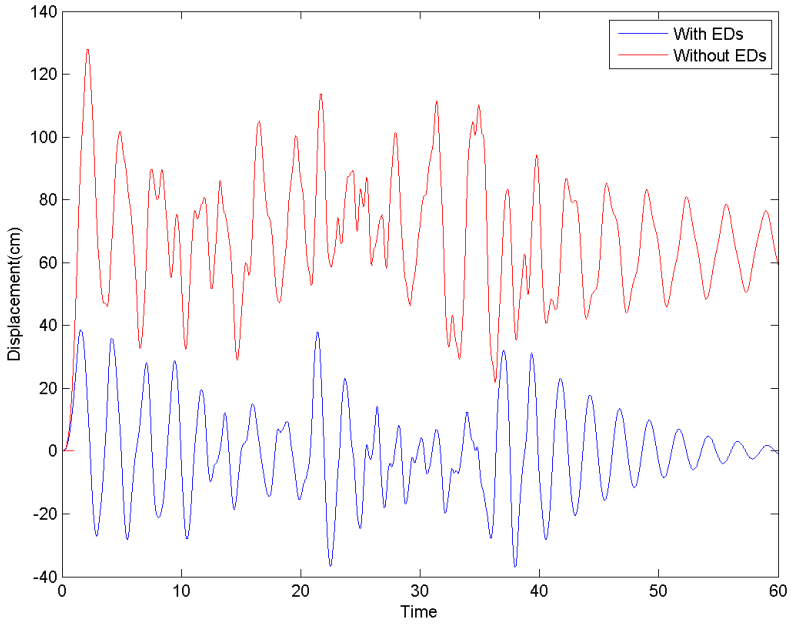

Figure 5.55: Top Storey Displacement comparison for the SMRF and DMRF under MCE

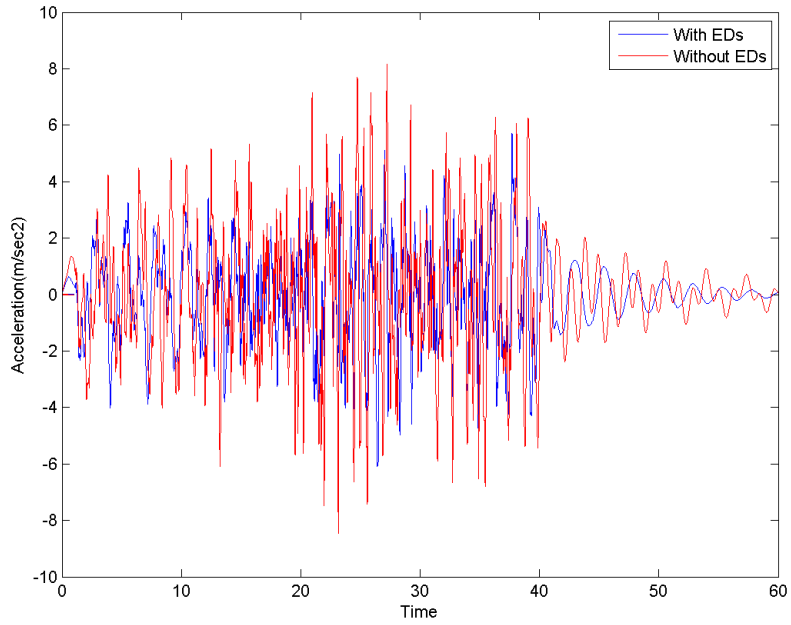

Figure 5.56: Top Storey Acceleration comparison for the SMRF and DMRF under MCE

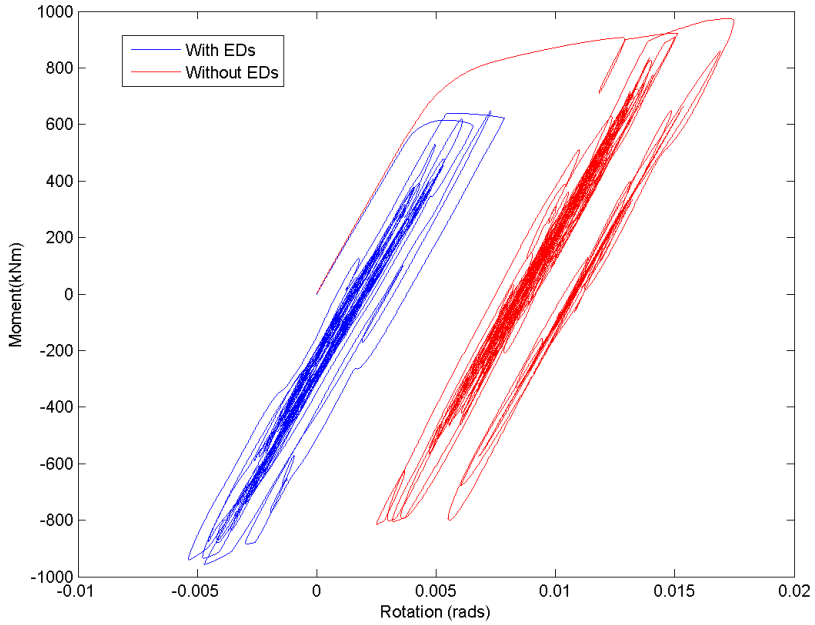

Figure 5.57: Moment Rotation relationship for base column under the$Tabas_Iran - FER - L1$ ground motion scaled to MCE

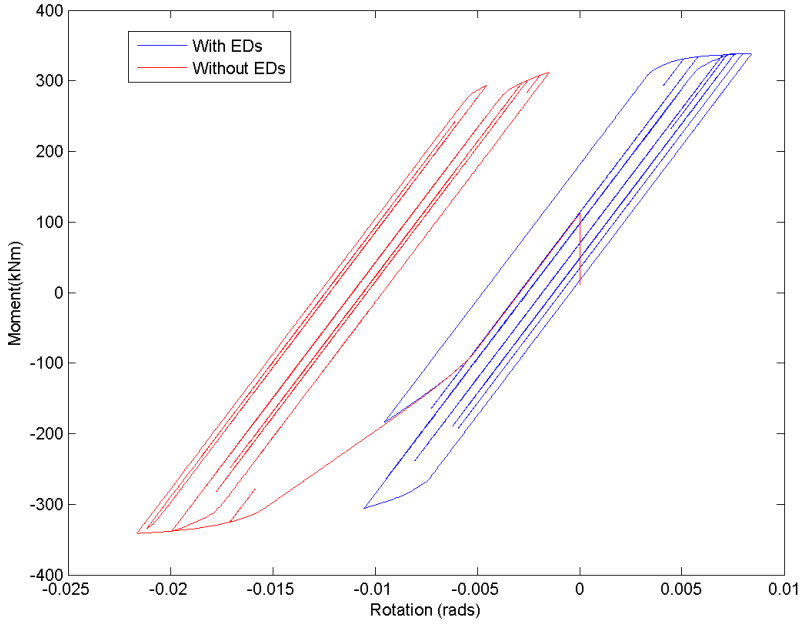

Figure 5.58: Moment Rotation relationship for base beam under the$Tabas_Iran - FER - L1$ ground motion scaled to MCE

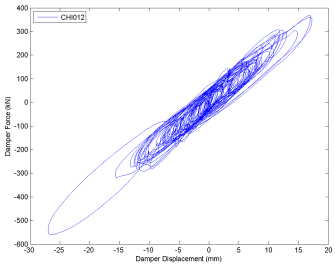

(a) 1st floor-MCE

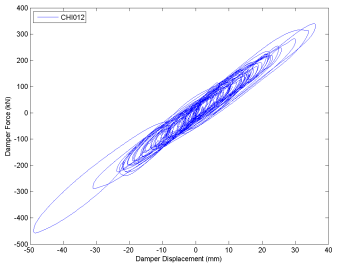

(b) 2nd floor - MCE

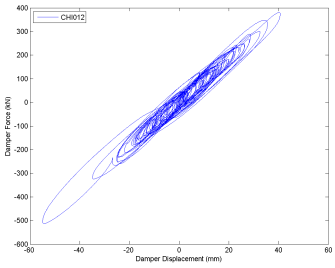

(c) 3rd floor-MCE

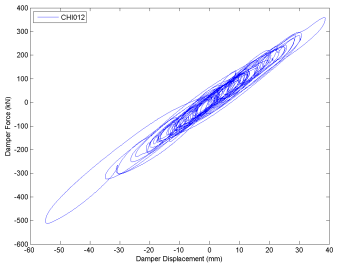

(d) 4th floor-MCE

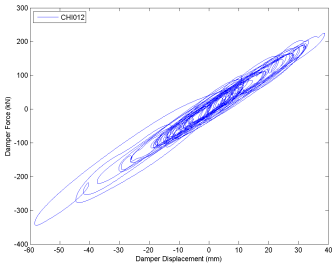

(e) 5th floor-MCE

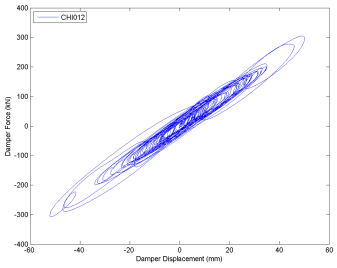

(f) 6th floor-MCE

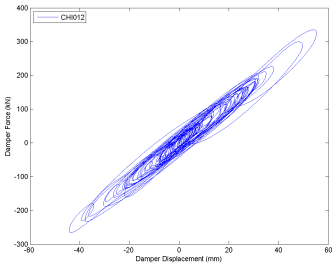

(g) 7th floor-MCE

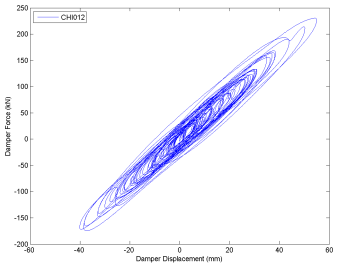

(h) 8th floor-MCE

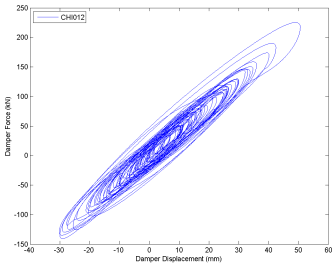

(i) 9th floor-MCE

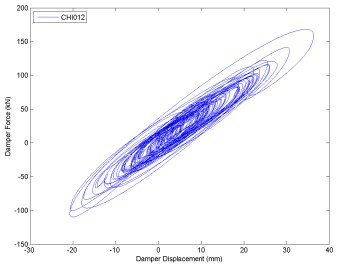

(j) 10th floor-MCE

Figure 5.59: ED hysteretic response for each floor under MCE

Table 5.8: Comparison of mean response of SMRF and DMRF under DBE and MCE

Evaluation Parameters	Performance Criteria	DBE			Performance Criteria	MCE		
		Without Eds	With Eds	Difference (%)		Without Eds	With Eds	Difference (%)
Roof Displacement (cm)	-	42	29	-30.95	-	62	41	-33.9
Residual Roof Displacement (cm)	-	12	2.6	-78.33	-	34	4.8	-85.9
Roof Drift (%)	-	1.2	0.67	-44.17	-	1.71	1.17	-31.6
InterStorey Drift (%)	**0.7-1.3**	2	1.1	-45.00	2.3-2.7	3.1	1.7	-45.2
Residual InterStorey Drift (%)	**0.2-0.5**	0.6	0.13	-78.33	0.5-1.0	1.3	0.22	-83.1
Base Shear (kN)	-	1020	915	-10.3	-	1276	1170	-8.3
Roof Acceleration (m/sec2)	-	5.5	4	-27.27	-	9.1	6.3	-30.8
Beam Plastic Rotation (Rad)	-	0.0086	0.0015	-82.56	-	0.0104	0.0076	-26.9
Column Plastic Rotation (Rad)	-	0.006	0.0002	-97.43	-	0.008	0.0023	-71.3
Column Axial Force (kN)	-	2052	2631	28.22	-	2103	2951	40.3

Table 5.9: Comparison of maximum response of SMRF and DMRF under DBE and MCE

Evaluation Parameters	Performance Criteria	DBE			Performance Criteria	MCE		
		Without Eds	With Eds	Difference (%)		Without Eds	With Eds	Difference (%)
Roof Displacement (cm)	-	79	35	-55.70	-	127	56	-55.9
Residual Roof Displacement (cm)	-	38	13.5	-64.47	-	77	23	-70.1
Roof Drift (%)	-	2.25	1	-55.56	-	3.6	1.6	-55.6
InterStorey Drift (%)	**0.7-1.3**	3.7	1.48	-60.00	2.3-2.7	5.1	2.4	-52.9
Residual InterStorey Drift (%)	**0.2-0.5**	1.8	0.6	-66.67	0.5-1.0	2.8	1.1	-60.7
Base Shear (kN)	-	1280	1180	-7.81	-	1449	1347	-7
Roof Acceleration (m/sec2)	-	6.7	5.5	-17.91	-	13.8	8.8	-36.2
Beam Plastic Rotation (Rad)	-	0.0124	0.0044	-64.52	-	0.0256	0.0137	-46.5
Column Plastic Rotation (Rad)	-	0.0094	0.0006	-93.73	-	0.0157	0.0048	-69.4
Column Axial Force (kN)	-	2150	2792	29.85	-	2171	3124	43.9

5.4 Effect of temperature

All the previous analyses were based on an ambient temperature of 20°C. In order to evaluate the effect of temperature, the worst case scenario will be taken into account in this section. Hence, the analysis of the DMRF will be shown here, assuming an ambient temperature of 35°C, where the decrease of the dampers' efficiency is greatest, according to Chapters 3 and 4. Since, the overall target of this section is only to simply illustrate the temperature's effect, and not to carry out design of the DMRF with different temperatures, only the results of the modified El Centro (I-ELC180 component) will be presented here. In the case of a full design of a DMRF, a parametric analysis should be carried out, and the worst case scenario should be taken into account for the design of the dampers in order for the DMRF to cope under the target performance criteria.

The adjusted proposed proposed model (see Chapter 4), with $\gamma = 0.82$ will be considered in this section. The analysis carried out here was focused on the DBE

level, since this hazard level formed the basis for the design of the EDs. The results were compared with the ones from the initial analysis carried out at 20°C. Figure 5.60 shows the top storey displacement under the modified El Centro (I-ELC180 component) ground motion for both 20°C, and 35°C. It can be observed a slightly better behaviour, but not significant, since the displacements' time histories almost coincide for both temperatures. This is the case for both top storey accelerations (Figure 5.61), and storey shear forces (Figure 5.62), where the difference is negligible. However, this is not the case when it comes to the hysteretic behaviour of individual members, where the beams' plastic deformations were increased, as can be seen from Figure 5.63. Moreover, the first storey columns' hysteretic behaviour, was also affected by the alteration of ambient temperature. Figure 5.64, shows that the column exhibits minor plastic deformations at 35°C, as opposed to the corresponding moment-rotation relationship under 20°C, where the column remained elastic. Therefore, even though the overall behaviour of the structure with regard to inter storey displacements, accelerations, and shear forces was not highly affected, it can be concluded that even this slight temperature alteration led the DMRF to fail the target performance criteria (see section 5.3.1), even though the performance of the structure was highly enhanced. The temperature alteration also affected the EDs' hysteresis loops. Figure 5.65 shows this effect on the dampers implemented on the first floor, comparing the EDs' behaviour under both temperatures. It can be seen that the dampers seem to experience a stiffness degradation, as expected. The above results and conclusions can only be extracted for the DMRF behaviour under this specific ground motion, and can not be generalised as a design tool. It should also be noticed at this point, that the alteration of the ambient temperature from 20°C to 35°C led the dampers to become less stiff, and therefore the structure more flexible. This has an overall effect on the applied seismic loads on the DMRF, even though this change is not huge. Hence, even though the dampers are less stiff (or probably less effective), this does not necessary means that the structure's behaviour will worsen as well. Depending on the frequency content of the applied ground motion, the structure may even have improved dynamic performance. It can be then concluded that a detailed design procedure, similar to section 5.3.4 should

be carried out for every temperature, in order to design the dampers.

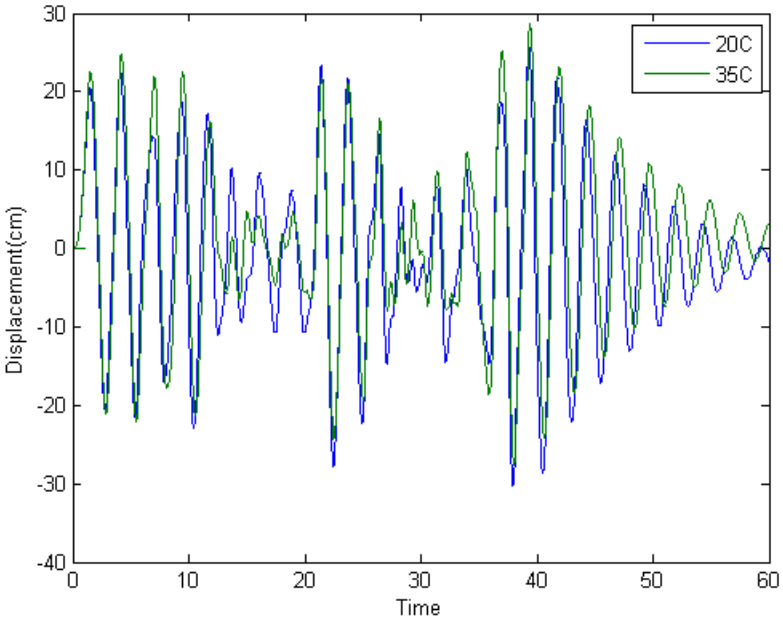

Figure 5.60: Top storey displacement (mm) - 35°C

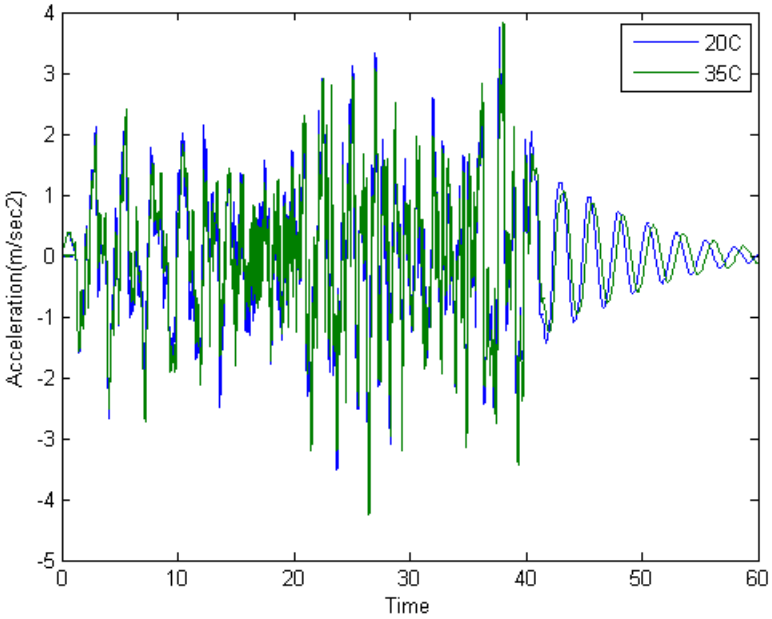

Figure 5.61: Top storey acceleration (m/sec^2) - 35°C

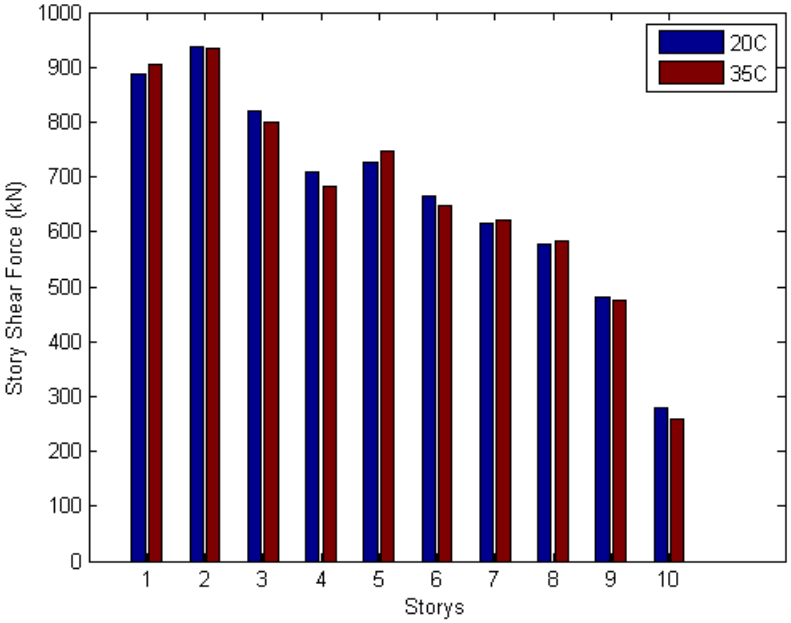

Figure 5.62: Storey shear forces - 35°C (kN)

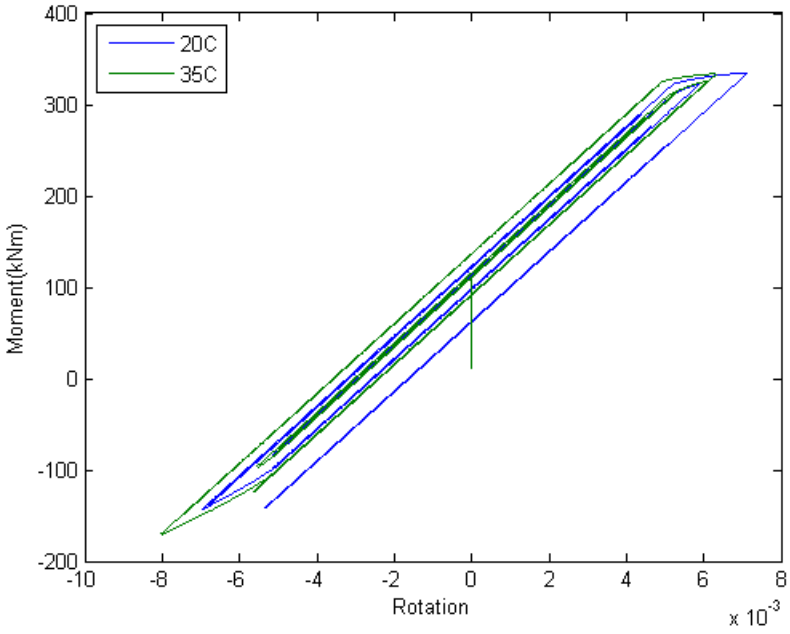

Figure 5.63: Top storey acceleration (m/sec^2)

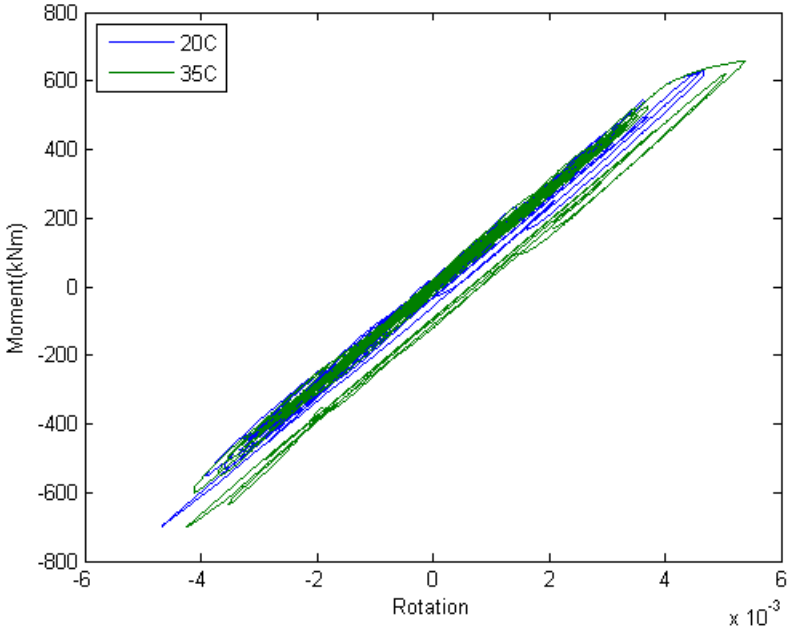

Figure 5.64: Top storey acceleration (m/sec^2)

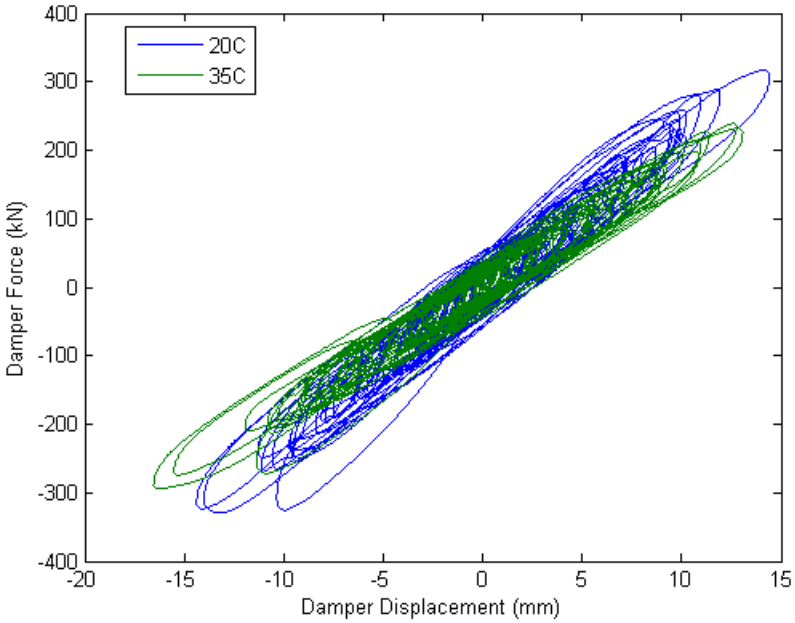

Figure 5.65: First storey ED's force-displacement relationship

5.5 Conclusions

The current chapter described the analysis of a 10 storey steel SMRF under both DBE and MCE hazard levels. 20 ground motions, scaled to these levels, were used to evaluate its seismic performance. EDs were then added at specific locations of the original frame, and the structure was tested again under the same seismic intensity, in order for the EDs efficiency to be determined. EDs were specifically designed, based on the characterization tests carried out at Dynamics Laboratory and the material model described in previous chapters, in order to add 10% of critical damping to the bare frame.

The results showed satisfying behaviour regarding the seismic response of the DMRF under both DBE, and MCE, while the initial performance criteria which had been set before the beginning of the analysis were all satisfied as well. The DMRF remained linear under most of the ground motions under the DBE, while the mean lateral drift was restricted to 1.1%, and the residual displacements were almost eliminated. The DMRF showed even more impressive results under the MCE, where the EDs efficiency increased since the displacements were larger. The mean inter storey drifts reduced by 45%, and the residual drifts by 83%. On the other hand, axial forces were found to be increased, which was anticipated, but at the same time the total behaviour of the members under axial loads were found to behave much more satisfactorily, where the plastic deformations were greatly reduced. Even though in this case, the increased axial forces do not cause any issues with regard with the capacity of the column, it is suggested that under certain circumstances columns may have to be strengthened.

A simple study of the temperature effect was also shown. Even though a full design process was not followed, but only illustration of results under a specific ground motion, the ambient temperature, did not seem to highly alter the dynamic behaviour of the DMRF. Individual structural members were found to be affected more, while the target performance criteria with regard to the behaviour of the individual members behaviour were slightly below the anticipated level. However, a more robust parametric analysis is recommended for the whole temperature range

of interest, similar to section 5.3.4.

Chapter 6

Real Time Substructure Test

6.1 Background

In seismically active regions, buildings are usually designed to exhibit a level of inelasticity under strong ground motions. Therefore, as mentioned earlier, by providing the structure the ability to dissipate energy, collapse should be avoided. In order to fully capture the inelastic structural performance experimental tests are often used. There are several experimental methods available for evaluating the inelastic performance of structures, or even isolated parts of the structure, such as dampers and bearings. Since many structures have their lowest natural frequency within the loading range of earthquakes (0-8 Hz), their damping and inertia characteristics may make a large contribution to their behaviour [18]. Some of the most well established experimental techniques are described in this section.

6.1.1 Shaking Tables

The shaking table test is one of the most realistic and reliable experimental methods for evaluating the inelastic seismic performance of structures. However, the size, weight and stiffness properties of the test structure are significantly limited by the capacity of available shaking tables [30]. Shaking table tests are carried out on a stiff platform, which is shaken in order to apply the appropriate base motion [140]. This way the ground motion is applied at the base, generating realistic inertia forces in every element of the structure. The motion of the shaking table is controlled

by servo-hydraulic actuators. The current trend is to provide active control in all six degrees of freedom, even when in some cases the motion in several directions is zero. The largest shaking table in the world is E-Defense, constructed by Japan's National Institute for Earth Science and Disaster Prevention (NIED), which is able to simulate at full scale the response of all types of structures to the full force of a magnitude-7 earthquake [123].

Regarding the control of the shaking table, accuracy requires knowledge of the system dynamics, which is generally not known prior to the test. Hence, an iterative tuning procedure can be followed, according to which a demand signal is adjusted, while the system remains in its linear phase, until the desired table motion is achieved. Therefore, the control of the table can be deternined. However, it is based on properties of the system being in its linear phase. The shaking table test is likely to generate non linearities in the test specimen during ground motions, and therefore the parameters of the controller cease to be optimal, and consequently the desired base motion will not be accurately reproduced. Adaptive controllers may be used to overcome this issue. The main concept behind this, is that the parameters of the controller are updated during the test, so they take into account any changes of the system's characteristics [117].

While the shaking table technique is the most reliable and able to produce the actual seismic forces to the structure, it is also very expensive while requiring state of the art testing facilities. In case of shaking tables where full scale models cannot be tested, primarily due to either cost or specimen' size, scaling extrapolation of the results has to be carried out. However, Nakashima [93] showed that scaling introduces discrepancies, mostly in the fidelity of ductility and yielding properties of structures.

6.1.2 Pseudo Dynamic Tests

In the Pseudo-Dynamic (PsD) method the displacements are computed, using integration algorithms, such as the central difference method, and then are imposed in a quasi-static way on the structure using actuators. The resulting resistance forces are measured and fed back into the computational model, so that the next displacement

step can be computed. Because the rate of the imposed displacements is relatively slow, it is possible to observe the behaviour of the specimen in detail during testing [35].

Using the central difference integration method, the main philosophy of the pseudo dynamic test will be presented. In an iterative procedure, the equation of motion for the $i+1$ time step of the tested structure can be described as:

$$\mathbf{M}\ddot{u}_{i+1} + \mathbf{C}\dot{u}_{i+1} + \mathbf{R}_{i+1} = \mathbf{F}_{i+1} \tag{6.1}$$

where $\mathbf{M}$ is the mass matrix, $\mathbf{C}$ is the damping matrix, $\mathbf{R}$ is the restoring force vector, and $\mathbf{F}$ is the applied force vector, and dots represent time differentiation. According to the central difference integration method:

$$u_{i+1} = u_i + dt\dot{u}_i + \tfrac{1}{2}dt^2\ddot{u}_i \tag{6.2}$$

$$\dot{u}_{i+1} = \dot{u}_i + \tfrac{1}{2}dt(\ddot{u}_i + \ddot{u}_{i+1}) \tag{6.3}$$

where dt is the time-step length. Since the restoring forces are measured experimentally, there is no uncertainty over the non linear stiffness characteristics of the structure [140]. Knowing the state of the structure at time step, i, the main steps of this method for the $i+1$ time step can be summarised as:

- Apply external force F_{i+1}
- Compute displacement u_{i+1} from Eq. 6.2
- Impose displacement u_{i+1} on test specimen
- Measure restoring force, R_{i+1}
- Compute velocity, $\dot{u}_{i+1}$, and acceleration $\ddot{u}_{i+1}$ based on Eqs 6.2, and 6.1
- Repeat process for $i+2$ time step

The PsD method has been proved to be a very effective and reliable technique with regard the simulation of the response of structural systems [94, 93, 79, 37]. However, Shing and Mahin [109] showed that the PsD method is very sensitive to errors, possibly resulting in an unstable response. The reason behind that is that the errors from an individual time step are fed back to the system and so introduce errors in computing the displacements for the new time step, and consequently wrong restoring forces. Hence, errors have a cumulative nature. These effects become more pronounce at higher frequencies, a fact which makes PsD method extremely inefficient for stiff structures. In order to minimize the errors, several approaches have been proposed such as increased viscous damping, numerical integrations to be based on previous computed displacements rather than measure displacements [109], PsD method to be based on an integrated form of the equation of motion [121], and finally integration algorithms to damp the higher modes [51].

However, this method may not be suitable for certain types of structures. Structures with concentrated masses are most easily modelled and tested, and this method is difficult to be applied to distributed mass structures [35]. Furthermore, since the method is based on imposing the computed displacements in a quasi-static way, structures constructed from materials which are sensitive to any loading rate alterations are not suitable to be tested using the Pseudo-Dynamic method. Lastly, structures where damping is anticipated to have a significant effect on the overall behaviour are not suitable for this methods as well, since both inertia and damping characteristics are numerically modelled [35]. On the other hand, imposing loads quasi-statically allows the test to be carried out with simpler static hydraulic actuators, which are able to produce higher forces comparing with dynamically rated equipment, making it possible to avoid scaling [18].

6.1.3 Effective Force Testing

The main philosophy of the Effective Force Testing (EFT) method is very similar to the PsD method. However, in this case the actuators are dynamically rated and force controlled. The structure is loaded in real time by actuators with an earthquake force equal to the ground acceleration multiplied with the lumped mass of the specimen.

The corresponding motion is equal to the relative motion of an equivalent system subjected to a ground motion. It is a very appealing method, since the loading can be determined in advance, while at the same time no numerical integration is needed [36, 140]. A major drawback however, is that the whole structural mass needs to be included in the specimen, which may be difficult to achieve in the majority of the available testing facilities. Another disadvantage of the EFT method is the inability of the hydraulic actuators to produce force close to the natural frequency of the structure, especially for lightly damped structures.

6.1.4 Pseudo Dynamic Substructure Tests

The PsD technique can be also implemented with the substructure concept. The main reason that the substructure technique is so appealing is its efficiency in terms of both economic and geometric restrictions. Full scale models are expensive to build, and require special large scale and high capacity test facilities. Therefore, it is not usually practical to construct a full scale model. For example in case of evaluating the effect of elastomeric bearings of a bridge, constructing the whole bridge in a laboratory is not a realistic project. Elastomeric bearings, however, could be experimentally tested at the laboratory, while the remainder of the bridge is numerically modelled. The first attempts at this approach were made by Takanashi and Nakashima [58], and Mahin [80]. According to this method the total structural system is divided into the analytical part, with predictable and well known behaviour, and the experimental substructure, which is tested in the laboratory. The experimental part is the main item of interest. Properly specified boundary conditions between the numerical and experimental substructure are necessary in order to provide force equilibrium and displacement compatibility. It is preferable to have a small number of experimental Degrees of Freedoms (DOFs), while care must be taken in order for the DOFs to accurately represent the true dynamic behaviour of the test specimen [35].

As an illustrative example Figures 6.1 and 6.2 show the PsD substructure method concept, and the main PsD substructure technique steps. The total structure consists of a 1-storey 1-bay frame connected with dampers. In this example the main

interest is on the behaviour of the damper. Hence, the damper along with the diagonal braces makes up the physical substructure, while the remainder of the structure is numerically modelled. The test commences by determining the response of the numerical substructure for the first ground motion acceleration step. The displacement at the interface between the experimental and analytical substructures is calculated based on a time integration algorithm, and then is applied at the test specimen using hydraulic actuators. The restoring force, which is experimentally calculated is then fed back to the numerical model along with the next ground motion increment. This process is repeated until the test is complete. In the PsD substructure case Eq. 6.1 takes a different form:

$$\mathbf{M}\ddot{u}_{i+1} + \mathbf{C}\dot{u}_{i+1} + \mathbf{R}^{E}_{i+1} + +\mathbf{R}^{A}_{i+1} = \mathbf{F}_{i+1} \tag{6.4}$$

where $\mathbf{R}^A$ is the restoring force corresponding to the analytical part, and $\mathbf{R}^E$ is the restoring force corresponding to the physical specimen. In the case of a linear elastic frame , $\mathbf{R}^A$ is expressed as $\mathbf{R}^A = k^A u$, where u represents the displacements. With regard to the displacement calculations, a similar process to that described in Section 6.1.2 can be followed, where the central difference method was used. The effect of a range of numerical time integration algorithms on the dynamic behaviour and stability of MDOF systems was the focus of the research of Bonnet [18].

Even though the PsD substructure method seems to be very appealing and more efficient than the PsD method, with regard to the facilities and economical restrictions, is still not suitable in cases when loading rate effects become important parameters on the behaviour of the specimens tested.

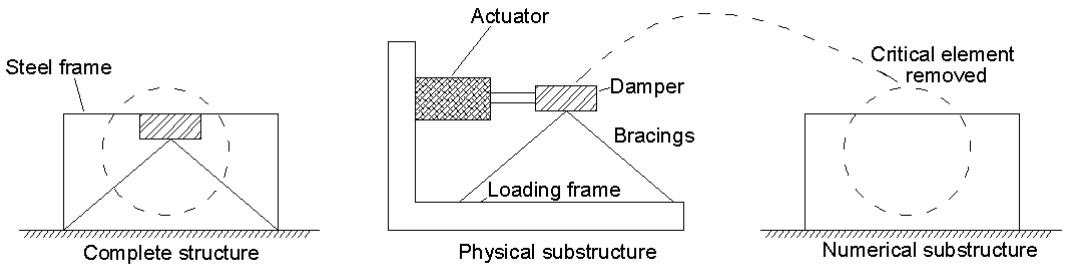

Figure 6.1: Main concept of PsD substructure' technique

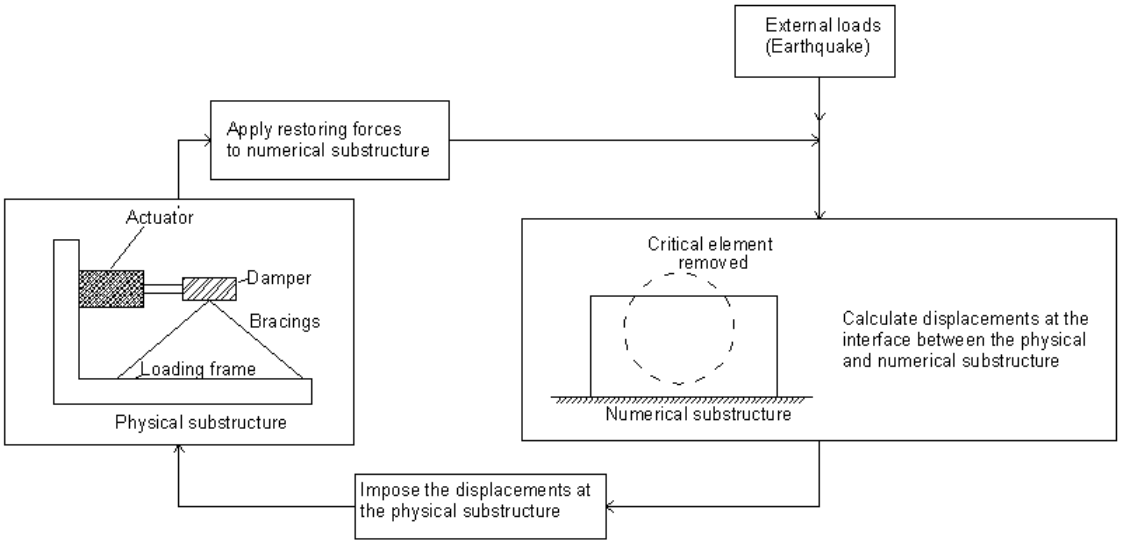

Figure 6.2: Basic steps of PsD substructure' technique

6.1.5 Real Time Substructure Tests

PsD methods are actually time-scaled expanded versions of the real seismic events, normally restricted to materials assumed to behave in a rate-independent manner [78]. In order to test structural components which exhibit velocity dependent characteristics, the concept of Real Time Substructure (RTS) tests has been the focus of several researchers [78, 93, 18, 61]. The concept remains almost the same as the PsD substructure technique described earlier. The total structure is again divided into the physical and the numerical substructure. Also, the test again proceeds according to Figure 6.2. However, now the tests are performed in real time, where the actuator needs to act continuously, eliminating the quasi-static phase described in 6.1.4. In

order to achieve this, each cycle described in Figure 6.2 has to be completed within the time interval between the load increments, so that the loading and structural response occur at the same rate in the test as in a real dynamic loading event in a prototype structure [140], meaning that each cycle has to be completed within a few milliseconds. It should be noted that the force feedback in RTS tests includes both inertia and damping components, and these therefore do not need to be taken into account in the numerical substructure, as opposed to the PsD method. One of the first RTS tests was conducted by Nakashima [94], where the physical substructure was a viscous damper located at the base of a multi-storey building, which was numerically modelled.

However, one of the main problems that RTS tests face is the time delay, mainly due to the finite response of the hydraulic actuators. This delay is the time difference between the command signal and the actual response of the actuator to the desired position. Consequently, the corresponding forces are based on wrong displacements, creating cumulative error leading to instability. More specifically, it has been proved [124] that the effect of this error is equivalent to adding negative damping to the system. Several procedures have been proposed [124, 52, 18, 17, 21] in order to mitigate the effect of time delay. The focus of this chapter is to carry out RTS tests using a new method for minimizing the delay, which is based on an extension of the work of Chae et al [21].

6.2 RTS testing in Oxford

The main equipment in the Oxford University Structural Dynamics Laboratory (OUSDL) consists of six servo-hydraulic actuators: two 10 kN actuators (piston stroke: ± 75 mm), two 100 kN actuators (piston stroke: ± 125 mm), and two 250 kN actuators (piston stroke: ± 125 mm). For the needs of the tests carried out as part of this thesis, one of the 100 kN actuators was used (Figure 6.3). The actuators can move via pressurised oil through servo-valves, which control the piston movement. The oil is distributed to the valves by a hydraulic substation. In order to achieve a large supply of pressurised oil, three 60 l/min pumps are connected in

parallel over a large oil reservoir at one end of the high pressure line with a set of hydraulic accumulators, which are capable of storing 180 l at the other end. Hence, during peak flow consumptions the pressurised oil flow rate can be doubled for a short period of time, when the instantaneous supply of the pumps is not enough. The hydraulic substation is connected with the pressure line as well. All this equipment is installed on a 166 tonnes concrete block, with 9.1 m x 4.2m surface area, and 1.6 m deep. An overview of the main equipment installation of the OUSDL can be seen at Figure 6.4.

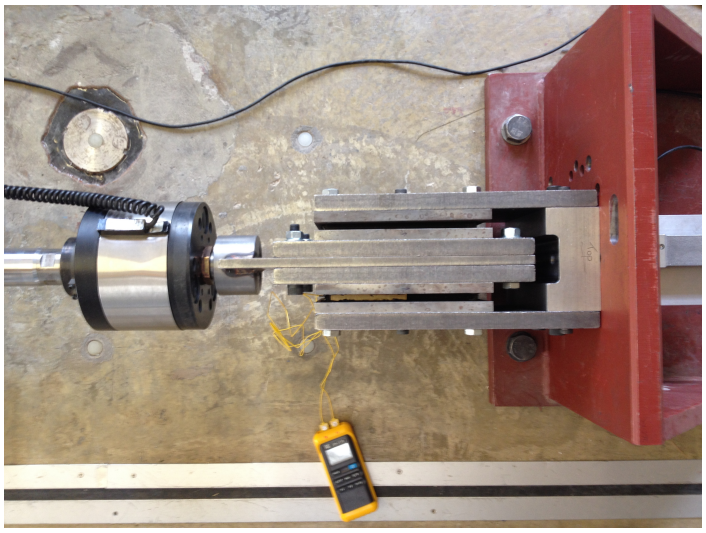

Figure 6.3: 100 kN actuator used for tests

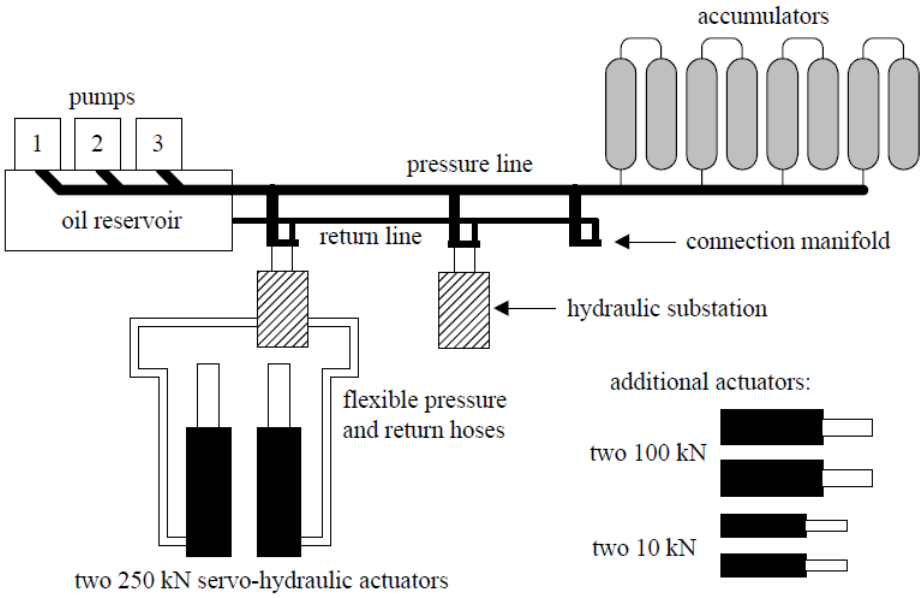

Figure 6.4: Schematic overview of OUSDL equipment [15]

The closed loop control between the substation and the actuator is conducted through an Instron Labtronic 8800 controller, which provides four channels of position or force control. The controller parameters are accessible to the user through the Instron program RS+. The Instron controller is based on a Proportional-Integral-Derivative-Lag (PIDL) algorithm, the parameters of which can be determined either manually or by an auto-tuning process based on minimizing the error of the command signal and the actual response of the actuator with regads to a square wave displacement command. The output displacement $u(t)$ of the controller is based on the error between the desired displacement, u_{des}, and the actual displacement achieved by the actuator, u_{act}. The displacement feedback, u_{act}, is determined by a linear variable differential transformer (LVDT) fitted inside the actuators' body and outputs the effective piston displacement relative to the actuators' body [18]. Moreover, the actuator is also equipped with a load cell which connects the end of the piston with the test specimen and is responsible to determine the force. The two transducers send their signals to the Instron controller. Although both force and displacement control of the actuators can be achieved, only displacement control was used in this research. However, in each case, the signal of the corresponding transducer is determined, and compared with the command signal. Here is where

the aforementioned PIDL controller is being used, producing a closed loop control generating command signals every 0.2 ms (sampling frequency: 5 kHz).

Real time control of the substructure testing loop, however, is achieved via a Digital Signal Processing (DSP) board, which is connected with a 32-channel Data Acquisition (DAQ) system, creating an additional control loop around the system. During RTS tests, monitoring the force and displacement of the actuator, along with the encoder's displacement is possible through the PC hosting the DSP. The numerical substructure, which is modelled using Simulink [7], is downloaded to the DSP for execution. The DSP's host PC communicates with the Instron controller to fully capture the interaction between the numerical and physical substructure. A main and simplified overview of the RTS procedure is shown at Figure 6.5.
The ground acceleration is the input to the numerical part. The corresponding displacements at the physical-numerical interface, x_n, are calculated at the DSP's host PC, and sent to the delay compensator (outer loop control) producing u_c. In order to take into account any rig flexibilities, the difference between the actual displacement extracted by the linear encoder and the actuator's LVDT is added to u_c to generate the final command displacement which is sent to the Instron controller and from there to the actuators. The resulting force extracted from the actuator is sent back to the numerical part in order to produce the next desired displacement increment. The corresponding measured displacements, x_m are used as input commands to the delay compensator, so the final command displacements, u_c, can be determined. All this procedure will be described in detail in the following sections. It is worth mentioning that the integration algorithm, along with the delay compensator, is solved in a different time step to the one used for the Instron controller, called the main step, taken as 1 ms for the tests in current chapter. Then, the controller generates the required displacements based on the PIDL algorithm described earlier in finer time steps called sub-steps (0.2 ms), in order to obtain good experimental control. However, actuators are known not to respond instantaneously. The characterization of actuators in terms of time delay and amplitude error time histories is a very practical way of approaching this non-instantaneous actuator response, as will be seen in this chapter.

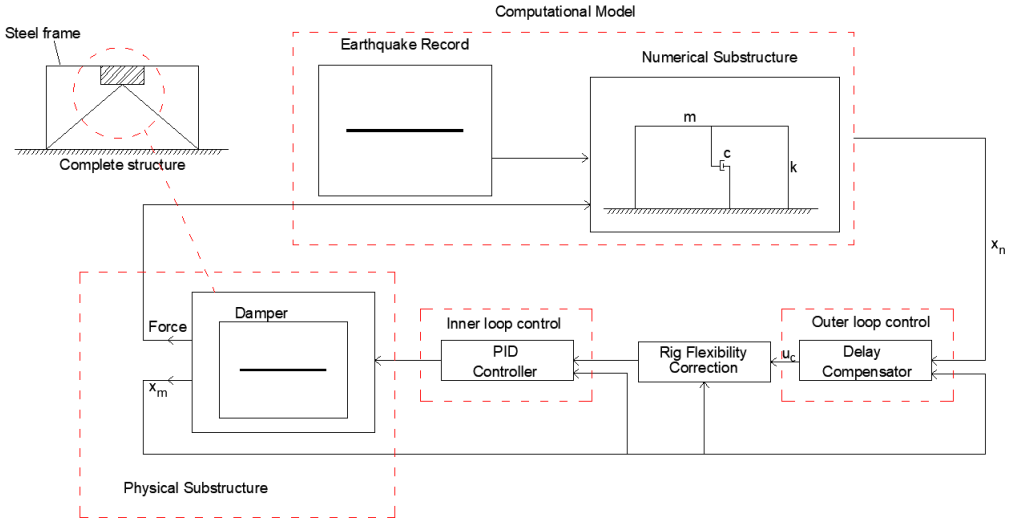

Figure 6.5: Simplified Overview of Hybrid Procedure

6.2.1 Time Delay

Among other researchers [124, 52, 17, 21], the effect of time delay has been thoroughly studied by Bonnet [18]. He carried out a large series of tests at the OUSDL, and estimated that the minimum time delay of a 10 kN actuator was approximately at 4.7 ms. This value was not constant, since most of Bonnet's research was focused on the parameters which may affect the delay. He concluded, that the time delay highly depended on loading frequency, specimen stiffness, proportional gain parameter of the PID controller, and loading magnitude, where the maximum value of time delay observed during tests Bonnet conducted was approximately 30 ms. The amplitude error on the other hand, was estimated as of secondary importance compared to the time delay. These delays can be generally ignored in an open loop test (where there is no feedback from the actuator's response). However, it has been proved [124] that time delays in closed loop tests, as in the case of RTS tests, can considerably change the behaviour of the system, make it unstable. Specifically, Horiuchi [124] proved that for an SDOF system, with displacement $x(t)$, a time delay δt, leads to addition of negative damping to the system:

$$c_{eq} = -k\delta t \tag{6.5}$$

$$\zeta_{eq} = -\omega_n \delta t/2 \tag{6.6}$$

where $w_n = \sqrt{k/m}$ is the natural frequency of the system. If the negative damping is larger than the inherent damping of the system, the system becomes unstable.

As already mentioned a lot of procedures and algorithms have been considered in previous research [124, 52, 18, 17, 21], in order to improve the stability of the system in RTS testing. These actuation compensation schemes aim to force the actual output to mimic the desired output [18]. Once the displacement, x_t, of the numerical integration algorithm is solved, it is fed into the delay compensation algorithm, and a new displacement command, u_c, is generated based on the delay scheme, and sent to the actuator producing the actual displacement measured experimentally, x_m. The general aim of the delay compensation schemes is to correct the displacement determined from the numerical part of the RTS. This is done in such a way, so the error between the actual displacement which will be achieved by the actuator after a time equal with the time delay, and x_t is minimised, extrapolating x_t by an amount equal with an estimation of the time delay. The most widely used actuation compensation schemes are briefly presented here:

- Exact Polynomial Fitting Extrapolation

  Horiuchi [124] proposed a mathematical model which is based on fitting a third order polynomial equation on the last data points. The polynomial is then used to extrapolate, x_t by an amount equal with an estimation of the time delay. The number of data points used for the fitting of the polynomial is equal with the chosen polynomial order, n, plus one. The estimation of the time delay is assumed constant during the RTS test, and is based on previous tests and highly depends on the specimens and loadings requirements.

- Least Square Polynomial Fitting

  A similar approach has been followed by Wallace [134], and Zhu [146]. However, more points than $n+1$ are taken into account for the fit of the polynomial in this case. This method is based on a least square approximation and not an exact fit, however. In terms of noise this can be very effective, since simulation

results showed that the fewer data points used the more sensitive the system becomes to noise. Nevertheless, this may cause some potential problems when the polynomial changes from point to point, since each polynomial of n order is a best fit between m data points (where $m > n$), no point actually lies on it.

- Linear Predicted Acceleration

  This method is not based on a polynomial fitting as the previous ones. Instead, assuming that the acceleration at the interface varies linearly, the corresponding displacement can be then determined through integration. The need for the knowledge of the acceleration of the current step leads to the assumption of extrapolating the acceleration in a time equal with the estimated delay, since most of the explicit time integration algorithms do not provide this information. Horiuchi [53] showed that this method is theoretically superior in terms of stability compared to the exact polynomial fitting.

- Live Delay Estimation

  All the aforementioned delay compensation schemes assume an estimation of the time delay, which remains constant during the RTS tests, and is usually based on open loop tests which have preceded the RTS tests. To eliminate this uncertainty Darby [15] suggested a live estimate of the time delay which is updated for every time step. The update of the time delay, δ, is based on the error between the target (or desired) displacement and the measured displacement, along with the time delay of the previous time step. Additional empirical parameters along with a velocity estimate are used in Darby's algorithm. The time delays are determined based on the zero-crossing method. According to this method, the time delay is calculated each time the target and measured displacement become zero. However, this also creates a limitation of the method since no updates are available between zero crossings.

6.2.2 Adaptive Time Series

A new method, based on an adaptive actuator compensation scheme was proposed by Chae [21], called Adaptive Time Series (ATS). The ATS method continuously updates its coefficients, taking into account any non linearities of both the actuator and the test specimen, resulting in an accurate actuator control. Unlike most existing adaptive methods, the ATS scheme does not involve user-defined adaptive gains. Furthermore, most of the adaptive delay compensation techniques are based on gains extracted from calibration tests prior to the RTS testing, or on a tuning and optimizing procedures with moderate force or displacement amplitudes. However, these gains are not valid for larger amplitudes where the behaviour of the testing specimen may be different, whether due to its inherent material properties or due to damage/fracture. The ATS method is based on the following basic relationship between the input displacement command, u, and the output displacement of the servo-hydraulic system, x:

$$u(t) = \tfrac{1}{A} x(t+\tau) \tag{6.7}$$

where A is the amplitude error which represents the ratio between the output and the input displacement, and τ is a constant time delay. Figure 6.6 shows the relationship between u, and x. Using the Taylor series Eq. 6.7 can be approximated as:

$$u(t) = \tfrac{1}{A}\Big[x(t) + \tau\dot{x}(t) + \tfrac{\tau^2}{2}\ddot{x}(t) + \ldots + \tfrac{\tau^n}{n!}\tfrac{d^n x}{dt^n}\Big] \tag{6.8}$$

According to Eq. 6.8 the input command of the actuator, can be determined based on the constant time delay, amplitude error, and the output displacement at time t. If we want to achieve a target displacement, x_t, at a time-step k (the measured displacement x_m would ideally be equal to the target displacement x_t), then the command signal u_c is approximated as :

$$u_{c,k} = \alpha_0 x_{t,k} + \alpha_1 \dot{x}_{t,k} + \ldots + \alpha_n \tfrac{d^n x_{t,k}}{dt^n} \tag{6.9}$$

where

$$\alpha_j = \frac{\tau_j}{A_j}, j = 0, 1, 2, .., n \tag{6.10}$$

If in Eq. 6.9 the measured displacement is used instead of the target one, the estimated command signal would have been:

$$u_{est,k} = \alpha_0 x_{m,k} + \alpha_1 \dot{x}_{m,k} + \ldots + \alpha_n \frac{d^n x_{m,k}}{dt^n} \tag{6.11}$$

Varying adaptively, the coefficients α_j of Eq. 6.9, ATS can take into account any alterations of time delay and amplitude error during the RTS tests, and not assuming these parameters as constant. The main concept of the ATS can be shown at Figure 6.7, where it is compared with delay compensators without feedback.

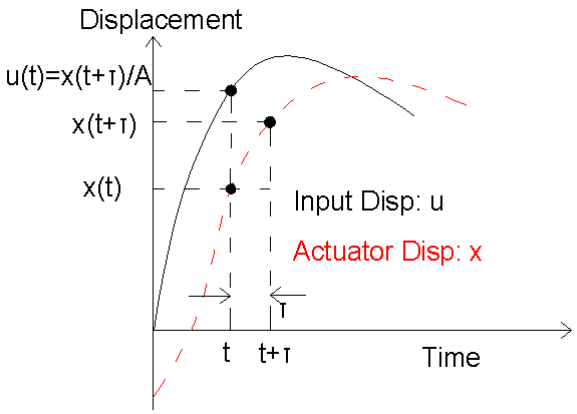

Figure 6.6: Comparison between input and output displacements of a servo-hydraulic system

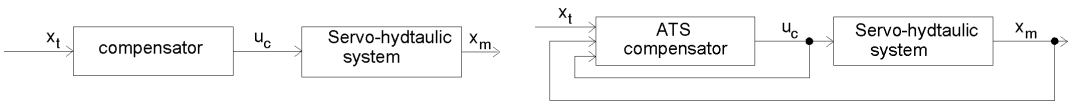

(a) (b)

Figure 6.7: a: Actuator delay compensator without feedback, b: Actuator delay compensator with feedback

In order to minimize the time delay and amplitude error, the measured displacement and the target displacement should be as close as possible. This can

be achieved by minimizing the error between u_c, and u_{est}, using the least squares method:

$$J_k = \sum_{i=1}^{q} (u_{c,k-1} - u_{est,k-1})^2 \tag{6.12}$$

Where q is the number of time steps which are taken into account for the minimization of the error, and represents the size of the time window over which the α_j coefficients are determined. Minimizing the cost function J_k the following relationship can be obtained:

$$A = (X_m^T X_m)^{-1} X_m^T U_c \tag{6.13}$$

Where $A = [\alpha_{0,k} \quad \alpha_{1,k} \quad \alpha_{2,k} \ldots \alpha_{n,k}]^T$, $X_m = [x_m, \dot{x}_m, \ldots \frac{d^n x_m}{dt^n}]$, $x_m = [x_{m,k-1}, x_{m,k-2}, x_{m,k-q}]^T$, $U_c = [u_{c,k-1}, u_{c,k-2}, \ldots, u_{c,k-q}]^T$ Since the coefficients of A are now known, they can be substituted into Eq. 6.9, and the new command signal at time t_k can be determined:

$$u_{c,k} = \alpha_{0,k} x_{t,k} + \alpha_{1,k} \dot{x}_{t,k} + \ldots + \alpha_{n,k} \frac{d^n x_{t,k}}{dt^n} \tag{6.14}$$

From Eq. 6.13 the amplitude error and the time delay for the specific time step, t_k can be determined based on the first two A coefficients:

$$A_k = \frac{1}{\alpha_{0,k}}, \tau_k = \frac{\alpha_{1,k}}{\alpha_{0,k}} \tag{6.15}$$

It should be noted that when the amplitude error is not significant ($A_k = 1$), then $\alpha_{1,k}$ is approximately equal to the time delay, τ_k. Even though good displacement control could be, theoretically, achieved using higher order derivatives in Eq. 6.14, this might cause problems in RTS tests amplifying noise and leading to probable instability of the system. Choosing $n = 2$, Eq 6.14 can be simplified to:

$$u_{c,k} = \alpha_{0,k} x_{t,k} + \alpha_{1,k} \dot{x}_{t,k} + + \alpha_{2,k} \ddot{x}_{t,k} \tag{6.16}$$

The velocity and the acceleration are calculated by using the finite difference method:

$$\dot{x}_k^t = \frac{x_k^t - x_k^t - 1}{T}, \ddot{x}_k^t = \frac{\dot{x}_k^t - \dot{x}_{k-1}^t}{T} \tag{6.17}$$

The measured displacement, however, will contain noise and must therefore be filtered. A 6th order Butterworth filter was used by Chae [21] in order to achieve better estimate of $\dot{x}_m$, and $\ddot{x}_m$. The implementation of the filter unavoidably introduces a time delay. Hence, the exact same filter should be used in the compensated actuator command displacement, $u_{c,k}$, so a set of synchronised data of $u_{c,k-1}$, and $u_{est,k-1}$ is obtained. Furthermore, user-defined limit values were used for the ATS coefficients in order to avoid any erroneous values, and prevent any potential instability. With regard to the value, q, of the number of time steps which are taken into account in the minimization of the function J_k of Eq. 6.12, if it is too short, then the corresponding coefficients lack accuracy. If, on the other hand, q takes a very large value then the calculation time increases and the coefficients will not respond as quickly to a change in delay. Based on the speed of the computer, the coefficients may not be available by the end of the simulation time step (1/1024 in case of Chae tests [21]). Hence, this data was obtained based on a 1 second time-window, corresponding to a value of q equal to 1024 time steps. In order to minimize computational time, data was retained every $16th$ time step decreasing the size of X_m at Eq. 6.13 from 1024x3 to 64x3.

6.2.3 Modified ATS

A modified version of the ATS compensator has been proposed by Malloy and Blakeborough (unpublished). When these lines were written, no journal paper or written work had been submitted with regard to this method. The main target of this method was the further minimization of the computational time when the ATS coefficients were determined. This was achieved by changing the time window of 1 second, from a rectangular to an exponentially decaying window. Every sample has the same weighting when the rectangular time window is used. However, when the proposed decaying window is used a new parameter, ρ, is introduced where $0 < \rho \leq 1$

(see Eq. 6.18). Hence, the most recent samples are weighted more, in contrast with the older samples. A schematic overview of the comparison of these two methods can be seen at Figure 6.8 where the influence of different values of ρ are illustrated and compared with the original ATS method. In comparison with the original ATS where only 1 in every 16 data points were used, all the sample data are used in the modified ATS compensator in order to determine the corresponding coefficients.

The minimization function of Eq. 6.12 has to be adjusted as well. The new weighted function, Z_k can be written as:

$$\mathbf{Z}_k = \sum_{i=1}^{q} \rho^{i-1}(u_{c,k-1} - u_{est,k-1})^2 \tag{6.18}$$

If the parameter, $\rho = 1$, then $\mathbf{Z}_k = \mathbf{J}_k$, and the delay compensator method is the ATS method described earlier. In order to obtain the new parameters of the modified ATS compensator, $\mathbf{Z}_k$ has to be minimized taking the following form:

$$\mathbf{X}_\rho^T \mathbf{U}_c = \mathbf{X}_\rho^T \mathbf{X}_m \mathbf{A}_k \Rightarrow \mathbf{A}_k = (\mathbf{X}_\rho^T \mathbf{X}_m)^{-1} \mathbf{X}_\rho^T \mathbf{U}_c \tag{6.19}$$

where:

$$\mathbf{X}_\rho^T = \begin{bmatrix} x_{m,k-1} & \rho x_{m,k-2} & \rho^2 x_{m,k-3} & ... \\ \dot{x}_{m,k-1} & \rho \dot{x}_{m,k-2} & \rho^2 \dot{x}_{m,k-3} & ... \\ \ddot{x}_{m,k-1} & \rho \ddot{x}_{m,k-2} & \rho^2 \ddot{x}_{m,k-3} & ... \end{bmatrix} \tag{6.20}$$

$$\mathbf{U}_c = \begin{bmatrix} u_{c,k-1} \\ u_{c,k-2} \\ u_{c,k-3} \\ ... \end{bmatrix} \tag{6.21}$$

$$\mathbf{X}_m = \begin{bmatrix} x_{m,k-1} & \dot{x}_{m,k-1} & \ddot{x}_{m,k-1} \\ x_{m,k-2} & \dot{x}_{m,k-2} & \ddot{x}_{m,k-2} \\ x_{m,k-3} & \dot{x}_{m,k-3} & \ddot{x}_{m,k-3} \\ \dots & \dots & \dots \end{bmatrix} \tag{6.22}$$

$$A_k = \begin{bmatrix} \alpha_{0,k} \\ \alpha_{1,k} \\ \alpha_{2,k} \end{bmatrix} \tag{6.23}$$

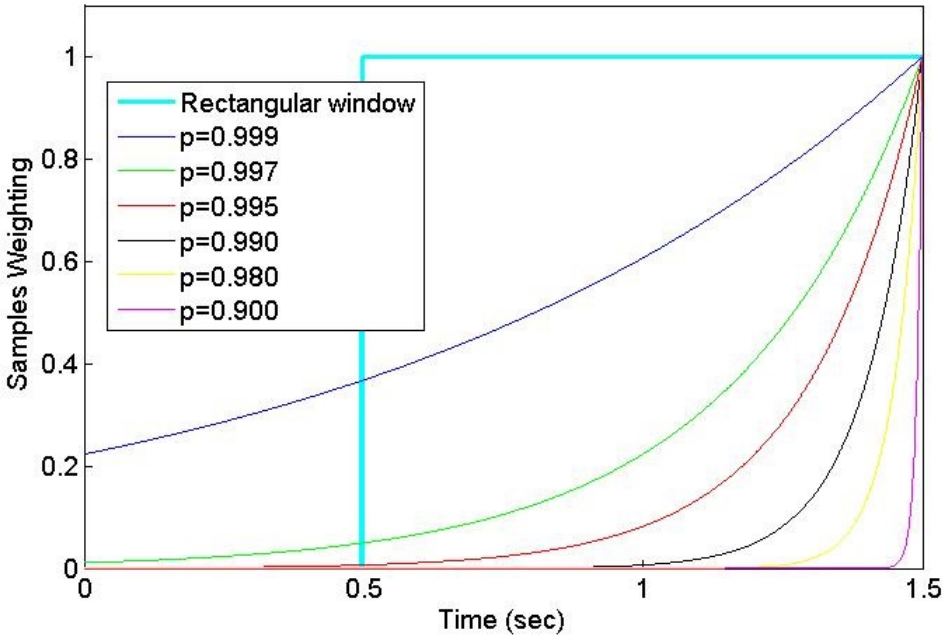

Figure 6.8: Comparison of weighting of samples between ATS and modified ATS compensators

The matrices $\mathbf{X}_\rho$ and $\mathbf{X}_m$ have dimensions qx3, the vector $\mathbf{U}_c$ has dimensions qx1, and the vector $\mathbf{A}_k$ 3x1. Defining $\mathbf{M}_k = (\mathbf{X}_\rho^T \mathbf{X}_m)$ and $\mathbf{W}_k = \mathbf{X}_\rho^T \mathbf{U}_c$, Eq. 6.19 becomes:

$$\mathbf{A}_k = \mathbf{M}_k^{-1} \mathbf{W}_k \tag{6.24}$$

It can be seen that $\mathbf{M}_k$ is a 3x3 matrix, and $\mathbf{W}_k$ a 3x1 vector, regardless of the value of q. It can be seen that $\mathbf{M}_k$ can be updated at each time step according to:

$$\mathbf{M}_k = \rho \mathbf{M}_{k-1} + x_k x_k^T \tag{6.25}$$

Where

$$x_k = \begin{bmatrix} x_{m,k} \\ \dot{x}_{m,k} \\ \ddot{x}_{m,k} \end{bmatrix} \tag{6.26}$$

Similarly, $\mathbf{W}_k$ can be also updated to:

$$\mathbf{W}_k = \rho \mathbf{W}_{k-1} + u_{c,k} x_k \tag{6.27}$$

From the above equations it can be concluded that the modified ATS method is no longer based on Eq. 6.13, where a 64x3 matrix $\mathbf{X}_m$ is used every time the coefficients are updated. The modified ATS is much more efficient since only current values of x_m, $\dot{x}_m$, and $\ddot{x}_m$ are used as feedback to Eq. 6.24 in order to obtain the ATS coefficients, instead of vectors of previous measurements.

Figure 6.9 shows how the modified ATS method was implemented using Simulink. The whole process described earlier can be overviewed in this Figure, where the *Pseudo-Inverse* block takes measured displacements and their derivatives, along with the command displacements as inputs, and the ATS coefficients are extracted and updated for every time step, based on Eq. 6.24. In this block the matrices W_k, and M_k are calculated in order to produce the vector A_k and the corresponding coefficients: α_0, α_1, and α_2. These coefficients are used as an input to the *Compensator* block where the final command signal is determined based on Eq. 6.16 and sent to the actuator.

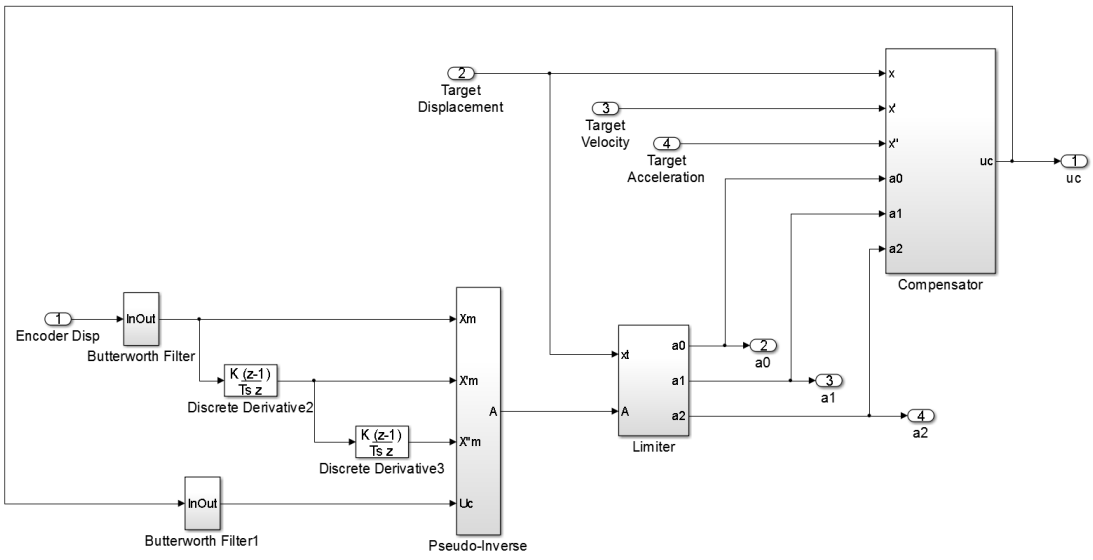

Figure 6.9: Schematic overview of the modified ATS delay compensator

6.2.4 Implementation of ATS

A preliminary set of experiments was carried out in order to safely assign the parameters for the RTS test. Based on both the characterization tests described in Chapter 3, along with the tests of this section, the following values of the PID controller were used, based on the auto-tuning process: $P = 34.98dB, I = 0, D = 0, L = 0.0008$.

An additional parameter had to be taken into consideration with regard to the final implementation of the modified ATS compensator. Rig flexibility is something that occurs in all experimental rigs to some extent. As already mentioned in Chapter 3, where the characterization tests were described, a linear encoder was attached at the mid-height of the central steel plate of the EDs in order to capture the actual elastomer's deformation, since some rig flexibility is expected. The displacements extracted from the encoder are used to determine the ATS coefficients, whereas the PID controller uses data from the LVDT mounted on the actuator. The difference between the actuator's displacement x_m, and the encoder's displacement, x_{enc}, which is determined based on the actual movement of the damper gives the rig deflection, x_{rig}. This displacement is added to the already determined command displacement, extracted from the modified ATS compensator, in order to give the corrected displacement, which is also the displacement which is sent to the actu-

ator. A predefined displacement time history (Figure 6.10a), which was extracted by analysis of an SDOF steel frame equipped with elastomeric dampers subjected to scaled El Centro ground motion and corresponds to the dampers displacements, was used in order to evaluate the importance of rig deflection. This time history is based on a user-defined command which included cycling tests in a range of $\pm$ 5 mm amplitudes, and $0.25 - 5Hz$ frequencies. Despite the fact that the rig was designed to be as stiff as possible Figure 6.10 shows that this factor is not negligible.

Two experiments were carried out in order to provide an initial estimate of the modified ATS coefficients, with no real time substructure feedback loop. Both of them were based on pre-defined displacement time histories. The first one is based on a white noise signal with a maximum displacement 5.5 mm (corresponding to 45% shear strain of the damper) and a 5 Hz bandwidth in order to cover the whole range of displacements and frequencies where the main interest is. The second test was the user-defined time history with the range of $\pm$ 5 mm amplitudes, and $0.25 - 5Hz$ frequencies, which was used in order to present the effect of the rig deflection. Figure 6.11 shows the displacement time histories and the corresponding measured displacements, x_m, without the implementation of the modified ATS method.

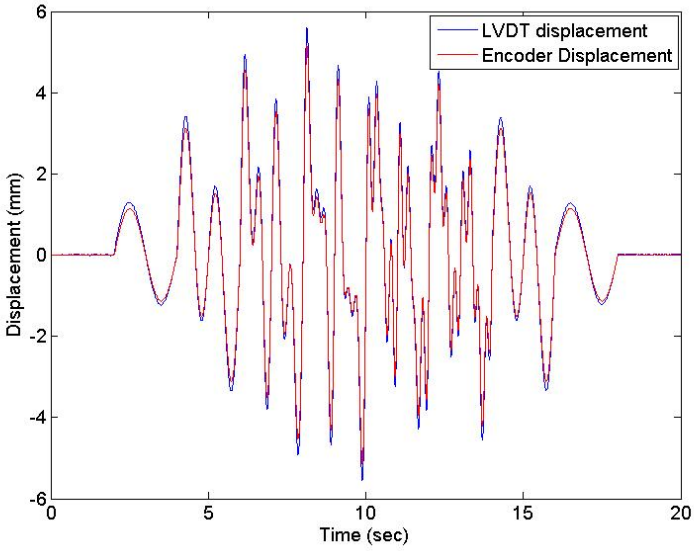

(a)

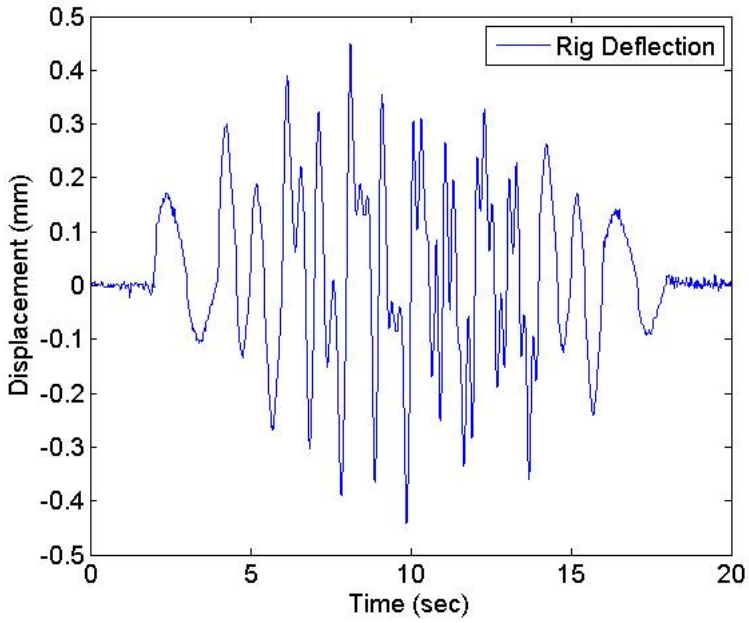

(b)

Figure 6.10: User defined time history a: Comparison of Instron controller displacement with encoder's displacement, b:Corresponding rig deflection

Amplitude error was measured based on the peaks of these signals, while the time delay was measured based on the zero-crossings method. The aforementioned tests had an average delay of 10.2 ms, and an amplitude error of 0.6%. Based on minimization of the difference of u_c, and x_m, and Eq.6.13 the mean values of the α_i coefficients are determined for the duration of the tests: $\alpha_0 = 1.0$, $\alpha_1 = 0.01s$, and

$\alpha_2 = 0.00006s^2$. These values will be used as initial estimates of the α_i coefficients when modified ATS compensator is going to be used in these initial tests. Moreover, similar values for the time delay and the amplitude error can be determined from Eq. 6.10, using the ATS coefficients as functions of time delay and amplitude error. The aforementioned values were also in a very good agreement with the cyclic tests which were carried out as part of the thesis, and are described in detail in Chapter 3. Based on these values, limits were assigned to the coefficients. These limits prevent system instability by providing minimum and maximum values for α_0, α_1, and α_2, along with the rate of change of these coefficients. Furthermore, the modified ATS method holds these coefficients to their initial values until the actuator has moved through enough displacements, so that Eq. 6.24 is able to provide accurate estimates. When the measured actuator's displacements are relatively small, then the matrix $X_\rho^T X_m$ may cause instability to the system producing unrealistic coefficients. Hence, user-defined limit values have been assigned.

Eq. 6.15 shows the relationship between the coefficient $\alpha_{0,k}$ and the amplitude error, A_k. Since the actuator response is not anticipated to achieve more than $\pm 30\%$ of the actuator's command during an RTS test, the permitted range of values for the $\alpha_{0,k}$ would be $0.7 < \alpha_{0,k} < 1.3$. A maximum rate of change for $\alpha_{0,k}$ of 2 per second is assumed, implying that the change in the amplitude response cannot be more than 2 within a second. The lower permitted values for $\alpha_{1,k}$, and $\alpha_{2,k}$ are taken as 0, and correspond to zero time delay. Assuming that the maximum time delay cannot surpass 40 ms, which is a reasonable assumption based on the tests described in Chapter 3, then based on Eq. 6.10: $\alpha_{1,k}^{max} = 0.04$, and $\alpha_{2,k}^{max} = 0.008$, under the assumption that $A = 1$. The maximum rate of change of $\alpha_{1,k}$ is assumed not to exceed 0.05. Based on Eq. 6.15 this corresponds to a change in the time delay of 50 ms. Larger values were considered as irrational. The maximum limit value for $\alpha_{2,k}$ is calculated based on Eq. 6.10. Hence $\alpha_{2,k}^{max} = (\tau_k^{max})^2/2 = 0.0008s^2$. Differentiating α_2 with respect to time in 6.10: $\frac{d\alpha_2}{dt} = \frac{d}{dt}(\frac{\tau^2}{2}) = \tau\frac{d\tau}{dt} = \alpha_1\frac{d\alpha_1}{dt}$. Therefore, the maximum rate of change of α_2, assuming $A = 1.0$, equals with $[\alpha_1^{max}(\frac{d\alpha_1}{dt})_{max}]/2$. The product $\alpha_1^{max}(\frac{d\alpha_1}{dt})_{max}$ was divided by 2, because is not expected that both α_1, and $\frac{d\alpha_1}{dt}$ will reach their maximum values. These limits are set for the given system,

and may be updated based on the actuator and specimen characteristics and the anticipated time delay and amplitude error.

Figure 6.11 shows the displacement time history when no compensator is used, and Figure 6.12 shows the same time history displacements when the modified ATS compensator has been used, comparing the target and the encoder displacements. A much better performance has clearly been achieved. A trial and error procedure was followed in order to determine the decay factor, which corresponded to using $\rho = 0.996$. Table 6.1 shows the effectiveness of the modified ATS method in terms of Normalised Root Mean Square (NRMS) error, time delay, and amplitude error. NRMS is calculated as:

$$NRMS = \frac{\sum_{i=1}^{N}(x_{t,k} - x_{m,k})^2}{\sum_{i=1}^{N}(x_{t,k})^2} \tag{6.28}$$

It can be noticed that the compensator is highly effective for both of these tests. The NRMS error was decreased from 10.1% to 0.9% for the Multi-Frequency and from 15.9% to 1.7% for the White-Noise displacement time history. The time delay was substantially decreased, producing approximately 1 ms time delay for both of the tests. With regard to the amplitude response, the associated error was almost eliminated. The modified ATS compensator therefore seems to be highly effective regardless of the displacement and frequency alterations, since its coefficients are updated in every time step, and therefore it is able to take into account any changes of the time delay and amplitude error during the RTS test. Figure 6.12 shows the comparison between the target and encoder's displacement, where the influence of the compensator can be clearly seen, comparing with Figure 6.11. However, in order to have a better insight into these comparisons, Figure 6.13 compares the target and encoder displacements and their synchronization for both of the aforementioned tests, with and without the compensator. The effectiveness of the proposed delay compensator is clearly shown.

With regard to the values of the α_i coefficients, and their behaviour under the time histories, Figure 6.14 shows that at the start of the experiments these coeffi-

cients are the same as the initial values. Once, x_m exceeds the limit value of 0.1 mm then the modified ATS compensator starts to calculate the α_i coefficients. The mean values for both of these tests are summarised in Table 6.2. These mean values will be used as better estimates for the RTS tests which are going to be described in the following sections. Observing Table 6.2, and Figure 6.14 it can be noticed that α_0 coefficients are almost 1, implying that the amplitude error in the servo-hydraulic system is almost negligible, comparing to the time delay. Furthermore, α_1 coefficients are very close to the initial assumptions carried out before the beginning of the tests, which correspond to a mean time delay of approximately 10 ms. The time variation of the coefficients shows that they correspond very well within the maximum and minimum values which were assigned to the α_i coefficients and their corresponding rate of change.

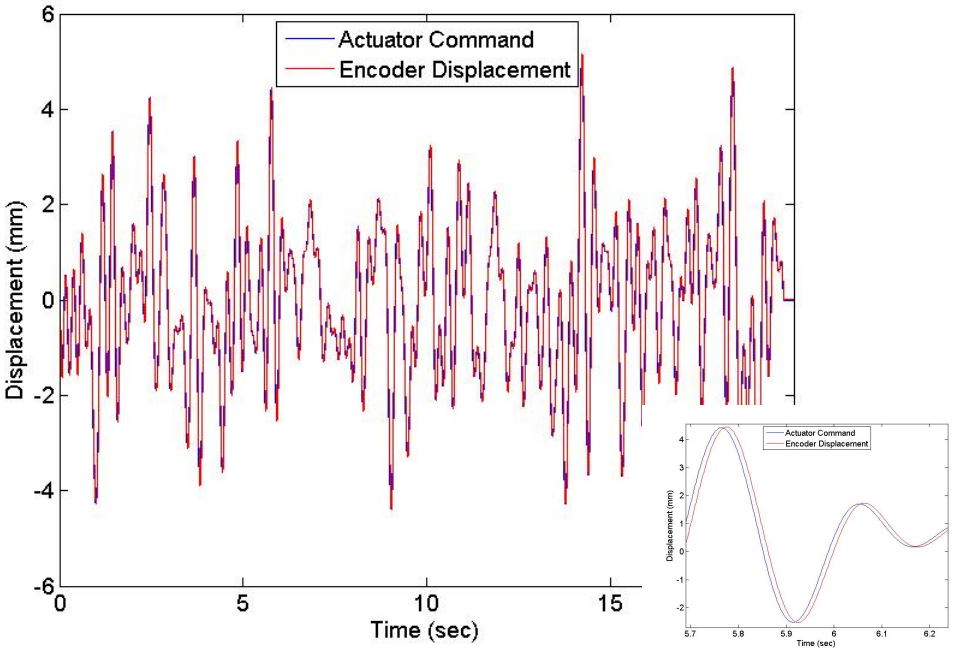

(a) White noise displacement time history

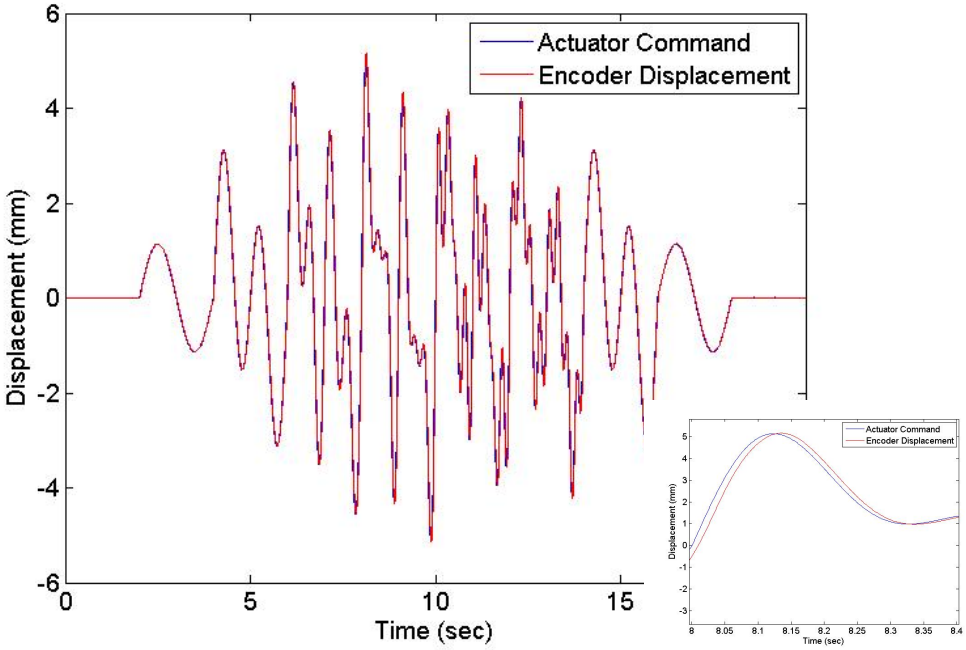

(b) Multi-Frequency displacement time history

Figure 6.11: Comparison of target displacement displacement with encoder's displacement without modified ATS compensator

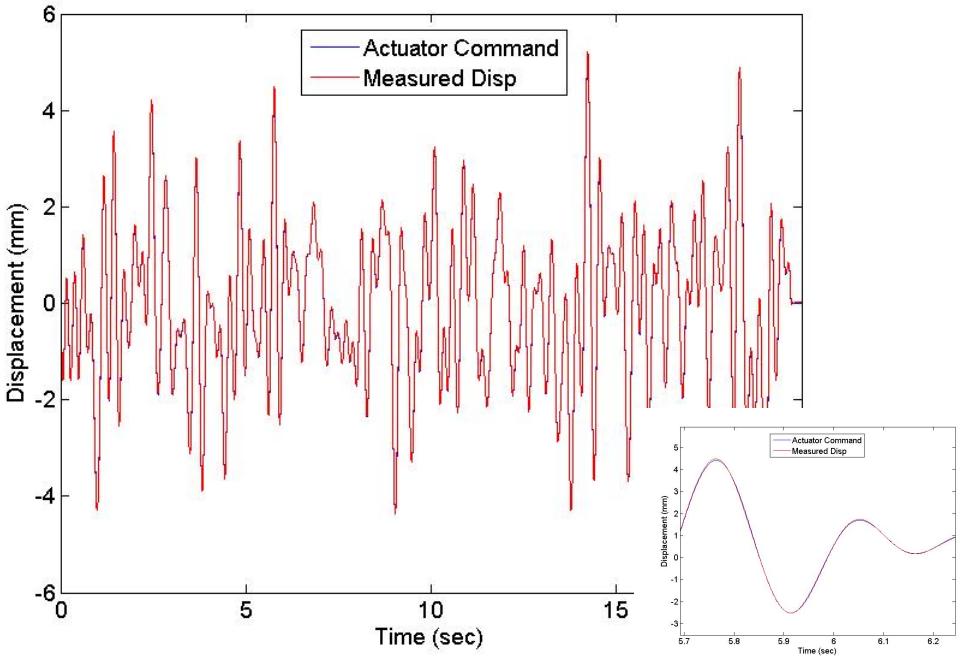

(a) White noise displacement time history

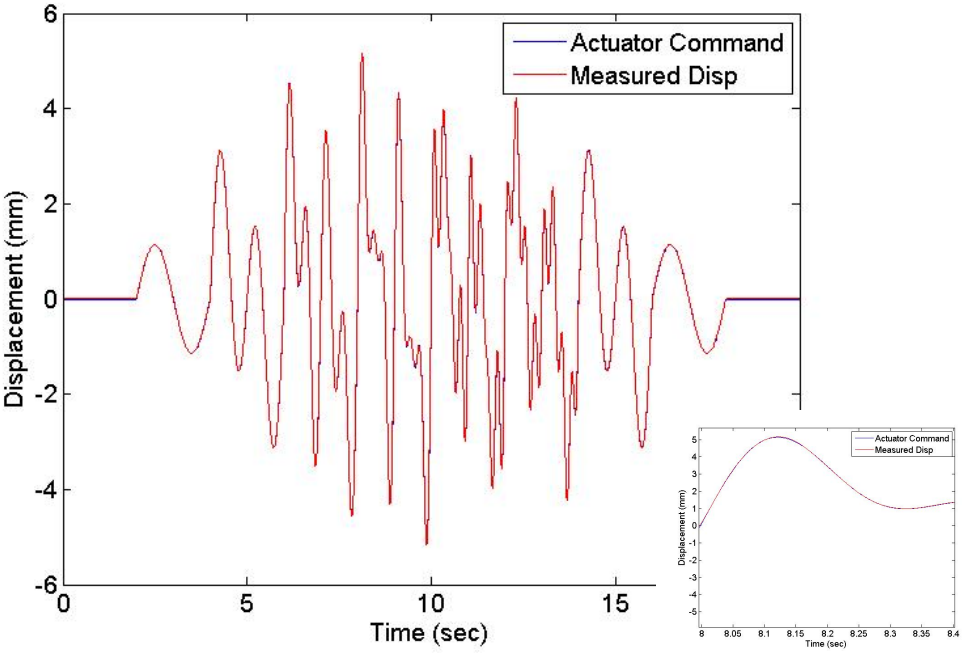

(b) Multi-Frequency displacement time history

Figure 6.12: Comparison of target displacement displacement with encoder's displacement with modified ATS compensator

Table 6.1: Evaluation of modified ATS delay compensator

Parameters	MultiFrequency Command		White-Noise command	
	without modified ATS	with modified ATS	without modified ATS	with modified ATS
NRMS (%)	10.1	0.9	15.9	1.7
Time Delay (ms)	10.3	1.1	10	0.9
Amplitude error (%)	0.3	0.02	0.6	0.09

Table 6.2: Mean values of α_i coefficients

Displacement Time History	Mean Values		
	α_0	α_1(sec)	α_2(sec2)
Multi-Frequency command	1.0045	0.0106	0.000108
White-Noise command	1.0058	0.0108	0.000081

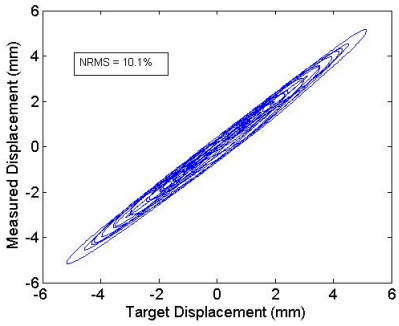

(a) Multi-Frequency without modified ATS compensastor

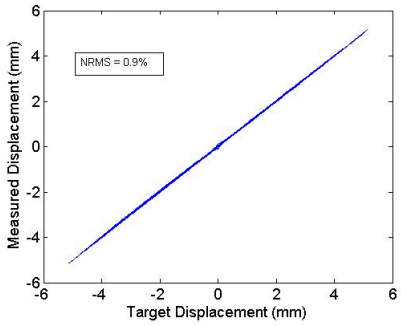

(b) Multi-Frequency with modified ATS compensastor

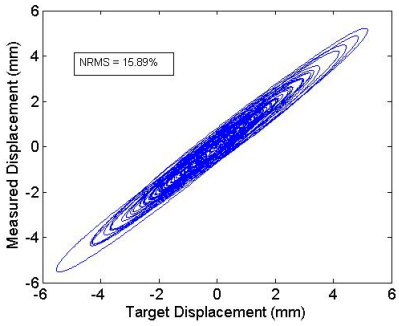

(c) White-Noise without modified ATS compensastor

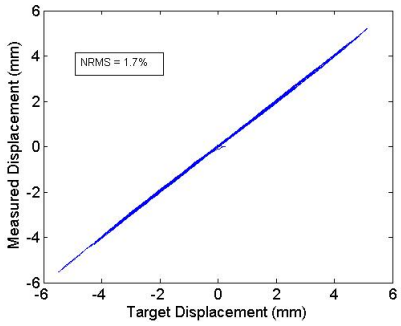

(d) White-Noise with modified ATS compensastor

Figure 6.13: Comparison of target displacement displacement with encoder's displacement - Sychronization plots

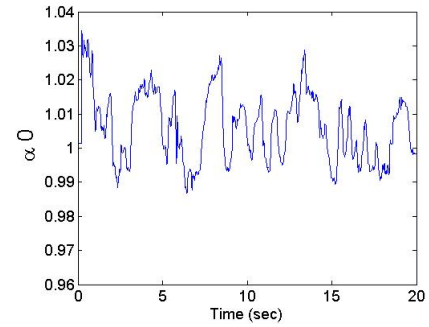

(a) α_0 (White Noise)

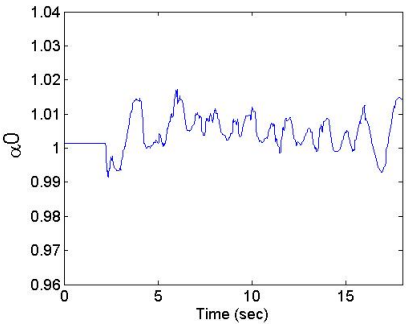

(b) α_0 (Multi-Frequency)

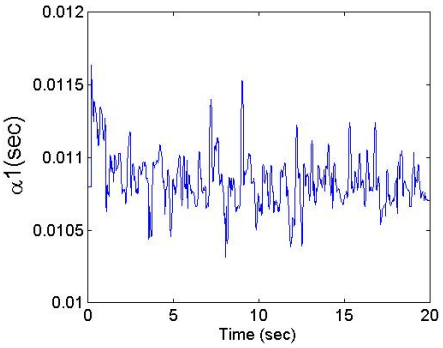

(c) α_1 (White Noise)

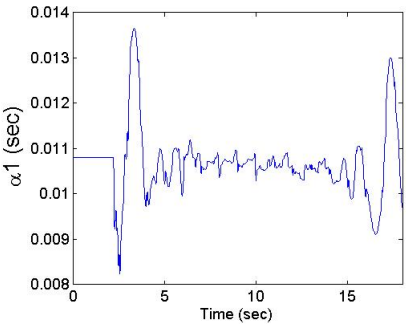

(d) α_1 (Multi-Frequency)

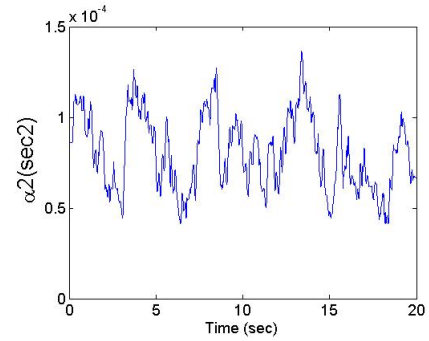

(e) α_2 (White Noise)

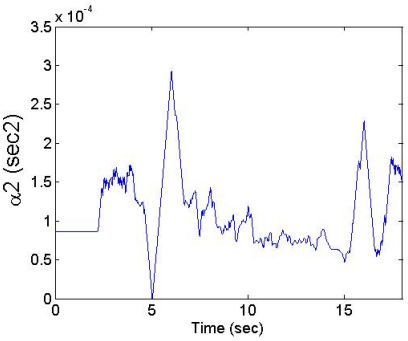

(f) α_2 (Multi-Frequency)

Figure 6.14: Time variation of α_i coefficients

6.2.5 RTS test in SDOF structure

The total emulated system which is going to be tested in real time, will be a 1-storey, 1-bay steel frame connected with diagonal braces equipped with EDs (Figure 6.16). The behaviour of the EDs along with the proposed hysteretic model was described in Chapters 3 and 4. The EDs described in these chapters will comprise the physical substructure here (Figure 6.15).

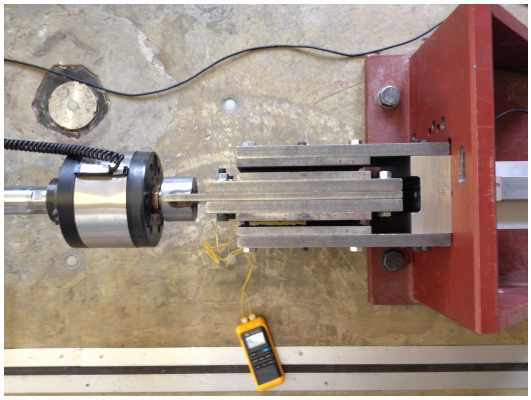

Figure 6.15: Physical substructure for RTS testing

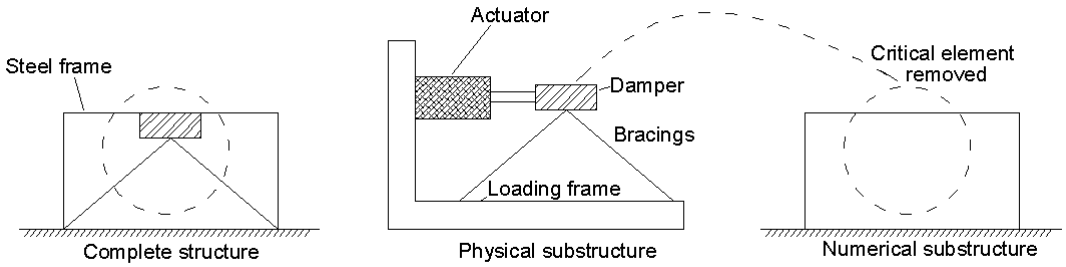

Figure 6.16: Physical and numerical part of the RTS test

The numerical part consists of the remaining part of the emulated structure: the steel frame. As already mentioned in Section 5.3.4 (where the influence of the bracing to the frame's lateral stiffness and damping is being considered), assuming a large value of the stiffness of the diagonal braces leads to the rational assumption of neglecting the influence of the diagonals in terms of lateral resistance. Therefore, only the EDs along with the steel frame were assumed to contribute at the

ground motions, which is consistent with the research carried out in Chapter 5. The schematic presentation of the RTS process was shown at Figure 6.5, and is presented here as well for convenience at Figure 6.17

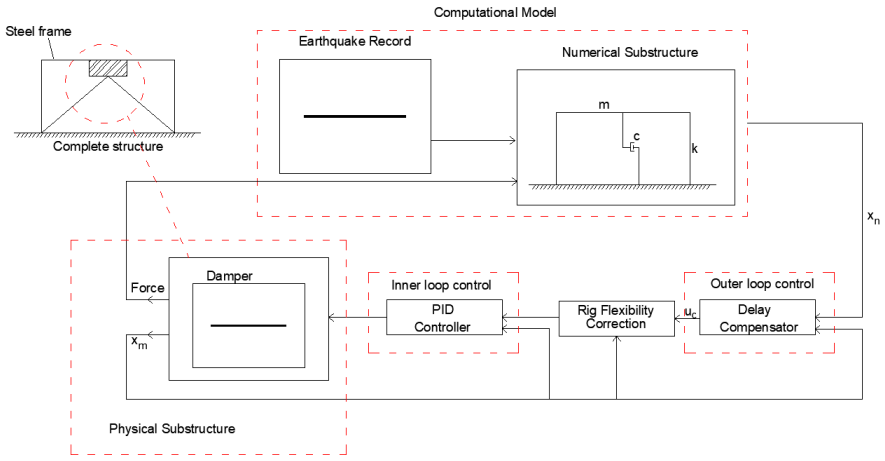

Figure 6.17: Schematic overview of the RTS process

Movement has been assumed to be restrained to the horizontal, so only one DOF will be tested. The equation of motion for the Single Degree of System (SDOF) is expressed as:

$$m\ddot{x}(t) + c\dot{x}(t) + kx(t) + F_D(t) = -m\ddot{x}_g(t) \tag{6.29}$$

where k, m, and c are the elastic story stiffness, damping coefficient, and mass which were assigned to the analytical model, and F_D is the force component which is extracted by the EDs. This equation was modelled in Simulink, and is presented in Figure 6.18. The equation of motion numerically determines the target position, velocity, and acceleration, which are used as input to Eq. 6.16 in order to produce the signal sent to the actuator. The integration of the differential equation of motion was based on the Bogacki and Shampine method [16]. The numerical models used in this chapter were very simple, and the integration algorithm selected is not critical factor for the system's stability.

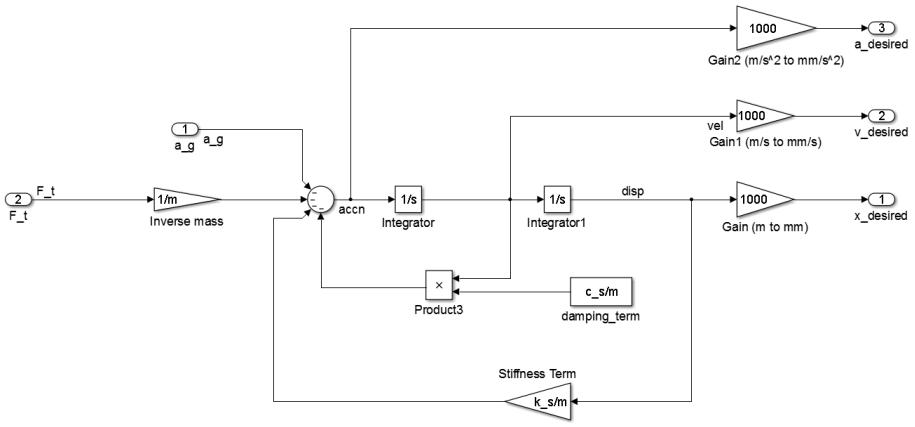

Figure 6.18: Implementation of equation of motion for SDOF structure

The storey elastic stiffness was taken as 5.2 times larger than the effective stiffness of the EDs (based on the results extracted from the characterization tests under $2Hz$ loading frequency, 30% shear strain, and 20°C), which corresponds to a story stiffness of 22.6x10^6 N/m. A mass of 143.26 *tons* was numerically assigned to the system, so that an undamped natural frequency of the SDOF structure of $1.99Hz$ has been achieved. However, this frequency corresponds to the frame without the EDs. Assuming the aforementioned EDs' parameters, the natural frequency of the emulated system increases to 2.18 Hz, which is in very good agreement with natural frequencies obtained from free response tests of the total system. With regard to the inherent structural damping, a value of $\zeta = 0.02$ was used.

It should be noted that relatively small value of natural frequency of the frame (which resulted from the large value of the mass) has been intentionally used in the RTS tests. Based on Eq. 6.6 higher frequency corresponds to larger values of negative damping and higher probability of causing instability. The main aim of this chapter was to carry out simple RTS tests as a validation tool of the new proposed modified ATS method. The results of these tests were also used as further validation techniques of the the hysteretic model proposed in Chapter 3 under more realistic conditions and loading histories compared to simple cyclic or sweep amplitude tests. Hence, not the full range of capabilities of this method will be captured here; therefore small values of natural frequencies were used for stability purposes. However, Malloy and Blakeborough, who developed this method, are currently evaluating it

under more realistic, and demanding conditions.

For the initial estimates of the α_i coefficients of the modified ATS delay compensator, the mean values of the aforementioned tests were used: $\alpha_0 = 1.00515$, $\alpha_1 = 10.7s$, and $\alpha_2 = 9.45\text{x}10^{-6}s^2$. The ground motion which was used in order to excite the frame, was the 1940 El Centro earthquake (Figure 6.19), scaled to 0.0576 g (equivalent to 0.18 scaled factor) in order not to produce EDs' displacements larger than the ones corresponding to 50% shear strain. The relatively small scaling factor used in the El Centro ground motion was due to the size of the EDs. In reality, bigger dampers would have been used (as was also seen in Chapter 5) in a realistic building. This could have been achieved by scaling the dampers' forces and displacement during a test applying stronger ground motions, or by directly scaling down the ground motion keeping the size of the dampers and their corresponding displacements the same. The latter approach was preferred here.

The results (Figures 6.20 and 6.21) showed a very good agreement between measured and target displacement, while the time delay was decreased from approximately 13.5 ms (this value was based on Figure 6.22) to 1.2 ms. The amplitude error reached a maximum of 0.03%, while the NRMS error between target and measured displacement was 1.57%, demonstrating the effectiveness of the method. The time variation of the α_i coefficients shows that even though a relative large peak was observed for the α_0, and α_1 coefficients at the beginning of the RTS test, it can be concluded that the initial estimates of these coefficients were capable of capturing the characteristics of the servo-hydraulic system. The corresponding force-displacement relationship of the EDs and its comparison with the hysteretic model proposed in Chapter 4 is shown in Figure 6.23. A very good agreement (1.9% NRMS error) was achieved between the proposed MGMM and the force data extracted from the RTS test, giving confirmation of the model's predictive ability under realistic dynamic loading conditions.

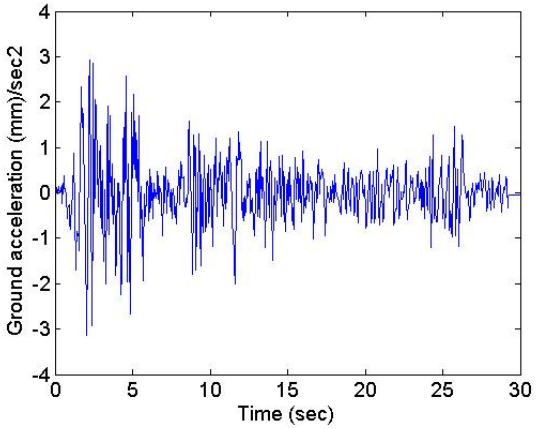

Figure 6.19: ElCentro ground acceleration

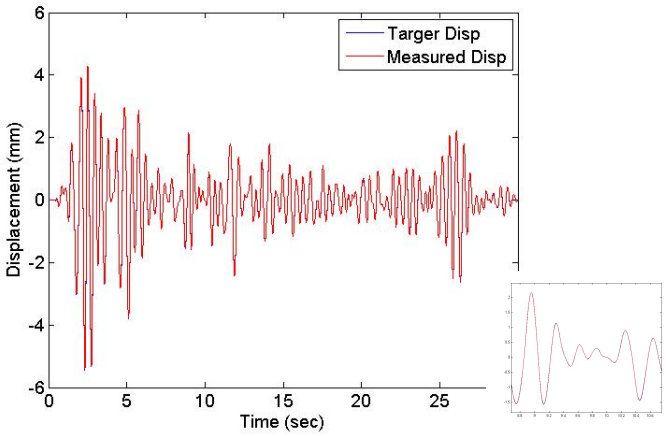

Figure 6.20: Comparison of target and measured displacements during RTS test for SDOF frame

Table 6.3: Evaluation of the modified ATS compensator for SDOF frame under ElCentro

Evaluation Parameters	**ElCentro Earthquake**
NRMS (%)	1.57
Time Delay (ms)	1.2
Amplitude error (%)	0.03

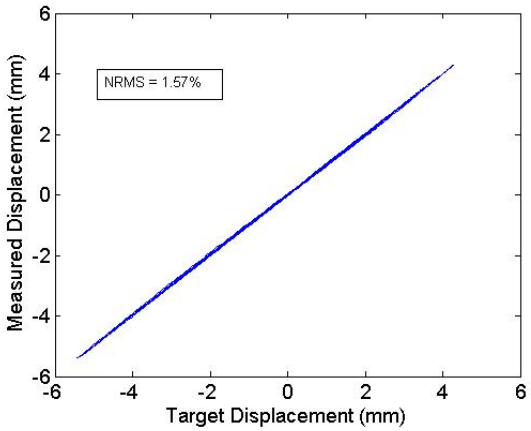

Figure 6.21: Comparison of target and measured displacement during RTS test for SDOF frame - Sychronization plot

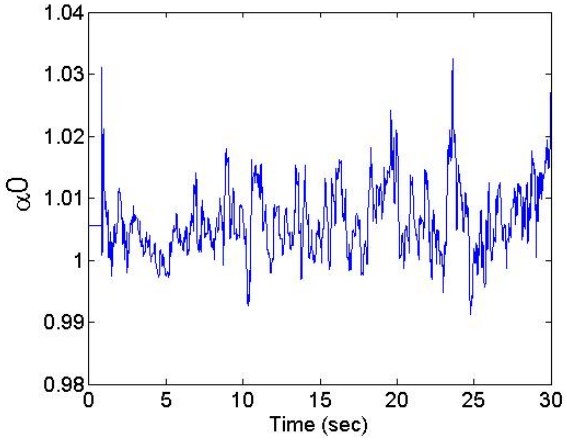

(a) α_0 - SDOF frame

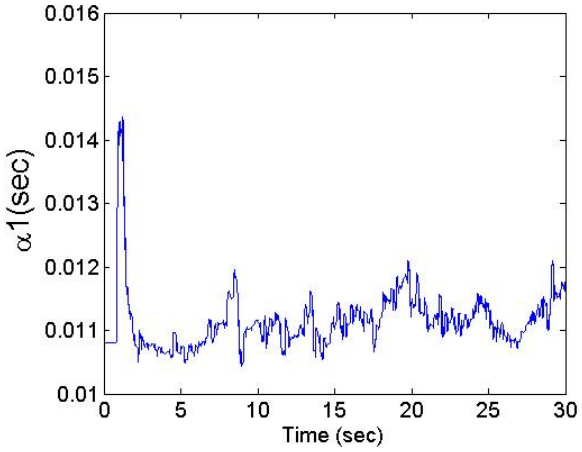

(b) α_1 - SDOF frame

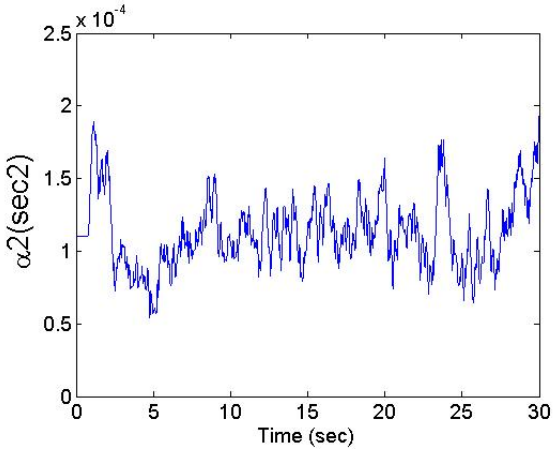

(c) α_2 - SDOF frame

Figure 6.22: Time variation of the α_i coefficients of the modified ATS compensator during the scaled ElCentro Earthquake for SDOF frame

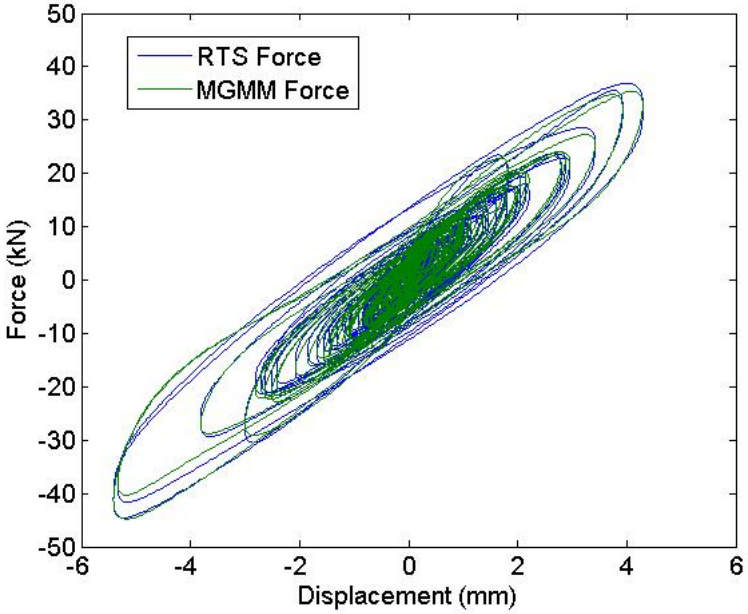

(a) Force-displacement domain

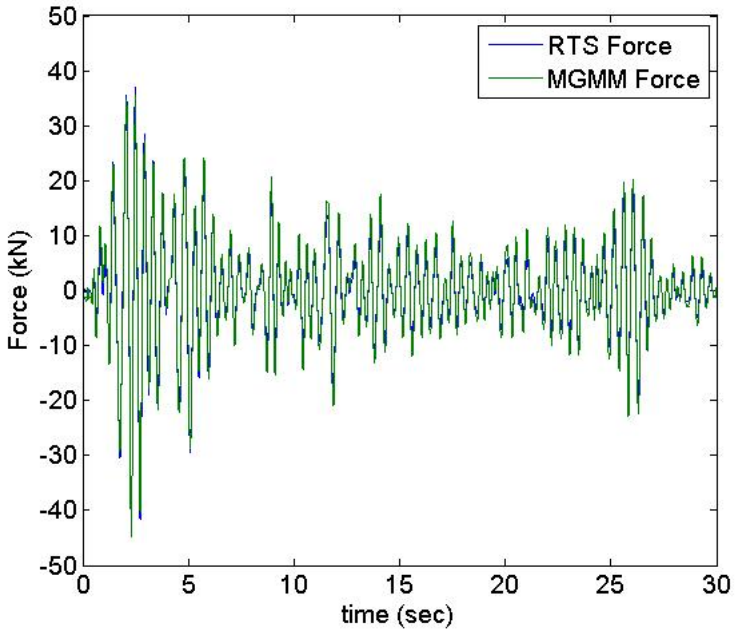

(b) Force-time domain

Figure 6.23: Comparison of MGMM and RTS force under scaled ElCentro Earthquake for SDOF frame

6.2.6 RTS test in MDOF structure

The final series of tests was focused on capturing the behaviour of the EDs under the El Centro earthquake in a very simple MDOF frame. A 1-bay, 3 storey shear-type structure was modelled in Simulink, in a similar way to the SDOF case. EDs were added at the first story only. The storey stiffnesses assigned were 22.6x10^6, 22.6x10^6, and 18.08x10^6, N/m for the first, second, and third floor respectively. The analytical frame also included masses of 143.26, 143.26, and 71.63 *tons* assigned at the first, second, and third floor respectively. The corresponding natural frequencies are 1.0826, 2.7746, and 3.67 Hz. The same limitations with the SDOF numerical substructure which was tested in the previous section apply to the MDOF frame as well, resulting in relatively low values of natural frequencies. The damping matrix assigned to the numerical substructure was based on Rayleigh damping, and a ratio, ζ, of 0.02 for the first and third mode. Since, the addition of the dampers alters the dynamic characteristics of the MDOF frame, it was decided not to analyse the RTS test based on modal time history analysis, but proceed with the original time integration time history analysis:

$$[M]\{\ddot{x}\} + [C]\{\dot{x}\} + [K]\{x\} + [F_D] = -[M]\{e\}\{\ddot{x}_g\} \tag{6.30}$$

where K is the elastic storey stiffness, C is the damping matrix, M is the mass matrix, $\{e\}$ is a 3x1 vector of ones, $\{\ddot{x}\}$, $\{\dot{x}\}$, and $\{x\}$ are 3x1 vectors representing the acceleration, velocity, and displacement of each floor. $[F_d]$ is a 3x1 vector representing the EDs contribution to the MDOF frame: $[0\ 0\ F_{ED}]^{\mathrm{T}}$, where F_{ED} is the force feedback from the device during the RTS test. The same ground motion was selected (1940 El Centro earthquake), but in order to produce slightly less than 50% EDs' shear strain, it had to be scaled down to 0.0288 g (equivalent to a 0.09 scale factor).

RTS tests for the MDOF frame validated the effectiveness of the proposed delay compensator as well. The NRMS error reached the value of 1.17%, while Figures 6.24 and 6.25 show that good agreement was achieved between the measured and the target displacement. The maximum time delay observed during the RTS test was

1.6 ms, while the amplitude error was shown once again to play a minimal role to the behaviour of the servo-hydraulic system since the corresponding error was not more than 0.1%. Figure 6.26 shows the time variation of the α_i coefficients. The mean values which were used as initial assumptions were found to effectively capture the mean values of these coefficients during the RTS test. The α_0 coefficient was almost 1 during the whole test, concluding that the amplitude error was minimal, while the time variation of the α_1 coefficient shows that the mean actuation time delay is approximately 11 ms, a value which is very close to the initial assumption. With regard to the hysteretic behaviour, Figure 6.27 shows again that the proposed MGMM is capturing the dynamic characteristics of the EDs very well under realistic conditions (1.95% NRMS error).

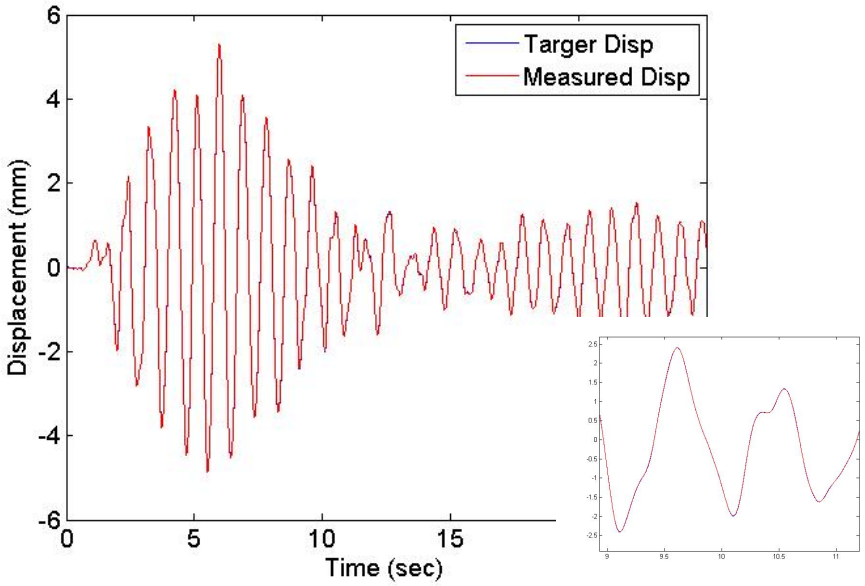

Figure 6.24: Comparison of target and measured displacements during RTS test for MDOF frame

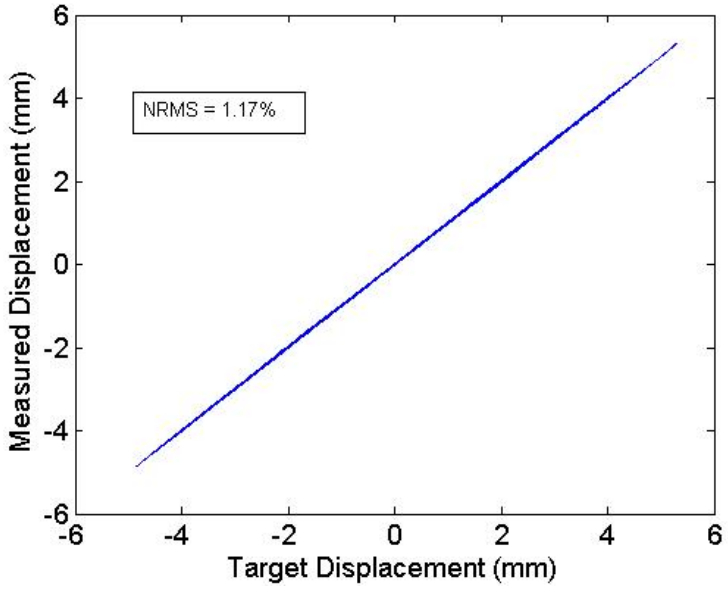

Figure 6.25: Comparison of target and measured displacement during RTS test for MDOF frame - Sychronization plot

Table 6.4: Evaluation of the modified ATS compensator for MDOF frame under ElCentro

Evaluation Parameters	**ElCentro Earthquake**
NRMS (%)	1.17
Time Delay (ms)	1.6
Amplitude error (%)	0.09

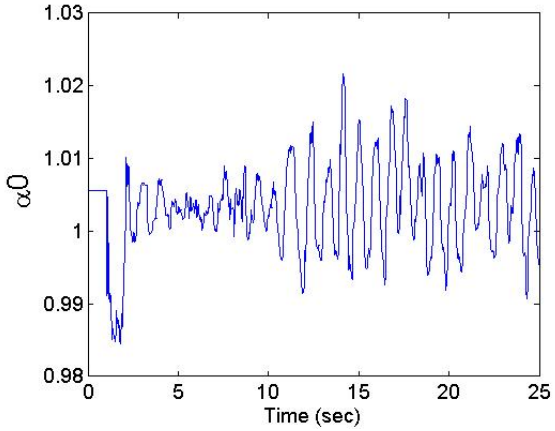

(a) α_0 - MDOF frame

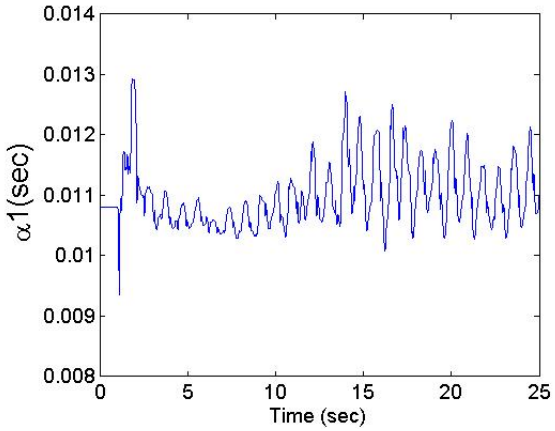

(b) α_1 - MDOF frame

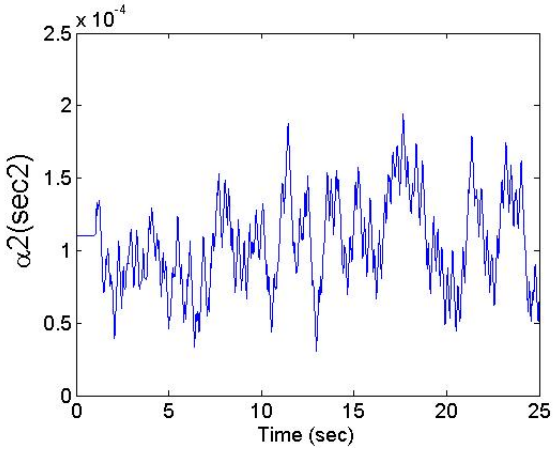

(c) α_2 - MDOF frame

Figure 6.26: Time variation of the α_i coefficients of the modified ATS compensator during the scaled ElCentro Earthquake for MDOF frame

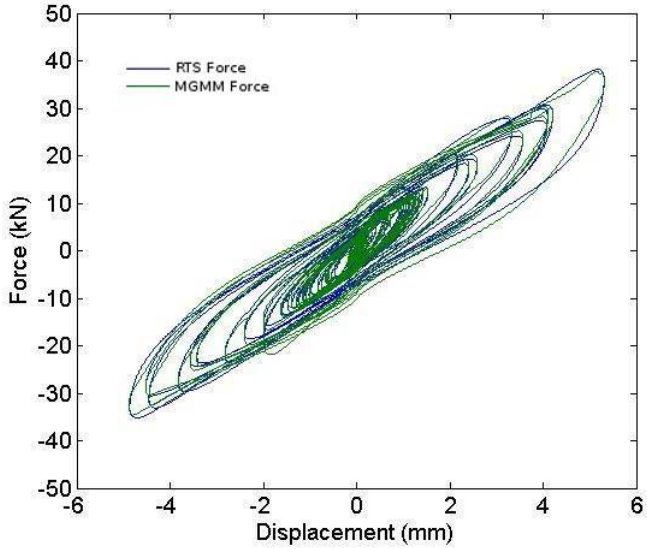

(a) Force-displacement domain

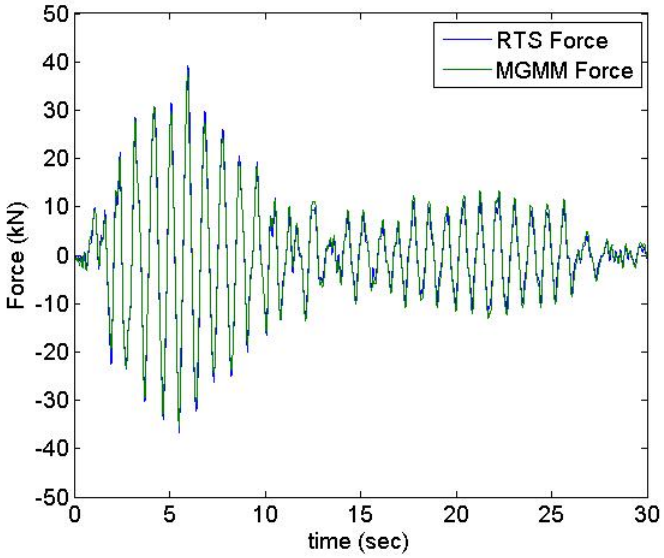

(b) Force-time domain

Figure 6.27: Comparison of MGMM and RTS force under scaled ElCentro Earthquake for MDOF frame

6.3 Conclusions

The use of real time substructure testing to achieve additional validation of the MGMM and the effectiveness of elastomeric dampers was the focus of this chapter. A new method based on the Adaptive Time Series (ATS) method was proposed by Malloy and Blakeborough (unpublished), in order to minimize the delay between the target and measured displacement, since it has been proven that this parameter highly affects the stability of servo-hydraulic systems. This method is based on the original ATS method proposed by Chae [21]. However, in comparison with the original ATS where only 1 every 16 data was used, all the sample data are being used in the modified ATS compensator in order to determine the corresponding coefficients. The results showed that this method reduces the time delay by approximately 90% to a range of 0.5-1.6 ms. The amplitude error was shown to have minimal effect. The corresponding NRMS errors were largely decreased as well.

Relatively small values of natural frequencies were selected for both SDOF and MDOF numerical substructures. Since the primary aim of this chapter was to evaluate the performance of the EDs hysteretic model, which was proposed in Chapter 4, and its dynamic behaviour under relevantly realistic conditions, and not to extensively evaluate and optimize every parameter of the proposed modified ATS method, the numerical substructures were kept simple and stability of the actuation system was prioritised. Due to the dependence of instability of the system of the natural frequency of the system, it was preferred to use low frequency frames. Further research is currently being carried out by Malloy and Blakeborough in order to further validate this new modified ATS method on Buckling Restrained Braces with more sophisticated numerical substructures, and parametric analyses.

Regarding the validation of the dampers hysteresis model, a very good agreement was achieved for both SDOF and MDOF cases (1.9%, and 1.95% NRMS error respectively). This further boosts our confidence that the specific model can be used in the analysis of real structures, and not necessarily be useful only for academic purposes.

Chapter 7

Conclusions

7.1 Overview of thesis

Passive dissipative devices have been proved to be effective under strong earthquakes with regard to the seismic protection of buildings. Elastomeric dampers can be a very efficient method of seismic enhancement as well. However, limited experimental studies, lack of information regarding how elastomeric dampers behave in a macroscopic way through time, along with the fact that the majority of the elastomers have been used in base isolation techniques creates the need for further analytical and experimental validation regarding their effectiveness and modelling approach for improvement of earthquake response of structures.

Two elastomeric dampers were provided by TARRC. In order to determine the main characteristics of these dampers a series of tests was carried out in a range of strain amplitudes, frequencies, and ambient temperatures in a form of sinusoidal displacement time history commands. Based on the corresponding force-displacement relationships the main characteristics of the dampers were extracted: shear storage modulus, G', and loss factor, n. It was shown that the displacement was the dominant factor which affected the dampers' characteristics the most, in contrast with the frequency. Especially the loss factor remained almost constant regardless of any frequency alteration. Moreover, it was shown that for strain amplitudes below 30% both G', and n exhibit large decrease. However, above 30% the rate of decrease massively decreases. It also seems that loading frequency and strain amplitude have

the exact opposite effects. Another noticeable conclusion is that the dampers exhibit approximately linear visco-elastic behaviour for strain below 30%. The value of strain amplitude of 30% works as some type of trigger point of the material. Above this point the dampers exhibit a more classical elastomeric behaviour, which shows to be less and less dependent on the frequency. With regard to the temperature effect, both G' and n decrease with any increase of temperature. However, it was shown that only strain amplitude effect could change the dampers hysteretic loop; whereas the frequency and the temperature affect the mechanical properties of the damper, but not its hysteretic shape.

As part of this thesis a new hysteretic model (MGMM) for capturing the behaviour of elastomeric dampers under dynamic loading has been developed and experimentally validated. This model was based on a modified version of the well known Generalised Maxwell Model. Part of the proposed model, is the development of a force-displacement relationship for N Maxwell elements in time domain. However, it was seen that using $N = 1$ Maxwell element was able to capture well the dynamic characteristics of the damper, where the maximum NRMS error observed was 1.83%. Furthermore, based on a simplified assumption that all the parameters of the MGMM alter with the same rate with temperature, a new parameter γ_T was introduced. Hence, keeping all the parameters of the MGMM constant and change only the new parameter γ_T was adequate and efficient enough to capture the behaviour of the dampers under different temperatures. Hence, the proposed model was able to represent the dampers performance under a range of strain amplitudes, loading frequencies, and ambient frequencies with accuracy.

MGMM was incorporated into OpenSees in order to evaluate the dampers' contribution to the seismic resistance of a 10 storey steel moment resisting frame. The frame was analytically evaluated under 20 ground motions, which were scaled in order to match the EC8 response spectrum, using non linear analyses. Great improvement was observed, since the addition of the dampers led the structure to achieve an enhanced performance level compared to the one which was initially designed. The structure was tested under both DBE and MCE levels for two different cases: with and without elastomeric dampers. When dampers were added an addi-

tional damping of 10% was achieved which caused the building to exhibit only minor damage even under ground motions scaled to MCE level. More specifically, DMRF exhibited a mean lateral drift of 1.1% under DBE which was one of the main initial target performance criteria, while residual displacements were almost eliminated. The results were more impressive when the frame was tested under MCE level; the mean interstorey drifts were decreased by 45%, and the residual drifts by 83%.

In order to further validate the proposed constitutive model RTS tests were carried out for both simple SDOF and MDOF frames equipped with elastomeric dampers. The analytical model was shown to be able to capture the dynamic characteristics of the damper even under realistic conditions. In order to minimise the unavoidable time delay and amplitude error an unpublished method (modified ATS method) proposed by Malloy and Blakeborough was used, which was found to highly decrease the time delay.

Overall, it can be concluded that essential progress was achieved in advancing the usability of elastomeric dampers for seismic mitigation. Furthermore, a clear understanding on how elastomeric dampers behave with regard to their dynamic characteristics was achieved.

7.2 Recommendations for future work

The proposed model was validated under a series of tests in a range of strain amplitudes, loading frequencies and ambient temperatures. The model can be further validated or optimised under wider range of these parameters, especially under lower values of ambient temperature. Unfortunately due to lack of funds no approach could be followed in this research to carry out series of tests while keeping the temperature constant under lower values of the ambient temperature (lower than 20^{o}C).

One other possible idea for future work would be the effect of the elastomeric dampers in structures designed based on different materials, such as concrete or timber. Furthermore, keeping the material the same but changing the dynamic characteristics of the building could provide us with an optimization tool regarding the effect of the dampers in different type of structures. Then a total comparison of

the effect of the dampers in any type of structure would be possible. Another useful modelling approach of elastomeric dampers could be the combination of elastomers with a type of either steel dampers/fuses which could be able to control the maximum force extracted from the dampers during strong ground motions, probably resulting in a more visco-plastic behaviour.

Lastly, a more advanced RTS tests could give a better understanding and confidence to the proposed hysteretic model. Furthermore, more advanced numerical substructures could be carried out to evaluate the effect of the dampers in more realistic conditions.

Appendix A

Mechanical Properties of the Elasomteric Dampers

Table A.1: Mechanical Properties at a range of strain amplitudes, frequencies at 20°C

Shear Strain %	**Frequency (Hz)**	**G′(Mpa)**	**Geq (Mpa)**	**n**
10	0.25	1.356	1.677	0.407
	0.5	1.362	1.656	0.414
	1	1.469	1.770	0.409
	2	1.616	1.912	0.402
	3	1.701	2.002	0.398
	4	1.765	2.068	0.394
20	0.25	1.042	1.295	0.355
	0.5	1.075	1.258	0.352
	1	1.149	1.344	0.354
	2	1.244	1.438	0.350
	3	1.298	1.507	0.349
	4	1.338	1.559	0.347
30	0.25	0.875	1.089	0.334
	0.5	0.916	1.074	0.333
	1	0.976	1.139	0.334
	2	1.048	1.226	0.336
	3	1.090	1.278	0.333
	4	1.119	1.321	0.332
40	0.25	0.807	1.046	0.329
	0.5	0.843	0.990	0.326
	1	0.892	1.051	0.330
	2	0.948	1.121	0.331
	3	0.983	1.167	0.329
	4	1.013	1.209	0.327
50	0.25	0.766	0.946	0.301
	0.5	0.801	0.937	0.304
	1	0.844	0.986	0.308
	2	0.893	1.049	0.310
	3	0.920	1.095	0.311
	4	0.948	1.132	0.309

Table A.2: Mechanical Properties at a range of strain amplitudes, frequencies at 25°C

Shear Strain %	**Frequency (Hz)**	**G′(Mpa)**	**Geq (Mpa)**	**n**
10	0.25	1.314	1.732	0.388
	0.5	1.328	1.622	0.377
	1	1.431	1.722	0.371
	2	1.547	1.843	0.367
	3	1.622	1.921	0.363
	4	1.663	1.992	0.364
20	0.25	1.007	1.245	0.329
	0.5	1.010	1.201	0.330
	1	1.076	1.274	0.330
	2	1.157	1.359	0.327
	3	1.207	1.419	0.325
	4	1.246	1.470	0.323
30	0.25	0.829	1.046	0.319
	0.5	0.860	1.022	0.312
	1	0.911	1.076	0.312
	2	0.974	1.158	0.315
	3	1.008	1.202	0.310
	4	1.041	1.243	0.309
40	0.25	0.746	0.931	0.302
	0.5	0.773	0.916	0.299
	1	0.816	0.970	0.303
	2	0.861	1.036	0.306
	3	0.893	1.079	0.304
	4	0.917	1.108	0.301
50	0.25	0.696	0.878	0.296
	0.5	0.720	0.854	0.291
	1	0.755	0.904	0.297
	2	0.795	0.962	0.301
	3	0.823	1.002	0.296
	4	0.839	1.030	0.300

Table A.3: Mechanical Properties at a range of strain amplitudes, frequencies at 30°C

Shear Strain %	**Frequency (Hz)**	**G′(Mpa)**	**Geq (Mpa)**	**n**
10	0.25	1.126	1.373	0.361
	0.5	1.129	1.370	0.369
	1	1.206	1.449	0.367
	2	1.307	1.553	0.361
	3	1.375	1.619	0.355
	4	1.420	1.684	0.355
20	0.25	0.875	1.052	0.317
	0.5	0.893	1.050	0.319
	1	0.951	1.116	0.320
	2	1.021	1.194	0.319
	3	1.068	1.254	0.315
	4	1.096	1.294	0.314
30	0.25	0.764	0.937	0.306
	0.5	0.797	0.935	0.301
	1	0.841	0.987	0.305
	2	0.894	1.053	0.304
	3	0.932	1.106	0.300
	4	0.952	1.135	0.302
40	0.25	0.674	0.775	0.278
	0.5	0.707	0.818	0.284
	1	0.749	0.873	0.289
	2	0.788	0.934	0.294
	3	0.819	0.976	0.291
	4	0.839	1.005	0.290
50	0.25	0.656	0.806	0.281
	0.5	0.680	0.802	0.280
	1	0.710	0.837	0.283
	2	0.748	0.892	0.286
	3	0.778	0.940	0.286
	4	0.817	0.969	0.278

Table A.4: Mechanical Properties at a range of strain amplitudes, frequencies at 35°C

Shear Strain %	**Frequency (Hz)**	**G′(Mpa)**	**Geq (Mpa)**	**n**
10	0.25	1.005	1.208	0.350
	0.5	1.017	1.192	0.352
	1	1.079	1.266	0.352
	2	1.169	1.370	0.349
	3	1.219	1.431	0.346
	4	1.266	1.484	0.343
20	0.25	0.804	0.934	0.297
	0.5	0.819	0.946	0.305
	1	0.874	1.006	0.306
	2	0.936	1.082	0.306
	3	0.972	1.124	0.302
	4	1.004	1.166	0.300
30	0.25	0.726	0.833	0.284
	0.5	0.765	0.882	0.288
	1	0.814	0.945	0.290
	2	0.814	0.945	0.290
	3	0.848	0.987	0.287
	4	0.864	1.017	0.287
40	0.25	0.644	0.779	0.281
	0.5	0.669	0.775	0.279
	1	0.705	0.818	0.283
	2	0.746	0.875	0.285
	3	0.770	0.908	0.282
	4	0.791	0.936	0.279
50	0.25	0.609	0.719	0.260
	0.5	0.632	0.728	0.266
	1	0.660	0.767	0.272
	2	0.695	0.817	0.274
	3	0.715	0.851	0.274
	4	0.732	0.877	0.274

Appendix B

MGMM validated against sweep amplitude tests in different temperatures

This appendix presents how the MGMM is efficient to capture the dynamic response of the EDs with regard to test under different temperatures:

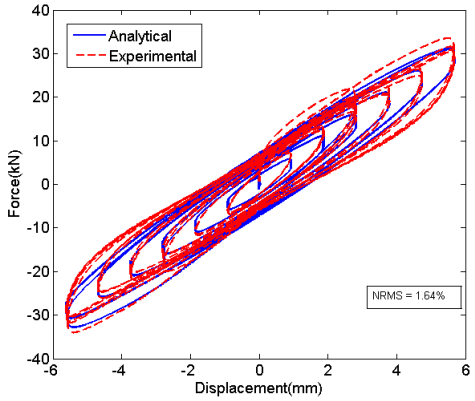

Figure B.1: Comparison of force between experiment and MGMM model for sweep amplitude test - 0.25 Hz, 25°C

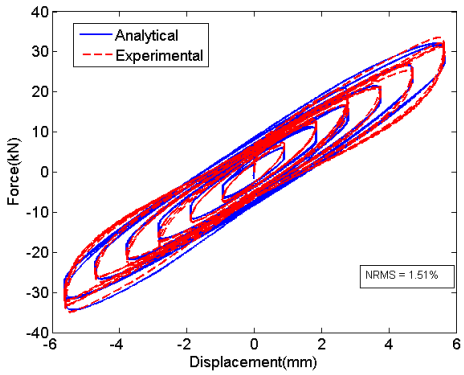

Figure B.2: Comparison of force between experiment and MGMM model for sweep amplitude test - 0.5 Hz, 25°C

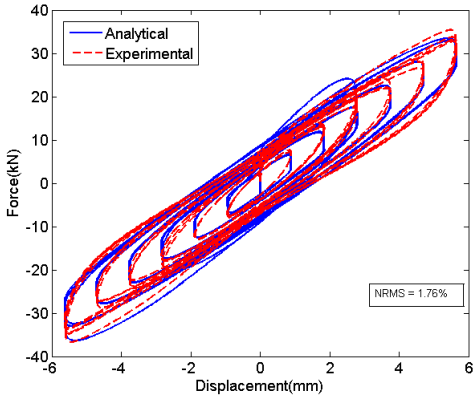

Figure B.3: Comparison of force between experiment and MGMM model for sweep amplitude test - 1.0 Hz, 25°C

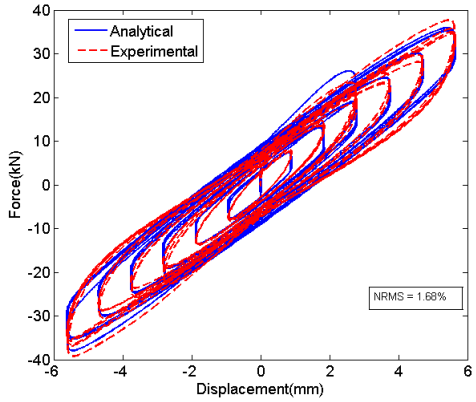

Figure B.4: Comparison of force between experiment and MGMM model for sweep amplitude test - 2.0 Hz, 25°C

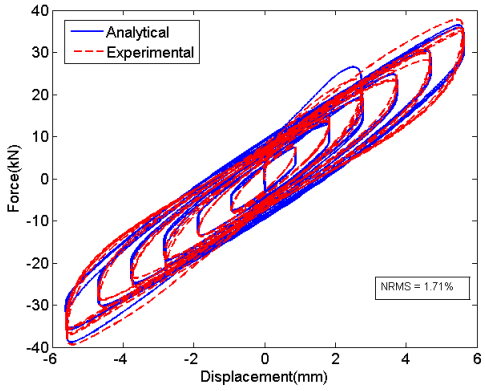

Figure B.5: Comparison of force between experiment and MGMM model for sweep amplitude test - 3.0 Hz, 25°C

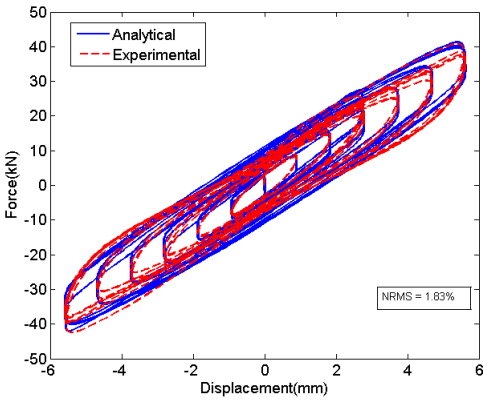

Figure B.6: Comparison of force between experiment and MGMM model for sweep amplitude test - 4.0 Hz, 25°C

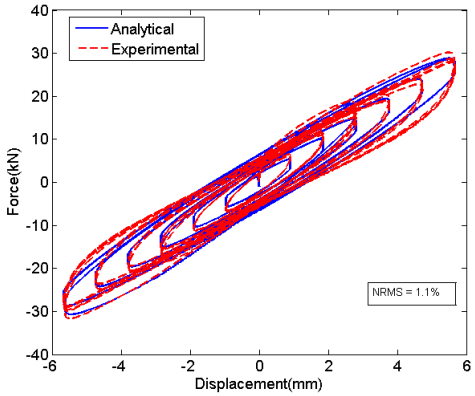

Figure B.7: Comparison of force between experiment and MGMM model for sweep amplitude test - 0.25 Hz, 30°C

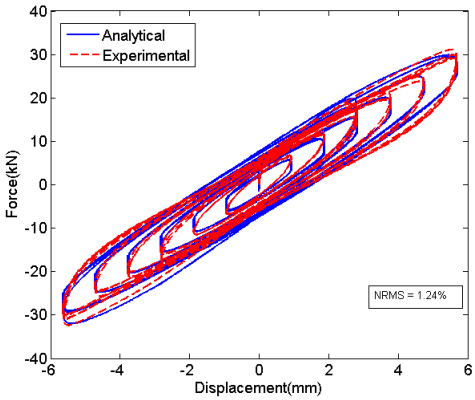

Figure B.8: Comparison of force between experiment and MGMM model for sweep amplitude test - 0.5 Hz, 30°C

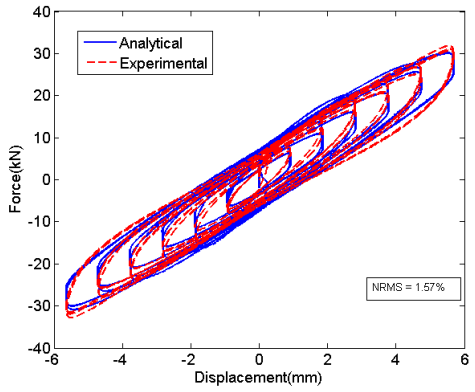

Figure B.9: Comparison of force between experiment and MGMM model for sweep amplitude test - 1.0 Hz, 30°C

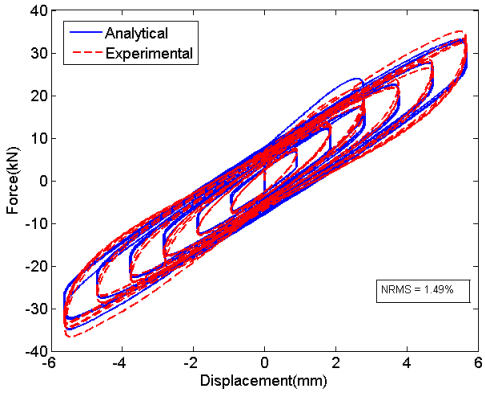

Figure B.10: Comparison of force between experiment and MGMM model for sweep amplitude test - 2.0 Hz, 30°C

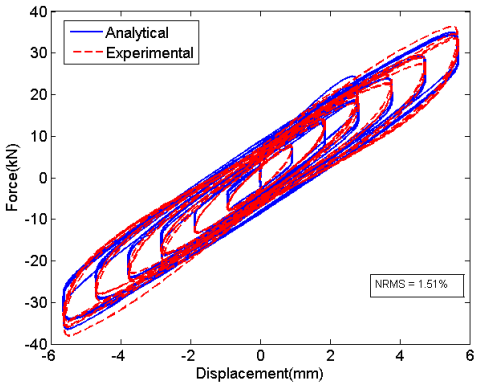

Figure B.11: Comparison of force between experiment and MGMM model for sweep amplitude test - 3.0 Hz, 30°C

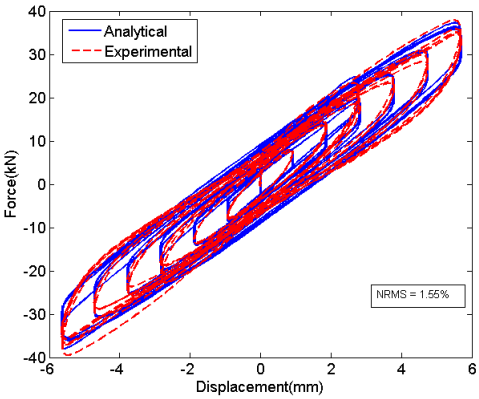

Figure B.12: Comparison of force between experiment and MGMM model for sweep amplitude test - 4.0 Hz, 30°C

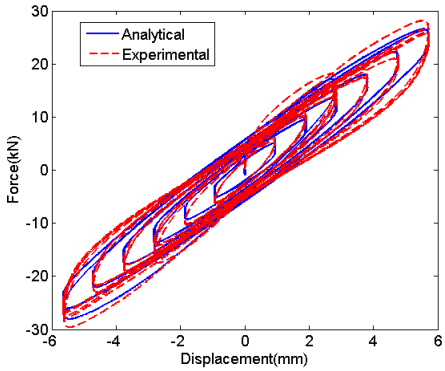

Figure B.13: Comparison of force between experiment and MGMM model for sweep amplitude test - 0.25 Hz, 35°C

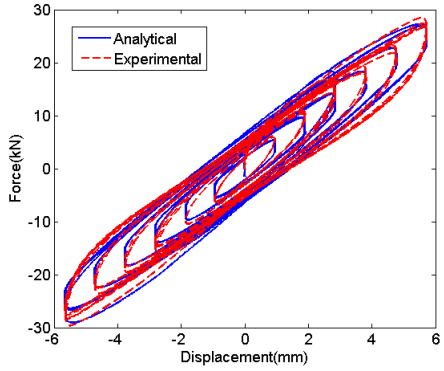

Figure B.14: Comparison of force between experiment and MGMM model for sweep amplitude test - 0.5 Hz, 35°C

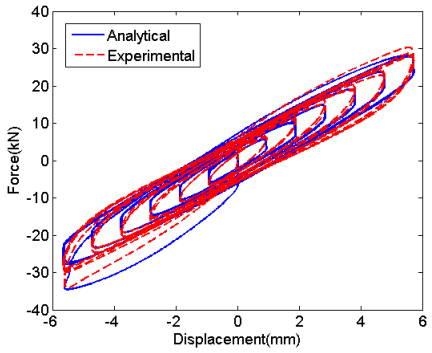

Figure B.15: Comparison of force between experiment and MGMM model for sweep amplitude test - 1.0 Hz, 35°C

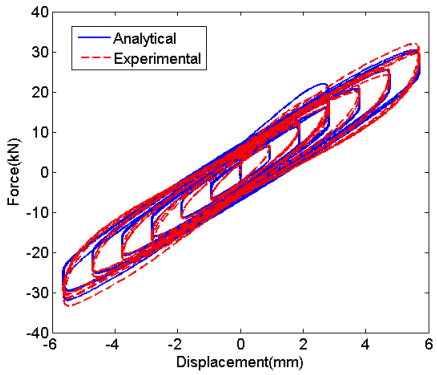

Figure B.16: Comparison of force between experiment and MGMM model for sweep amplitude test - 2.0 Hz, 35°C

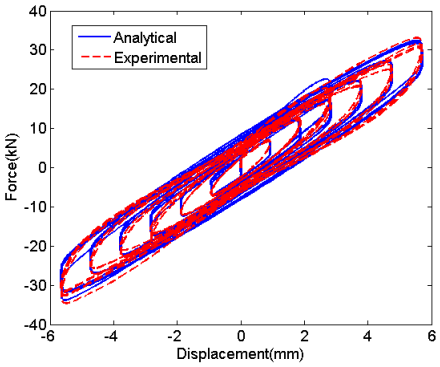

Figure B.17: Comparison of force between experiment and MGMM model for sweep amplitude test - 3.0 Hz, 35°C

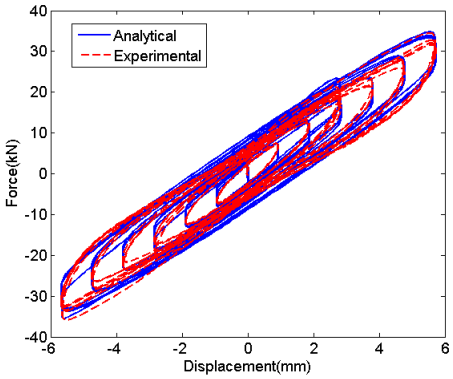

Figure B.18: Comparison of force between experiment and MGMM model for sweep amplitude test - 4.0 Hz, 35°C

Bibliography

[1] Eurocode 3: Design of steel structures —part 1-1:general rules and rules for buildings, cen, brussels.

[2] Eurocode 8: Design of structures for earthquake resistance—part 1: General rules, seismic actions and rules for buildings, cen, brussels.

[3] Peer (pacific earthquake engineering research center). 2015. opensees v2.4.6. berkeley: University of california berkeley.

[4] Structural applications of taylor fluid viscous dampers. `http://taylordevices.com/pdf/Yearly-updates/YearlyUpdatedStructuralApplicationChart.pdf`. Accessed: 2017-12-11.

[5] *FEMA. Prestandard and Commentary for the Seismic Rehabilitation of Buildings. Report No. FEMA356, Federal Emergency Management Agency: Washington, DC*, 2001.

[6] *VERLAG MODERNE INDUSTRIE Technical Elastomers, The basis of high-tech sealing and vibration control technology solutions*, 2006.

[7] *MathWorks, Mathworks MATLAB Simulink, Available: http://www.mathworks.com/products/simulink/*, 2007.

[8] Rodolfo A., Francesco B., Gabriella C. M., Ahmadi H., Goodchild I, and Fuller K. Viscoelastic dampers for seismic protection of buildings: An application to an existing building. In *Fifth World Congress on Joints, Bearings and Seismic Systems for Concrete Structures*, 2002.

[9] I Aiken. An analytical hysteresis model for elastomeric seismic isolation bearings. *Earthquake Engineering and Structural Dynamics*, 26(2), 1997.

[10] I.D. Aiken and J.M. Kelly. *Earthquake simulator testing and analytical studies of two energy-absorbing systems for multistory structures.* University of California, Berkeley, 1990.

[11] F. Arima, M. Miyazaki, H. Tanaka, and Y. Yamazaki. A study on buildings with large damping using viscous damping walls. In *Proceedings of the 9th World Conference on Earthquake Engineering*, volume 821, 1988.

[12] Michael J Astrella and Andrew Stuart Whittaker. *The performance-based design paradigm.* Number 11. Multidisciplinary Center for Earthquake Engineering Research, 2005.

[13] Klaus-Jürgen Bathe and Edward L Wilson. *Numerical methods in finite element analysis.* Prentice-Hall Englewood Cliffs, NJ, 1976.

[14] C.J. Black, N. Makris, and I.D. Aiken. Component testing, seismic evaluation and characterization of buckling-restrained braces. *Journal of Structural Engineering*, 130(6):880–894, 2004.

[15] A Blakeborough, MS Williams, AP Darby, and DM Williams. The development of real–time substructure testing. *Philosophical Transactions of the Royal Society of London A: Mathematical, Physical and Engineering Sciences*, 359(1786):1869–1891, 2001.

[16] P. Bogacki and L.F. Shampine. A 3(2) pair of Runge - Kutta formulas. *Applied Mathematics Letters*, 2(4):321 – 325, 1989.

[17] P. A. Bonnet, C. N. Lim, M. S. Williams, A. Blakeborough, S. A. Neild, D. P. Stoten, and C. A. Taylor. Real-time hybrid experiments with newmark integration, m.c.smd outer-loop control and multi-tasking strategies. *Earthquake Engineering & Structural Dynamics*, 36(1):119–141, 2007.

[18] P.A. Bonnet. *The development of multi-axis real-time substructure testing.* PhD thesis, University of Oxford, 2006.

[19] R. Bouc. Forced vibration of mechanical system with hysteresis. In *Proc., 4th Conf. on Nonlinear Oscillation, Prague, Czechoslovakia.*, 1967.

[20] Eduardo C.C. *Overview of Eurocode 8*, 2011 (accessed February 3, 2016). `http://eurocodes.jrc.ec.europa.eu/doc/WS_335/S1_EC8-Lisbon_E%20CARVALHO.pdf`.

[21] Y. Chae, K. Kazemibidokhti, and J.M. Ricles. Adaptive time series compensator for delay compensation of servo-hydraulic actuator systems for real-time hybrid simulation. *Earthquake Engineering & Structural Dynamics*, 42(11):1697–1715, 2013.

[22] K.C. Chang, ML Lai, Tsu T Soong, DS Hao, and YC Yeh. Seismic behavior and design guidelines for steel frame structures with added viscoelastic dampers, technical report nceer-93-0009. 1993.

[23] K.C. Chang, YY Lin, and ML Lai. Seismic analysis and design of structures with viscoelastic dampers. *ISET Journal of Earthquake Technology*, 143-166, 1998.

[24] K.C. Chang, TT Soong, and ML Lai. Development of a design procedure for structure with added viscoelastic dampers. *Applied Technology Council, ACT-17-1*, 1993.

[25] K.C. Chang, TT Soong, ML Lai, and EJ Nielsen. Viscoelastic dampers as energy dissipation devices for seismic applications. *Earthquake Spectra*, 9(3):371–387, 1993.

[26] Kuo-Chun Chang, Yu-Yuan Lin, and Chang-Yu Chen. Shaking table study on displacement-based design for seismic retrofit of existing buildings using nonlinear viscous dampers. *Journal of structural engineering*, 134(4):671–681, 2008.

[27] A.K. Chopra. *Dynamics of structures: theory and applications to earthquake engineering*. Prentice-Hall, 2001.

[28] C. Christopoulos and A. Filiatrault. *Principles of Passive Supplemental Damping and Seismic Isolation*. IUSS Press, 2006.

[29] C. Christopoulos and M. Montgomery. Viscoelastic coupling dampers (vcds) for enhanced wind and seismic performance of high-rise buildings. *Earthquake Engineering & Structural Dynamics*, 42(15):2217–2233, 2013.

[30] W.J. Chung, C.B. Yun, N.S. Kim, and J.W. Seo. Shaking table and pseudodynamic tests for the evaluation of the seismic performance of base-isolated structures. *Engineering Structures*, 21(4):365 – 379, 1999.

[31] M.C. Constantinou, T.T. Soong, and G.F. Dargush. *Passive energy dissipation systems for structural design and retrofit*. Multidisciplinary Center for Earthquake Engineering Research Buffalo, New York, M.C.EER Monograph No. 1, 1998.

[32] M.C. Constantinou, MD Symans, P Tsopelas, and DP Taylor. Fluid viscous dampers in applications of seismic energy dissipation and seismic isolation. *Proceedings ATC 17*, 1:581–592, 1993.

[33] M.C. Constantinou and I.G. Tadjbakhsh. Hysteretic dampers in base isolation: random approach. *Journal of Structural Engineering*, 111(4):705–721, 1985.

[34] JP Den Hartog and JP Den Hartog fourth edition Mechanical. *Vibrations*. M.C.Graw-Hill Book Company, Inc., New York, 1956.

[35] S.N. Dermitzakis and S.A. Mahin. Development of substructure techniques for online computer controlled seismic performance testing. Technical report, College of Engineering, University of California, Berkeley, California, 1985.

[36] J. Dimig, C. Shield, C. French, F. Bailey, and A. Clark. Effective force testing a method of seismic simulation for structural testing. *Journal of Structural Engineering*, 125(9):1028–1037, 1999.

[37] J. Donea, G. Magonette, P. Negro, P. Pegon, A. Pinto, and G. Verzeletti. Pseudodynamic capabilities of the ELSA laboratory for earthquake testing of large structures. *Earthquake Spectra*, 12(1):163–180, 1996.

[38] Pant D.R., Montgomery M., Christopoulos C., and Poon D. Viscoelastic coupling dampers for the enhanced seismic resilience of a megatall building. In *16th World Conference on Earthquake Engineering, 16WCEE 2017*, volume 1318, 2017.

[39] U. Droka and J. Garcia. Seismic qualification of passive mitigation devices. Report no.1,2005, Cooperative Advancements in Seismic and Dynamic Experiments (CASCADE), 2005.

[40] RM Elhassan, A Arminak, GC Hart, G Brandow, and X Liu. The design of analysis of a seismic retrofit of a tall concrete building using supplemental viscous dampers. In *1996 Tall Buildings Annual Meeting. Los Angeles Tall Buildings Structural Design Council*, pages 96–7, 1996.

[41] Y Fahjan and Z Ozdemir. Scaling of earthquake accelerograms for nonlinear dynamic analysis to match the earthquake design spectra. In *The 14th World Conference on Earthquake Engineering*, pages 12–17. Chinese Society for Earthquake Engineering Beijing, China, 2008.

[42] C.P. Fan. *Seismic Analysis, Behavior, and Retrofit of Non-Ductile Reinforced Concrete Frame Buildings with Viscoelastic Dampers*. Ph.D. Dissertation, Department of Civil and Environmental Engineering, Lehigh University, 1998.

[43] John D Ferry. *Viscoelastic properties of polymers*. John Wiley & Sons, 1980.

[44] TF Fitzgerald, Thalia Anagnos, Mary Goodson, and Theodore Zsutty. Slotted bolted connections in aseismic design for concentrically braced connections. *Earthquake Spectra*, 5(2):383–391, 1989.

[45] H. Frahm. Device for damping vibrations of bodies., April 18 1911. US Patent 989,958.

[46] Ozdemir H. *Nonlinear Transient Dynamic Analysis of Yielding Structures*. Ph.D. Dissertation, Department of Civil and Environmental Engineering, Lehigh University, 1976.

[47] T Hale and R Pall. Seismic upgrade of the freeport water reservoir, sacramento, california. In *Twelfth World Conference on Earthquake Engineering, Auckland, New Zealand*, 2000.

[48] R.D. Hanson and T.T. Soong. *Seismic design with supplemental energy dissipation devices*. Earthquake Engineering Research Institute, 2001.

[49] CB Haselton, AS Whittaker, A Hortacsu, JW Baker, J Bray, and DN Grant. Selecting and scaling earthquake ground motions for performing response-history analyses. In *Proceedings of the 15th World Conference on Earthquake Engineering*, 2012.

[50] C. Hepburn and R.J. Reynolds. *Elastomers: Criteria for Engineering Design*. Applied Science Publishers, London, 1979.

[51] H.M. Hilber, T.J. R. Hughes, and R.L. Taylor. Improved numerical dissipation for time integration algorithms in structural dynamics. *Earthquake Engineering and Structural Dynamics*, 5(3):283–292, 1977.

[52] T. Horiuchi, M. Inoue, T. Konno, and Y. Namita. Real-time hybrid experimental system with actuator delay compensation and its application to a piping system with energy absorber. *Earthquake Engineering & Structural Dynamics*, 28(10):1121–1141, 1999.

[53] T. Horiuchi and T. Konno. A new method for compensating actuator delay in real–time hybrid experiments. *Philosophical Transactions of the Royal Society of London A: Mathematical, Physical and Engineering Sciences*, 359(1786):1893–1909, 2001.

[54] Chien-Yuan Hou, Deh-Shiu Hsu, and Hsing-Yuan Chen. Experimental verification of the restoring-stiffness concept used in fluid dampers for seismic energy dissipation. *The Structural Design of Tall and Special Buildings*, 14(1):1–13, 2005.

[55] J.S. Hwang and J.C. Wang. Seismic response prediction of HDR bearings using fractional derivative Maxwell model. *Engineering Structures*, 20(9):849–856, 1998.

[56] Vayas I., Ermopoulos I., and G. Ioannidis. *Steel Structures Design*. Klidarithmos, Athens, 2005.

[57] Conor D Johnson and David A Kienholz. Finite element prediction of damping in structures with constrained viscoelastic layers. *AIAA Journal*, 20(9):1284–1290, 1982.

[58] M. Nakashima. K. Takanashi. Japanese activities on online testing. *Journal of Engineering Mechanics*, 113:1014–1032, 1987.

[59] R. Kanitkar, M. Harms, P. Crosby, and M.L. Lai. Seismic retrofit of a steel moment frame structure using viscoelastic dampers. *J. of Earthquake Technology*, 354:207–219, 1998.

[60] T.L. Karavasilis, A. Blakeborough, and M.S. Williams. Development of nonlinear analytical model and seismic analyses of a steel frame with self-centering devices and viscoelastic dampers. *Computers & Structures*, 89(11):1232–1240, 2011.

[61] T.L. Karavasilis, J.M. Ricles, R. Sause, and Cheng Chen. Experimental evaluation of the seismic performance of steel mrfs with compressed elastomer dampers using large-scale real-time hybrid simulation. *Engineering Structures*, 33(6):1859 – 1869, 2011.

[62] T.L. Karavasilis, R. Sause, and J.M. Ricles. Seismic design and evaluation of steel moment-resisting frames with compressed elastomer dampers. *Earthquake Engineering & Structural Dynamics*, 41(3):411–429, 2012.

[63] K. Kasai, Y. Fu, and A. Watanabe. Passive control systems for seismic damage mitigation. *Journal of Structural Engineering*, 124(5):501–512, 1998.

[64] K. Kasai, J.A Munshi., M.L. Lai, and B.F. Maison. *Viscoelastic Damper Hysteretic Model: Theory, Experiment and Application.* ATC-17-1, 521-532, San Franscisco, CA, March, 1993.

[65] J.M. Kelly. Earthquake-resistant design with rubber. 1993.

[66] J.M. Kelly, R.I. Skinner, and A.J. Heine. Mechanisms of energy absorption in special devices for use in earthquake resistant structures. *Bulletin of NZ Society for Earthquake Engineering*, 5(3):63–88, 1972.

[67] Donald Knuth. *PEER (Pacific Earthquake Engineering Research Center). 2013. PEER NGA-WEST 2 ground motion database.*, 2011 (accessed February 3, 2016). `http://ngawest2.berkeley.edu/`.

[68] C.G. Koh and J.M. Kelly. Application of fractional derivatives to seismic analysis of base-isolated models. *Earthquake engineering & structural dynamics*, 19(2):229–241, 1990.

[69] A. Kontopanos. Experimental investigation of a prototype elastomeric structural damper, MSc Thesis in Civil Engineering, Lehigh University, 2006.

[70] ML Lai, P Lu, DA Lunsford, K Kasai, and K.C. Chang. Viscoelastic damper: a damper with linear or nonlinear material. In *Proceedings of 11th World Conference on Earthquake Engineering*, 1996.

[71] J. Lee. Optimal weight absorber designs for vibrating structures exposed to random excitations. *Earthquake Engineering & Structural Dynamics*, 19(8):1209–1218, 1990.

[72] K.S. Lee. *Seismic Behavior of Structures with Dampers Made from Ultra High Damping Natural Rubber.* Ph.D. Dissertation, Department of Civil and Environmental Engineering, Lehigh University, 2003.

[73] K.S. Lee, C.P. Fan, R. Sause, and J. Ricles. Simplified design procedure for frame buildings with viscoelastic or elastomeric structural dampers. *Earthquake engineering & structural dynamics*, 34(10):1271–1284, 2005.

[74] TG Lepelletier and F Raichlen. Nonlinear oscillations in rectangular tanks. *Journal of Engineering Mechanics*, 114(1):1–23, 1988.

[75] Lyan-Ywan Lu, Ging-Long Lin, and Ming-Hsiang Shih. An experimental study on a generalized maxwell model for nonlinear viscoelastic dampers used in seismic isolation. *Engineering Structures*, 34:111–123, 2012.

[76] Fardis M. *EARTHQUAKE-RESISTANT DESIGN OF CONCRETE BUILDINGS ACCORDING TO EN1998-1 (EUROCODE 8)*, 2008 (accessed October 21, 2015). `http://eurocodes.jrc.ec.europa.eu/doc/WS2008/Fardis_2008.pdf`.

[77] Paul Macioce. Viscoelastic damping 101.

[78] G. Magonette. Development and application of large–scale continuous pseudo–dynamic testing techniques. *Philosophical Transactions of the Royal Society of London A: Mathematical, Physical and Engineering Sciences*, 359(1786):1771–1799, 2001.

[79] S.A. Mahin and P.S.B. Shing. Pseudodynamic method for seismic testing. *Journal of Structural Engineering*, 111(7):1482–1503, 1985.

[80] S.A. Mahin, P.S.B. Shing, C.R. Thewalt, and R.D. Hanson. Pseudodynamic test method;current status and future directions. *Journal of Structural Engineering*, 115(8):2113–2128, 1989.

[81] P Mahmoodi, LE Robertson, M Yontar, C Moy, and L Feld. Performance of viscoelastic dampers in world trade center towers. In *Dynamics of structures*, pages 632–644. ASCE, 1987.

[82] N. Makris and M.C. Constantinou. Fractional-derivative Maxwell model for viscous dampers. *Journal of Structural Engineering*, 117(9):2708–2724, 1991.

[83] N. Makris, M.C. Constantinou, and GF Dargush. Analytical model of viscoelastic fluid dampers. *Journal of Structural Engineering*, 119(11):3310–3325, 1993.

[84] A. Manzoori and H. Toopchi-Nezhad. Application of an extended Bouc-Wen model in seismic response prediction of unbonded fiber-reinforced isolators. *Journal of Earthquake Engineering*, pages 1–18, 2016.

[85] M Martinez-Rodrigo and ML Romero. An optimum retrofit strategy for moment resisting frames with nonlinear viscous dampers for seismic applications. *Engineering Structures*, 25(7):913–925, 2003.

[86] E. Martinez-Romero. Experiences on the use of supplementary energy dissipators on building structures. *Earthquake Spectra*, 9(3):581–625, 1993.

[87] R.L. Mayes and I.N. Wassim. Comparative seismic performance of four structural systems and assessment of recent aisc brb test requirements. In *SEAOC 74th Annual Convention*, pages 251–264, 2005.

[88] Fabio Mazza and Alfonso Vulcano. Control of the earthquake and wind dynamic response of steel-framed buildings by using additional braces and/or viscoelastic dampers. *Earthquake Engineering & Structural Dynamics*, 40(2):155–174, 2011.

[89] N.G. M.C.Crum, C.P. Buckley, and C.B. Bucknall. *Principles of polymer engineering*. Oxford University Press, USA, 1997.

[90] C.C. Mei. *The Applllied Dynamics of Ocean Waves*. John Wiley, New York, 1983.

[91] M.S. Montgomery. *Fork configuration damper (FCDs) for enhanced dynamic performance of high-rise buildings, University of Toronto*. PhD thesis, 2011.

[92] S. Nagarajaiah, A.M. Reinhorn, and M.C. Constantinou. Nonlinear dynamic analysis of 3-d-base-isolated structures. *Journal of Structural Engineering*, 117(7):2035–2054, 1991.

[93] M. Nakashima. Development, potential, and limitations of real–time online (pseudo–dynamic) testing. *Philosophical Transactions of the Royal Society of London A: Mathematical, Physical and Engineering Sciences*, 359(1786):1851–1867, 2001.

[94] M. Nakashima, H. Kato, and E. Takaoka. Development of real-time pseudo dynamic testing. *Earthquake Engineering and Structural Dynamics*, 21(1):79–92, 1992.

[95] A.D. Nashif, D.I.G. Jones, and J.P. Henderson. *Vibration damping*. John Wiley & Sons, 1985.

[96] A. Neuenhofer and F.C. Filippou. Evaluation of nonlinear frame finite-element models. *Journal of structural engineering*, 123(7):958–966, 1997.

[97] YQ Ni, JM Ko, and CW Wong. Nonparametric identification of nonlinear hysteretic systems. *Journal of Engineering Mechanics*, 125(2):206–215, 1999.

[98] Douglas K Nims, Phillip J Richter, and Robert E Bachman. The use of the energy dissipating restraint for seismic hazard mitigation. *Earthquake Spectra*, 9(3):467–489, 1993.

[99] D.E. Olson and D.A. Reed. A nonlinear numerical model for sloped-bottom tuned liquid dampers. *Earthquake engineering & structural dynamics*, 30(5):731–743, 2001.

[100] A.V. Oppenheim, A.S. Willsky, and S.H. Nawab. *Signals & Systems (2Nd Ed.)*. Prentice-Hall, Inc., Upper Saddle River, NJ, USA, 1996.

[101] A.S. Pall and C. Marsh. Response of friction damped braced frames. *Journal of Structural Engineering*, 108(9):1313–1323, 1982.

[102] A.S. Pall, C. Marsh, and P. Fazio. Friction joints for seismic control of large panel structures. *PCI JOURNAL*, 25(6):38–61, 1980.

[103] K.D. Papoulia and J.M. Kelly. *Material characterization of elastomers used in earthquake base isolation*. Earthquake Engineering Research Center, University of California, 1994.

[104] W. Ramberg and W.R. Osgood. Description of stress-strain curves by three parameters. 1943.

[105] SE Randall, DM Halsted, and DL Taylor. Optimum vibration absorbers for linear damped systems. *Journal of Mechanical Design*, 103(4):908–913, 1981.

[106] David Roylance. Lecture notes in engineering viscoelasticity, 2001. Department of Materials Science and Engineering Massachusetts Institute of Technology Cambridge, MA 02139.

[107] R. Sause, K.S. Lee, and J. Ricles. Rate-independent and rate-dependent models for hysteretic behavior of elastomers. *Journal of Engineering Mechanics*, 133(11):1162–1170, 2007.

[108] KL Shen, TT Soong, K.C. Chang, and ML Lai. Seismic behaviour of reinforced concrete frame with added viscoelastic dampers. *Engineering Structures*, 17(5):372–380, 1995.

[109] P.S.B. Shing and S.A. Mahin. Experimental error propagation in pseudodynamic testing. Technical report, College of Engineering, University of California, Berkeley, California, 1983.

[110] S. Silvestri, G. Gasparini, and T. Trombetti. A five-step procedure for the dimensioning of viscous dampers to be inserted in building structures. *Journal of Earthquake Engineering*, 14(3):417–447, 2010.

[111] Clive Siviour. Lecture notes in polymers, 2017. University of Oxford.

[112] R. I. Skinner, J. M. Kelly, and A. J. Heine. Hysteretic dampers for earthquake-resistant structures. *Earthquake Engineering and Structural Dynamics*, 3(3):287–296, 1974.

[113] RI Skinner, JM Kelly, and AJ Heine. Hysteretic dampers for earthquake-resistant structures. *Earthquake Engineering & Structural Dynamics*, 3(3):287–296, 1974.

[114] Tsu T Soong and Gary F Dargush. *Passive energy dissipation systems in structural engineering*. Wiley, 1997.

[115] TT Soong. Active structural control: theory and practice. 1990. *Essex, UK: Longman Scientific and Technical*.

[116] TT Soong and ML Lai. Correlation of experimental results with predictions of viscoelastic damping for a model structure. In *Proceedings of Damping*, volume 91. San Diego, California:[sn], 1991.

[117] D.P. Stoten and E.G. Gómez. Adaptive control of shaking tables using the minimal control synthesis algorithm. *Philosophical Transactions of the Royal Society of London A: Mathematical, Physical and Engineering Sciences*, 359(1786):1697–1723, 2001.

[118] R.H. Sues, Y.K. Wen, and A.H.S. Ang. Stochastic evaluation of seismic structural performance. *Journal of Structural Engineering*, 111(6):1204–1218, 1985.

[119] P. Summers, P. Jacob, J. Marti, G. Bergamo, L. Dorfmann, G. Castellano, A. Poggianti, D. Karabalis, H. Silbe, and S. Triantafillou. Development of new base isolation devices for application at refineries and petrochemical facilities. In *13th World Conference on Earthquake Engineering, Vancouver, BC, Canada*, pages 1–6, 2004.

[120] L.M. Sun, Y. Fujino, P. Chaiseri, and B.M. Pacheco. The properties of tuned liquid dampers using a TMD analogy. *Earthquake engineering & structural dynamics*, 24(7):967–976, 1995.

[121] Chang S.Y. A time integration pseudodynamic algorithm. In *Proceedings of the 11th World Conference on Earthquake Engineering, Paris*, volume Rotterdam: A.A. Balkema.

[122] M.D. Symans and M.C. Constantinou. Semi-active control systems for seismic protection of structures: a state-of-the-art review. *Engineering structures*, 21(6):469–487, 1999.

[123] Alastair T. *Testing Buildings to Destruction*, 2015 (accessed September 19, 2016). `http://www.alatown.com/testing-buildings-destruction/`.

[124] Horiuchi T., Nakagawa M., Sugano M., and Konno T. Development of a real-time hybrid experimental system with actuator delay compensation. In

Eleventh World Conference on Erthquake Engineering, volume paper 660, 1996.

[125] Teramoto T., Kitamura H., and Ozaki H. Practical application of high-damping rubber dampers to a slender building. In *11th World Conference on Earthquake Engineering, 11WCEE 1996*, volume 1801, 1996.

[126] Vesna T. *Force based Element vs.Displacement-based Element*, 2011 (accessed February 3, 2016). `http://opensees.berkeley.edu/wiki/images/c/c5/FBEvsDBE.pdf`.

[127] W Taniwangsa and JM Kelly. Studies on seismic isolation for housing in developing regions. In *Proceedings of the 11th World Conference on Earthquake Engineering, Acapulco, Mexico*, 1996.

[128] R.S. Thyagarajan. Modeling and analysis of hysteretic structural behavior. 1989.

[129] P. J. Torvik and R. L. Bagley. On the appearance of the fractional derivative in the behavior of real materials. *Journal of Applied Mechanics, Transactions ASME*, 51(2):294–298, 6 1984.

[130] Keh-Chyuan Tsai, Huan-Wei Chen, Ching-Ping Hong, and Yung-Feng Su. Design of steel triangular plate energy absorbers for seismic-resistant construction. *Earthquake spectra*, 9(3):505–528, 1993.

[131] RG Tyler. Tapered steel energy dissipators for earthquake resistant structures. *Bulletin of the New Zealand National Society for Earthquake Engineering*, 11(4):282–294, 1978.

[132] E.E. Ungar and E.M. Kerwin Jr. Loss factors of viscoelastic systems in terms of energy concepts. *Journal of the Acoustical Society of America*, 34(7):954–957, 1962.

[133] E.H. Vanmarcke and D.A. Gasparini. Simulated earthquake ground motions. In *Structural mechanics in reactor technology*. 1977.

[134] M. I. Wallace, J. Sieber, S. A. Neild, D. J. Wagg, and B. Krauskopf. Stability analysis of real-time dynamic substructuring using delay differential equation models. *Earthquake Engineering & Structural Dynamics*, 34(15):1817–1832, 2005.

[135] GB Warburton and EO Ayorinde. Optimum absorber parameters for simple systems. *Earthquake Engineering & Structural Dynamics*, 8(3):197–217, 1980.

[136] D. Way, B. Taylor, T. Dooley, and G. Stice. Seismic retrofit of the trans world bank building with the use of friction dampers for energy dissipation. In *Proceedings of the 5th US National Conference on Earthquake Engineering*, volume 1, pages 765–774, 1994.

[137] Y. K. Wen. Method for random vibration of hysteretic systems. *Journal of the Engineering Mechanics Division*, 102(2):249–263, 1976.

[138] Yi-Kwei Wen. Method for random vibration of hysteretic systems. *Journal of the engineering mechanics division*, 102(2):249–263, 1976.

[139] A.S. Whittaker, V.V. Bertero, C.L. Thompson, and L.J. Alonso. Seismic testing of steel plate energy dissipation devices. *Earthquake Spectra*, 7(4):563–604, 1991.

[140] M. S. Williams and A. Blakeborough. Laboratory testing of structures under dynamic loads: an introductory review. *Philosophical Transactions of the Royal Society of London A: Mathematical, Physical and Engineering Sciences*, 359(1786):1651–1669, 2001.

[141] A.S. Wineman and K.R. Rajagopal. *Mechanical response of polymers: an introduction*. Cambridge University Press, 2000.

[142] CW Wong, YQ Ni, and SL Lau. Steady-state oscillation of hysteretic differential model. i: Response analysis. *Journal of engineering mechanics*, 120(11):2271–2298, 1994.

[143] Jin Kyu Yu. *Nonlinear characteristics of tuned liquid dampers*. PhD thesis, 1997.

[144] Y. Yu, Y. Li, J. Li, and X. Gu. A hysteresis model for dynamic behaviour of magnetorheological elastomer base isolator. *Smart Materials and Structures*, 25(5):055029, 2016.

[145] R.H. Zhang, T.T. Soong, and P. Mahmoodi. Seismic response of steel frame structures with added viscoelastic dampers. *Earthquake engineering & structural dynamics*, 18(3):389–396, 1989.

[146] F. Zhu, J. Wang, F. Jin, M. Zhou, and Y. Gui. Simulation of large-scale numerical substructure in real-time dynamic hybrid testing. *Earthquake Engineering and Engineering Vibration*, 13(4):599–609, 2014.